Three-dimensional porous scaffolds for cell culture and SERS sensing

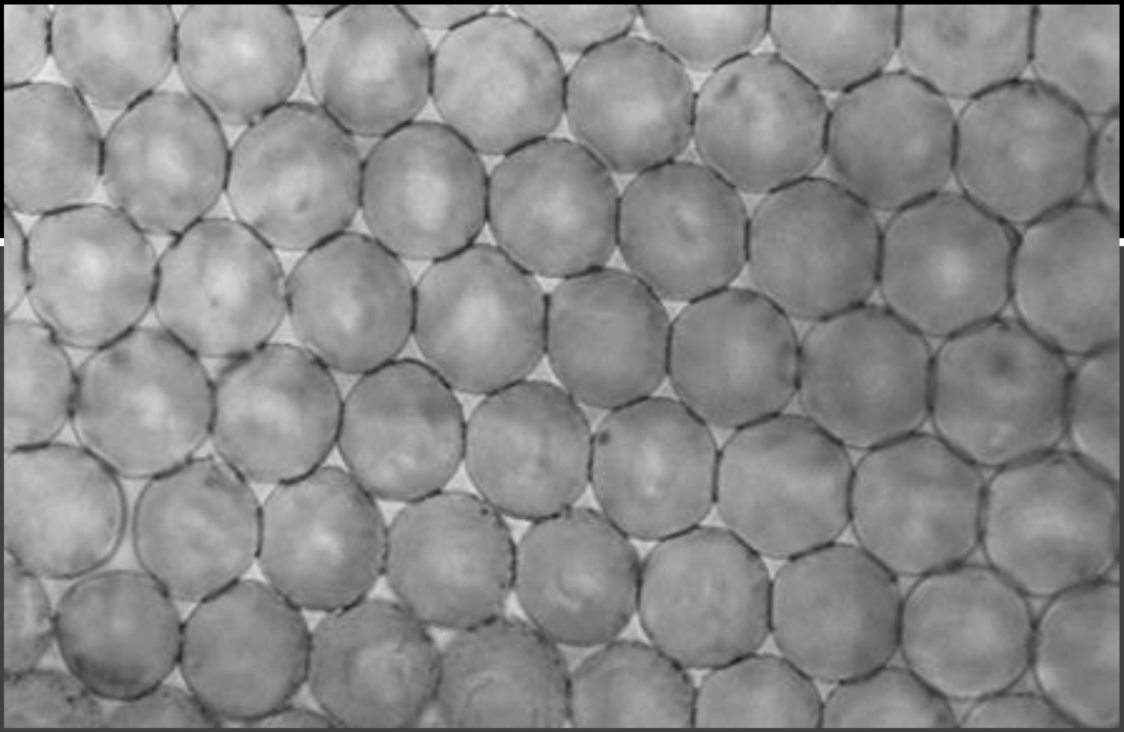

Christian Vila Parrondo

Supervised by: Prof. Luis Liz-Marzán,
Dr. Clara García Astrain

Donostia-San Sebastián, 2023

eman ta zabal zazu
Universidad del País Vasco
Euskal Herriko Unibertsitatea

Three-dimensional porous scaffolds for cell culture and SERS sensing

PhD thesis
Christian Vila Parrondo

Supervised by:
Prof. Luis Manuel Liz Marzán
Dr. Clara García Astrain

eman ta zabal zazu

Universidad del País Vasco
Euskal Herriko Unibertsitatea

Donostia-San Sebastián, 2023

Three-dimensional porous scaffolds for cell culture and SERS sensing

Manuscript submitted to the University of the Basque Country

For the degree of Doctor in Sciences

Presented by Christian Vila Parrondo

Under supervision of:

Prof. Luis Manuel Liz Marzán (CIC biomaGUNE)

Dr. Clara García Astrain (CIC biomaGUNE)

CIC biomaGUNE
MEMBER OF BASQUE RESEARCH
& TECHNOLOGY ALLIANCE

eman ta zabal zazu
Universidad del País Vasco
Euskal Herriko Unibertsitatea

"In this life you always start with a "No", all you can do is fight for the "Yes""

My mother, Elena Parrondo Avila

Agradecimientos

Durante estos 4 años de doctorado muchas han sido las personas que me han acompañado y ayudado a vivir una experiencia inolvidable. Primeramente, quería agradecer a Luis M. Liz Marzán por haberme permitido realizar mi tesis en su grupo de investigación. El poder haber trabajado en un proyecto de investigación tan puntero e interesante me ha ayudado a poder aprender y mejorar como investigador. Los conocimientos y experiencia que he podido conseguir durante este tiempo serán sin duda serán de gran importancia para mi futuro, muchas gracias.

Por supuesto junto con el tiempo dedicado a toda esta experiencia no puedo olvidar de mencionar toda aquella gente con la que he tenido el placer de conocer y trabajar. A todos os agradezco el haber compartido conmigo este tiempo tan único e importante para mí. ¡Empezando con la gente del laboratorio! Elisa y Javi: ¡enhorabuena por vuestros doctorados! Han sido más que merecidos de verdad. Muchas gracias por los momentos de tranquilidad y charlas que hemos tenido incluso en épocas de estrés importantes. Elisa, sin duda tu compañía desde que empezamos el doctorado a la vez ha sido una suerte muy grande para mí y como amigo espero lo mejor en tu futuro. Todas las charlas que hemos tenido y tus palabras de apoyo han sido sin duda de gran ayuda para poder seguir y poder terminar mi época como doctorando. Y Javi; no cambies nunca XD. Esa actitud tan positiva y amigable es sin duda un don único que atrae a la gente y les permite vivir momentos de verdadera alegría. Lo sé porque soy uno de ellos jaja. A todos los compañeros que he ido conociendo durante mi tiempo en el grupo, tanto los que aún están como los que ya han seguido con sus vidas en otros lugares: Pablo, David, Uxue, Mathias, Vished, Cristina, Paula, Isa, Malou, Judith, Bea, Ana… gracias por aportar vuestro grano de arena en el grupo creando un ambiente muy amigable y cómodo. Personas como vosotros no se encuentran a menudo y os deseo lo mejor. Claramente también quería mencionar a Carlos y a Christian Kuttner. Aparte de lo profesional como investigadores, el poder hablar de otros temas como videojuegos, parodias, hobbies etc. han sido momentos de gran alegría que siempre me permitían descansar y ver las cosas de manera más positiva. Carlos de verdad que eres una alegría de persona (y no lo digo por tu risa tan contagiosa XDD). Haber compartido esos momentos de paz y risas ha sido un verdadero placer. Te deseo lo mejor.

A la gente que he tenido más próxima durante este tiempo y que sin duda su ayuda y apoyo han sido lo más importante durante esta etapa de mi vida. Clara, sin duda no puedo estar más agradecido de lo que estoy. Desde el momento en que te ofreciste para ayudarme con mis progresos en la tesis he podido disfrutar mucho más de toda esta experiencia. Recuerdo que fue cerca de Navidades cuando decidiste acompañarme y guiarme para crear lo que es ahora mi tesis. Para mi ese fue el regalo más preciado que tuve durante todo el año y ha sido un placer el poderte conocer y poder trabajar contigo. Todos los consejos, charlas y enseñanzas combinadas con tu buen humor y suavidad han hecho de esta época mucho más agradable y enriquecedora. ¡Muchas gracias por todo este tiempo y por toda la paciencia que has tenido conmigo! (sé que no ha sido nada fácil, jaja) Te deseo todo lo mejor en tu carrera y ahora como madre!

A mi querida Ana Sánchez, por dónde empezar y sobre todo hasta donde parar. Si tuviera que darte la gracias por cada cosa que has hecho por mi esta parte sería más larga que la propia tesis XD. No se puede describir en palabras lo agradecido que estoy contigo desde un nivel profesional hasta como persona. Has sido la persona que más me ha apoyado en esta etapa tan difícil de mi vida. Desde el momento que empecé fuiste la primera en enseñarme, explicarme el porqué de las cosas y demostrarme lo profundo e interesante que puede llegar a ser la investigación. Por supuesto muchas gracias por tu paciencia y por las más de mil veces que me repetiste como hacer correctamente algunos procedimientos... prometo que ya me han quedado claro jaja. El dedicarme tanto de tu tiempo, tanto en enseñanzas como en compañía como amiga, en tantos momentos difíciles ha sido sin duda la razón principal que a día de hoy puedo estar escribiendo estas palabras. Muchas gracias por tu amabilidad, simpatía y sobre todo por ser como eres. Por favor no cambies nunca. Espero en estos tiempos futuros poder seguir contando contigo como amiga. Te deseo todo lo mejor en esta vida, que sin duda te mereces todo y más. ¡Y ya me dirás si escribes el libro! Por supuesto querré que me lo firmes el primero XD.

Y finalmente quería dedicarle estas últimas palabras a mi familia, muy especialmente a mi madre. Aunque estos han sido de los años más difíciles de nuestras vidas, has sido capaz de continuar apoyándome con todo cada día sin descanso. Puedo decir de todo corazón que no puedo estar más agradecido de ser tu hijo. Aun estando lejos de casa, el poder hablar contigo ya me traía momentos de tranquilidad que me ayudaron a seguir y pensar de manera optimista que cada paso que se hace en esta vida vale la pena. No existen las palabras para expresar lo orgulloso que estoy de ti y de lo mucho que significan para mí estos momentos. El poder ahora mismo escribir estas palabras y no arrepentirme de nada te lo debo a ti. Te quiero mucho. Por supuesto también dedico unas últimas palabras a nuestras mascotas, Shiro y Lucky, por darnos tantas alegrías cada día. Y por último también a Queca, mi querida perrita que ha estado conmigo en todas mis épocas como estudiante: todo mi amor y título que tengo también es tuyo, ahora y siempre.

Moltes gràcies per tot!!!

Contents

Resumen

El objetivo principal de esta tesis ha consistido en el desarrollo de estructuras 3D porosas para su aplicación como cultivos celulares *in vitro*. Juntamente con su aplicación como soporte celular, los soportes también han sido diseñados para contener nanopartículas de oro en su interior, adquiriendo así la capacidad como biosensor, usando la espectroscopía Raman mejorada en superficie (SERS) como método de análisis. En comparación con otros soportes convencionales para cultivo celular, el uso de materiales porosos ha demostrado ser capaz de recrear microambientes celulares más realistas debido a sus propiedades de difusión (incluyendo oxígeno, nutrientes y biomoléculas) en todo el complejo celular.

Con relación al estudio de células dentro de las estructuras 3D, una de las principales desventajas es el difícil acceso a las células debido a su confinamiento. Hasta la fecha, la mayoría de técnicas aplicadas para analizar dichos sistemas tendían a ser demasiado invasivas, llegando a causar daños a las propias células o degradando el propio soporte. Por este motivo, alternativas como la microscopia Raman resultan de gran utilidad para realizar dichos estudios de una manera menos invasiva. La técnica de SERS permite obtener señales Raman amplificadas haciendo uso de las propiedades plasmónicas de nanopartículas (principalmente de oro). Esta estrategia hace uso de la interacción de una fuente de luz externa con los plasmones superficiales de dichas nanopartículas metálicas.

Dicha interacción de resonancia de la luz incidente con los electrones de conducción da lugar a un incremento del campo electromagnético en la superficie de las nanopartículas, que a su vez incrementa la señal Raman de moléculas adsorbidas cerca de la superficie metálica. Este mecanismo permite la diferenciación de señales Raman previamente demasiado débiles, requiriendo solamente de una fuente de luz externa. Teniendo en consideración dichas estrategias, los soportes han sido construidos para combinar su capacidad como cultivo celular y recrear ambientes adecuados al tipo celular de estudio, junto con la detección de biomoléculas presentes en el medio celular, mediante métodos no invasivos para las células.

Con estos objetivos, para esta tesis se han construido diferentes soportes, principalmente usando estrategias de impresión 3D y réplicas negativas (conocidas como ópalos inversos). En un primer escenario, se ha desarrollado un sistema impreso para recrear un caso de infección de hueso, pudiendo estudiar así la presencia de biomoléculas secretadas por la especie infecciosa, en este caso *Pseudomonas Aeruginosa*. Por otra parte, el segundo soporte (ópalo inverso) ha

servido para intentar recrear un modelo de cáncer. En este sistema, se han realizado estudios tanto de detección de biomoléculas presentes en el ambiente celular como de imagen empleando nanopartículas combinadas con moléculas Raman, funcionando como agentes de contraste para imagen (SERS tags). La creación de estos soportes debe ser de utilidad como referencia para el desarrollo de nuevos sistemas, capaces de obtener información más precisa en escenarios biológicos *in vitro* más "realistas". Además, se ha pretendido demostrar la versatilidad de SERS como técnica de biodetección en ambientes celulares en tres dimensiones.

A continuación, se presenta un breve resumen del contenido de cada uno de los capítulos en los que se divide esta tesis.

En el **Capítulo 1** se presenta la introducción general de los aspectos relacionados con el diseño de soportes para modelos celulares en 3D, especificando los requisitos que deben cumplir estos soportes y describiendo los materiales y técnicas más representativas empleadas para la fabricación de estos. Además, se especifican las principales limitaciones de las actuales técnicas de detección e imagen en sistemas 3D, así como la necesidad de implementar nuevas técnicas que permitan un mejor estudio de la complejidad de estos modelos. Por último, se plantea el uso de la nanotecnología y la espectroscopía SERS como herramienta de bionálisis y bioimagen en este tipo de sistemas como se resume a continuación.

Durante las últimas décadas ha habido un creciente interés en el campo de la biomedicina, centrado en entender los mecanismos que tienen lugar durante el crecimiento celular y la curación del tejido. El tener una mejor comprensión de dichos procesos ayudaría en el desarrollo de nuevas técnicas y tratamientos para poder afrontar los retos de la medicina actual. Actualmente, para poder estudiar dichos escenarios se hace uso de modelos *in vivo* e *in vitro*. Aunque los modelos *in vivo* permiten obtener información más realista en comparación con otras estrategias, las restricciones para el uso de animales, así como las limitaciones de estos modelos no siempre permiten obtener información trasladable al ámbito clínico. Por otro lado, la investigación realizada durante los últimos años usando estrategias *in vitro* ha permitido realizar importantes descubrimientos empleando modelos más sencillos. No obstante, la mayoría de estas estrategias han estado estandarizadas y limitadas a soportes en solo dos dimensiones. Dichos soportes no son capaces de proveer a las células con los estímulos necesarios para recrear un ambiente similar al caso real. Por este motivo, uno de los mayores puntos de interés en la investigación biomédica se centra en el desarrollo de nuevas estructuras celulares en tres dimensiones.

Los soportes 3D para estudios celulares *in vitro* se han convertido en un objetivo de gran interés biomédico debido a sus capacidades para recrear un ambiente más próximo al caso *in vivo*. En comparación con estrategias clásicas en dos dimensiones, estos sistemas son capaces de promover interacciones entre células adyacentes y junto a las paredes del soporte. Dichas interacciones permiten la estimulación de las células y, por ende, la formación de complejos celulares más realistas. Para poder recrear tales escenarios, las propiedades del soporte tienen que ser adecuadas al tipo celular, teniendo en cuenta diferentes factores como la biocompatibilidad, las propiedades mecánicas y la morfología del propio sustrato. Todas estas características pueden ser controladas mediante el método de fabricación, además de por la gran variedad de materiales aplicables para cultivos celulares. En el capítulo 1 se especifican con más detalles las ventajas y desventajas de cada sistema, junto con las características requeridas para obtener un soporte adecuado para estudios *in vitro* con células.

De entre los diferentes tipos de soportes celulares tridimensionales actualmente disponibles, se ha puesto especial interés en aquellas estructuras que tengan cierta porosidad. Dichos soportes porosos han demostrado proporcionar mejores características que otros sistemas, dando la capacidad de promover la difusión de oxígeno, nutrientes y células, a través de toda la estructura 3D. Para crear una porosidad controlable existen diversos métodos en los que se incluye la impresión 3D, la creación de emulsiones, la infiltración con aire o fluidos supercríticos, además del uso de partículas sólidas como molde. Todas estas estrategias permiten obtener estructuras con una red interconectada de poros que facilita la formación de medios celulares estables y adecuados al tipo celular estudiado.

A pesar de todas las ventajas mencionadas anteriormente, este tipo de estructuras más delimitadas dificulta el estudio de las células debido a su confinamiento, impidiendo su visualización y dificultando el acceso para su análisis. Por este motivo, se necesitan nuevas estrategias no invasivas que permitan superar estas limitaciones y poder estudiar el comportamiento celular sin alterar el microambiente celular. Con este objetivo, la nanotecnología se ha convertido en un tema de gran interés gracias a la pequeña dimensionalidad de los nanomateriales y su amplio margen de aplicación. De entre los diversos nanomateriales creados hasta la actualidad, las nanopartículas metálicas (especialmente de oro y plata) han demostrado tener ventajas importantes en la investigación biomédica. Dichas propiedades no solamente dependen de su alta biocompatibilidad sino también de sus propiedades conductoras y ópticas. Este tipo de nanopartículas han demostrado ser capaces de interaccionar con fuentes de luz externas, induciendo la oscilación resonante de sus electrones localizados en la superficie, también conocido como resonancias plasmónicas superficiales localizadas (LSPR). Este comportamiento puede ser usado para la detección de moléculas situadas en su proximidad, estrategia que recibe el nombre de espectroscopía Raman mejorada en superficie (SERS por sus siglas en inglés).

Por estas razones, SERS ha sido considerada como una alternativa menos invasiva para la detección y el estudio de biomoléculas presentes en el microambiente celular. Brevemente, la técnica de SERS se basa en la adquisición de señales Raman más intensas que con el método convencional haciendo uso de las propiedades plasmónicas de nanopartículas (especialmente hechas de oro). Estos nanomateriales pueden interactuar en resonancia con una fuente de luz incidente, creando un incremento sobre la señal Raman de biomoléculas localizadas cerca de la superficie de dichas nanopartículas. De esta manera, es posible detectar diferentes tipos de analitos que suelen tener una señal Raman débil, obteniendo así una información química única sin la necesidad de estrategias externas. Por este motivo, el interés de este trabajo ha sido el combinar esta técnica con soportes 3D para crear sistemas biocompatibles para biodetección e imagen celular, como se explicará en los siguientes capítulos.

En el **Capítulo 2** se propuso construir una estructura 3D capaz de recrear un ambiente adecuado para la formación de tejido óseo y poder estudiar un fenómeno de infección de hueso, originado por la bacteria *Pseudomonas Aeruginosa*. El soporte ha estado compuesto de una matriz cerámica (hecha de alúmina) construida usando impresión 3D. Para proporcionar al soporte la capacidad como biosensor para SERS, la estructura impresa se cubrió de una membrana de polímero que serviría tanto para alojar las nanopartículas plasmónicas como para reforzar la biocompatibilidad del soporte.

Las tintas para impresión 3D se sintetizaron de forma que proporcionasen porosidad interna y favoreciesen estímulos para las células óseas que se cultivarían posteriormente. Dichas tintas se obtuvieron mediante el uso de emulsiones, combinando el uso de un material cerámico con moléculas anfifílicas y polímeros, para controlar las propiedades viscoelásticas de las diferentes tintas. Mediante diversos ensayos en los que se variaron las concentraciones de los diferentes componentes, las pastas cerámicas obtenidas se pudieron imprimir mediante impresión 3D, creando una estructura sólida (tras sinterizar) con espaciados internos entre líneas. Además de estos espacios, el uso de emulsiones para la síntesis de la tinta facilitó la obtención de una red interna interconectada de poros con diámetros micrométricos. Estas dimensiones estaban dentro del rango deseado para crear puntos de contacto con las células, mientras que se evitaba su difusión hacia el interior del material cerámico.

Para la capacidad biosensora del soporte se usaron nanopartículas de oro con su LSPR localizada en torno a 785 nm. Este criterio era necesario para estar en resonancia con el láser incidente durante los estudios de SERS y para trabajar dentro del rango de longitudes de onda que evita daños en células y tejidos, también conocido como ventana biológica. La matriz polimérica debía estar compuesta de materiales que fueran biocompatibles y translúcidos, para asegurar la supervivencia de las células y permitir el paso de la luz dentro de la estructura. De entre diversos candidatos, se escogió la gelatina metacrilada (GelMA) debido a su mayor facilidad de manipulación para cubrir el cerámico y, posteriormente, poderse entrecruzar bajo luz ultravioleta. La adición de las nanopartículas plasmónicas dentro del gel demostró no afectar demasiado a la integridad de este, mientras que las nanopartículas se mantenían dispersas sin necesidad de ningún recubrimiento especial.

El sistema compuesto demostró tener capacidad biosensora para SERS, tanto para azul de metileno como para el metabolito de comunicación bacteriana piocianina (PCN), esta última hasta concentraciones de 1 μM. Estudios realizados con incubación con bacterias *Pseudomonas Aeruginosa* indicaron que el soporte era capaz de identificar la presencia de PCN secretada por las propias bacterias. Dicha información se pudo utilizar para obtener mapas de la estructura, pudiendo identificar y localizar la presencia de la biomolécula de interés en áreas tanto de la superficie como del interior del soporte (**Figura 1**).

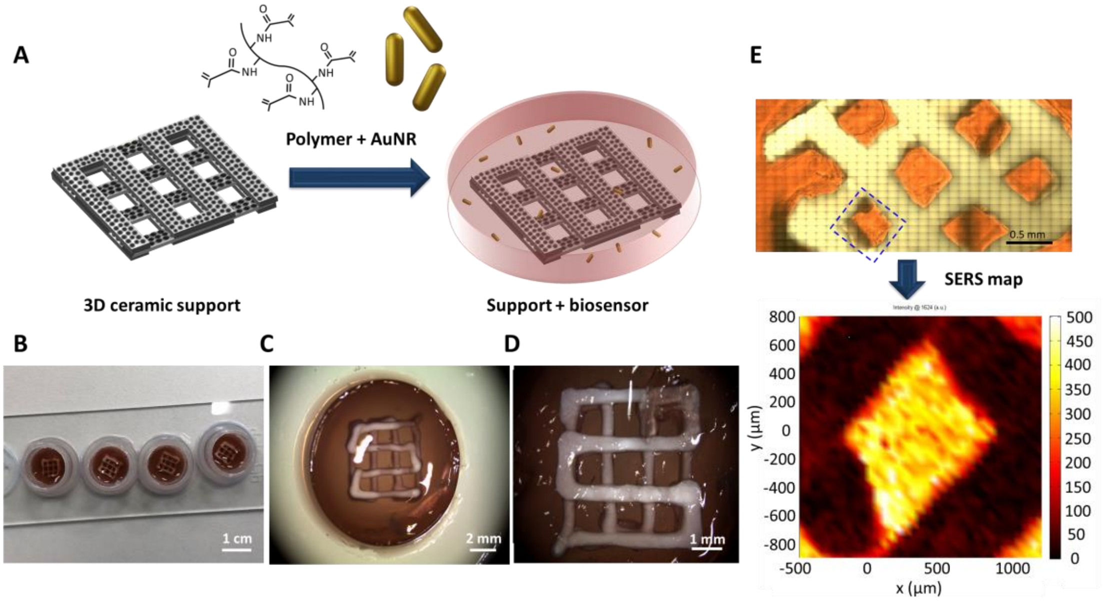

Figura 1. Combinación del soporte cerámico impreso con la membrana polimérica cargada con nanopartículas plasmónicas. **A)** Esquema de la preparación del soporte. **B-D)** Imágenes ópticas del soporte cerámico-polímero (B: imagen general, C: vista desde arriba, D: vista desde abajo). **E)** Detección SERS de azul de metileno (100 μM) dentro del soporte. Se muestran la imagen óptica de la zona estudiada y el mapa recreado usando la señal SERS a 1624 cm^{-1}.

Finalmente, respecto a la utilidad del soporte para estudios con células óseas, se observó que, aun siendo perfectamente biocompatible con las células de interés, el soporte debería tener mayor afinidad para asegurar la adhesión en la superficie del componente cerámico, de cara a imitar al hueso. Con este propósito se propuso recubrir la estructura cerámica con una capa de proteínas (colágeno y fibronectina), que favoreció la adhesión de células de hueso.

En el **Capítulo 3** se emplearon otro tipo de estructuras para recrear un microambiente celular adecuado, en este caso, para un modelo de cáncer. El método de síntesis de esta estructura se basa en el uso de moldes, compuestos de capas ordenadas de micropartículas (normalmente de poliestireno), para crear sistemas porosos con dimensiones e interconectividad determinada por las propiedades de éste. Para este sistema en concreto, se usó el tipo de estructuras conocidas como ópalos inversos. Para crear este tipo de sistemas, las micropartículas de interés son depositadas sobre una plataforma de modo que se colocan de manera ordenada y compacta. Posteriormente, el molde se somete a un tratamiento térmico para formar conexiones entre partículas adyacentes, que posteriormente crearan ventanas entre los poros de la matriz. Una vez el molde está preparado, se infiltra con el material de interés, se procesa y finalmente se elimina para obtener la réplica negativa (**Figura 2**).

Para este tipo de soporte, el objetivo clave era visualizar las células localizadas en capas interiores, de modo que se requería de un material translúcido. Para esta estrategia se utilizaron gelatina metacrilada (GelMA) y N-isopropilacrilamida (NIPAM) copolimerizada junto con 1-vinil-2-pirrolidona (NVP). Para los diferentes polímeros, la adición de nanopartículas de oro demostró tener diferentes efectos. Como se demostró previamente en el caso de GelMA, las nanopartículas eran capaces de retener su dispersión coloidal. No obstante, en presencia de NIPAM se observó cierta afinidad de las nanopartículas con el monómero, perdiendo su dispersión y alterando su LSPR dentro del gel. Para poder mantener las nanopartículas estables dentro de la disolución con NIPAM, la superficie fue parcialmente cubierta con polietilenglicol tiolado (PEG-SH), evitando así la agregación a costa de reducir el área superficial disponible para su uso como sensor.

Ambos polímeros demostraron poseer una adecuada biocompatibilidad y capacidad como sensores de SERS (usando azul de metileno como control). No obstante, la visualización de las capas internas del ópalo inverso sólo fue posible usando el polímero P(NIPAM-co-NVP). Los ópalos inversos producidos con este material demostraron buenas propiedades para la detección por SERS de moléculas modelo como el azul de metileno y el 4-aminotiofenol, siendo posible recrear imágenes tridimensionales usando la señal SERS adquirida. En dichas imágenes, fue posible diferenciar la forma circular/esférica de los poros internos. Esta información indicó que la señal provenía del contorno de las cavidades, manteniendo las nanopartículas fuera del alcance de las células a incorporar dentro de las mismas.

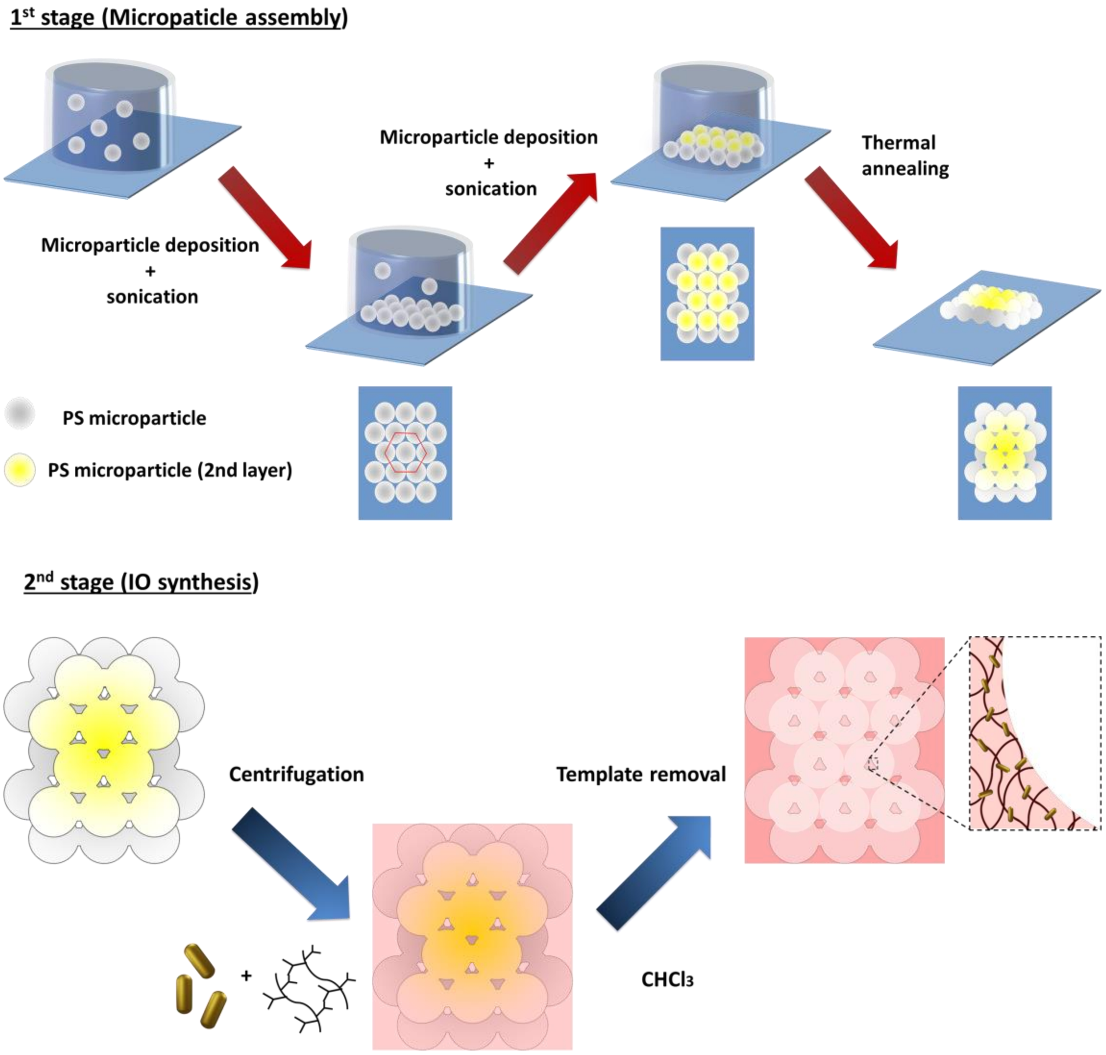

Figura 2. Esquema para la preparación de ópalos inversos. Inicialmente se crea un molde formado por estructuras ordenadas de micropartículas (normalmente de poliestireno). Las micropartículas se añaden sobre de una base donde, bajo sonicación suave, son depositadas como capas ordenadas. Este proceso incluye un tratamiento térmico para consolidar la estructura y formar "cuellos" entre partículas adyacentes. En la segunda etapa, el molde es infiltrado con el compuesto con el que se prepara el soporte. Finalmente, la estructura es consolidada y el molde es eliminado para obtener una porosidad interna basada en la réplica negativa de este.

Posteriormente, los cultivos celulares de células cancerígenas en estos materiales demostraron que las células se mantenían perfectamente adheridas a las cavidades del soporte, incluso siendo capaces de difundir hasta capas inferiores. Dichos ensayos permitieron mantener las células vivas durante un periodo de hasta 21 días, demostrando así la posibilidad de realizar estudios de larga duración.

En este sistema, además del uso de nanopartículas como sensores, se estudió una segunda estrategia para aplicar estos modelos 3D en bioimagen. El objetivo de este sistema consistía en el uso de nanopartículas decoradas con moléculas con alta señal Raman (SERS tags) como agentes de contraste, pudiendo así recrear imágenes de SERS tanto del soporte como de las células localizadas en su interior. Para este método, se usaron diferentes combinaciones de nanopartículas y SERS tags para poder diferenciar las señales SERS provenientes de los diferentes elementos. En el caso de las células, las nanopartículas marcadas fueron adicionalmente funcionalizadas con poliarginina a fin de facilitar su internalización celular. Usando una combinación apropiada de SERS tags fue posible recrear imágenes SERS, tanto de las cavidades del ópalo inverso como de las células en su superficie. No obstante, sería necesaria una optimización adicional de ambos sistemas para poder obtener imágenes combinadas de las células presentes dentro del soporte celular.

Abbreviations

2-Nat	2-naphthalenethiol
4-ATP	4-aminothiophenol
$AgNO_3$	Silver nitrate
AgNP	Silver nanoparticle
Al_2O_3	Alumina
APS	Ammonium persulfate
ATCC	American type culture collection
AuNP	Gold nanoparticle
AuNR	Gold nanorod
AuNSt	Gold nanostar
BIS	N,N'-methylenebis(acrylamide)
BPT	Biphenyl-4-thiol
CAD	Computer- assisted design
cDMEM	Complete DMEM
CFU	Colony forming units
CMFDA	5-chloromethylfluorescein diacetate
CPP	Cell-penetrating peptide
CTAB	Hexadecyltrimethylammonium bromide
CTAC	Cetyltrimethylammonium chloride
DIW	Direct ink writing
DMAE	N-N-dimethylaminoethanol
DPSS	Diode-pumped solid-state
ECM	Extracellular matrix
EM	Electromagnetic
EtOH	Ethanol
GelMA	Methacrylated gelatin
GFP	Green fluorescent protein
HAp	Hydroxyapatite
HCl	Hydrochloric acid
HCP	Hexagonal close-packed
hFOB	Human fetal osteoblasts
HIPE	High internal phase emulsion
HMW	High molecular weight
ICC	Inverted colloidal crystal
IO	Inverse opal
LB	Lysogenic broth
LCST	Lower critical solution temperature
LDH	Lactate dehydrogenase
LMW	Low molecular weight
LSFM	Light sheet fluorescence microscopy
LSPR	Localized surface plasmon resonance
LVE	Linear viscoelastic region
MA	Methacrylic acid

MB	Methylene blue
MTT	3-(4,5-dimethylthiazol-2-yl)-2,5-diphenyl-2H-tretrazolium bromide
MUT	Mutant
MW	Molecular weight
$NaBH_4$	Sodium borohydride
NaCl	Sodium chloride
NIR	Near-infrared
NP	Nanoparticle
NSA	Nonenyl succinic anhydride
NVP	1-vinyl-2-pyrrolidone
P(NIPAM-co-NVP)	Poly(N-isopropyl acrylamide-co-vinyl pyrrolidone)
P.Aureginosa	*Pseudomonas Aeruginosa*
PA	Propionic acid
PCL	Poly(caprolactone)
PCN	Pyocyanin
PEG	Poly(ethylene glycol)
PEG-SH	Polyethylene glycol thiolated
PGA	Poly(glycolic acid)
PI	Propidium iodide
PLA	Poly(lactic acid)
PMA	Polyisobutylene-*alt*-maleic
PNIPAM	Poly(N-isopropyl acrylamide)
PNIPAM	Poly(N-isopropylacrylamide)
PolyR	Polyarginine
PS	Polystyrene
PVA	Poly(vinyl alcohol)
QS	Quorum sensing
RaR	Raman reporter
SCF	Supercritical fluids
SEM	Scanning electron microscopy
SERS	Surface enhanced Raman scattering
SR	Swelling ratio
TCP	Tricalcium phosphate
TEM	Transmission electron microscopy
TEMED	N,N,N’,N’-tetramethylethylenediamine
UV-vis	Ultraviolet-visible
WT	Wild type
ZrO_2	Zirconia
3D	Three-dimensional
$HAuCl_4 \cdot 3\ H_2O$	Tetrachloroaurate (III) trihydrate

Motivation of the thesis

The main goal of this thesis has been the development of complex 3D porous scaffolds for Surface Enhanced Raman Scattering (SERS) sensing and imaging of complex cellular models. This thesis has been supported by the ERC Advance Grant entitled "Four Dimensional Monitoring of Tumour Growth by Surface Enhanced Raman Scattering (ERC AdG 787510, 4D BIOSERS) which focus on the use of SERS for the sensing and imaging of 3D complex tumour models.

The use of 3D supports for *in vitro* cell studies has become a major goal in current medicine research, towards the recreation of an artificial cellular environment, which closely mimics the *in vivo* scenario. Porous systems have demonstrated to provide enhanced properties due to their capacity to promote diffusion of oxygen and nutrients alongside the 3D model. Taking profit of such characteristics, porous supports have become an interesting tool towards the study of biological phenomena within a confined and controlled microenvironment. However, entrapment of cells into such 3D systems hinders their visualization and bioanalysis with currently available techniques. For this purpose, SERS is considered as a non-invasive alternative to study biological phenomena through the detection and monitoring of biomolecules present in the cellular microenvironment. Following this reasoning, porous 3D scaffolds were combined with SERS-active nanoparticles. Specifically, 3D printing and microparticle templating were chosen to create plasmonic supports aimed to study the presence of specific bioanalytes and to image the evolution of cells under diverse biological scenarios.

The thesis has then been aimed to create novel types of cellular supports with intrinsic biosensing properties. To acquire such complex systems, it has been necessary to combine both material chemistry, for building the support, and cell biology to ensure the suitability of the matrix. This research was carried out to meet all the required conditions of the support and was aimed at obtaining significant biological information through novel approaches. It should be clarified here that not all the initial goals were fully accomplished. The results presented in the thesis represent the concept behind each idea, demonstrating the suitability and capacity of combining such complex strategies and providing novel insights into biomaterials research. In this regard, the challenge of perfectly combining biodetection and scaffolds for the study of *in situ* biological scenarios still proved to remain a daunting task, therefore expecting new generations of researchers to take the baton.

In chapter 1, an introduction is given to provide an overview of all necessary requirements to create an adequate support for cell culture studies. Alongside describing such characteristics, we aimed to show some of the better currently available building strategies for 3D constructs and the utility of using novel biosensing approaches to gather further insight into cellular mechanisms for biomedical research.

In chapter 2, 3D printed supports were prepared to recreate and study a bone infection model. The scaffold was aimed to work as a support for the development of bone tissue, by seeding of bone-derived precursor cells. The combination of a ceramic-printed matrix with a polymer membrane (loaded with plasmonic nanoparticles) was then tested to monitor bacteria-secreted metabolites in an *in situ* scenario. For this project, the goal was aimed for the detection of pyocyanin (PCN), secreted by *Pseudomonas Aeruginosa*.

In chapter 3, a second strategy was developed, to study and image the evolution of a cancer model. For this biological scenario, scaffolds were prepared based on inverted colloidal crystals, also known as inverse opals, to acquire porous structures with a highly controllable porous network. The scaffold was tested using cancer cells (MCF7), to demonstrate its capabilities as long-term cellular support and to acquire SERS signals from biomolecules present in the nearby microenvironment. In addition to this strategy, the support was also combined with SERS tags to acquire 3D SERS images of both the support and the seeded cells. Such a method would provide useful information on the cell behaviour and their spatial distribution within the support, with no need for external labelling or removal of the scaffolding support.

In summary, this PhD thesis aimed at providing a new vision towards the use of 3D *in vitro* supports with intrinsic bioanalytical properties. Therefore, combination of more realistic cellular environments coupled with non-invasive biosensing strategies, such as SERS, would provide novel tools for biomedical research. The use of such scaffolds would thus reduce the need for animal models or other, more invasive, and expensive alternatives.

Chapter 1: Introduction

Over the last decades, research in the biomedical field has focused on understanding the biological mechanisms acting during cell growth and tissue repair. Further insight into cell behaviour mechanisms would allow the identification of key element factors toward the development of novel medical solutions for urgent medical challenges. To perform such studies, the current biomedical approaches make use of different strategies, commonly based on both *in vivo* and *in vitro* models. Although *in vivo* approaches – based on relevant animal models – can provide a closer insight into the real biological mechanisms present in the natural scenario, the use of living organisms, including animals, for research is clinically limited and fails to reproduce the same cellular microenvironment as in humans. In this regard, *in vitro* supports have been engineered to replicate *in vivo* conditions in a controllable environment. Nowadays, most *in vitro* cell culture assays are performed using standardized strategies based on the use of flat 2D supports.[1] Although diverse strategies have been optimized over the years per each type of cell, basic supports fail at mimicking the physicochemical properties required to properly imitate the unique characteristics present in the natural tissue.[1–3]

To overcome some of the limitations of 2D cell cultures, novel systems have been designed to better recreate the complex *in vivo* conditions, by the addition of a third dimension. The inclusion of this extra dimension permits the creation of complex matrixes where cells can further interact with each other (cell-cell interactions) and with the surrounding medium (cell-matrix interactions), while confined within a defined environment. These types of constructs, commonly regarded as 3D scaffolds, are suited with enhanced physicochemical properties to support cell culture, being capable of recreating a niche closer to what is found in the natural microenvironment. Consequently, current research is focused on the design of complex 3D cell models to better reproduce diverse biological mechanisms within an accessible and controllable biomimicking microenvironment.

1.1 2D vs 3D scaffolds: limitations and advantages of dimensions

In 2D cultures, the control over cell behaviour is mainly determined by the provided biocomponents in the cellular media and by the physicochemical nature of the flat support.[4] Standard cell cultures are generally based on simple seeding of cells onto polystyrene (PS) petri dishes, flasks or multi-well plates. The plates are then filled with cellular medium composed of a concentrated cocktail of nutrients and oxygen, higher than what is found in the natural tissue. Due to the low dimensionality of the support, cells remain far away from the adjacent ones, while being forcibly polarized onto the flat surface, thus limiting their adhesion and the formation of cell-cell interactions.[5] These effects, combined with the low control over the gradients of nutrients, inhibit cell growth and development into natural complexes composed of diverse cell populations. These alterations on the cell microenvironment tend to induce overoxygenation[6], overnutrition[7] and lack of signalling molecules[8], thus failing to obtain reliable biological data.

Therefore, the building of complex 3D structures is expected to create a controlled microenvironment capable to closely mimic the characteristics of the real scenario, promoting stimuli and specific cell interactions.[9] However, some limitations are still found in 3D cell models, which are summarized in **Table 1**.

Table 1. Advantages and limitations of 2D and 3D cell cultures

Model	Advantages	Limitations
2D	• Homogeneous cell distribution • Low background for imaging (high light penetration) • Standardized procedures (cell harvest, lysis, etc.) • High reproducibility • Free from cross-contamination	• Poor realistic model (limited cell-cell & cell-matrix interactions) • Planar cell polarization • Lack of control of extracellular matrix (ECM) (over oxygenation, overnutrition, etc.) • Basic/Limited biomaterial composition
3D	• Enhanced cell-cell and cell-matrix interactions • High biocompatibility (wide biomaterial composition) • Compatible with multiple bioanalytical techniques • High mechanical support (enhanced cell differentiation/ adhesion)	• Hard accessibility for bioanalysis (high light scattering and limited cell manipulation) • Limited gradient diffusion (oxygen, nutrients, ECM biomolecules) • High cost and specialized technique manufacturing • Poor reproducibility

In order to fully recreate an environment resembling a natural tissue, the support not only has to contain the basic nutrients to ensure cell survival but also requires recreating the tissue microenvironment, including the cell-cell and cell-matrix interactions.[10–12] Consequently, the support should provide both the necessary biochemical and physical stimuli necessary to promote cell growth, attachment, differentiation and migration (**Figure 1**)[13,14,15]. In contrast to the previously exposed standardized two-dimensional supports, addition of a third dimension delimits cell growth extent against the increased surface area of the matrix. Therefore, cells are closer to each other, allowing cellular systems to condense their own secreted biomolecules and growth factors, creating an original extracellular matrix (ECM) adequate for each type of cellular system.[16]

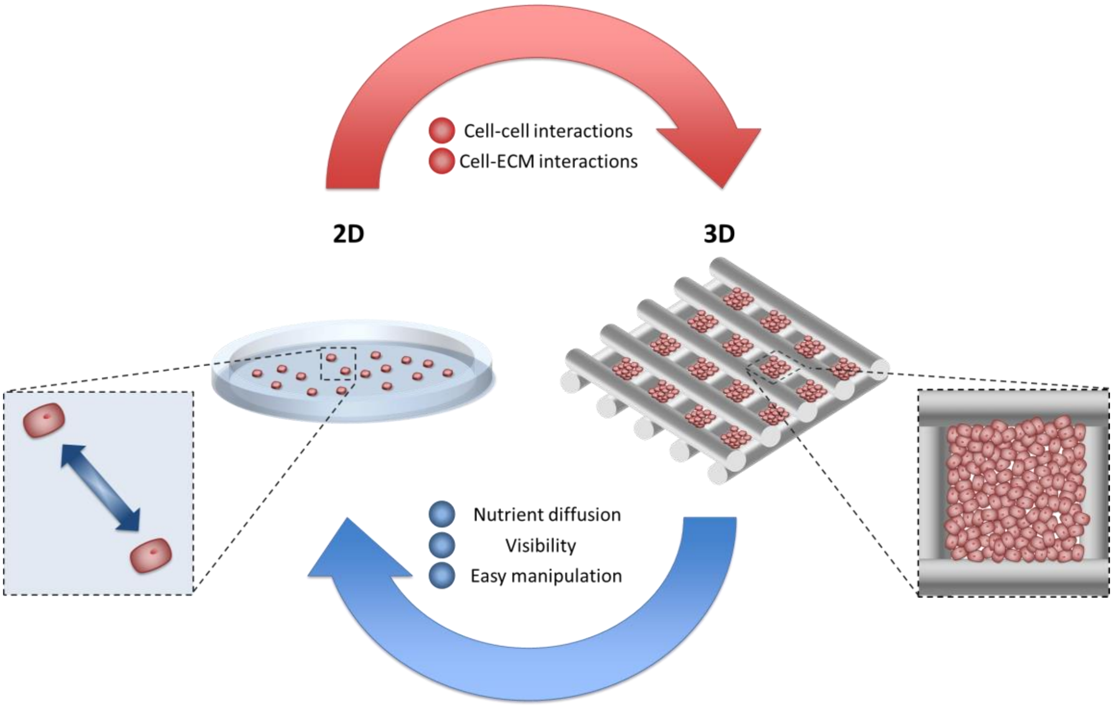

Figure 1. Schematic view of the advantages and disadvantages of 2D and 3D cell culture supports.

3D scaffolds for cell culture have been developed with different material compositions, including ceramics (e.g. zirconia, alumina and hydroxyapatite), smooth biocompatible gel-like membranes (e.g. gelatin, collagen and cellulose) or even composite mixtures.[17–19] The wide range of available materials provides additional complexity to the support, as well as specific properties such as bioactivity, internal morphology and mechanical properties, including stiffness and roughness.[20]

Despite the already mentioned advantages of 3D supports, a limiting factor observed in most 3D cell systems has been the inaccessibility to nutrients and oxygen, which impacts on cell viability.[21,22] Therefore, the support is required to promote the internal diffusion of these components to control the biomolecular environment alongside the matrix. Strategies such as building of internal porosity have been demonstrated to provide 3D complex cellular supports with interconnected empty networks able to promote gradients of oxygen, nutrients and signalling components towards the enclosed cells.[23–25]

Another major drawback that hinders the full applicability of 3D scaffolds for cellular culture is the difficulty to image and acquire biological information within the volumetric matrix. In contrast with 2D systems, in which cells are mostly exposed forming homogeneous monolayers, the presence of dense opaque walls in 3D supports hinders their visualization.[26,27] For microscopy imaging, light is scattered by the solid support, thereby reducing the amount of photons able to interact with the biological objects and reducing fluorophore excitation and fluorescence detection.[26] Moreover, the thickness of the built support also becomes a limiting factor for imaging, as microscopy objectives are limited to a certain working distance. Therefore, several improvements are still needed, such as the use of more transparent alternatives that allow for better imaging and sensing within the matrix.[28,29]

1.2 Requirements for a suitable cellular support

As mentioned in the previous section, in order to mimic the conditions present in a natural tissue, the synthetic support not only needs to work as a physical support but it is also required to contain the adequate physicochemical properties suitable for each type of cell.[30] Although there may be differences between systems, the basic characteristics defining any type of matrix can be summarized into: biocompatibility, porosity, mechanical properties and bioresorbability, which will be introduced below (**Figure 2**). [14,31–33]

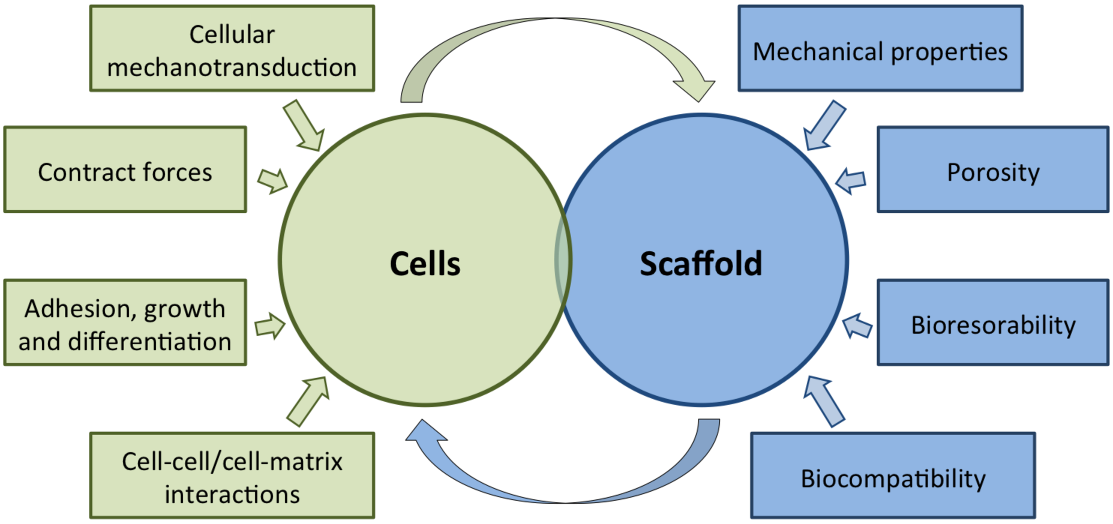

Figure 2. Summary of the required characteristics of 3D artificial supports for cell culture and cellular mechanisms involved in the evolution of the cellular system.

Porosity: The scaffold porosity should favor cell circulation within the matrix, allowing the formation of smaller cell populations within confined spaces. Moreover, the 3D matrix is required to ensure access to nutrients and oxygen towards cells. To provide such characteristics, generation of intrinsic interconnected porosity tends to be the most common approach. Ideally, the created empty channels should occupy a high volume fraction of the overall structure, with pore diameters large enough to create a flow gradient that allows constant renewal of nutrients and gases of the extracellular matrix (ECM) components.[32]

Inside a porous matrix it is possible to have pores of different sizes, ranging from few nanometers to the microscale, each one being able to provide specific properties to the whole system. The smaller sizes in pores tend to have diameters ranging from 0.3 to 100 nm. These empty windows are usually able to enhance the interactions between the matrix and the cells, thus influencing cellular properties such as cell adhesion, by increasing the available surface area.[34] Pores ranging from 0.3 to 100 µm are normally used as windows interconnecting adjacent cavities of bigger size, thus providing interconnectivity to the porous network and increasing cell diffusion by capillary forces.[35] Finally, the rest of pores are characterized by having diameters larger than 100 µm. These types of cavities are typically used as niches for cells to reside within an enclosed environment, promoting interactions between adjacent cells while allowing diffusion of oxygen and nutrients during tissue growth.[36] It is important to mention that each type of cell has its own optimal pore size for an optimal cell communication. However, there exists a limit in which the system loses the ability to work as a confined space, failing at promoting close interactions with cells, which is usually accepted for diameters larger than 300 µm.[37]

Biocompatibility: The biocompatibility of a scaffold can be defined as its ability to support cell survival and its natural biological mechanisms, without any cytotoxic effects on the growing tissue.[38] In order to acquire such a biocompatible nature, cellular supports are required to contain adequate physicochemical properties suitable for the cellular system of study.[30] *In vitro* biocompatibility is commonly evaluated using cytocompatibility tests to determine cell viability, proliferation and morphology. An important note with *in vitro* systems and biocompatibility assays is the fact that cells tend to be more sensitive in artificial niches than in the natural tissue. Following this reasoning, *in vitro* assays may show average cytotoxicity levels that do not directly correlate with damaging effects in *in vivo* scenarios.[4] Regarding the chemical biocompatibility of the synthesized matrix, this can be further optimized by post-processing methods. Functionalization with alternative biomolecules would expose other molecules towards the seeded cells, thereby retaining the morphology of the support while providing a more biocompatible surface for cells to adhere onto.[39]

Mechanical properties: Cellular supports should be able to withstand the loading after cell seeding and to handle the pressure exerted by the tissue during its development. Two different forces take place during the formation of tissue: cells apply stress on their surrounding during changes in their morphogenesis and differentiation, whereas the matrix exerts stress on cells both by direct matrix-cell interactions and through the density and stiffness of the material.[40] The extent of both stimuli becomes a factor that determines the capacity of cells to migrate, grow and differentiate. Regarding the stress applied by cells on the system, another important factor is the capacity of the support to maintain its shape during tissue growth. Small variations in the matrix morphology could influence the biological activity of the cells, limiting their natural mechanisms and hindering the suitability of the system. This behavior applies also to porous systems because the loss of internal bulk volume by empty cavities would induce a reduction in the internal mechanical forces and deformations in the matrix would change the dimensions and shape of the cavities, hindering their internal diffusion.[41] Additionally, other physical factors such as the morphology, roughness and rigidity of the support have also been shown to influence the cellular behavior, promoting cell adhesion and differentiation.[42]

Bioresorbability: This characteristic can be varied depending on the application of the system. Some types of artificial matrices are prepared to support the growing tissue over the whole process, whereas other alternatives should degrade at certain time points.[43] A simple example could be the comparison between joint implants, which will remain inert into the patient for years to hold the joints, with other temporal systems like osteosynthetic screws that are degraded after some time.[44] Following the latter example, degradation of the support becomes necessary and the chemical nature of the construct plays an important role to ensure the complete biocompatibility of the system. As an example, the degradation of metallic prosthetics over time produces an increase of inorganic salts and oxides into the adjacent tissues, therefore potentially eliciting toxic or hypersensitivity response in the body.[45,46] On the other hand, common organic materials such as polymers can be hydrolyzed by natural molecules, such as enzymes, degrading the matrix into non-toxic by-products.[47]

1.3 3D scaffold fabrication

In recent years, advances in material design have come across novel strategies for the building of 3D scaffolds. Novel supports are fabricated by combining the best knowledge and skills in materials engineering and biological sciences, to successfully recreate adequate niches for each targeted cell type. Regarding the strategies for building 3D supports, many different structures can be built by varying some characteristics such as morphology and/or chemical composition, together with the fabrication technique of choice. Therefore, the combination of multiple physical structures with diverse building materials opens the window to a wide range of solid supports with unique properties suitable for different specific applications. In the following section, the main materials and fabrication techniques for the generation of 3D scaffolds will be described. In the context of the main objective of this work, special attention will be paid to the preparation of porous supports

1.4 Materials for the synthesis of 3D supports

Biomaterials suitable for cellular studies are mainly classified, according to their chemical nature, into polymers (both of natural or synthetic origin), metals, ceramics (bioactive, bioinert or bioresorable), or composites combining more than one material type (**Figure 3**).[3]

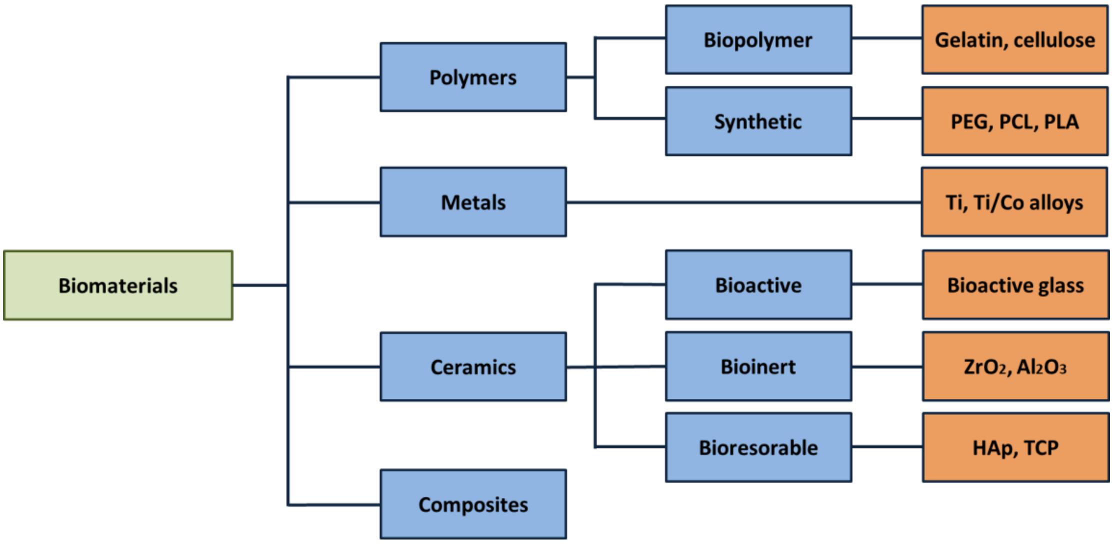

Figure 3. Classification of biomaterials for the building of cellular supports in dependence to their source and characteristics.

Natural polymers, such as gelatin, collagen, alginate, agarose or cellulose, are some of the most common materials used for designing cellular supports, due to their availability, high biocompatibility and bioactivity.[48] These biopolymers possess hydrogel-forming capacity, resulting in materials with swelling capacity, biodegradability and porosity, thus providing the system with higher diffusive characteristics. Moreover, due to their natural origin, some of them show also high affinity for biological systems, promoting cell mechanisms including cell adhesion, differentiation and migration.[49,50] Recently, the use of decellularized extracellular matrix has become very popular for the fabrication of 3D scaffolds because this material retains the main characteristic of the native tissue and helps promoting cell growth within the matrix.[51,52] On the other hand, synthetic polymers such as poly(ethylene glycol) (PEG), poly(lactic acid) (PLA), poly(glycolic acid) (PGA), poly(caprolactone) (PCL) and their copolymers have also been used for their enhanced properties. Some of the advantages of these types of polymers reside in their high degree of processing flexibility, lack of immunological effects and low toxicity of the degraded products.[18,53,54] Despite these polymers are mostly hydrophobic, therefore hindering their wetting and cellular adhesion, they can be combined with other natural polymers to improve their processability for biological applications.

Regarding other biomaterials, ceramic materials are mostly composed of metal oxide species known for their low corrosion, high hardness and high mechanical resistance.[55] Within this category, ceramics can also be divided into bioactive (bioactive glass), bioinert (alumina (Al_2O_3), zirconia (ZrO_2)) or bioresorable (hydroxyapatite (HAp) and tricalcium phosphate (TCP)), depending on their effect on cell activity.[33,56] The application of this category of materials is mainly focused on mimicking hard living tissues such as bone as implants for articulable joints. In a similar way, metals composed of multiple alloys (such as titanium (Ti) and cobalt (Co)) are usually applied in bone implants due their enhanced stability, low corrosion and high yield strength.[57,58]

Lastly, composites are biomaterials originated from a mixture of the previously mentioned materials. These combinations are able to acquire enhanced properties when compared to the individual units, such as for example the high biocompatibility of the polymer and the hardness of the ceramic.[59,60] However, there is also the risk that the combination of two different materials can accumulate cytotoxic effects from both units, thus hindering their applicability despite their enhanced mechanical properties.

1.5 Fabrication of porous scaffolds

In recent years, several building strategies have been engineered to prepare porous biomaterials applicable for cell growth. In contrast with other flat supports, the creation of an internal controlled porosity provides the system with an enhanced surface area for cells to adhere, as well as higher diffusive properties for the creation of a homogeneous extracellular microenvironment. Although these characteristics are desired in most supports, fabrication of controlled porosity still remains a challenge.[61] Among the different available strategies, some of the better performing approaches are the use of templates as sacrificial supports and the addition of secondary phases to create empty spaces within the matrix.

1.5.1 Solid sacrificial templates

One of the most used approaches towards the acquisition of internal porosity in 3D complexes is based on the use of microparticle assemblies or patterned solid structures as internal templates. After infiltrating the building material into the solid support, the template needs to be removed to reveal an internal porosity with the dimensions and interconnectivity of the removed object. A clear example of such a strategy comprises the porous 3D structures referred to as inverted colloidal crystals (ICC).[62] The building process of this type of structures derives from the use of self-assemblies of micro/nanoparticles to create ordered multi-layered templates.[63] After processing with the desired material, the template is removed creating an inverse negative replica within the support (**Figure 4**). The negative lattices then become porous matrixes with a well-defined porosity, determined by the dimensions and degree of order of the arranged particles.[64]

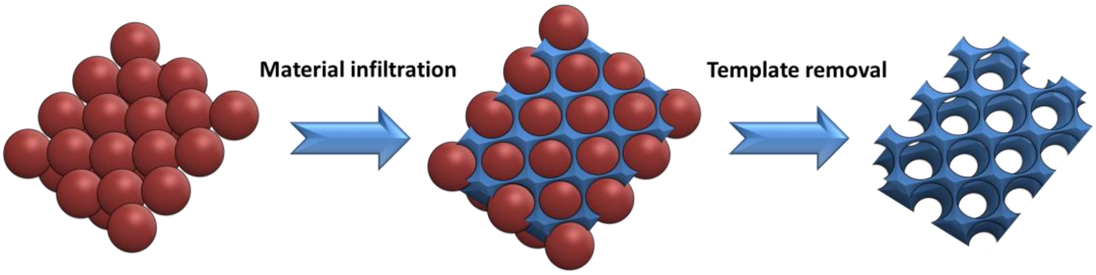

Figure 4. Schematic illustration for the building process of ICC using microparticle assemblies as sacrificial templates. The synthesis process is differentiated into 3 phases, including microparticle assembly, infiltration of the material into the template and later template removal.

The synthesis of ICC can be summarized in 3 main steps: assembly of particles into a multi-layered template, infiltration of the sol-gel building material within the template and final removal of the sacrificial template.[65] For the first process, microparticles, commonly made of polystyrene (PS) or silica, are assembled into ordered layers to create the template. Sedimentation is the most common approach for this process, by which particles are deposited at different intervals until fully occupying the dimensions of a holder. Coupling with external forces such as sonication or shaking can provide further support towards the correct ordering during microparticle deposition. Before entering the second stage, the template undergoes a process of thermal annealing in which particles are connected forming small bridges between them.

Once the template is prepared, a sol-gel solution containing the material of the final support is infiltrated within the particle assembly, filling the internal empty spaces between adjacent layers.[63,66] The infiltration process is commonly performed by soaking the template within the solution until completely filling the empty gaps. This process can be further enforced by using strategies such as centrifugation to force the diffusion of the sol-gel mixture into the template. The support is later processed to harden the infiltrated precursor and to solidify the structure. Due to the simplicity of this process, ICCs can be synthesized from a wide range of precursor materials, permitting the acquisition of specific supports with determined characteristics.[67] In the case of polymeric materials, hydrogels can be obtained by crosslinking of polymer chains or by freeze-drying, whereas inorganic supports have to undergo a sintering process at high temperature. Finally, the template is removed to create the empty negative replica within the formed matrix. This process varies depending on the chemical composition of the template. Polymer-based variants can be removed by either calcination or chemical etching while inorganic particles, such as the case of silica, can only be etched by chemical treatments. Either strategy allows to obtain ICC with a consolidated structure that can withstand the growth of the seeded cells, alongside providing specific niches to those cells.

Another commonly known strategy to acquire well-defined porosity is the use of ice crystals as sacrificial material, commonly known as ice templating.[68] Similar to the previously mentioned strategy in which microparticles are used as templates to acquire a determined internal porosity, the use of cryogenic processes is capable of creating different types of sacrificial templates from precursor aqueous solutions. Cryogenic methodologies are based on freezing precursor solutions (either organic or inorganic) to create a solid matrix from which the scaffold will be built. During the freezing process, the formation of ice crystals allows the entrapment of precursor components within a confined space delimited by ice walls.[69] After processing and later removal of the ice walls (either by freeze-drying or thawing), empty cavities are created within the support with dimensions proportional to the removed frozen walls. In contrast to ICC, in which porosity is delimited to the dimensions of the microparticle template, ice templating has the added advantage to further control the dimensions of the formed ice walls. By controlling the freezing conditions, such as temperature or the directionality of the forming spikes, the acquired negative replica can be controlled with a wide range of dimensions and morphologies.[70]

1.5.2 Emulsion templating

As the name indicates, this strategy makes use of the mixture of two immiscible phases to create a droplet system that will be used as template for the acquisition of a porous matrix.[71] This strategy, also referred at High Internal Phase Emulsion (HIPE), is able to create a high volumetric concentration of droplets that may occupy up to 74% of the total volume.[72] Emulsions are composed of two immiscible phases, in which one of them is “entrapped” within the second one, forming small droplets. The homogenous phase containing the droplets is known as the continuous phase, while the one constituted of the interconnected droplet network is referred to as the disperse phase.[73] The droplets contain a mixture of one of the phases, together with polymers or surfactants combined with solid particles that help creating the emulsion. Similarly to the above-mentioned approaches, the droplet system is used as a template to create internal cavities within the matrix. After processing and drying, the disperse phase is then removed creating a solid matrix that contains spherical cavities with the dimensions of the previous droplets (**Figure 5**).[74] An added advantage of this methodology is the possibility of creating diverse types of porous networks by varying the process conditions during the synthesis of the droplets.[75]

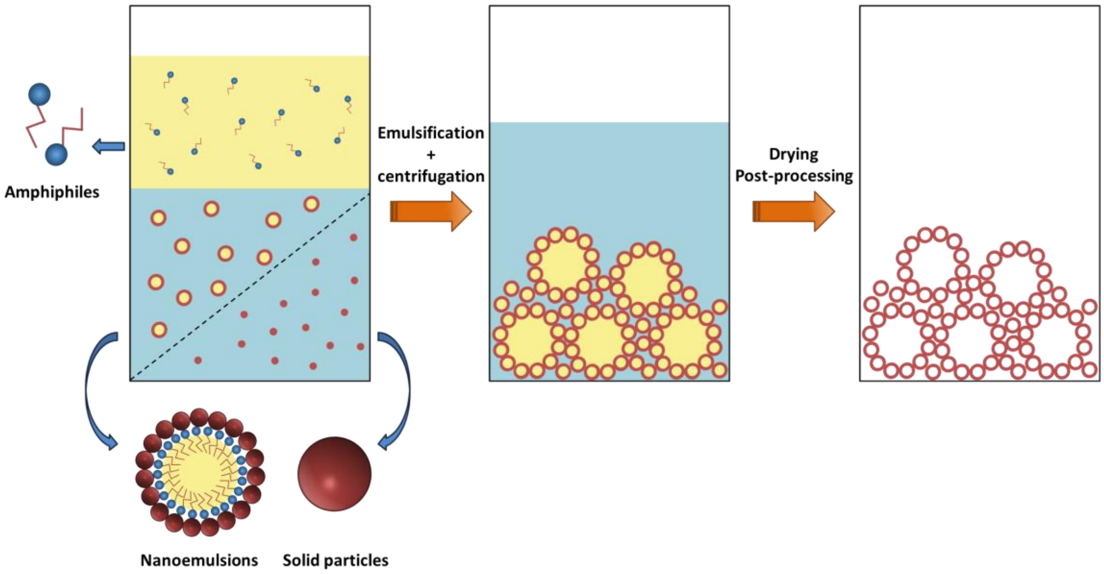

Figure 5. Schematic view of the emulsion templating processing. The final acquired porosity is comprised of both nanometric and micrometric size pores derived from the dimensions of the previous droplets.

Variations in the chemical composition and/or the mechanical emulsification allows controlling the dimensionality and population of the formed droplets. In addition to the pore dimensions, the degree of interconnectivity of the overall network is also dependent on the chemical constituents on the droplet formation. Common emulsions only dependent on surfactants can create closed pores in which each cavity is isolated form their neighbouring ones. However, by combining the droplets stabilizers with other organic materials such as polymers on the membrane, open pores can be created through the removal of the added component after scaffold processing.[76]

1.5.3 Gas foaming

This strategy makes use of gas as a template to create the internal porosity. Gas can be either injected into the solid or combined with the precursor material during block preparation to create gas bubbles inside the matrix (**Figure 6**).[77] This process can also be applied with supercritical fluids (SCF) where the added suspension can be controlled to perform at different states.[78] Therefore, this approach allows creating internal porous networks without the need of an organic/inorganic template, thereby allowing for direct manipulation with the precursor suspension.

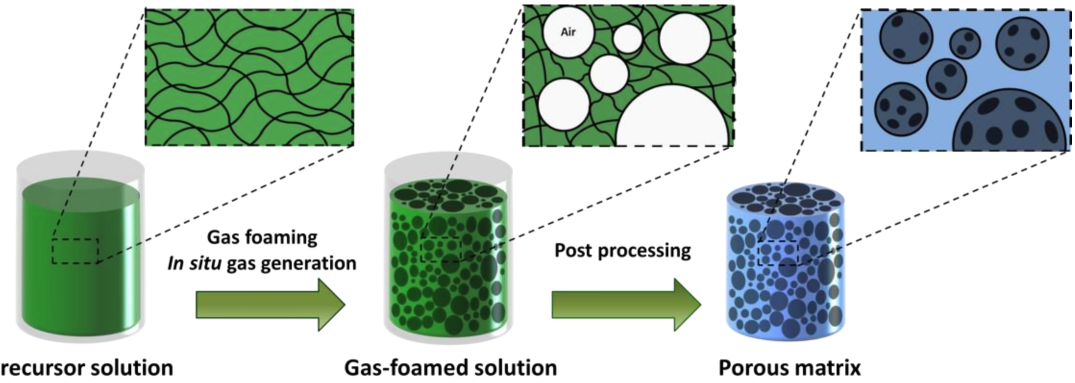

Figure 6. Diagram describing the gas foaming method. The building strategy can be either performed following chemical blowing (generation *in situ*) or physical (direct gas foaming).

Working with SCFs requires further control over several parameters, such as temperature, pressure and processing, to acquire specific interconnected porosity with defined dimensions.[79,80] Physical infiltration of the gas or fluid suspension at high pressure and temperature forces the displacement of the carbon chains in a precursor solution. Such a displacement provides room for the infiltrated material to rearrange into an extended shape, changing the crystalline structure of the complex and determining the later internal porosity. However, alterations on the crystalline structure of the polymer matrix may also change the mechanical properties of the system and their stability. This technique has the added drawback of producing pores with low interconnectivity. Nonetheless, improvements can be made by combination with other components such as polymers and micro/nanoparticles, which can create nexus to interconnect adjacent gas chambers. Regarding its suitability for the fabrication of cell supports, this approach allows adding biomolecules and growth factors within the matrix while avoiding damage of the internal structure.[81,82] Consequently, gas foaming using SCFs has proven to be a highly suitable strategy for the synthesis of complex porous supports applicable for cell studies.

1.5.4 Direct ink writing (DIW)

3D printing consists of a computer-assisted additive manufacturing process through layer-by-layer deposition of a printable ink. This strategy combines the use of printable inks as building material alongside a computer-assisted design (CAD) with 3D digital models to determine the morphology of the formed 3D support (**Figure 7**).[83] During the printing process, inks are extruded through a nozzle under an applied mechanical force, forming continuous fibres. The extruded material is then deposited onto a surface in an ordered assembly of arrays imitating the structure of the digital model.[84] Given the simplicity of this building method, one of the main advantages this system has to offer is a high compatibility with a wide range of both inorganic and organic materials.[85,86] This characteristic allows for the creation of multiple kinds of cell-compatible structures with controllable biocompatible properties, suitable for each type of cell under study.[87] In this regard, the most used materials for biomedical purposes are mainly polymers (such as thermoplastics and hydrogels) for soft materials, solid stiff ceramics (e.g., hydroxyapatite (HAp) and tricalcium phosphate (TCP)) for oxide-free and resistant prosthetics, and finally metals (mainly alloys) also for orthopaedic and dental implants.[88]

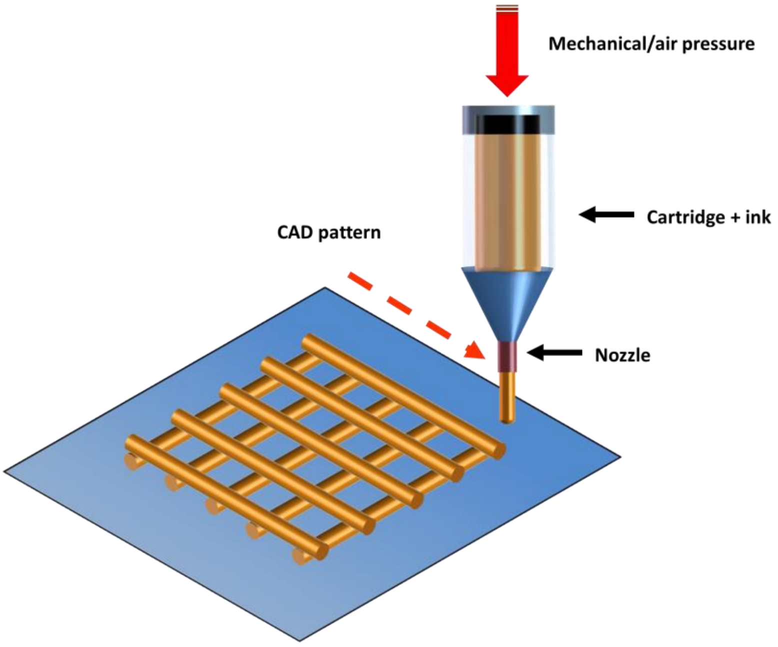

Figure 7. Summary of 3D printing using the DIW methodology. The material is extruded through a nozzle under mechanical/air pressure, following a pattern previously planned by computer assisted design (CAD).

There exists a wide range of 3D printing technologies, alongside with the diversity of printing methods and materials. Among them, some of the best-known techniques are inkjet printing, direct ink writing (DIW) and stereolithography. Briefly, in the inkjet printing approach the material is deposited following a finely, highly controlled ink droplet deposition method.[89] In the case of stereolithography, 3D objects are prepared through a layer-by-layer process induced by photoirradiation of a photocurable material.[90] Lastly DIW makes use of an extruder (either air pressure or mechanical force) to induce the flow of the material through a nozzle while following a CAD pattern.[91] All these strategies can create complex nano/micro-structures with high resolution, by making use of the diverse working parameters suited for the desired material ink.

Despite the high utility of this building method in the biomedical field, a limiting factor for most biomaterials is their adequacy as printable inks. To use a material as printable ink, the precursor is required to meet minimal rheological properties adequate to the printing system.[92] The material must demonstrate certain shear-thinning behaviour to avoid rupture of the forming fibres during printing. Additionally, the ink must be fluid enough to allow flowing through the printing nozzle when pressure is applied. Finally, the deposited ink is expected to have the mechanical strength necessary to retain its shape post-printing and avoid collapsing to preserve the patterning between adjacent arrays.[93] Printed materials can then undergo post-printing processes to modulate the physical and biochemical properties of the 3D construct, improving their applicability towards the biomedical objective.[94,95]

Regarding the porosity of the 3D printed constructs; 3D printing does not directly provide the build support with an internal porosity other than the one provided by the CAD design. However, this approach allows building of complex 3D structures with channelled patterns using diverse types of biomaterials that can already contain a natural or processed intrinsic porosity. As an example, HIPE-derived inks have been demonstrated to be applicable for 3D printing processing creating complex 3D supports with a controlled morphology that includes the presence of an interconnected internal porous network.[75,96] Therefore, by combining the natural biological properties of the building material with predefined physical morphologies, it is possible to create supports with specific characteristics suitable for various types of cellular studies.

1.6 Bioimaging and biosensing approaches and limitations in 2D/3D cell culture systems

Apart from recreating complex structures that support cell growth in 3D, scaffolds can also be used to study relevant biological information of the cellular processes that they support. However, most bioimaging and biosensing strategies have been standardized and adapted for 2D supports. Monolayer systems provide room to observe cells localized in plain sight, while permitting the uptake of biocomponents present in the exposed extracellular media for bioanalysis. In this regard, the applicability of these strategies in 3D systems has additional difficulties because the cells are entrapped within enclosed spaces, limiting the accessibly for bioimaging, and the release of cell-secreted factors is affected by diffusion processes within the system. [97,98]

Among the most used strategies in biosensing, fluorescence microscopy is regarded as the go-to strategy for the visualization of cellular complexes as well as other biomolecules present in the cellular microenvironment. When compared to the standardized 2D scaffolds, the presence of less transparent volumetric 3D matrixes results in more light scattering and reduced light penetration within the channelled support to reach the confined cells.[99] In regards to fluorescence imaging, interferences in light penetration diminish the probability for fluorescent label excitation, thus reducing the visibility of the cells within the matrix. To compensate the signal loss, the incubation time of the sensing molecules can be increased (such as in immunolabelling) to provide enough time for the biomolecules to diffuse within the scaffolds and bind to their specific receptor. Regarding light penetration, the chemical nature of the material affects the opacity of the system, thus the depth penetration of the incident light. Novel approaches on support synthesis aim to achieve low scattering materials using transparent hydrogels or glass-like bio ceramics, thereby allowing high light penetration into the matrix.

To overcome some of the observed limitations in conventional microscopy, alternative microscopy techniques like multi-photon laser scanning and light sheet microscopy have also become of interest for their wider applicability in complex volumetric systems. These strategies can acquire signal from fluorophores using different approaches towards photon detection. Multi-photon laser scanning microscopy can overcome some of the limitations present in confocal microscopy by not being limited to a pinhole that excludes what is out-of-focus, but rather imaging sections of thicker tissues by exciting the fluorophores using more light with a longer wavelength. The use of deeper penetration wavelengths makes it possible to have a longer-depth and more uniform excitation of fluorophores trapped within the thick walls of a 3D support and reducing photon absorption by the solid matrix.[100,101] Nonetheless, as both photons are required to be simultaneously absorbed, the subsequent fluorescence intensity depends on several nonlinear optical parameters that are not easily controllable during signal acquisition. On the other hand, photon collection in light sheet fluorescence microscopy (LSFM) is realized by using a light sheet formed by a laser with a low numerical aperture applied in the lateral directions.[102,103] During irradiation, detection is performed along a different axis, normally orthogonal to the light source, in order to maximize the detection while having the minimum in fluorescence. This strategy allows for fast imaging and tracking of thick organic 3D cell models but still limited to other opaque systems, including some scaffolds.

The same is applicable to biosensing approaches, where the limited access within the 3D support affects the detection of the biomolecules of interest. Therefore, novel strategies are required to provide relevant biological information while avoiding invasive approaches to reduce the impact on the cellular system. In this respect, nanotechnology-based techniques have raised as some of the main strategies capable of achieving important advances in imaging and sensing in the biomedical field.[104]

1.7 Nanotechnology as a biosensing and bioimaging tool

Nanotechnology focused in biomedical research makes use of nanomaterials as bioimaging and biosensing tools to acquire bioanalytical information for diagnosis, monitoring and treatment of complex diseases.[105] Relevant advances related to the incorporation of nanomaterials within living organisms have demonstrated that engineered materials with such a low dimensionality are able to trespass through natural barriers and reach hardly accessible areas. In this regard, nanomaterials can be used to facilitate the acquisition of images of complex cellular structures with no invasive effects, enhancing the biological relevance of the studied data.[106]

1.7.1 Optical properties of noble metal nanoparticles

Among the different types of available nanomaterials, the use of noble-metal nanoparticles (NPs) has become one of the main tools involved in the use of nanometre-scale materials in biomedicine. The use of gold (AuNPs) and silver (AgNPs) nanoparticles have improved advantages for biological applications due to their unique characteristics, not only regarding biocompatibility but also their conductive and optical properties.[107,108]

An interesting property of metal nanoparticles is their unique optical properties. The interactions of metal NPs with light are defined by the response of the conducting electrons on the surface of the nanoparticles. The collective oscillations of conduction electrons at the surface of the nanoparticles in resonance with an external electromagnetic radiation are known as localized surface plasmon resonances (LSPR) (**Figure 8**).[109–111] LSPR in noble nanoparticles lead to very efficient absorption of the energy of photons and its conversion into various effects such as near-field enhancement, heat release or light scattering.[112]

The LSPR depends mainly on the chemical nature of the nanoparticle and its morphology. Consequently, modification of the LSPR can be achieved through control over NP shape, dimensions, composition, state of aggregation and the surrounding medium. In this regard, metallic nanoparticles such as AuNPs have been in high demand because their LSPR frequency can be localized within the visible and near-IR region. Being possible to promote resonance of noble nanoparticles with readily accessible light sources encourages the use of these particles in a wide range of applications.[113,114] Although NPs synthesised from other precursors such as copper or silver can also provide enhanced LSPR, gold represents one of the best options due to their high colloidal and chemical stability, as well as their biocompatibility.

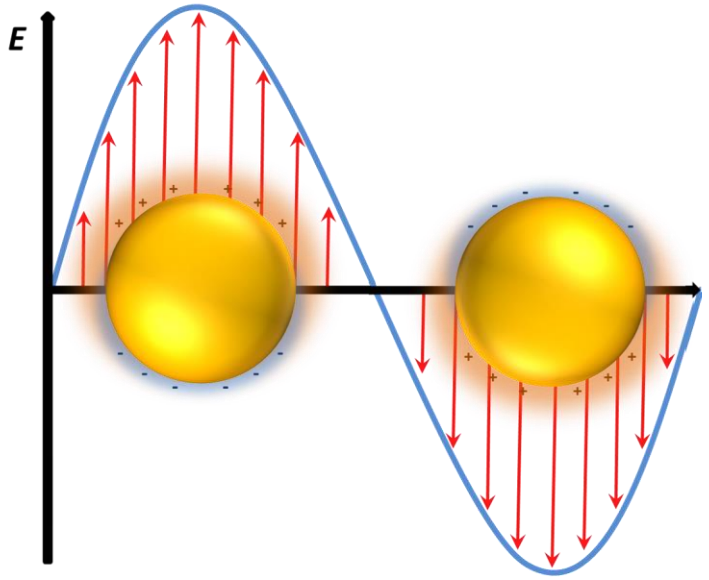

Figure 8. Illustration of the localized surface plasmon resonance (LSPR) on metal NPs under and incident electromagnetic radiation. The cloud of conduction electrons oscillates in resonance with the frequency of the incident wave, creating an oscillating dipole with the particle surface charge.

1.7.2 Surface-enhanced Raman scattering (SERS) as a biosensing tool

As mentioned above, monitoring of biological dynamic processes present in a cellular environment remains a topic of high interest in biomedical research, to further understand the biomolecular mechanisms taking place in natural organisms. Such knowledge could be applied for early diagnosis of complex diseases or for tissue engineering, providing novel tools towards wound healing. However, to have a deeper insight into the cellular mechanisms, information on the involved cell-secreted signalling biomolecules is required. To overcome the aforementioned drawbacks of imaging and sensing techniques in 3D, surface-enhanced Raman scattering (SERS) has been proposed as an alternative to monitor 3D cell models. This technique makes use of the plasmonic properties of noble NPs, to largely enhance Raman signals of adsorbed molecules and thereby obtain singular fingerprint information of chemical components present in a microenvironment.[115]

The enhancing effect of SERS-active nanoparticles is mainly attributed to a combination of an electromagnetic enhancement (EM) related to plasmon excitation and a chemical enhancement due to the transfer of electrons between the adsorbed molecule and the surface of the nanoparticle..[115–117] The chemical enhancement is mainly conditioned by the close interactions of the adsorbed molecules with the metallic surface of noble NPs. With distances within the few nanometres (> 10 nm) conduction electrons from the SERS substrate can resonate with chemisorbed molecules contributing to the Raman process. By resonating with different vibrational modes of the adsorbed molecules, specific spectroscopic fingerprints of the molecules are acquired. This enhancement mechanism is roughly able to increase the intensity of the Raman signal up 10-100 times, whereas the EM enhancement is the main contributor to SERS sensing. As previously explained, when a light source with a wavelength that matches the LSPR interacts with the metallic surface of a plasmonic NP, conduction electrons oscillate in resonance with the frequency of the incident field. The incident light generates high electric fields at the surface of the nanoparticles that have a direct effect in the polarizability of the adsorbed molecules, thereby enhancing the Raman signal up to several orders of magnitude (**Figure 9A**). The efficiency of the SERS enhancement can be further increased by bringing plasmonic NPs close to each other or using NPs with specific morphologies, creating areas known as “SERS hotspots” (small gaps between NPs or NP tips/sharp edges), in which SERS enhancement is more likely to occur at higher magnitude.[118]

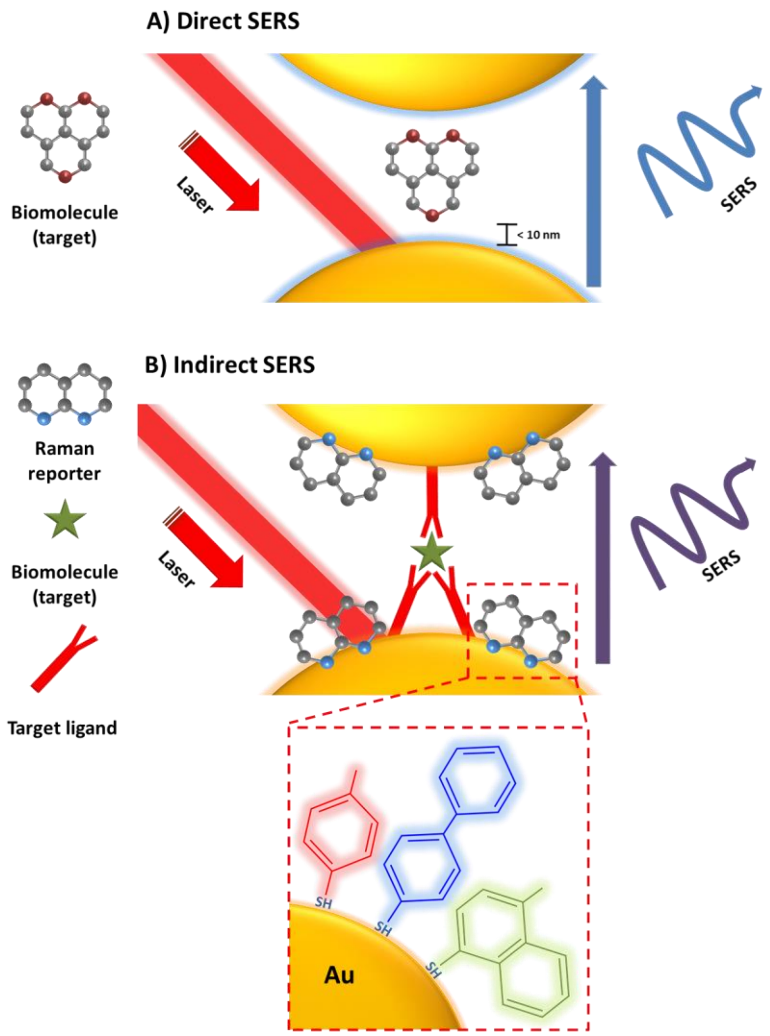

Figure 9. Schematic comparison of direct and indirect SERS-based biosensors. A) Direct SERS detection of adsorbed molecules. B) Indirect SERS detection with signalling acquired from functionalized coupled molecules.

Despite the improved properties that SERS can provide in the field of biosensing, the strategy requires meeting several criteria that are critical to reach its high sensitivity. In order for the enhanced field to interact with the chemical structure of the molecule of study, a nanogap distance is required.[119,120] As LSPR are localized on the surface of the NPs, the SERS enhancement factor is restricted to nearby molecules that can interact with the oscillating dipole.

In a related aspect, a significant limitation of this method is its dependence on the chemical affinity of biomolecules towards the surface of the plasmonic NPs, often requiring chemical adsorption to ensure close interaction with the metal surface.[121] In order to promote a close interaction of the analyte of interest with the metallic surface, NPs can be functionalized with purposely designed organic ligands. By creating new contact points onto the NP's surface, biomolecules present in the microenvironment can be attracted, thereby ensuring sensitive detection.[122,123]

The application of SERS as a biosensing tool to study the presence of biomolecules in cellular microenvironment has been successfully demonstrated. Plasmonic NPs can be effectively introduced in the extracellular microenvironment as biosensors, either as NPs dispersed in solution or upon self-assembly onto a solid substrate.[124] The maximum achievable SERS enhancement with dispersed NPs is limited by the plasmonic properties of the single particles that are able to interact with the analyte, in combination with the few hot spots created with other closely diffusing nanoparticles.[125] In this regard, SERS-active NPs have been assembled into larger substrates to create structures where close interactions between adjacent particles are enforced. Such plasmonic assemblies are then composed of a larger number of hotspots per unit area due to the close interactions between close-compacted NPs. The large amount of contact points present in the total area of the substrate provides a larger surface area, thereby facilitating the interactions with diffusing biomolecules present in the nearby environment.[126–128] Both interconnected properties provide the system with a large SERS performance, suitable as a non-invasive approach towards the detection of ECM biomolecules alongside creating a solid support for cellular culture. Some recent approaches have also demonstrated that noble NPs can be combined with 3D-printed scaffolds to create complex structures provided with SERS biosensing capacities. Plasmonic NPs were incorporated by either direct loading into the precursor solution, post-functionalization adhesion, or *in situ* synthesis inside the scaffold. All these strategies provide control over the presence and density of NPs in the system, promoting close-interactions with circulating biomolecules.[129–131]

While SERS has been proven to work as a versatile, highly sensible biodetection method, alternative SERS-based strategies can be applied also for bioimaging, by making use of the signal-enhancing properties of plasmonic NPs. In this regard, plasmonic cores carrying molecules with a high Raman cross-section (Raman reporters) have been used as multiplex imaging tools (**Figure 9B**).[132,133] Combination of both components provides a novel type of imaging probes with unique, stable and readily identifiable signals suitable for bioanalytical applications. Within the biomedical field, these types of SERS probes (also known as SERS tags) have been applied for bioimaging of cells, permitting their visualization and monitoring in complex cellular microenvironments with non-invasive effects and negligible photobleaching. This bioimaging strategy has been applied in several fields, such as cancer research or combined with alternative approaches like SERS-image-guided photothermal therapy.[134,135]

1.8 References

1. Antoni, D., Burckel, H., Josset, E. & Noel, G. Three-Dimensional Cell Culture: A Breakthrough in Vivo. *Int. J. Mol. Sci.* **16**, 5517–5527 (2015).
2. Fontoura, J. C. *et al.* Comparison of 2D and 3D cell culture models for cell growth, gene expression and drug resistance. *Mater. Sci. Eng.: C* **107**, 110264 (2020).
3. Charwat, V. & Egger, D. The Third Dimension in Cell Culture: From 2D to 3D Culture Formats. Cell Culture Technology; *Springer International Publishing*. 75-90 (2018)
4. Wothington, P., Darrin J. Pochan & Sigrid A. Langhans. Peptide hydrogels-versatile matrices for 3D cell culture in cancer medicine. *Frontiers in oncology.* **5**, 92 (2015)
5. Sensi, F., D'Angelo, E., D'Aronco, S., Molinaro, R. & Agostini, M. Preclinical three-dimensional colorectal cancer model: The next generation of in vitro drug efficacy evaluation. *J. Cell Physiol.* **234**, 181–191 (2019).
6. Abbas, M. *et al.* Vertebrate cell culture as an experimental approach – limitations and solutions. *Comparative Biochem. Physiol. Part B: Biochem. Molec. Biol.* **254**, 110570 (2021).
7. Langhans, S. A. Three-Dimensional in Vitro Cell Culture Models in Drug Discovery and Drug Repositioning. *Front. Pharmacol.* **9**, 6 (2018).
8. Havins, L., Capel, A., Christie, S., Lewis, M. & Roach, P. Gradient biomimetic platforms for neurogenesis studies. *J. Neural Eng.* **19**, 011001 (2022).
9. Ravi, M., Paramesh, V., Kaviya, S. R., Anuradha, E. & Solomon, F. D. P. 3D Cell Culture Systems- Advantages and Applications. *J. Cell. Physiol.* **230**, 16–26 (2015).
10. Bao, B., Jiang, J., Yanase, T., Nishi, Y. & Morgan, J. R. Connexon-mediated cell adhesion drives microtissue self-assembly. *FASEB J.* **25**, 255–264 (2011).
11. Sachar, A. *et al.* Cell-matrix and cell-cell interactions of human gingival fibroblasts on three-dimensional nanofibrous gelatin scaffolds: Human gingival fibroblast behaviour on 3D nanofibrous gelatin scaffolds. *J. Tissue Eng. Regen. Med.* **8**, 862–873 (2014).
12. Zhang, Y., Kanter, E. M. & Yamada, K. A. Remodeling of cardiac fibroblasts following myocardial infarction results in increased gap junction intercellular communication. *Cardiovasc. Pathol.* **19**, e233–e240 (2010).
13. Ou, K.-L. & Hosseinkhani, H. Development of 3D in Vitro Technology for Medical Applications. *Int. J. Mol. Sci.* **15**, 17938–17962 (2014).
14. Meng, X., Leslie, P., Zhang, Y. & Dong, J. Stem cells in a three-dimensional scaffold environment. *SpringerPlus* **3**, 80 (2014).
15. Dado, D. & Levenberg, S. Cell–scaffold mechanical interplay within engineered tissue. *Seminars in Cell & Developmental Biology* **20**, 656–664 (2009).

16. Dutta, R. C. & Dutta, A. K. Cell-interactive 3D-scaffold; advances and applications. *Biotechnol. Adv.* **27**, 334–339 (2009).
17. Hutmacher, D. W. Scaffold design and fabrication technologies for engineering tissues — state of the art and future perspectives. *J. Biomater. Sci., Polym. Ed.* **12**, 107–124 (2001).
18. Zhang, L., Yang, G., Johnson, B. N. & Jia, X. Three-dimensional (3D) printed scaffold and material selection for bone repair. *Acta Biomater.* **84**, 16–33 (2019).
19. Kumar, S. *et al.* 3D scaffold alters cellular response to graphene in a polymer composite for orthopedic applications: 3D scaffold alters cellular response to graphene. *J. Biomed. Mater. Res.* **104**, 732–749 (2016).
20. Carletti, E., Motta, A. & Migliaresi, C. Scaffolds for Tissue Engineering and 3D Cell Culture. *Methods Mol. Biol.* **695**, 17-39, (2011).
21. Sant, S., Hancock, M. J., Donnelly, J. P., Iyer, D. & Khademhosseini, A. Biomimetic gradient hydrogels for tissue engineering. *Can. J. Chem. Eng.* **88**, 899–911 (2010).
22. Di Luca, A. *et al.* Tuning Cell Differentiation into a 3D Scaffold Presenting a Pore Shape Gradient for Osteochondral Regeneration. *Adv. Healthc. Mater.* **5**, 1753–1763 (2016).
23. Loh, Q. L. & Choong, C. Three-Dimensional Scaffolds for Tissue Engineering Applications: Role of Porosity and Pore Size. *Tissue Eng. Part B: Rev.* **19**, 485–502 (2013).
24. Choi, N. W. *et al.* Microfluidic scaffolds for tissue engineering. *Nat. Mater.* **6**, 908–915 (2007).
25. Castiaux, A. D., Spence, D. M. & Martin, R. S. Review of 3D cell culture with analysis in microfluidic systems. *Anal. Methods* **11**, 4220–4232 (2019).
26. Graf, B. W. & Boppart, S. A. Imaging and Analysis of Three-Dimensional Cell Culture Models. *Methods Mo. Biol.,* 591, 211–227 (2010).
27. Lau, S. H. *et al.* Multiscale 3D bioimaging: from cell, tissue to whole organism. *Scanning Microscopy 2009.* **7378**, 332–340 (2009).
28. Soman, P. *et al.* Cancer cell migration within 3D layer-by-layer microfabricated photocrosslinked PEG scaffolds with tunable stiffness. *Biomaterials* **33**, 7064–7070 (2012).
29. Zhang, Y., Wang, S., Eghtedari, M., Motamedi, M. & Kotov, N. A. Inverted-Colloidal-Crystal Hydrogel Matrices as Three-Dimensional Cell Scaffolds. *Adv. Funct. Mater.* **15**, 725–731 (2005).
30. Williams, D. F. On the mechanisms of biocompatibility. *Biomaterials* **29**, 2941–2953 (2008).
31. Turnbull, G. *et al.* 3D bioactive composite scaffolds for bone tissue engineering. *Bioactive Mater.* **3**, 278–314 (2018).
32. Owen, S. C. & Shoichet, M. S. Design of three-dimensional biomimetic scaffolds. *J. Biomed. Mater. Res.* **94**, 1321-1331, (2010)

33. Deb, P., Deoghare, A. B., Borah, A., Barua, E. & Das Lala, S. Scaffold Development Using Biomaterials: A Review. *Mater. Today: Proceedings* **5**, 12909–12919 (2018).
34. Prasopthum, A., Cooper, M., Shakesheff, K. M. & Yang, J. Three-Dimensional Printed Scaffolds with Controlled Micro-/Nanoporous Surface Topography Direct Chondrogenic and Osteogenic Differentiation of Mesenchymal Stem Cells. *ACS Appl. Mater. Interfaces* **11**, 18896–18906 (2019).
35. Park, J. H. *et al.* Microporous cell-laden hydrogels for engineered tissue constructs. *Biotechnol. Bioeng.* **106**, 138-148, (2010)
36. Hwang, Y., Sangaj, N. & Varghese, S. Interconnected Macroporous Poly(Ethylene Glycol) Cryogels as a Cell Scaffold for Cartilage Tissue Engineering. *Tissue Eng. Part A* **16**, 3033–3041 (2010).
37. Han, L.-H., Yu, S., Wang, T., Behn, A. W. & Yang, F. Microribbon-Like Elastomers for Fabricating Macroporous and Highly Flexible Scaffolds that Support Cell Proliferation in 3D. *Adv. Funct. Mater.* **23**, 346–358 (2013).
38. Bose, S., Roy, M. & Bandyopadhyay, A. Recent advances in bone tissue engineering scaffolds. *Trends Biotechnol.* **30**, 546–554 (2012).
39. Carmagnola, I., Ranzato, E. & Chiono, V. Scaffold functionalization to support a tissue biocompatibility. Functional 3D Tissue Engineering Scaffolds. *Elsevier.* 255–277 (2018).
40. Maia, F. R., Fonseca, K. B., Rodrigues, G., Granja, P. L. & Barrias, C. C. Matrix-driven formation of mesenchymal stem cell–extracellular matrix microtissues on soft alginate hydrogels. *Acta Biomater.* **10**, 3197–3208 (2014).
41. Guarino, V., Causa, F. & Ambrosio, L. Porosity and Mechanical Properties Relationship in PCL Porous Scaffolds. *J. Appl. Biomater. Biomech.* **5**, 149-157, (2007).
42. Reilly, G. C. & Engler, A. J. Intrinsic extracellular matrix properties regulate stem cell differentiation. *J. Biomec.* **43**, 55–62 (2010).
43. Saska, S., Pilatti, L., Blay, A. & Shibli, J. A. Bioresorbable Polymers: Advanced Materials and 4D Printing for Tissue Engineering. *Polymers* **13**, 563 (2021).
44. Sheikh, Z. *et al.* Biodegradable Materials for Bone Repair and Tissue Engineering Applications. *Materials* **8**, 5744–5794 (2015).
45. Do, A.-V., Khorsand, B., Geary, S. M. & Salem, A. K. 3D Printing of Scaffolds for Tissue Regeneration Applications. *Adv. Healthc. Mater.* **4**, 1742–1762 (2015).
46. Abudula, T. *et al.* 3D Printing of Metal/Metal Oxide Incorporated Thermoplastic Nanocomposites With Antimicrobial Properties. *Front. Bioeng. Biotechnol.* **8**, 568186 (2020).
47. Toong, D. W. Y. *et al.* Bioresorbable Polymeric Scaffold in Cardiovascular Applications. *Int. J. Mol. Sci.* **21**, 3444 (2020).

48. Afewerki, S., Sheikhi, A., Kannan, S., Ahadian, S. & Khademhosseini, A. Gelatin-polysaccharide composite scaffolds for 3D cell culture and tissue engineering: Towards natural therapeutics. *Bioeng. Transl. Med.* **4**, 96–115 (2019).
49. Singh, M. R., Patel, S. & Singh, D. Natural polymer-based hydrogels as scaffolds for tissue engineering. Nanobiomaterials in Soft Tissue Engineering. *Elsevier.* 231–260 (2016)
50. Yang, Y. *et al.* Combinatorial Polymer Scaffold Libraries for Screening Cell-Biomaterial Interactions in 3D. *Adv. Mater.* **20**, 2037–2043 (2008).
51. Baiguera, S. *et al.* 3D Printing Decellularized Extracellular Matrix to Design Biomimetic Scaffolds for Skeletal Muscle Tissue Engineering. *BioMed. Res. Int.* **2020**, 1–13 (2020).
52. Yazdanian, M. *et al.* Decellularized and biological scaffolds in dental and craniofacial tissue engineering: a comprehensive overview. *J. Mater. Res. Technol.* **15**, 1217–1251 (2021).
53. Place, E. S., George, J. H., Williams, C. K. & Stevens, M. M. Synthetic polymer scaffolds for tissue engineering. *Chem. Soc. Rev.* **38**, 1139 (2009).
54. Liu, X., Holzwarth, J. M. & Ma, P. X. Functionalized Synthetic Biodegradable Polymer Scaffolds for Tissue Engineering: Functionalized Synthetic Biodegradable Polymer Scaffolds. *Macromol. Biosci.* **12**, 911–919 (2012).
55. Hutmacher, D. W., Schantz, J. T., Lam, C. X. F., Tan, K. C. & Lim, T. C. State of the art and future directions of scaffold-based bone engineering from a biomaterials perspective. *J. Tissue Eng. Regen. Med.* **1**, 245–260 (2007).
56. Carson, J. S. & Bostrom, M. P. G. Synthetic bone scaffolds and fracture repair. *Injury* **38**, S33–S37 (2007).
57. Alvarez, K. & Nakajima, H. Metallic Scaffolds for Bone Regeneration. *Materials* **2**, 790–832 (2009).
58. Lv, Y. *et al.* Metal Material, Properties and Design Methods of Porous Biomedical Scaffolds for Additive Manufacturing: A Review. *Front. Bioeng. Biotechnol.* **9**, 641130 (2021).
59. Boccaccini, A. R. & Blaker, J. J. Bioactive composite materials for tissue engineering scaffolds. *Exp. Rev. Med. Devices* **2**, 303–317 (2005).
60. Anita Lett, J. *et al.* Recent advances in natural polymer-based hydroxyapatite scaffolds: Properties and applications. *Eur. Polym. J.* **148**, 110360 (2021).
61. Hollister, S. J. Porous scaffold design for tissue engineering. *Nat. Mater.* **4**, 518–524 (2005).
62. Kotov, N. A. *et al.* Inverted Colloidal Crystals as Three-Dimensional Cell Scaffolds. *Langmuir* **20**, 7887–7892 (2004).
63. Velev, O. D. & Lenhoff, A. M. Colloidal crystals as templates for porous materials. *Curr. Op. Colloid Interface Sci.* **5**, 56–63 (2000).
64. Zhang, Y. S., Zhu, C. & Xia, Y. Inverse Opal Scaffolds and Their Biomedical Applications. *Adv. Mater.* **29**, 1701115 (2017).

65. Meseguer, F. *et al.* Synthesis of inverse opals. *Colloids Surf. A: Physicochem. Eng. Asp.* **202**, 281–290 (2002).
66. Stein, A., Li, F. & Denny, N. R. Morphological Control in Colloidal Crystal Templating of Inverse Opals, Hierarchical Structures, and Shaped Particles. *Chem. Mater.* **20**, 649–666 (2008).
67. MacLachlan, M. J., Manners, I. & Ozin, G. A. New (Inter)Faces: Polymers and Inorganic Materials. *Adv. Mater.* **12**, 675-681 (2000)
68. Deville, S. Ice-templating, freeze casting: Beyond materials processing. *J. Mater. Res.* **28**, 2202–2219 (2013).
69. Gutiérrez, M. C., Ferrer, M. L. & del Monte, F. Ice-Templated Materials: Sophisticated Structures Exhibiting Enhanced Functionalities Obtained after Unidirectional Freezing and Ice-Segregation-Induced Self-Assembly. *Chem. Mater.* **20**, 634–648 (2008).
70. Joukhdar, H. *et al.* Ice Templating Soft Matter: Fundamental Principles and Fabrication Approaches to Tailor Pore Structure and Morphology and Their Biomedical Applications. *Adv. Mater.* **33**, 2100091 (2021).
71. Studart, A. R. *et al.* Hierarchical Porous Materials Made by Drying Complex Suspensions. *Langmuir* **27**, 955–964 (2011).
72. Hu, Y. *et al.* Facile preparation of bioactive nanoparticle/poly(ε-caprolactone) hierarchical porous scaffolds via 3D printing of high internal phase Pickering emulsions. *J. Colloid Interface Sci.* **545**, 104–115 (2019).
73. Chevalier, Y. & Bolzinger, M.-A. Emulsions stabilized with solid nanoparticles: Pickering emulsions. *Colloids Surf. A: Physicochem. Eng. Asp.* **439**, 23–34 (2013).
74. Alison, L. 3D printing of sacrificial templates into hierarchical porous materials. *Sci. Rep.* **9**, 409 (2019).
75. Minas, C., Carnelli, D., Tervoort, E. & Studart, A. R. 3D Printing of Emulsions and Foams into Hierarchical Porous Ceramics. *Adv. Mater.* **28**, 9993–9999 (2016).
76. Viswanathan, P., Johnson, D. W., Hurley, C., Cameron, N. R. & Battaglia, G. 3D Surface Functionalization of Emulsion-Templated Polymeric Foams. *Macromolecules* **47**, 7091–7098 (2014).
77. Costantini, M. & Barbetta, A. Gas foaming technologies for 3D scaffold engineering. Functional 3D Tissue Engineering Scaffolds. *Elsevier*. 127–149 (2018).
78. Quirk, R. A., France, R. M., Shakesheff, K. M. & Howdle, S. M. Supercritical fluid technologies and tissue engineering scaffolds. *Curr. Op. Solid State Mater. Sci.* **8**, 313–321 (2004).
79. García-González, C. A., Concheiro, A. & Alvarez-Lorenzo, C. Processing of Materials for Regenerative Medicine Using Supercritical Fluid Technology. *Bioconjugate Chem.* **26**, 1159–1171 (2015).

80. Beckman, E. J. Supercritical and near-critical CO2 in green chemical synthesis and processing. *J. Supercritical Fluids* **28**, 121–191 (2004).
81. Duarte, A. R. C., Mano, J. F. & Reis, R. L. Supercritical fluids in biomedical and tissue engineering applications: a review. *Int. Mater. Rev.* **54**, 214–222 (2009).
82. Howdle, S. M. *et al.* Supercritical fluid mixing: preparation of thermally sensitive polymer composites containing bioactive materials. *Chem. Commun.* 109–110 (2001)
83. Chia, H. N. & Wu, B. M. Recent advances in 3D printing of biomaterials. *J. Biol. Eng.* **9**, 4 (2015).
84. Wan, X., Luo, L., Liu, Y. & Leng, J. Direct Ink Writing Based 4D Printing of Materials and Their Applications. *Adv. Sci.* **7**, 2001000 (2020).
85. Poomathi, N. *et al.* 3D printing in tissue engineering: a state of the art review of technologies and biomaterials. *Rapid Prototyping J.* **26**, 1313–1334 (2020).
86. Jammalamadaka, U. & Tappa, K. Recent Advances in Biomaterials for 3D Printing and Tissue Engineering. *J. Funct. Biomater.* **9**, 22 (2018).
87. Garcia, J., Yang, Z., Mongrain, R., Leask, R. L. & Lachapelle, K. 3D printing materials and their use in medical education: a review of current technology and trends for the future. *BMJ Simul. Technol. Enhanc. Learn.* **4**, 27–40 (2018).
88. Yan, Q. *et al.* A Review of 3D Printing Technology for Medical Applications. *Engineering* **4**, 729–742 (2018).
89. Zhou, L., Fu, J. & He, Y. A Review of 3D Printing Technologies for Soft Polymer Materials. *Adv. Funct. Mater.* **30**, 2000187 (2020).
90. Fritzler, K. B. & Prinz, V. Y. 3D printing methods for micro- and nanostructures. *Physics-Uspekhi* **62**, (2019).
91. Solís Pinargote, N. W., Smirnov, A., Peretyagin, N., Seleznev, A. & Peretyagin, P. Direct Ink Writing Technology (3D Printing) of Graphene-Based Ceramic Nanocomposites: A Review. *Nanomaterials* **10**, 1300 (2020).
92. Liu, Z., Zhang, M., Bhandari, B. & Wang, Y. 3D printing: Printing precision and application in food sector. *Trends Food Sci. Technol.* **69**, 83–94 (2017).
93. Zhu, S., Stieger, M. A., van der Goot, A. J. & Schutyser, M. A. I. Extrusion-based 3D printing of food pastes: Correlating rheological properties with printing behaviour. *Innovative Food Sci. Emerging Technol.* **58**, 102214 (2019).
94. Jaidev, L. R. & Chatterjee, K. Surface functionalization of 3D printed polymer scaffolds to augment stem cell response. *Mater. Design* **161**, 44–54 (2019).
95. Pan Jiang, Zhongying Ji, Xiaolong Wang, & Feng Zhou. Surface functionalization - a new functional dimension added to 3D printing. *J. Mater. Chem. C* **8**, 12380–12411 (2020).
96. Li, X. *et al.* High Internal Phase Emulsion for Food-Grade 3D Printing Materials. *ACS Appl. Mater. Interfaces* **12**, 45493–45503 (2020).

97. Van Zundert, I., Fortuni, B. & Rocha, S. From 2D to 3D Cancer Cell Models—The Enigmas of Drug Delivery Research. *Nanomaterials* **10**, 2236 (2020).
98. Booij, T. H., Price, L. S. & Danen, E. H. J. 3D Cell-Based Assays for Drug Screens: Challenges in Imaging, Image Analysis, and High-Content Analysis. *SLAS Discovery* **24**, 615–627 (2019).
99. Martinez, N. J., Titus, S. A., Wagner, A. K. & Simeonov, A. High-throughput fluorescence imaging approaches for drug discovery using *in vitro* and *in vivo* three-dimensional models. *Exp. Op. Drug Discovery* **10**, 1347–1361 (2015).
100. Williams, R. M., Zipfel, W. R. & Webb, W. W. Multiphoton microscopy in biological research. *Curr. Op. Chem. Biol.* **5**, 603–608 (2001).
101. Kim, M. J. *et al.* Multiphoton imaging of myogenic differentiation in gelatin-based hydrogels as tissue engineering scaffolds. *Biomater. Res.* **20**, 2 (2016).
102. Gualda, E. J., Simão, D., Pinto, C., Alves, P. M. & Brito, C. Imaging of human differentiated 3D neural aggregates using light sheet fluorescence microscopy. *Front. Cell. Neurosci.* **8**, (2014).
103. Adams, M. W., Loftus, A. F., Dunn, S. E., Joens, M. S. & Fitzpatrick, J. A. J. Light Sheet Fluorescence Microscopy (LSFM). *Curr. Protoc. Cytometry* **71**, (2015).
104. Xiao, Y., Wu, Z., Yao, Q. & Xie, J. Luminescent metal nanoclusters: Biosensing strategies and bioimaging applications. *Aggregate* **2**, 114–132 (2021).
105. Moghimi, S. M., Hunter, A. C. & Murray, J. C. Nanomedicine: current status and future prospects. *FASEB J.* **19**, 311–330 (2005).
106. Liang, R., Wei, M., Evans, D. G. & Duan, X. Inorganic nanomaterials for bioimaging, targeted drug delivery and therapeutics. *Chem. Commun.* **50**, 14071–14081 (2014).
107. Huang, X. & El-Sayed, M. A. Gold nanoparticles: Optical properties and implementations in cancer diagnosis and photothermal therapy. *J. Adv. Res.* **1**, 13–28 (2010).
108. Jiang, P. *et al.* Applications of Gold Nanoparticles in Non-Optical Biosensors. *Nanomaterials* **8**, 977 (2018).
109. Mayer, K. M. & Hafner, J. H. Localized Surface Plasmon Resonance Sensors. *Chem. Rev.* **111**, 3828–3857 (2011).
110. Eustis, S. & El-Sayed, M. A. Why gold nanoparticles are more precious than pretty gold: Noble metal surface plasmon resonance and its enhancement of the radiative and nonradiative properties of nanocrystals of different shapes. *Chem. Soc. Rev.* **35**, 209–217 (2006).
111. Krajczewski, J., Ambroziak, R. & Kudelski, A. Substrates for Surface-Enhanced Raman Scattering Formed on Nanostructured Non-Metallic Materials: Preparation and Characterization. *Nanomaterials* **11**, 75 (2020).
112. Xu, T. & Geng, Z. Strategies to improve performances of LSPR biosensing: Structure, materials, and interface modification. *Biosens. Bioelectron.* **174**, 112850 (2021).

113. Jans, H. & Huo, Q. Gold nanoparticle-enabled biological and chemical detection and analysis. *Chem. Soc. Rev.* **41**, 2849–2866 (2012).
114. Zhao, W., Brook, M. A. & Li, Y. Design of Gold Nanoparticle-Based Colorimetric Biosensing Assays. *ChemBioChem* **9**, 2363–2371 (2008).
115. Langer, J. *et al.* Present and Future of Surface-Enhanced Raman Scattering. *ACS Nano* **14**, 28–117 (2020).
116. Wang, X. & Guo, L. SERS Activity of Semiconductors: Crystalline and Amorphous Nanomaterials. *Angew. Chem. Int. Ed.* **59**, 4231–4239 (2020).
117. Stiles, P. L., Dieringer, J. A., Shah, N. C. & Van Duyne, R. P. Surface-Enhanced Raman Spectroscopy. *Annu. Rev. Anal. Chem.* **1**, 601–626 (2008).
118. Asiala, S. M. & Schultz, Z. D. Characterization of hotspots in a highly enhancing SERS substrate. *Analyst* **136**, 4472 (2011).
119. Schlücker, S. Surface-Enhanced Raman Spectroscopy: Concepts and Chemical Applications. *Angew. Chem. Int. Ed.* **53**, 4756–4795 (2014).
120. Zong, C. *et al.* Surface-Enhanced Raman Spectroscopy for Bioanalysis: Reliability and Challenges. *Chem. Rev.* **118**, 4946–4980 (2018).
121. Szlag, V. M. *et al.* Molecular Affinity Agents for Intrinsic Surface-Enhanced Raman Scattering (SERS) Sensors. *ACS Appl. Mater. Interfaces* **10**, 31825–31844 (2018).
122. Li, P. *et al.* Fundamentals and applications of surface-enhanced Raman spectroscopy–based biosensors. *Curr. Op. Biomed. Eng.* **13**, 51–59 (2020).
123. Shiqiang Wang *et al.* Development of Affinity between Target Analytes and Substrates in Surface Enhanced Raman Spectroscopy for Environmental Pollutants Detection. *Anal. Methods* **12**, 5657–5670 (2020).
124. Mosier-Boss, P. Review of SERS Substrates for Chemical Sensing. *Nanomaterials* **7**, 142 (2017).
125. Vinod, M. & Gopchandran, K. G. Au, Ag and Au:Ag colloidal nanoparticles synthesized by pulsed laser ablation as SERS substrates. *Progr. Natural Sci.: Materials International* **24**, 569–578 (2014).
126. Plou, J. *et al.* Multiplex SERS Detection of Metabolic Alterations in Tumor Extracellular Media. *Adv. Funct. Mater.* **30**, 1910335 (2020).
127. Matricardi, C. *et al.* Gold Nanoparticle Plasmonic Superlattices as Surface-Enhanced Raman Spectroscopy Substrates. *ACS Nano* **12**, 8531–8539 (2018).
128. Solís, D. M., Taboada, J. M., Obelleiro, F., Liz-Marzán, L. M. & García de Abajo, F. J. Optimization of Nanoparticle-Based SERS Substrates through Large-Scale Realistic Simulations. *ACS Photonics* **4**, 329–337 (2017).
129. Almohammed, S. *et al.* 3D-Printed Peptide-Hydrogel Nanoparticle Composites for Surface-Enhanced Raman Spectroscopy Sensing. *ACS Appl. Nano Mater.* **2**, 5029–5034 (2019).
130. Wu, M. *et al.* 3D Ultrasensitive Polymers-Plasmonic Hybrid Flexible Platform for In-Situ Detection. *Polymers* **12**, 392 (2020).

131. dos Santos, D. S., Goulet, P. J. G., Pieczonka, N. P. W., Oliveira, O. N. & Aroca, R. F. Gold Nanoparticle Embedded, Self-Sustained Chitosan Films as Substrates for Surface-Enhanced Raman Scattering. *Langmuir* **20**, 10273–10277 (2004).
132. Jimenez de Aberasturi, D. *et al.* Surface Enhanced Raman Scattering Encoded Gold Nanostars for Multiplexed Cell Discrimination. *Chem. Mater.* **28**, 6779–6790 (2016).
133. Serrano-Montes, A. B. *et al.* A General Method for Solvent Exchange of Plasmonic Nanoparticles and Self-Assembly into SERS-Active Monolayers. *Langmuir* **31**, 9205–9213 (2015).
134. Ly, N. H. & Joo, S.-W. Recent advances in cancer bioimaging using a rationally designed Raman reporter in combination with plasmonic gold. *J. Mater. Chem. B* **8**, 186–198 (2020).
135. He, J., Dong, J., Hu, Y., Li, G. & Hu, Y. Design of Raman tag-bridged core–shell Au@Cu $_3$ (BTC) $_2$ nanoparticles for Raman imaging and synergistic chemo-photothermal therapy. *Nanoscale* **11**, 6089–6100 (2019).

Chapter 2: Composite 3D scaffolds for bacterial-bone infection sensing by SERS

Abstract

This chapter focuses on the design of a model for monitoring bacterial infection in bone, using surface-enhanced Raman scattering (SERS) as a biosensing approach for the detection of bacterial-secreted metabolites. Infectious bacteria, such as *Pseudomonas aeruginosa* have been found responsible for post-operation infections in bone transplants and bone-derived prosthetics, damaging the tissue and causing infections in patients. The study of bacterial-secreted biomolecules might be useful as an early-stage indication of potential infections, so that sufficient time is provided to administer the adequate treatment. In order to recreate an *in vitro* bone-infection scenario, three-dimensional (3D) porous scaffolds were synthesized to build a matrix with physicochemical properties similar to those of the natural bone tissue. Such a structure was composed of a porous 3D-printed ceramic support, generated by the high internal phase emulsion (HIPE) technology combined with a polymer matrix made of methacrylated gelatin (GelMA). The ceramic support was designed to recreate a niche similar to a natural bone tissue, while the polymer matrix would imitate the surrounding cartilage. The latter was additionally loaded with gold nanoparticles as plasmonic substrates for SERS biosensing. As such, the aim of this chapter was to mimic an *in vitro* bacterial bone infection and detect the presence of the bacterial-secreted metabolite pyocyanin over time, using SERS.

2.1 Introduction

In recent years, there have been important advances in the field of biomedicine, regarding the synthesis of novel supports for *in vitro* cellular studies.[1–3] Most of the current *in vitro* approaches make use of conventional 2D flat surfaces for the seeding and development of cell cultures. However, such environments usually lack physicochemical constituents similar to those present in natural tissue, thus failing to provide an adequate environment to simulate natural processes.[4–6] To better recreate the *in vivo* scenario, the model is required to further promote interaction with cells, including adhesion, differentiation and proliferation.[7–9]

In this regard, novel 3D approaches are being considered as alternatives capable of creating new types of structures with enhanced characteristics (e.g., better biocompatibility, cell adhesion, mechanical stimuli, etc.), all of which are required to better mimic the biological conditions present in the natural tissue.[7,8,10,11] Among the different strategies that have been proposed to create 3D structured materials, 3D printing and, particularly, direct ink writing (DIW) are considered the main candidates, mainly thanks to their simplicity and computer-controlled building of complex structures made of selected working materials.[12–15] Due to the simple operation and high compatibility with multiple biomaterials, this strategy opens the way to a wide range of different structures, mainly dependent on the selected 3D digital model and the chemical nature of the printed material.[16] Therefore, both chemical composition and internal morphology of the printable material become key elements in their applicability to cellular studies.

Common inks used in 3D printing must be composed of materials with high printability and, in the case of biomedical applications, biocompatibility.[8] Such factors restrict the available materials that can provide the desired physical and biochemical characteristics of the 3D scaffold. In this sense, novel approaches in the development of ink formulations have succeeded in synthesizing biologically-compatible and printable materials that can also result in suitable morphologies, aimed to enhance the interactions with the cellular systems. As an example, porous materials featuring open cavities and non-uniform surfaces have been studied to induce well-defined stimuli to cells, promoting cellular mechanisms, such as cell adhesion, by providing a larger surface area.[17] Following this reasoning, alternative processes toward the synthesis of 3D-printable materials have been considered, including the high internal phase emulsion process (HIPE).[18–21] The HIPE methodology makes use of emulsion systems to create materials with both internal and external interconnected porosities, determined by the dimensionality of the emulsion droplets.[19,22] The addition of such architectures to the final scaffold opens the way for the synthesis of complex structures, not only based on the chemistry of the working material, but also incorporating unique features at smaller scales.[23,24] In particular, the incorporation of a tuneable microstructure results particularly interesting to mimic the bone structure. For this reason, DIW using emulsion-based inks has recently focused on the fabrication of bone-biomimicking supports and implants.[24–26]

One of the major hurdles faced when dealing with prosthetics is the lack of completely sterile conditions during surgery and the affinity of some infectious bacteria species towards the prosthetic surface. Among such bacterial species, *Pseudomonas Aeruginosa* (*P.aeruginosa*) is a common gram-negative rod-shaped bacterium, which is regarded as an opportunistic pathogen due to its association with hospital-acquired infections. Surveys carried out in community hospitals have determined that *P. aeruginosa* is the cause of up to 12% of the total reported infected cases in bone transplants and prosthetics.[27,28] Additionally, these bacteria have been known for their capacity to acquire high antibiotic resistance, by forming impenetrable biofilms while releasing multiple virulence factors to promote infection.[29,30] Due to the complexity and high diversity of the *Pseudomonas* genus, the presence of such organisms not only has an important effect on prosthetic infections, but they have also become relevant in other medical conditions such as burns and immunocompromised patients.

During the infection process, bacteria are known to secrete different types of specific biomolecules to communicate with other bacteria, promoting growth and propagation of the infectious species on the affected tissue. Early-stage detection of such bacterial biomarkers could thus be employed as a useful tool to identify the presence of bacteria in infected patients, thereby providing time to avoid further damage on the infected tissues. Among the different types of identified bacterial-secreted metabolites, *P. aeruginosa* is known to secrete several biomolecules, some of the best known ones being pyocyanin (PCN), pyoverdine, and pyorubin.[28] In particular, PCN is particularly associated with quorum sensing (QS), a process involved in the regulation of the expression of virulence genes in response to changes in bacterial population density.[31,32] Studies of this biomolecule have determined its major role in ominous effects on human cells, ranging from disruption of cellular metabolic activity and calcium homeostasis.[33] Previous work within the field has shown that PCN is detectable via surface-enhanced Raman scattering (SERS), thanks to the clear Raman fingerprint and affinity of PCN to plasmonic SERS substrates.[34,35] These results suggest that the evolution of a *P. aeruginosa* bacterial infection could be studied through differences in PCN concentration measured using the SERS technique.

Although several approaches can be used for the detection of specific bacterial biomarkers, in the case of bone implants, invasive approaches such as surgery are often required to confirm infection.[36] In this chapter, we propose the use of SERS as a non-invasive approach for the detection of *P. aeruginosa*-secreted PCN in a bone infection model. A 3D porous composite matrix capable of recreating a bone-like niche was prepared using a 3D-printed HIPE ceramic paste, embedded in a polymer matrix loaded with plasmonic nanoparticles (NP). As such, the ceramic porous matrix was expected to create a support with a hard consistency similar to bone matrix, while the addition of a multichannel porosity by a HIPE approach would include a certain surface roughness capable of stimulating interactions with seeded cells. The internal, interconnected multichannel porosity of the system would also enhance diffusion of biomolecules and nutrients alongside the whole structure, thus avoiding gradients over long-term studies. On the other hand, addition of a polymeric coating was expected to be applicable as a highly biocompatible matrix, while being loaded with plasmonic nanoparticles to allow the detection of biomolecules released by embedded *P. aeruginosa* bacteria. As such, we aimed to fabricate a scaffold in which osteoblast cells could undergo osteoblast-to-osteocyte differentiation, while having intrinsic SERS biosensing capabilities for biomolecule-detection in the cellular microenvironment (**Figure 1**).

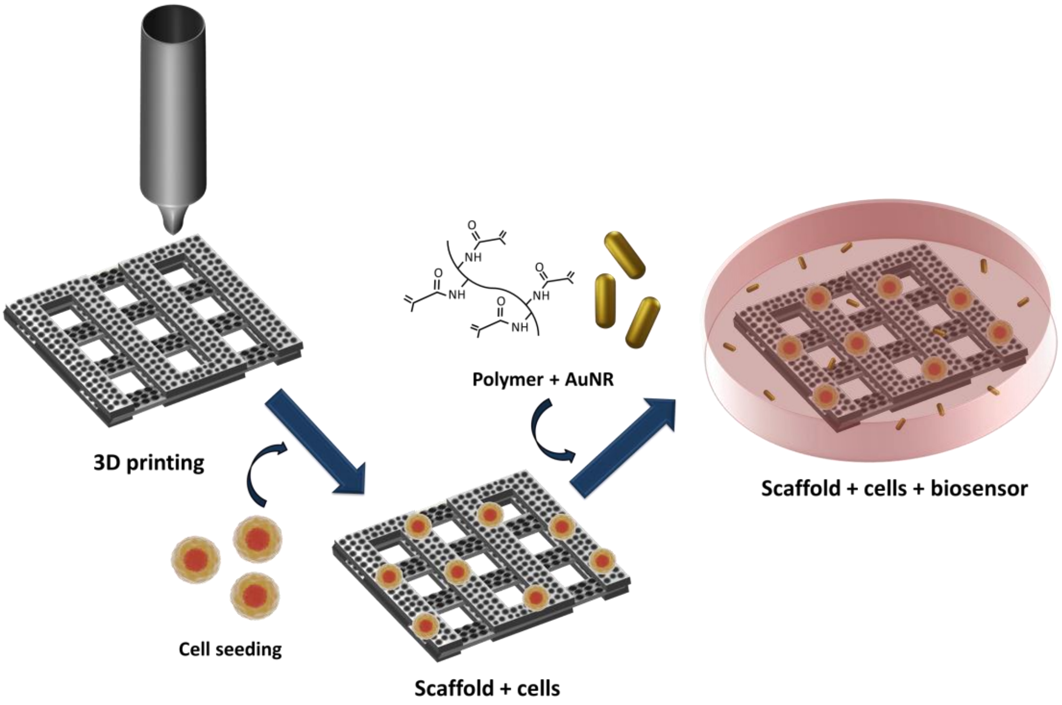

Figure 1. Scheme of the fabrication of 3D porous composite scaffolds for cell growth and SERS biosensing. The building process starts with the 3D-printing of the ceramic support, followed by cell seeding and, finally, the system is embedded in a polymer matrix containing NPs as the biosensing substrate.

2.2 Results and discussion

2.2.1 HIPE-based 3D-printing of porous ceramic scaffolds

The role of the ceramic support within the 3D model involved creating a physical matrix with similar physicochemical properties as the ones found in the human bone tissue, thus mimicking its particularly high stiffness, porosity, and composition. The fabrication of the ceramic component for the scaffold was performed by 3D-printing of ceramic pastes composed mainly of alumina (Al_2O_3), using HIPE-based formulations previously reported in the literature.[21] This technique involves three main steps, as depicted in **Figure 2**: the preparation of a dense paste using HIPE as the building strategy; 3D-printing of the ceramic ink into a multi-layered support; and a final sintering step to harden the overall structure into a porous solid matrix.

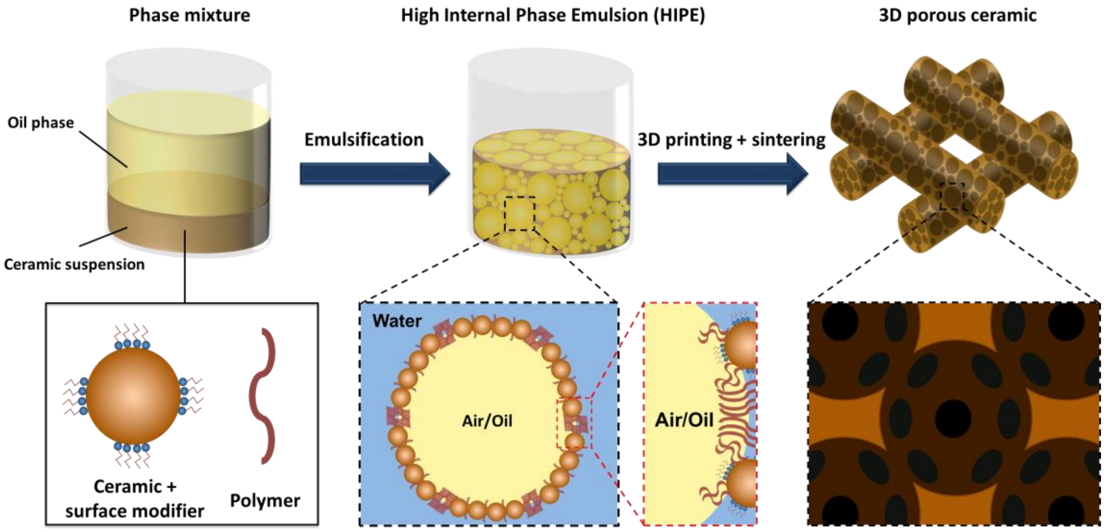

Figure 2. Schematic view of the method for the synthesis of 3D porous ceramic supports based on HIPE. An emulsion is prepared by combining an oil phase with an aqueous solution containing surfactant-functionalized ceramic particles and a selected polymer. After emulsification, the formed paste comprising internal oil droplets coated by ceramic particles and a surface modifier is printed and sintered to acquire a solid ceramic matrix with internal porosity derived from the droplet system.

The use of HIPE as the building strategy was aimed at creating a solid matrix with a highly interconnected internal channel structure.[21,37,38] The creation of such an expanded surface area was expected to provide further physicochemical stimuli to cells, promoting cell adhesion and proliferation. In addition to an increase in the surface area, the presence of interconnected porous cavities would further facilitate diffusion of nutrients and oxygen to the seeded cells, creating a microenvironment adequate for their growth and differentiation into mature cells.

To create a particle-stabilized emulsion paste, the multiphase solution required amphiphilic components to form an interface capable of interacting with both the aqueous and the oil phases. For this purpose, alumina particles were functionalized with short-chain amphiphilic moieties to partially increase their hydrophobicity. For this role, the surfactant propionic acid (PA) was added for its short-chain amphiphilic nature, capable of modifying the surface of ceramic alumina as described in previous works.[38] In this way, the overall hydrophobicity of the solid material is increased by binding to the hydrophilic head groups while exposing the lipophilic component towards the oil phase. Such a modification of the solid surface induced a transition from a dense paste into a more liquid-like aqueous white dispersion. In addition to the incorporation of short-chain surface modifiers, the inks were also tuned by introducing polymers, namely poly(vinyl alcohol) (PVA). The addition of a polymer into the ceramic suspension was aimed to work as a binder to provide sufficient mechanical strength to the ink and ease its later printing. In the emulsion system, the presence of PVA would both replace part of the adsorbed amphiphiles on the ceramic particles and create "soft" spots on the membrane interface of the newly formed oil droplets, consequently tuning the viscoelastic properties of the ink.[38]

To identify the most suitable ink for 3D-printing of the ceramic support, different inks were prepared by varying the ratios of PVA and propionic acid in the emulsion mixture. The effect of propionic acid was tested at different ratios with respect to the total solid content (0.04, 0.06 and 0.08 mmol/g Al_2O_3), whereas PVA was kept at a constant concentration of 1 wt% with respect to water. On the other hand, effect of PVA in the HIPE paste was studied using two different molecular weights (Mw; 31-50 and 85-124 kDa) (**Table 1**).

Table 1. Ink formulations of HIPE pastes for 3D printing.

Name	Al_2O_3 (wt%)	Propionic acid ratio (mmol/g Al_2O_3)	PVA Mw (kDa)
Ink 1	50	0.04	31-50
Ink 2	50	0.06	31-50
Ink 3	50	0.08	31-50
Ink 4	50	0.04	85-124
Ink 5	50	0.06	85-124
Ink 6	50	0.08	85-124

In addition to their chemical composition, emulsification of all inks (see Experimental Section for details) was also tested at different stirring rates of 3000, 4500 and 6600 rpm, to acquire dense pastes. Experimental assays indicated that, when using lower stirring rates, we were only able to obtain pastes with low consistency, even after longer periods of emulsification. By increasing the speed up to 6600 rpm, a dense paste could be consistently prepared within a short time frame. Upon optimization of the stirring rate, all inks were prepared at the same experimental conditions: 6600 rpm for 3 minutes.

2.2.2 Rheological characterization of the inks

3D-printing is a technique designed to build objects though a layer-by-layer deposition process.[39] This method requires extrusion of the building material through a nozzle following a computer-aided pattern. Viscoelastic suspensions aimed for printing are therefore expected to meet several criteria for their suitability as printable inks. First of all, the material is required to both have suitable viscoelastic properties capable to withstand the applied pressure during printing while showing a sufficient fluidity to be extruded through the nozzle. Once printed, the deposited material should retain its shape to avoid collapsing and merging of adjacent layers before post-printing processing.[40] Moreover, when using HIPE materials as "porous" inks the internal emulsion porosity must be retained during printing. The latter aspect is needed because the obtained multichannel internal network will be determined by the dimensions of the internal oil droplet system.[37]

Rheological measurements allow us to determine the viscoelastic limits of the ink by testing its deformability under imposed stress.[41–43] In this particular work, rheological studies were carried out to determine the suitability of each ink formulation for 3D printing. Therefore, amplitude sweep assays and flow curves were performed to study the viscoelastic properties of the prepared HIPE emulsions when varying the amount of PA and the molecular weight of PVA in each formulation.

Figure 3 shows the differences in rheological behaviour for each emulsified ceramic paste. Amplitude sweep assays (**Figure 3A, B and C**) tested the resistance of the material against deformability by applying different shear deformations to the pastes with a constant frequency. To estimate the resistance of the material against deformation, a study of the behaviour of the storage (G') and loss moduli (G'') under shear was required. Briefly, the storage modulus can be defined as the endurance of the material to be elastically deformed under an external force, whereas the loss modulus relates to the viscous response to the applied force.[44] With regards to viscoelastic printable inks, the material is expected to show a range of applied strain in which both moduli remain parallel and independent of the applied strain until a limiting point (yield point or yield stress), where the ink moduli would vary. The constant range of values in which both moduli remain parallel to each other is known as the linear viscoelastic region (LVE) and it is required to demonstrate the ink´s ability to retain its shape under an applied force. Having surpassed this limit, the paste is no longer capable of withstanding the applied force, causing the material to flow and thus losing its structure.

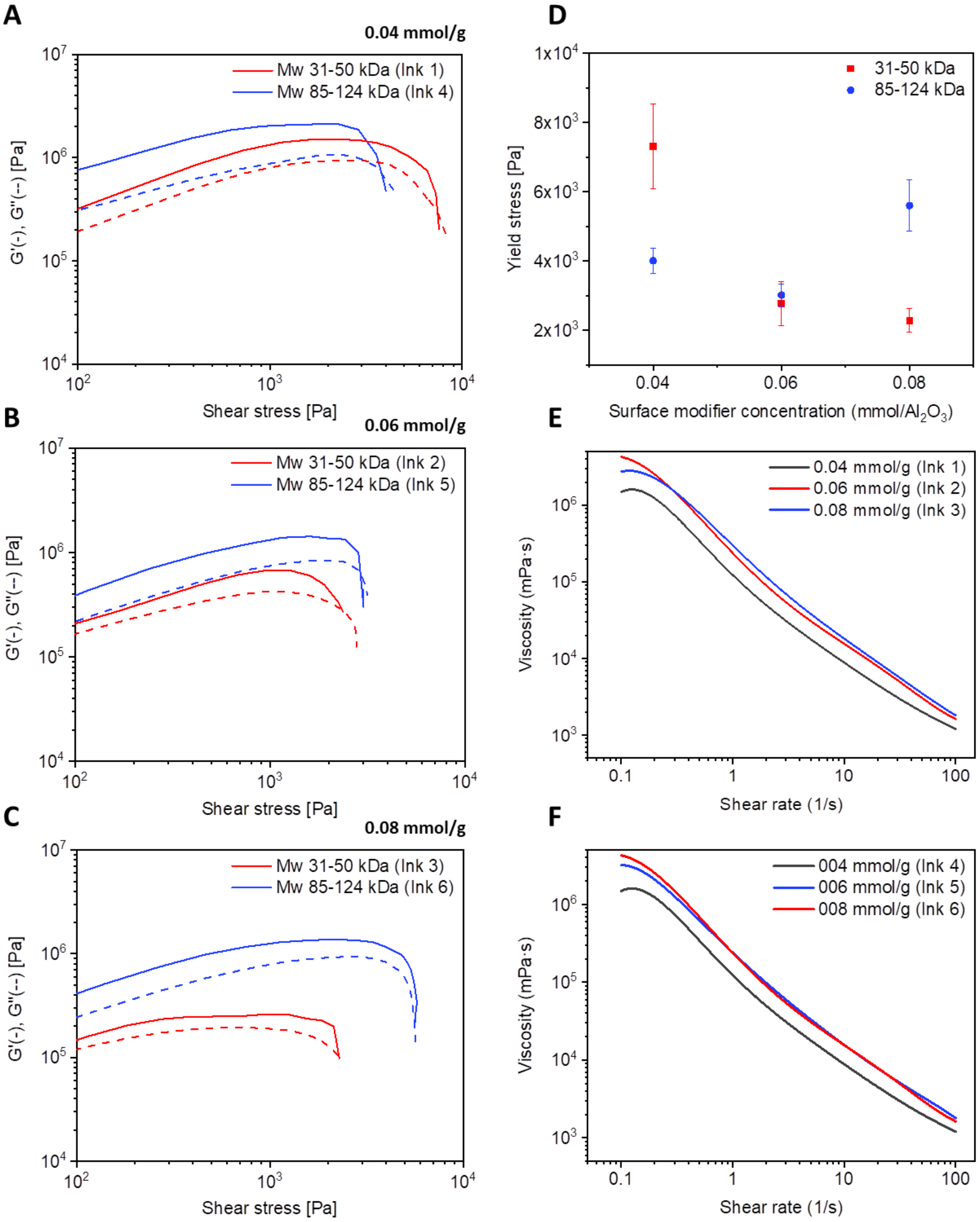

Figure 3. Rheological data for different HIPE alumina inks. **A, B and C)** Strain sweeps of the diverse inks comparing between different concentrations of PA (0.04 mmol/g, 0.06 mmol/g, 0.08 mmol/g respectively). **D)** Yield stress studies of inks comprising PVA of same molecular weight (31-50 kDa and 85-124 kDa respectively) while varying the amount of PA and **E and F)** Flow curves of all the inks prepared.

According to the data plotted in **Figure 3A, B and C**, all pastes exhibited changes under high shear stress, discarding the idea of potentially having solid-like materials. Thickening of ceramic pastes by introduction of the internal phase using emulsions allowed us to obtain dense suspensions from the liquid phases with high deformability under increasing stress. In all samples, both storage (bold line, G’) and loss moduli (broken line, G") were found to remain parallel under increasing applied stress, until reaching the limit in which G’ intersected with G’’. This effect demonstrated that the inks had a viscoelastic behaviour, allowing them to retain their shape until a certain applied force, thus indicative of their suitability as printable materials. Regarding the effect of the chemical composition on the rheological performance, a comparison between different samples was carried out to check the importance of both PA (surface modifier) and PVA toward the printing suitability of the various inks. Inks composed of different ratios of PA (0.04, 0.06 and 0.08 mmol per g of Al_2O_3) (**Figure 3A, B and C**) showed similar profiles under increasing stress. Both moduli proved to have similar values in all samples, indicating that the increasing proportion of surface modifier did not have a relevant effect on the moduli values. On the other hand, the use of PVA of different molecular weight (Mw 31-50 or 85-124) did have a significant effect on the overall deformability of the paste. The addition of a high molecular weight (HMW) PVA resulted in inks with higher mechanical strength, as reflected in an increase of both moduli as compared with the lower molecular weight (LMW) PVA. This effect seemed to be more relevant in inks with the highest concentration of PA (0.08 mmol/g Al_2O_3) and with HMW PVA (ink 6). The use of a high concentration of PA combined with HMW PVA resulted in significantly more dense pastes with higher mechanical stability as compared to those made of the LMW PVA. Nonetheless, all formulations could be easily deformed demonstrating an initial behaviour as printable inks with viscoelastic properties.

Data shown in **Figure 3D** were obtained by comparing the yield stress between inks with different PVA molecular weights and PA contents. Comparison between the different ratios of PA showed appreciable differences in dependence of the used PVA. In the case of inks composed of LMW (inks 1, 2 and 3) a decrease in the yield stress was observed when increasing PA concentration from 0.04 to 0.06 mmol/g of Al_2O_3. However, almost no change could be appreciated when using higher concentrations of PA. An important observation during the studies with ink 1 (LMW PVA, 0.04 mmol/g of Al_2O_3) showed that, in contrast with the other inks, this one still had a more liquid-like consistency, even after emulsification. Due to its low processability, it became difficult to acquire precise measurements of its yield stress, providing high error and low reliable information. Regarding the other ink formulations, samples synthesized using HMW PVA showed an initial weak decrease in yield but with a more significant increase when using the maximum concentration of PA. The observed differences were indicative that the increasing presence of short amphiphiles induced the formation of inks with diverse consistencies. Such a behaviour would be explained following the previous reasoning, in which PVA molecules were substituted on the droplet system by an increasing number of PA molecules adsorbing onto the solid ceramic particles. HMW inks (inks 4, 5 and 6) demonstrated that HMW PVA molecules had a more significant softening effect on inks than their LMW counterparts. With the replacement of the polymer molecules by the increasing concentration of PA, the formed droplets become more capable to adsorb at the oil-water interface. Such an increase in the solid hydrophobicity would increase the strength of the formed droplet network, requiring of further shear to disrupt the structure. On the other hand, LMW PVA proved to have a weaker effect on the paste consistency, indicating that the hydrophobicity of the droplet systems was barely affected by the presence of PVA and showing no significant differences when replaced by more PA-adsorbed solid particles.

Finally, flow curves revealed the viscosity profile of the inks, simulating the shear rate applied during the printing process. Systems that can be used for 3D-printing usually feature a shear-thinning behaviour characterized by a decrease in the viscosity under increasing shear rates. This property is desired for inks, so they can change from a dense material in the syringe into a more liquid-like state capable of passing through the nozzle and yet ultimately depositing with high mechanical strength. Flow curves in **Figure 3E and F** show that all the prepared inks had a decreasing viscosity under increased applied shear, thus showing the shear thinning properties required to flow through the needle during extrusion. Comparison between different ratios of PA in the ink formulations showed that increasing the PA concentration resulted in an increase in the viscosity of the inks. This effect would be explained by the increasing concentration of short amphiphiles on the droplet system, replacing the polymer on the droplet membrane and increasing the number of solid particles in the multi-droplet network, thus diminishing the presence of PVA and creating a more solid-like structure.

Overall, the acquired rheology data demonstrates that the addition of PVA and variations in the concentration of the surface modifier PA resulted in important modifications of the viscosity of the ceramic pastes. The use of PVA with different molecular weights was demonstrated to have an important effect on the ink deformation, where longer polymer chains promoted an increase in the moduli of the acquired pastes. On the other hand, an increase in the number of PA molecules diminished the fluidizing effect of the added polymer in the ink composition when using HMW PVA, resulting in more viscous pastes with higher shape retention and being more adequate for 3D printing.

2.2.3 3D printing

As most of the prepared ink formulations demonstrated suitable characteristics as printable inks, the different pastes were printed to determine which formulation was best suited for building the ceramic support. Building of the ceramic matrix was carried out using a multi-layered 3D square design (**Figure 4A-C**). The printed construct was designed following a grid-like pattern with a total dimension of 4.5×4.5 mm^2, creating smaller square cavities of 0.8 mm (1.2 mm spacing between lines) and a total height of around 1.2 mm (total of 3 layers) (**Figure 4D-H**). Pastes were extruded by air pressure through a nozzle with an inner diameter of 0.4 mm. Although most inks proved to flow under high shear, those containing HMW PVA (inks 4, 5 and 6) could not be extruded, even after applying the maximum available pressure in the printing system (0.5 MPa). On the other hand, ceramic suspensions composed of LMW PVA (inks 1, 2 and 3) could be extruded using pressures of 0.10, 0.17 and 0.20 MPa for inks 1, 2 and 3, respectively. To determine which ink should be used for building the scaffold, all three remaining inks (inks 1, 2 and 3) were printed.

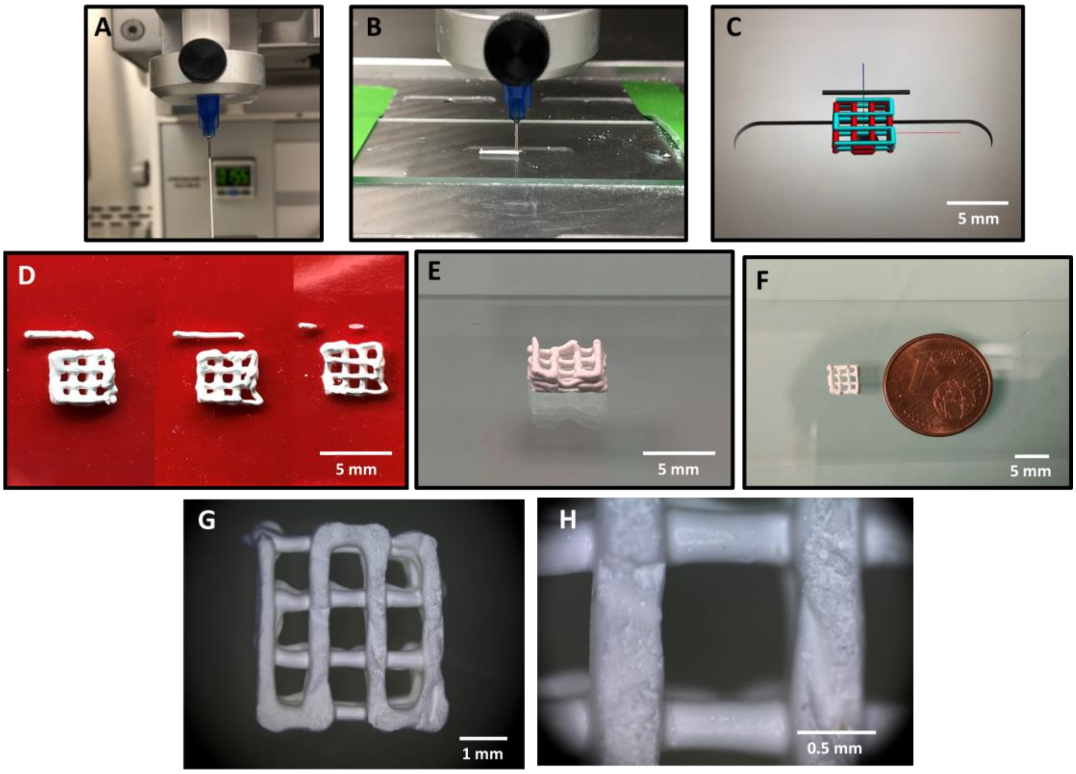

Figure 4. Images illustrating the 3D-printing of ceramic inks. **A, B)** Photographs of the printhead through which the ceramic ink flows. **C)** 3D model of the ceramic support designed with a CAD software. **D, E, F)** Photographs of printed 3D ceramic supports. In image D the printed inks were composed with 0.04, 0.06 and 0.08 mmol/g alumina (inks 1,2 and 3, from left to right). E and F were printed using ink 2. **G, H)** Optical microscopy images of a 3D printed ceramic support at different magnifications (ink 2).

After several printing trials, the ink with the lowest concentration of PA (ink 1) was found to result in scaffolds with lower resolution. Such a decrease in shape retention was observed by comparing the thickness of the printed arrays, being 507 ± 63 µm for ink 1, 382 ± 47 µm for ink 2 and 360 ± 40 µm. Consequently, both inks 2 and 3 could be used to build a stable ceramic support retaining their printing resolution from the nozzle diameter (proportional to 80% of the nozzle diameter, thus 0.32 µm). Comparison between both selected inks revealed that ink 2 (lower PA content) could be more reproducibly printed, being the most suitable candidate for the fabrication of the ceramic support.

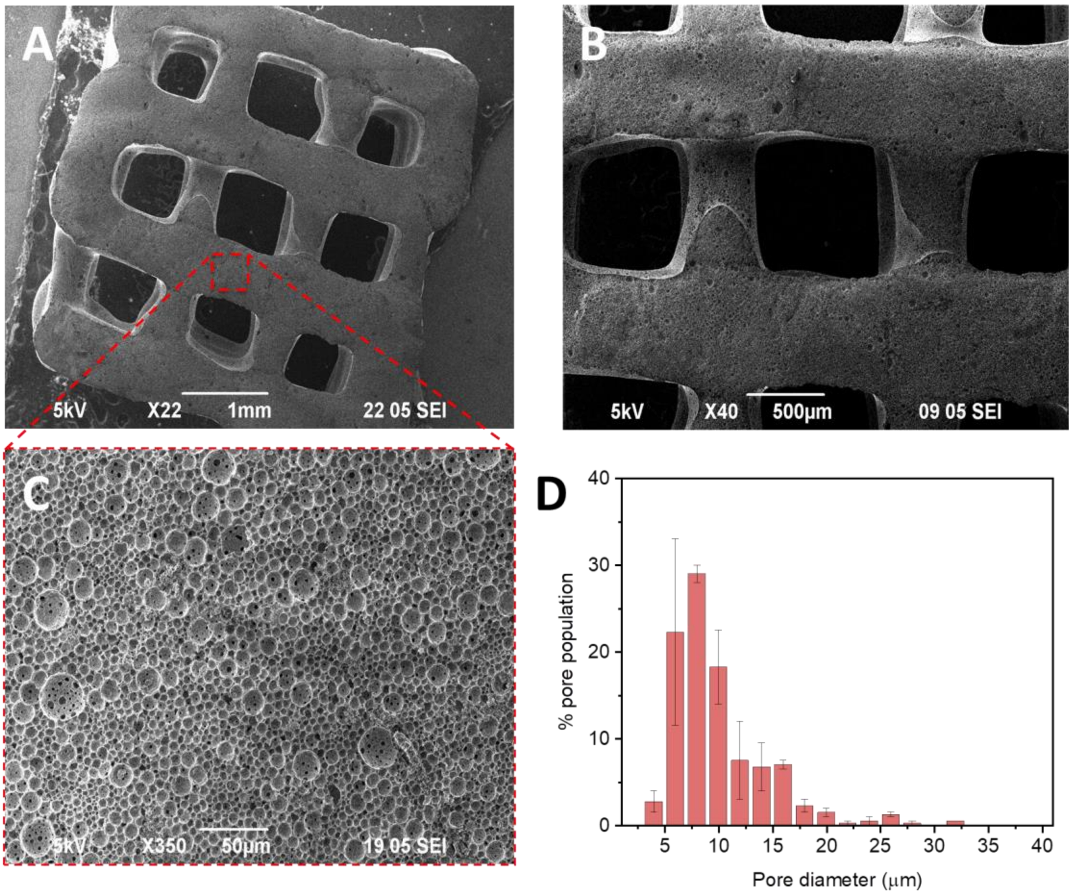

Figure 5. A-C) SEM Images of a 3D HIPE ceramic support, showing its porosity. **D)** Pore diameter distribution determined from SEM images (ink 2).

In addition to the cavities determined by the grid-like design of the 3D pattern, the use of HIPE for the ink synthesis created a different level of porosity within the ceramic strands. Scanning electron microscopy (SEM) images (**Figure 5A to C**) showed the presence of a high density of spherical cavities inside the printed ceramic, with diameters ranging from 2 to 30 µm (**Figure5 D).** The presence of these pores is correlated with the size of the oil droplets produced during the emulsification process.[21] In common emulsion systems; droplet size depends on several parameters such as the emulsifier type, the water/oil volume fraction, and the working emulsifying speed. As a result of the chosen working parameters, a wide distribution of pore sizes was obtained, with the largest population corresponding to cavities with diameters below 10 µm, whereas voids with larger diameters were only filling up to 5 % of the overall volume. Despite the observed differences in pore dimension, this range of pore sizes lies within the desired range of roughness on the surface of the support to enhance cell adhesion yet limiting cell migration inside the matrix.

As already reported, the addition of PVA not only provided further control on the printability of the ink but was also able to create a multi-channelled structure composed of pores interconnected through small "windows".[38] The addition of a weak amphiphilic polymer (in this case PVA) would induce partial occupation of the membranes forming the air/oil droplets. After sintering, the spots previously occupied by the polymer would become empty spaces interconnecting adjacent droplets. These small holes could be seen inside the pores of the ceramic support, with dimensions around 1-2 µm (**Figure 5C**). The dimensions of these windows were too small for cells (average diameter of 10 µm when in suspension) to infiltrate inside matrix, but the interconnected network was expected to promote diffusion of oxygen and nutrients to create an adequate microenvironment for the later seeded cells.

2.2.4 Synthesis of plasmonic nanoparticles

In order to build a scaffold with suitable properties for SERS biosensing, the 3D-printed ceramic was covered with a polymer layer loaded with plasmonic nanoparticles. For this goal, gold nanorods (AuNRs) were prepared and characterized by transmission electron microscopy (TEM) and ultraviolet-visible (UV-vis) near-infrared (NIR) spectroscopy (**Figure 6**).

AuNRs were synthesized according to a previously published procedure.[45,46] In an initial step, gold seeds were prepared by reduction of the gold salt ($HAuCl_4$) with sodium borohydride. The reaction was carried out in the presence of hexadecyltrimethylammonium bromide (CTAB), leading to single crystalline spherical seeds. For the seeded-growth into AuNRs, a growth solution containing $HAuCl_2$ (pre-reduced $HAuCl_4$), ascorbic acid and $AgNO_3$ was prepared, into which the gold seeds were added.[46] Overtime, the spherical seeds grew into larger rods with final average dimensions of 78 ± 5 nm in length and 22 ± 1 nm of width. As a result, the obtained AuNRs displayed a longitudinal localized surface plasmon resonance (LSPR) close to 785 nm. This LSPR is located within the range of the biological transparency window (from 650 to 1350 nm), as well as being in resonance with the wavelength of the NIR laser beam used for the SERS experiments.[47]

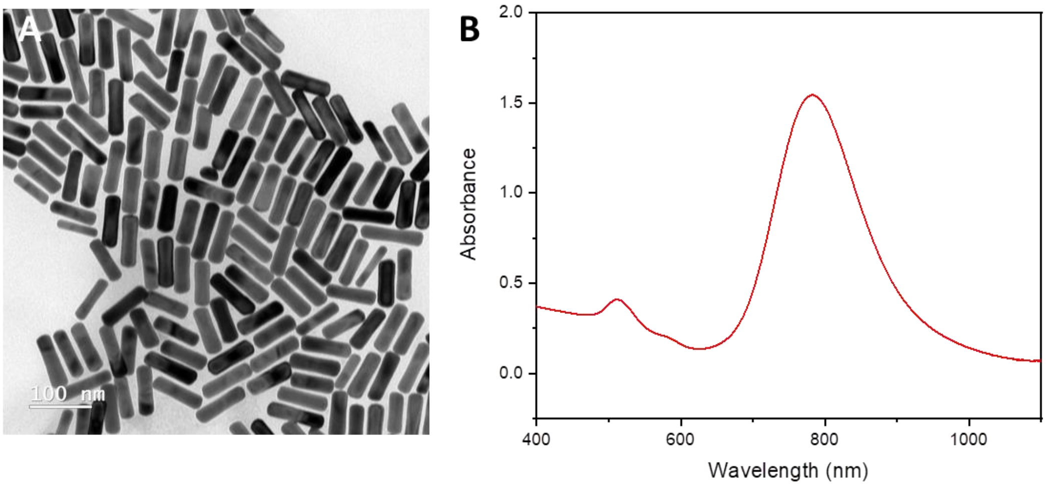

Figure 6. Gold nanorods (AuNRs) for SERS biosensing. **A)** TEM images of AuNRs and **B)** UV-vis-NIR spectrum.

2.2.5 Preparation of hydrogel-based plasmonic composites

The plasmonic biosensing component of this scaffold was formulated by covering the previously described ceramic grid-scaffold with a AuNR-containing hydrogel. For the preparation of the plasmonic polymeric matrix, several commonly used polymers were considered as candidates: alginate, gelatin methacrylate (GelMA) and chitosan. All these polymers are known for having high biocompatibility, a crucial factor for the synthesis of 3D scaffolds for cell culture. In the case of chitosan, the polymer was mixed with water at different weight percentages ranging from 1% to 10%. Due to its high viscosity, the addition of this suspension onto the ceramic support was inhomogeneous and poorly reproducible and, therefore, not suitable for the targeted application. In the case of alginate, gels acquired by cross-linking with calcium chloride ($CaCl_2$) proved to have low mechanical strength, becoming too brittle for the integrity of the support. On the other hand, gelatin methacrylate (GelMA) (**Figure 7A**), which ensures a rapid photo-crosslinking process under UV-light irradiation, provided a biocompatible matrix for coating the ceramic support. Therefore, GelMA was the matrix of choice to build the plasmonic hydrogel.

For the preparation of the GelMA@AuNR gel, an aqueous solution containing AuNRs (10 mM) was added dropwise into a GelMa solution (7 wt%) to reach a final AuNR concentration of 1 mM (**Figure 7B**). As AuNR colloidal suspensions were previously kept stable in the presence of CTAB, before adding them to GelMA, a previous washing step was required to remove the excess of CTAB, which is cytotoxic.[48,49] Ideally, the removal of CTAB from AuNRs via washing, mixing with GelMA and subsequent gelation, should take place as quick as possible to avoid AuNR aggregation and entrap the particles within the polymer, thus preventing further aggregation.

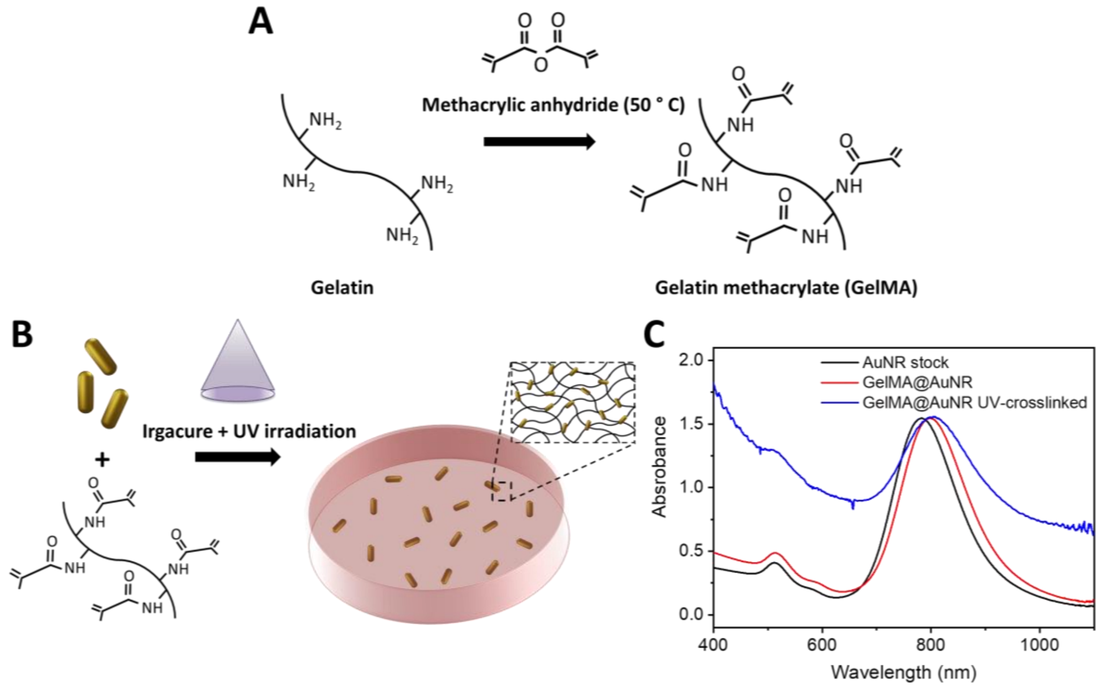

Figure 7. A) Scheme of the methacrylation reaction of gelatin to form GelMA. **B)** Preparation of the plasmonic polymer composite by mixing AuNR with GelMA and subsequent UV-light irradiation, and **C)** Comparison of UV-vis-NIR spectra. for AuNRs in water (black), embedded in GelMA (red), and after crosslinking by UV irradiation (blue).

The stability of AuNRs inside the polymer matrix was assessed by UV-vis-NIR spectroscopy (**Figure 7C**). The composite system comprised of AuNRs within a polymer matrix was found to display a small red-shift from 785 to 795 in the LSPR maximum, which could be explained by the different index of refraction of the polymeric material compared to water.[50] This effect could be further observed after UV-induced crosslinking of the polymer matrix indicating an increase of the index of refraction after gelation. Nonetheless, such an increase in the LSPR wavelength did not hinder the applicability of the system because it was still located near the wavelength of the NIR laser (785 nm). With regards to the monodispersity of the AuNRs, no significant signs of aggregation were observed upon their inclusion in the polymer solution, as shown by the lack of broadening of the LSPR. However, upon cross-linking we did observe a slight broadening, possibly due to an increase in the overall scattering of the material. This argument was supported by the largely increased extinction at lower wavelengths, compared to the previous stages.

Once AuNRs were incorporated in the mixture, the viscoelastic properties of the loaded gel were characterized. For this study, the viscoelastic properties of disc-shaped gels were tested by rheology measurements based on amplitude and frequency sweeps. The amplitude sweep in **Figure 8A** was performed to determine the viscoelastic region of the gel, where both the storage and the loss moduli (G' and G'' respectively) in both samples were found to be independent of the applied strain at similar values. This behaviour indicated that both gels were able to withstand external increasing amplitudes (under constant frequency) without breaking. Using this initial information following frequency sweeps, assays were performed using a constant strain at 0.01% to work within the stable viscoelastic range.

Frequency sweep assays were subsequently carried out to determine G' and G'' of the polymer matrix at increasing frequencies (at constant amplitude). The obtained data showed that the addition of the plasmonic nanoparticles appeared to influence the gel strength (**Figure 8B**), lowering the storage modulus from 323 ± 22 to 230 ± 55 Pa and the loss modulus from 12 ± 2 to 7 ± 3 Pa (values at a frequency of 1 Hz). This reduction in both moduli might have been caused by a reduced degree of crosslinking in the methacrylate variant, originated by the affinity of the polymer towards the added nanoparticles[51,52]. Despite the observed difference in their modulus, both cross-linked gels were still able to retain their solid integrity, demonstrating that the addition of NPs did not significantly alter the mechanical properties of the GelMA gel.

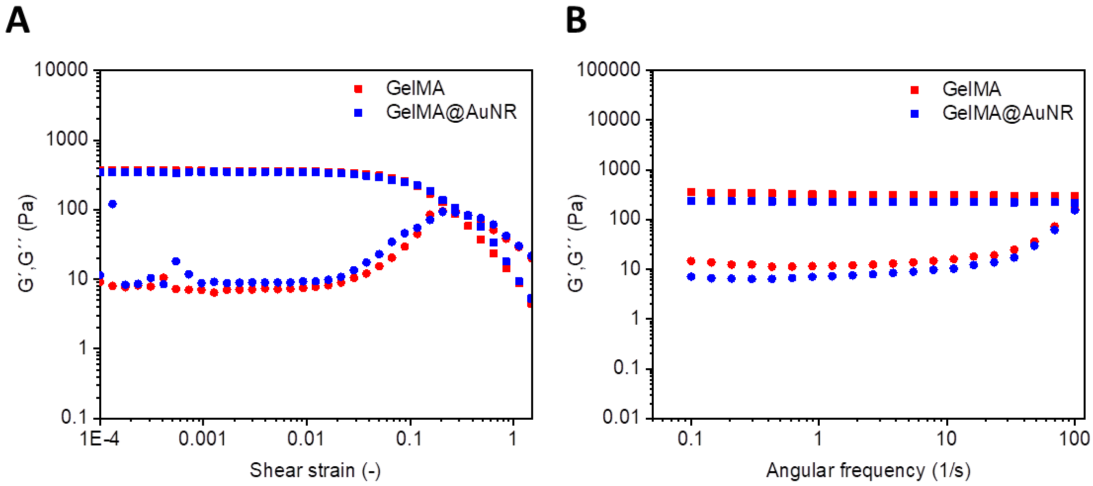

Figure 8. Rheology studies of GelMA gels (control and loaded with AuNR (1 mM) (GelMA@AuNR)). The tests consisted of amplitude **(A)** and frequency **(B)** sweeps. The plotted values are the average of three different measurements.

After studying the viscoelastic properties of the matrix, the stability in aqueous cell media was also evaluated for subsequent cell studies. Henceforth, the polymer matrix loaded with the plasmonic nanoparticles was also required to retain its physical structure over long periods of time under cell culture conditions. Swelling studies were performed by incubating the GelMa hydrogel in cell media (supplemented with 10% v/b fetal bovine serum), then recording the weight changes at certain time points over a 21-day period (**Figure 9**). This period of time was chosen because it has been demonstrated that this is the necessary time to ensure maturity of osteoblasts.[53]

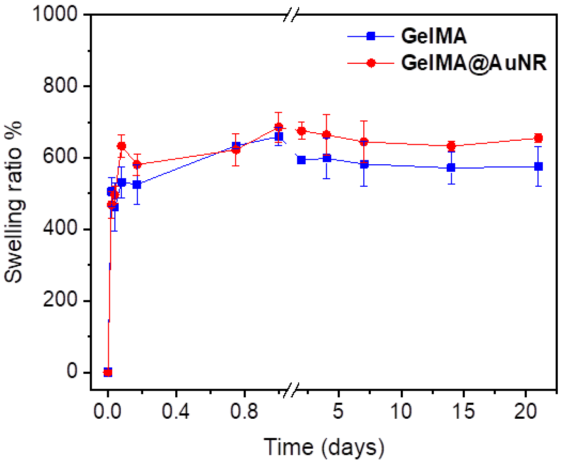

Figure 9. Swelling studies of GelMA in cell media up to 21 days

Swelling studies indicated that, during the first 24 hours, the swelling ratio (SR) of the matrix increased by up to 630% in both polymer systems, with and without AuNR. No significant differences in the SR could be appreciated between the samples during the incubation time of study. Measurements at longer times indicated that both GelMA gels were able to remain in a constant swollen state, even when incubated together with other components present in the cell media. Neither of the samples showed signs of degradation, even after 21 days, thus supporting their suitability as a biosensing support.

2.2.6 SERS biosensing control assays

After characterization of the polymer matrix upon loading with the plasmonic nanoparticles, the following step comprised the evaluation of the SERS sensing capacity of the biosensing platform. To work as a sensing substrate, the plasmonic hydrogel should both allow diffusion of the environmental biomolecules into the matrix to reach the internalized plasmonic nanoparticles and enhance the SERS signal of the analyte of interest uniformly over the whole volume.

The biosensing performance of the SERS substrate was tested using commercial PCN and methylene blue (MB). MB was used for the initial tests due to its wide use as a Raman probe, thereby providing a highly identifiable chemical fingerprint.[54,55] The acquired SERS spectra (**Figure 10A**) confirmed the presence of the analyte by clearly distinguishing some of its characteristic Raman peaks, located at 1394 (C-N stretching, CH bending) and 1620 (ring C-C and C-N stretching) cm^{-1} respectively.[56] SERS efficiency was further assessed by incubating the hydrogel with different concentrations of MB (ranging from 100 µM to 100 nM) to determine the limit of detection (**Figure 10B**). The SERS spectra showed that the composite biosensor was able to identify the characteristic Raman peaks down to concentrations close to 1 µM. However, for lower concentrations the peaks could not be distinguished from the background signal.

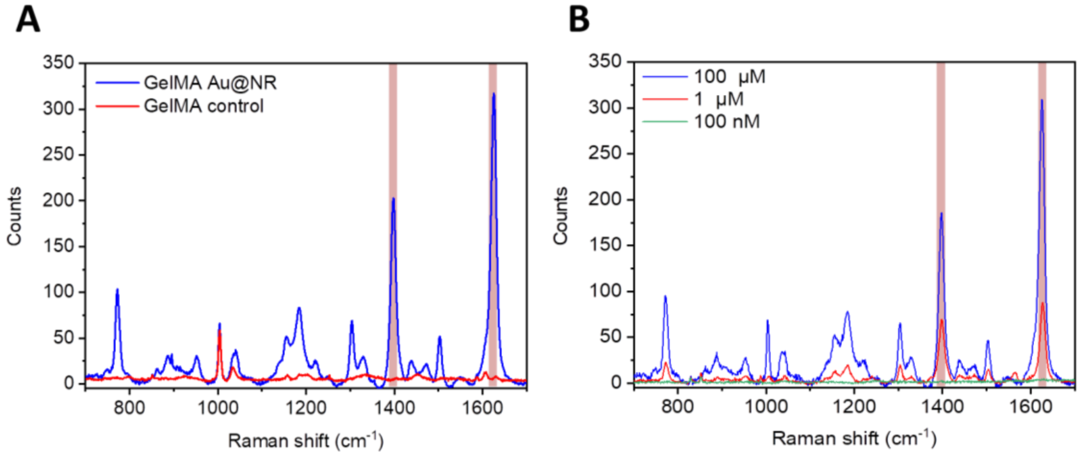

Figure 10. SERS sensing controls with MB. **A)** SERS spectra from MB (100 µM) in GelMA, with and without AuNR. **B)** Comparison of the SERS intensity for GelMA@AuNR (1 mM) with different concentrations of MB.

In addition to obtaining the SERS signal at specific spots, we conducted volumetric SERS mapping, thereby obtaining an overview of MB SERS intensity across the substrate, followed by probing the maximum penetration depth for imaging. SERS maps were acquired using the maximum SERS intensity at 1624 cm^{-1} (**Figure 11**), which demonstrated the presence of MB covering the whole area of the nanoparticle-loaded polymer substrate. SERS maps acquired at different heights in the hydrogel additionally proved that the detection was possible down to 1 mm in depth (**Figure 11B**). Differences in SERS intensity could be observed in some regions, probably due to the roughness and porosity of the sample.

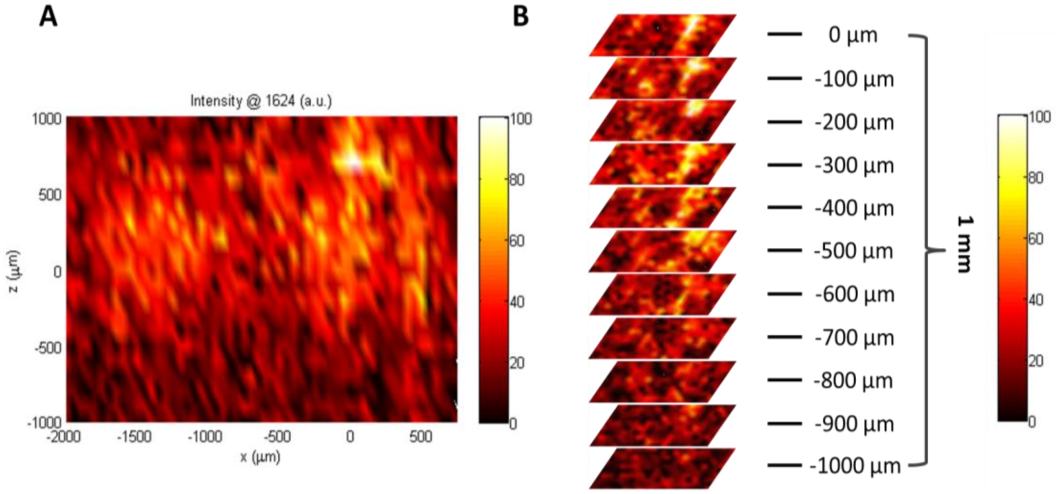

Figure 11. SERS maps of MB (10 µM) incubated in GelMA@AuNR scaffolds. **A)** SERS map in depth (2 mm). **B)** SERS maps (2x1 mm) from different planes of the hydrogel down to 1 mm in depth (distance between planes of 100 µm, representation of the intensity from the peak at 1624 cm^{-1}).

Having demonstrated the SERS sensing capability of the AuNR-loaded polymer matrix, the following step comprised testing the SERS performance of the composite support combined with the printed HIPE ceramic matrix (**Figure 12A**). For the following set of assays, the ceramic support was embedded in GelMA@AuNR (1 mM) and subsequently cross-linked by UV irradiation (365 nm) until achieving the hardening of the polymer matrix covering the whole volume of the printed ceramic (**Figure 12B-D**).

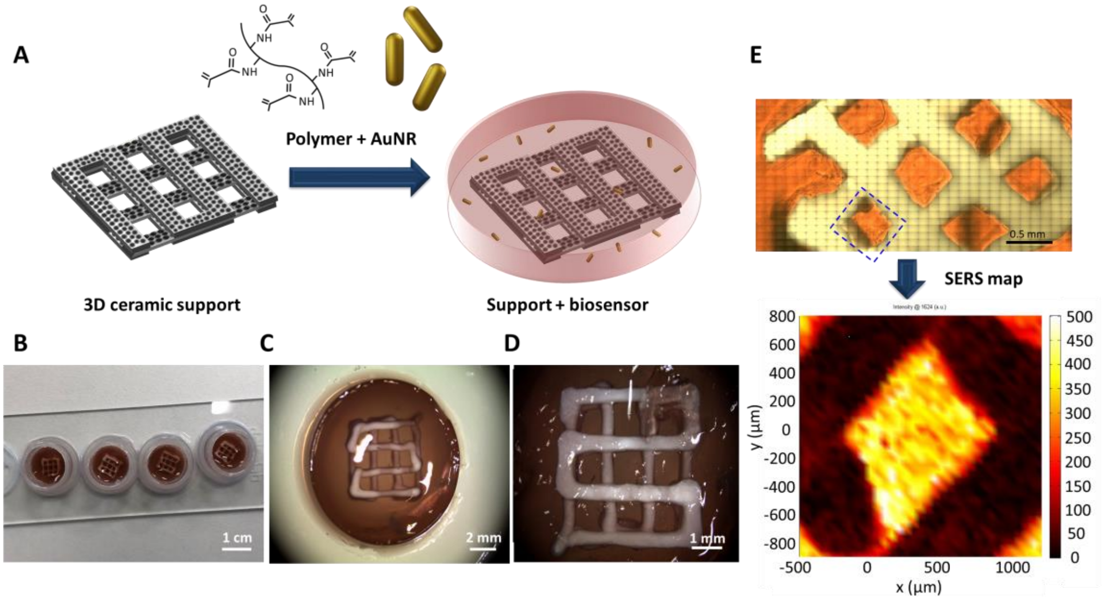

Figure 12. Combination of the ceramic support with the AuNR-loaded polymer matrix. **A)** Scheme of the scaffold preparation. **B-D)** Optical images of the combined ceramic-polymer scaffolds (B: general, C: top view; D: bottom view). **E)** SERS sensing of MB (100 µM) in the combined support. Shown are the optical images of the tested area and the acquired SERS map following the intensity at 1624 cm^{-1}.

The cross-linked ceramic-polymer scaffolds were subsequently incubated in a solution of MB (100 µM) for 2 h and measured by SERS mapping. **Figure 12E** shows both an optical image of the scanned area (dashed blue box) and the acquired SERS map. The SERS results demonstrated that the signal from the tested analyte (MB) could be recorded within the polymer matrix located within the patterned well, whereas the walls of the ceramic did not provide any signal (black areas in **Figure 12E**), likely because of the high level of light scattering by the ceramic material. The acquired data not only showed that the polymer matrix retained its SERS sensing capabilities, but also provided an insight regarding the possibility of acquiring SERS maps at determined locations within the support.

Following a similar approach, detection of commercial PCN (**Figure 13**) was also tested using concentrations down to 1 µM. Pyocyanin (PCN, 1-methoxy-

5-methylphenazine) is a phenazine secondary metabolite that is produced in significant amounts by *P. aeruginosa* **(Figure 13A).**[31] PCN has been an object of study due to its redox-active nature and important role during bacterial communication, through the quorum sensing mechanism.[30,36] SERS studies of the biomolecule might provide information on the survival and growth of bacteria over the course of bacterial bone-infection processes. SERS spectra were thus acquired at different depths inside the hybrid scaffold, to demonstrate the diffusion of the analyte inside the porous matrix and to determine the limit of detection in depth. The SERS spectra in **Figure 13B** show that the signal from PCN could be reliably detected down to 300 µm in depth, whereas for 1 mm in depth the signal could be hardly differentiated at this concentration.

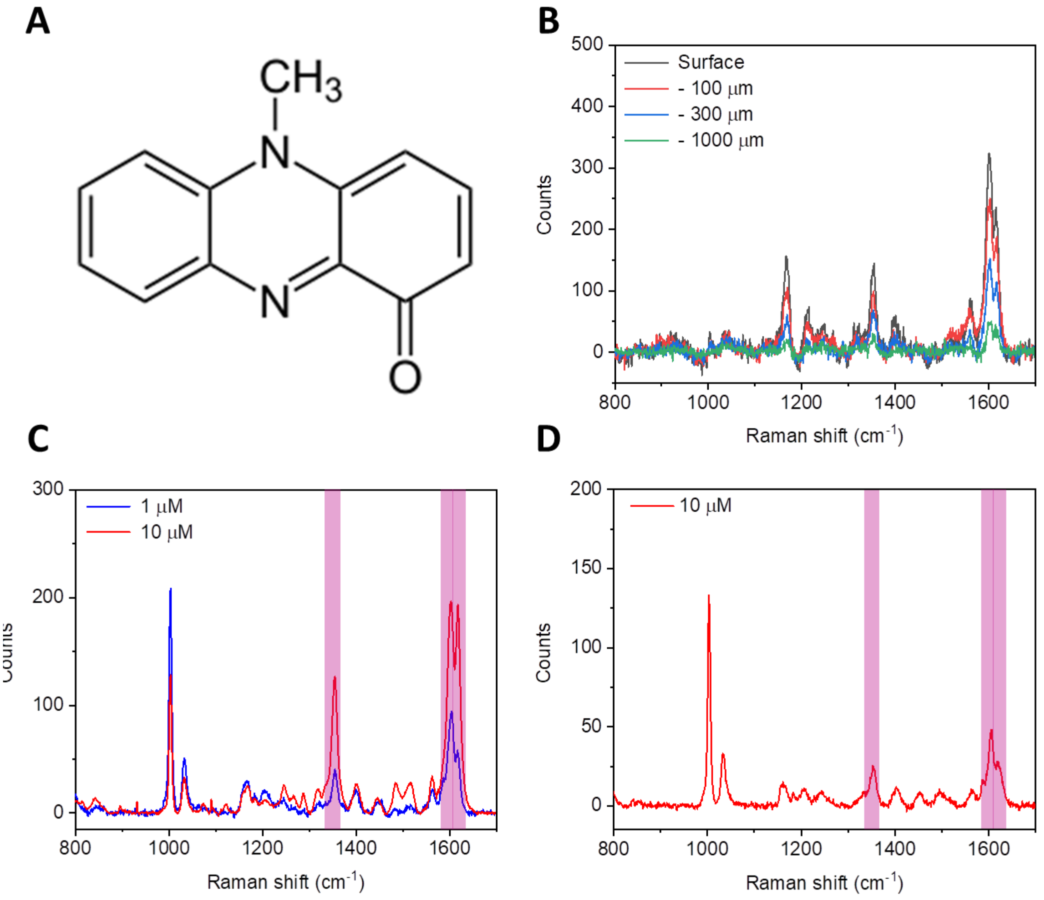

Figure 13. Biosensing control assays for PCN detection. **A)** Molecular structure of pyocyanin. **B)** In-depth SERS sensing of PCN (1 mM) inside GelMA@AuNR, down to 1 mm in depth. **C and D)** Comparison of the SERS intensity of PCN in different media and concentrations (limit of detection assay). C) Milli-Q water, D) LB broth.

After proving the detection and SERS mapping of PCN within the composite support, a final control assay was performed varying the media of the suspension to further imitate the conditions in the subsequent bacterial studies.

For these assays, PCN was mixed in either MilliQ water or Lysogenic broth (LB, also known as Luria broth), as an example of bacteria culture media, at concentrations of 1 and 10 µM. SERS data shown in **Figure 13C** indicate that, whereas PCN could be detected in MilliQ water at both concentrations, when LB was used (**Figure 13D**), detection was only possible at 10 µM, mainly indicated through the main peaks at 1350 (C=C and C-N stretching, and CH_3 bending) and 1624 cm^{-1} (C=N stretching).[57] Despite the observed limitation in concentration using the LB media, control assays demonstrated the possibility of detecting PCN in media containing other biomolecules, rather than in simple MilliQ water, therefore proving the capacity of the system to detect this analyte in more complex media

2.2.7 SERS studies of bacterial-secreted PCN

After demonstrating the biosensing capacities of the composite support for commercial PCN, the system was tested for the detection of natural bacteria-secreted PCN. SERS detection of bacteria-secreted PCN was carried out using two different strains of *P. aeruginosa*: wild type (WT) and mutant (Δphz14). The mutant variant was altered to inhibit the synthesis and release of PCN (**Figure 14**). We initially detected PCN in the supernatant of bacteria. For SERS measurements of supernatants containing bacterial-secreted analytes, bacteria were initially streaked onto agar-LB plates and left to grow for 24 h. After incubation, a single colony was retrieved and incubated in LB to acquire a solution of *P. aeruginosa*. The growth of *P. aeruginos*a was checked over time by measuring the UV-vis absorbance at 600 nm, in which a value of 3 corresponds to $1\cdot10^9$ colony forming units (cfu)/mL. [35]

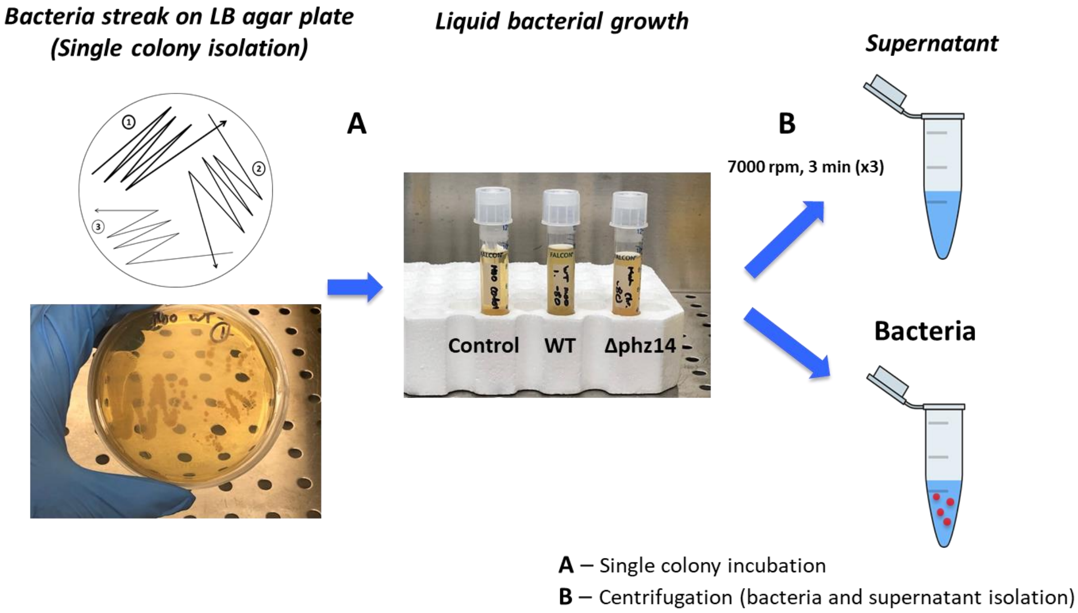

Figure 14. Summary of the bacteria culture procedure for acquisition of PCN from *P. aeruginosa.*

To incubate the scaffold with the bacterial media, an in-house devised setup was prepared using a 3D-printed holder (**Figure 15**). The holder was designed to contain a well in which the plasmonic scaffold and the media could be in contact within a confined space. After loading the bacteria and incubating for several days, a thin quartz slide was deposited on top of the well to create a closed compartment in which bacteria could be confined during SERS signal acquisition, thus avoiding contamination of the objective.

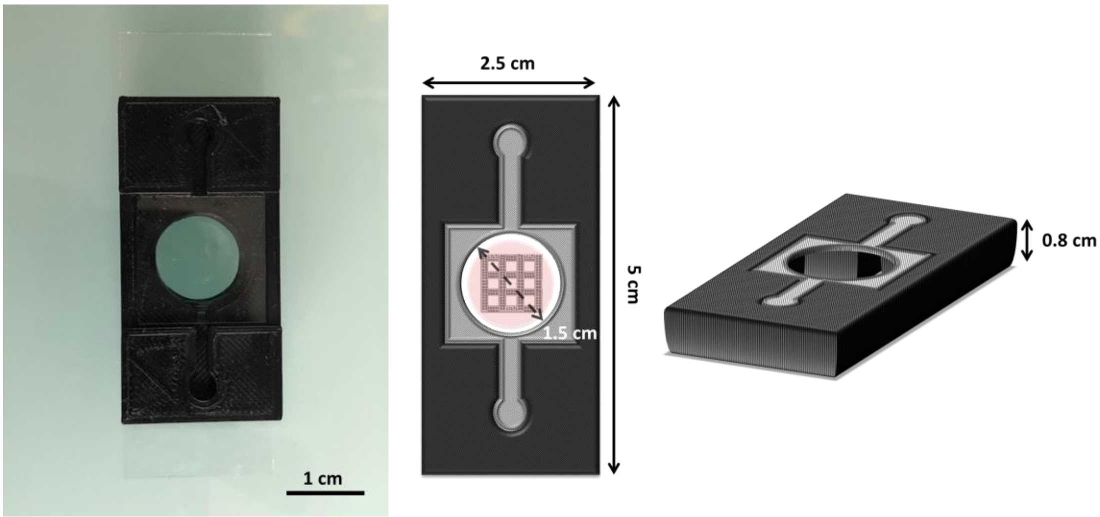

Figure 15. 3D-printed holder for bacteria incubation and SERS studies.

SERS sensing assays of bacterial-secreted PCN were carried out following two different approaches, as shown in **Figure 16**. In the first case, only the supernatant from the bacterial culture (free of bacteria) was incubated with the plasmonic scaffold to detect the presence of bacteria-secreted PCN. In the second approach, bacteria were directly inoculated to the ceramic support and allowed to grow for 18 hours to achieve PCN production.

For the first approach, once bacteria growth was achieved and visible changes in colour (a sign of PCN production) and turbidity were observed in the tube (ca. 18 h of incubation), a small aliquot was retrieved. PCN present in the media was subsequently separated from bacteria via several centrifugation steps (**Figure 14**). Using fresh liquid media as a control, changes in the colour of the suspension of the wild type variant could be already appreciated, acquiring a darker blue tone compared to the normal yellow colour of LB, and compared to the *P. aeruginosa* mutant Δphz14. After incubation of the supernatant with the scaffold, SERS measurements were able to identify the principal Raman peaks, 1350 and 1624 cm^{-1}, in the supernatant obtained from the WT variant, whereas these were not observed in the supernatant derived from the Δphz14 bacteria (**Figure 16A and C**). SERS maps of the scanned area clearly showed the ability of the GelMA@AuNR to act as a SERS sensor for PCN.

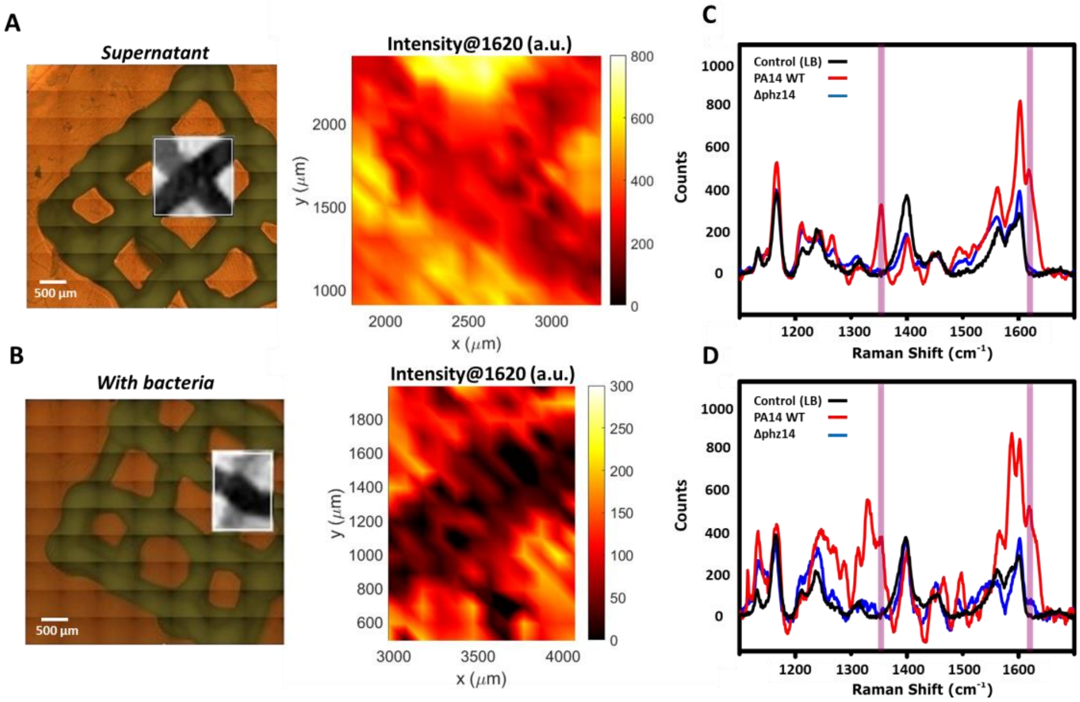

Figure 16. Comparison of PCN SERS signals inside ceramic/polymer composite scaffold using the supernatant from bacterial culture **(A, C)** and in the presence of *P. aeruginosa* in the scaffold **(B, D)**, for both the wild type (PA14 WT) and the phenazine-deleted mutant (Δphz14). The square boxes shown in black and white in A and B mark the scanned areas used for SERS mapping.

For the second type of SERS assay, *P. aeruginosa* bacteria were incubated at a final concentration of $1\cdot10^7$ cfu/mL with the plasmonic support. After 18 h of incubation, the presence of PCN was measured using SERS mapping, demonstrating the biosensing capacity of the scaffold (**Figure 16B and D**). When comparing SERS maps of the wild type and mutant varieties (**Figure 17**), almost no signal was observed for the mutant variant. Despite the presence of bacteria during signal acquisition, SERS data of secreted PCN could be clearly recorded. However, a reduction in the intensity was observed in experiments performed with bacteria in comparison with those performed with the supernatant. This reduction in the signal intensity could be explained by either a difference in the amount of PCN present in the media when secreted *in situ* by the bacteria, or by the increased turbidity caused by the presence of bacteria, which could increase light scattering and reduce the intensity of the SERS signal.

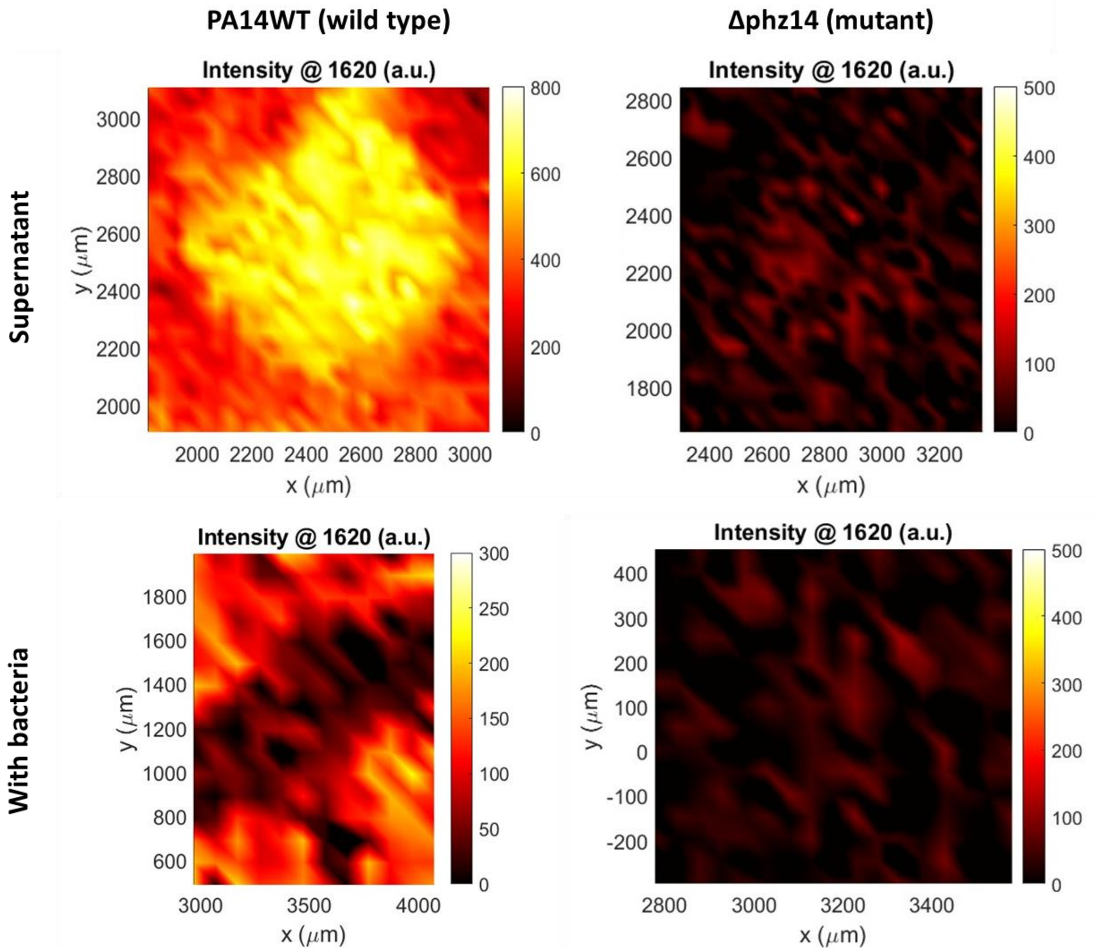

Figure 17. Comparison of SERS maps recorded from the detection of PCN secreted by different *P. aeruginosa* strains (wild type and mutant). For each system, the samples were incubated either with the supernatant after removing the bacteria (upper panel) or directly incubated with bacteria (lower panel).

2.2.8 Biological compatibility with osteoblast cell lines

Once the sensing capabilities of the system were demonstrated, we assessed its use as a support for osteoblasts and subsequent osteoblast-to-osteocyte differentiation observed during the mineralization process. We first choose to focus on the biocompatibility of the scaffolds with Human fetal osteoblasts (hFOB). These types of cells were chosen to try and replicate the formation of a natural bone tissue by interacting with the solid support. The designed ceramic material was proposed as a 3D cell model that supports bone-like tissue formation while allowing for the biosensing of a bacterial infection. Due to the complex composition of the biosensing support (mainly regarding the HIPE alumina ceramic support and the nanoparticle-loaded polymer GelMA@AuNR), it was necessary to evaluate the cell viability of each component, to discard any possible cytotoxic effect for the complete scaffold. Two commercial cell viability assays were used, 3-(4,5-dimethylthiazol-2-yl)-2,5-diphenyl-2H-tetrazolium bromide (MTT) and lactate dehydrogenase (LDH), to determine the biocompatibility of each component (namely, the ceramic, GelMA@AuNR, and ceramic + GelMA@AuNR). The MTT assay is traditionally considered a test of cell viability because it detects the metabolic activity of the cells themselves. In contrast, the LDH assay measures cytotoxicity via detection of an otherwise intracellular enzyme, which is released upon cell membrane damage. To determine if any cytotoxic components leach from the scaffolds, the scaffolds were incubated in Dulbecco's Modified Eagle Medium supplemented with 10% v/v FBS, collectively known as complete DMEM (cDMEM), for 24 h or 48 h. Subsequently, the media was transferred to wells containing adhered hFOB cells, and cells were incubated in this new media for 24 h prior to MTT and LDH assays. Data shown in **Figure 18** discarded the presence of cytotoxic effects on the cells as most of the cell viability values were above 80% and cytotoxicity not even reaching 5%. Therefore, the acquired data demonstrated that all the scaffold components were biocompatible to hFOB cells.

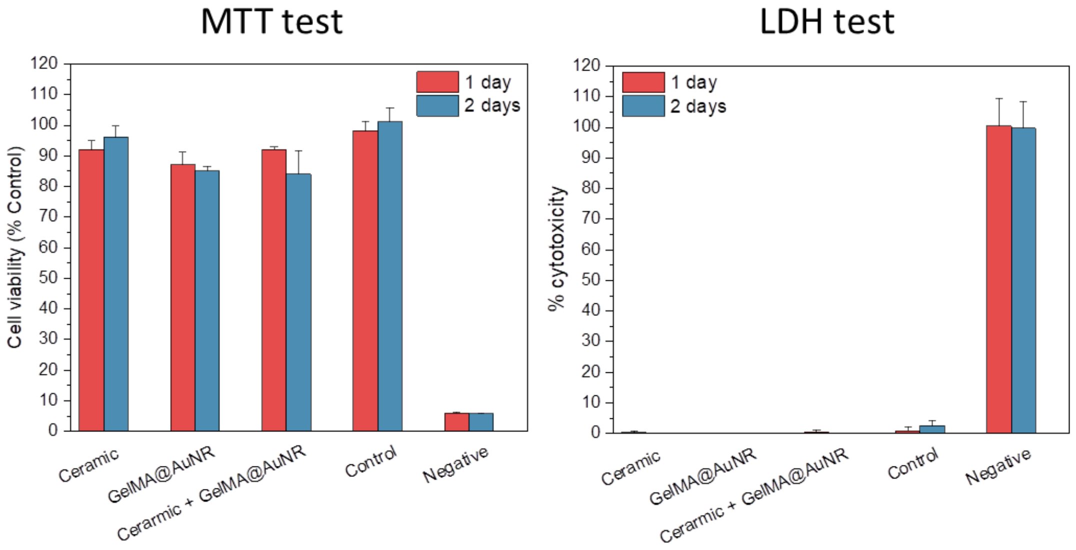

Figure 18. MTT and LDH biocompatibility assays of the different components of ceramic/polymer composite scaffolds.

2.2.9 *In vitro* cell culture studies on the composite 3D porous scaffold (3D ceramic matrix + GelMA@AuNR)

Cell seeding of osteoblasts assessed the suitability of the ceramic support to mimic a human bone tissue. Osteoblast cells require a minimal time of approximately 20 days until differentiation into mature osteoblasts is completed.[58–60] Due to the prolonged required time, the bone-like support was required to provide an adequate environment for the cells to migrate and develop into mature osteoblasts after several weeks post-seeding. To study cell adhesion onto our ceramic support, an initial assay was carried out by seeding of $3 \cdot 10^4$ cells per scaffold and later embedding in Geltrex, which was initially used as media to enhance cell adhesion onto the ceramic support, alongside providing factors to promote cell differentiation.[61–63] After 24 h, the seeded support was coated with GelMA@AuNR. UV crosslinking of GelMA was performed using a minimum amount of irradiation over a short period of time (40 s at a low intensity of 50 mW/s) to avoid damaging the cells while ensuring complete crosslinking of the polymer gel. During the incubation time, seeded supports were incubated at 37 °C in a well containing cell culture media (cDMEM), to provide the required nutrients to the cells alongside avoiding drying of the polymer matrix.

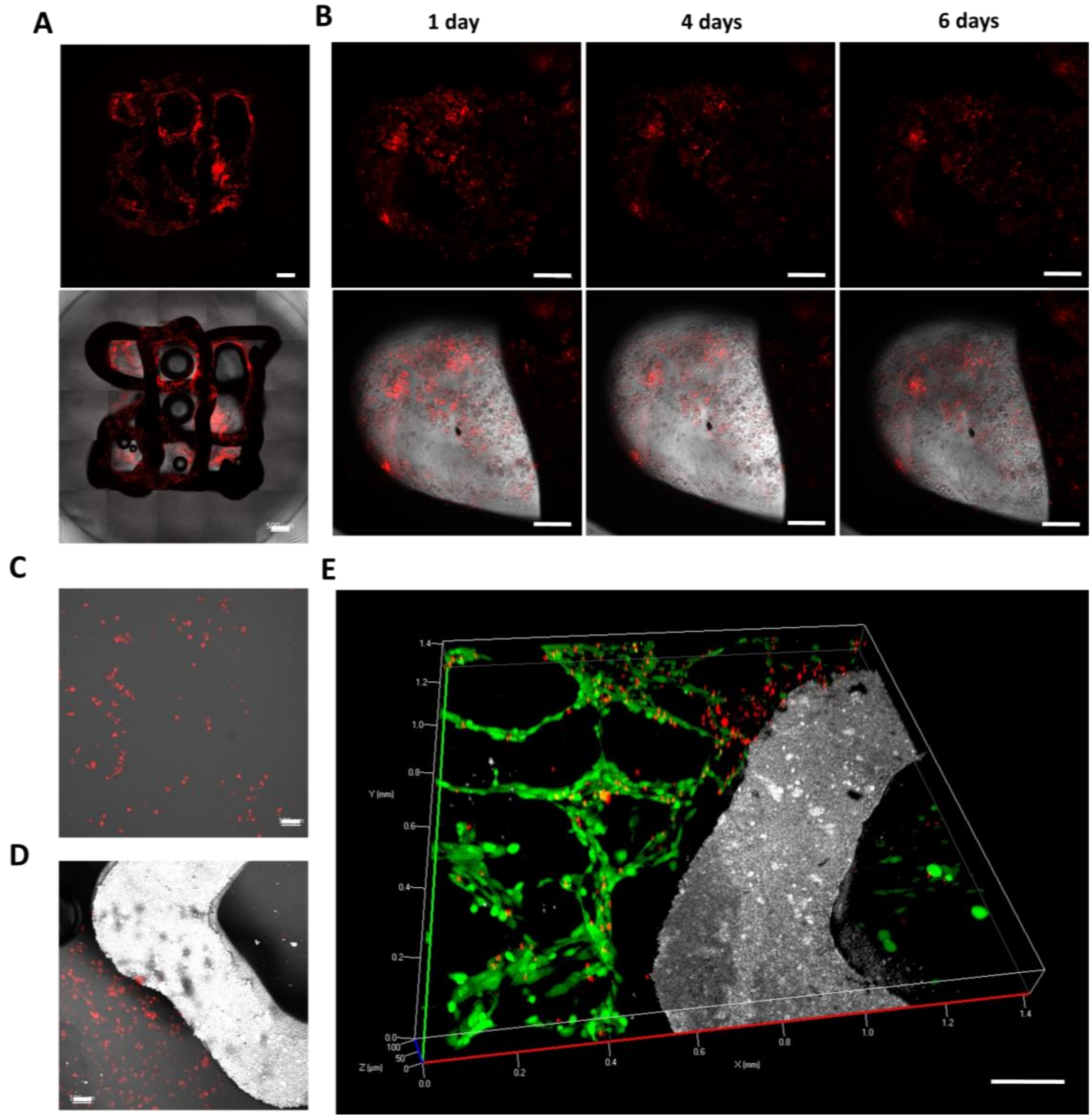

Figure 19. Confocal fluorescence images of osteoblasts seeded on the composite scaffold. **A and B)** Fluorescence imaging of osteoblasts seeded onto the ceramic support before adding GelMA@AuNR and labelled with cell tracker deep red (without geltrex). Images in B were taken at different days after seeding. **C and D)** Fluorescence images of cells seeded on top of GelMA@AuNR. Image C was taken on top of a control GelMA@AuNR (no ceramic) gel and D at the side of the GelMA@AuNR coated ceramic scaffold. **E)** Live/dead cell viability staining of cells on top of the composite support (green: calcein, alive; red: PI, dead). Scale bars represent 500 µm in A, 200 µm in B and E and 100 µm in C and D.

3D confocal fluorescence imaging (**Figure 19A and B**) shows that whilst the overall cell distribution around the scaffold was good, no changes were observed in cell growth or movement over time in the GelMA@AuNR, suggesting that the cells were dead from an early timepoint. Then, to determine the suitability of the polymer matrix, various experiments with the GelMA@AuNR substrate were carried out as a control, having cells seeded on top of GelMA@AuNR (with and without the ceramic scaffold). The latter images suggested that cells could indeed grow on top of the gel in both samples (**Figure 19C and D**), even with the presence of the 3D-printed ceramic. Therefore, this behaviour was further demonstrated when left for up to 3 weeks, as it could be observed that osteoblasts colonized the GelMA@AuNR surface and live/dead cell viability staining suggested a high percentage of viable cells (**Figure 19E**).

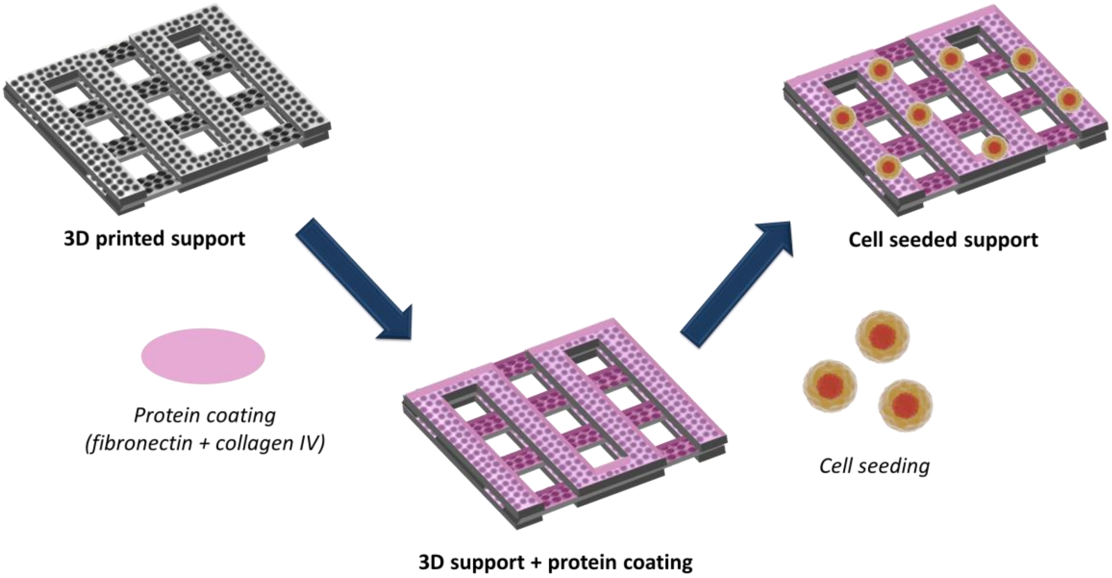

Figure 20. Scheme of the synthesis of a 3D cell culture support with SERS biosensing properties. The HIPE alumina support was 3D-printed and sintered to acquire the solid structure. The support was then coated with a protein layer to enhance cell adhesion after seeding.

With the acquired information we subsequently focused on the growth of the osteoblasts on the ceramic scaffold, leaving out the plasmonic sensing support for the initial studies. In order to enhance the diffusion and adhesion of osteoblasts onto the 3D HIPE ceramic, a new approach was tested consisting of the addition of a protein coating. Bone-derived cells present in natural bone matrix can synthesize several proteins during healing and growth of the bone tissue, collagen being the most common one. Therefore, a protein layer made of collagen IV and fibronectin (labelled with AF633 labelled antibody) was added before cell seeding (**Figure 20**). Addition of a protein layer onto the HIPE ceramic was expected to further promote the interaction of the seeded osteoclasts with the matrix by enhancing their adhesion. The creation of a niche with a similar composition to the natural bone tissue would also enlarge the lifetime of osteoblasts, providing time and nutrients until reaching their maturation into osteoclasts. For this method we applied a protein-coating rotating technique, which had been shown to be successful in previous work by the group. This involved immersing the ceramic scaffolds in a solution of fibronectin and collagen and leaving the samples rotating at 10 rpm for 3 h at room temperature. Scaffolds were subsequently washed and then osteoblasts added, also taking advantage of the rotation to ensure a homogenous interaction with the scaffold.

As observed in **Figure 21A,** fluorescence imaging was able to demonstrate the presence of a labelled-protein membrane (immunostained fibronectin) coating most of the support's surface, which is a suitable indicator of protein adhesion. Unfortunately, collagen IV presence could not be tested due to lack of the relevant primary antibody due to COVID-related distribution issues.

In order to demonstrate the suitability of the newly coated supports for bone cells studies, two types of osteoblasts were seeded. For these assays hFOB (osteoblast type 1) and Mg63 (osteoblasts type 2) were labelled with a cell tracker and seeded onto the protein-coated ceramic matrix. Bright-field microscopy of the seeded cells (**Figure 21B**) revealed the presence of cells adhered onto the edges of a ceramic support. In addition, fluorescence images in **Figure 21C and D** demonstrated that both bone-derived cells were capable to remain adhered across the ceramic surface. Consequently, observations on both cell lines indicated a similar behaviour with little sign of cell death and an enhanced adhesion onto the 3D-printed support.

Despite the promising results obtained after protein coating, further assays using the complete polymer-ceramic support combined with the newly protein coating could not be performed. Therefore, it would be necessary to further optimize the conditions to ensure the survival of osteoblasts while retaining the stability of the support over possible degradation.

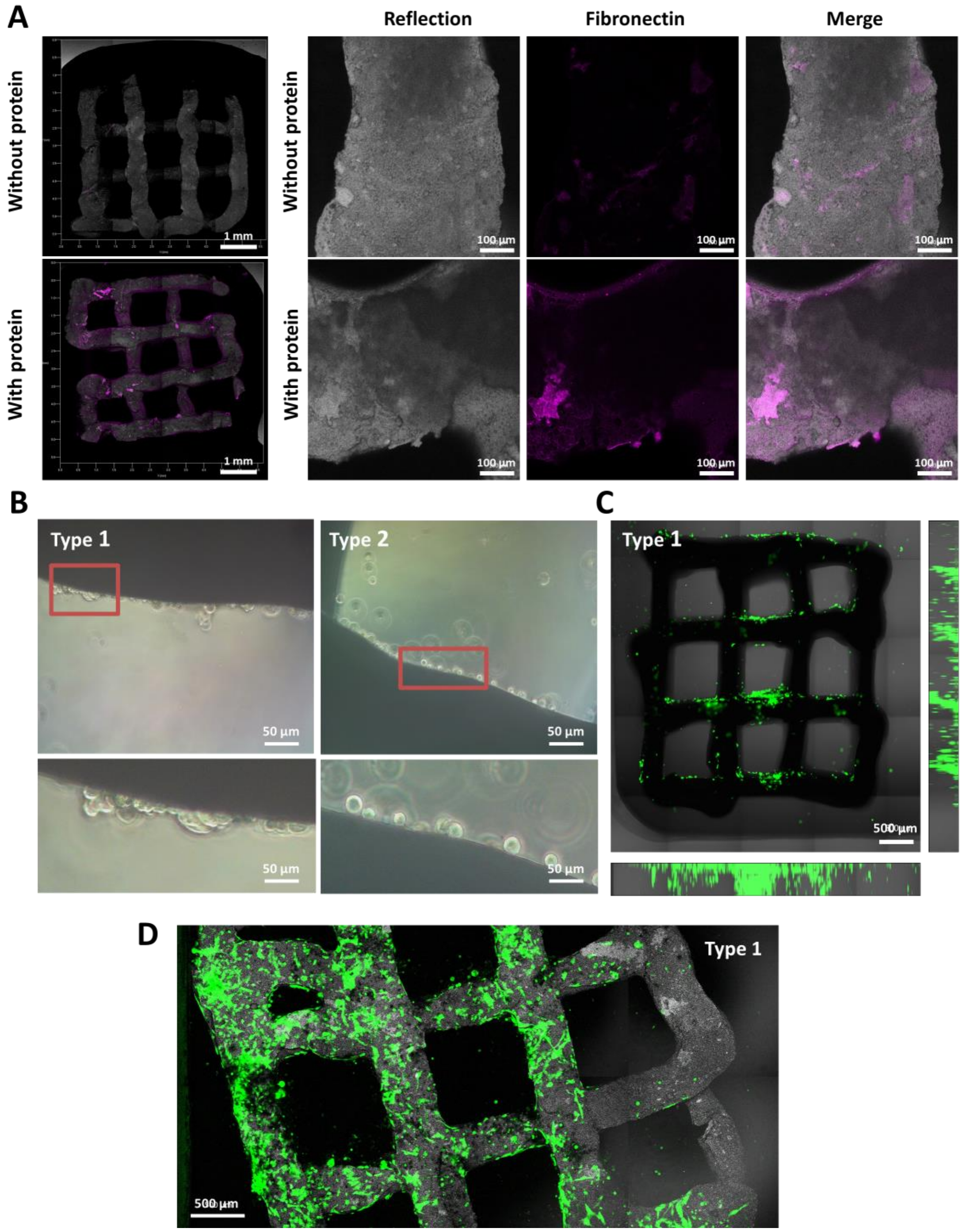

Figure 21. Fluorescence microscopy images of 3D-printed ceramic scaffolds coated with a fibronectin/collagen IV layer and cell studies with seeded osteoblasts. **A)** Comparison of ceramic supports with and without the protein layer (scaffold overview). **B)** Bright-field images of seeded osteoblasts (at different magnifications) into the composite scaffold using the protein coating. **C and D)** Fluorescence images of labelled osteoblasts onto the protein-coated 3D printed ceramic support. In these images osteoblast type 1 and 2 are hFOB and Mg63, respectively.

2.3 Conclusions

In this chapter, a porous composite scaffold was prepared to create a 3D cellular support with biosensing capabilities, to study bacterial infection *in situ*. The composite support was composed of a 3D-printed ceramic scaffold based on porous alumina inks obtained by the HIPE method and a polymeric matrix loaded with AuNRs as the SERS sensing support. Synthesis of the composite support for 3D cell culture proved to be challenging due to the complexity and the multiple characteristics required for recreating a biocompatible environment similar to the natural human tissue. The combination of a ceramic support with a polymer matrix was found to be a suitable initial approach towards the creation of unique scaffolds with specific properties for selected cellular scenarios.

Ceramic HIPE pastes could be readily tuned by varying both the particle surface modifier and the polymer (propionic acid and PVA, respectively). The addition of a high concentration of surface modifier increased the strength of the multi-droplet network, thus increasing its resistance to flow under shear conditions. However, the addition of a polymer component proved to be useful as a fluidizing agent, by partially occupying spaces in between the droplet membrane and reducing the overall strength of the internal phase. Such a variability represented an advantage to acquire specific inks for each printing system, opening the way to a wide range of different applications and particular scenarios. The main advantage of using a HIPE methodology for the synthesis of printable inks is the acquisition of a multi-channelled porosity inside the printed paste. The creation of a microstructure provided higher surface area for cells to interact and promote other cell behaviours such as cell adhesion, as well as diffusion of nutrients and other metabolites. Even though the ceramic inks were tuned for printing and to increase their active surface area, the inert chemical nature of alumina seemed to have a major relevance on the biocompatibility of the system.

The incorporation of a plasmonic composite hydrogel surrounding the 3D-printed ceramic scaffold provided biosensing properties to the material. SERS sensing of bacteria-secreted PCN was achieved using a GelMA matrix loaded with 1 mM of AuNR. Clear differences were observed when comparing the wild type with the mutant variant of *P. aeruginosa*, as only the characteristic SERS peaks of PCN could be identified in the WT sample. The scaffold also proved affinity towards the detection of the desired analyte, even in the presence of other cellular components in the media. However, high turbidity or complexity of the growth media composition would easily reduce the acquired SERS signal. The observed contrast in the acquired SERS maps originated from the difference in opacity and chemical composition of the ceramic support (higher refractive index) allowing control over local SERS imaging to study specific areas.

Therefore, the system demonstrated SERS biosensing capabilities to study the analyte of interest, with the possibility to focus on specific areas within the support.

Finally, biocompatibility assays demonstrated that neither the ceramic nor the polymeric matrix components were cytotoxic, but whilst osteoblasts were able to adhere and grow on ceramic scaffolds, they could not survive when coated with GelMA@AuNR. Due to time limitations, it was not possible to perform further assays combining the plasmonic polymeric gel with the protein-coated ceramic. In this regard, it would have been required to tune the hydrogel properties or change the building method to ensure cell survival and allow for subsequent differentiation into mature bone tissue. Another important limitation is the degradation of the polymer gel by bacteria after several days of incubation, as the long-term stability of the gel for biosensing should be ensured.

In summary, 3D-structured materials were fabricated as *in vitro* 3D models for the *in-situ* detection of biological phenomena such as bacterial bone infection. The system proved to be biocompatible and capable of acquiring SERS information of specific bacteria-secreted biomolecules. However, the incorporation of cells into such a complex system alongside remodelling of the matrix in the presence of bacteria, due to the secretion of proteases, are still challenges to be faced. In the future, sensing studies in the presence of bone-derived cells and infectious bacteria, recreating a more realistic *in vitro* bone-infection scenario, will be considered. Such a controlled environment could be used as a platform to study the evolution of biological phenomena, thereby providing further insight into the involved biomolecular components and stages of such complex processes.

2.4 Experimental section

Chemicals

For the synthesis of gold nanorods (AuNR), hydrogen tetrachloroaurate(III) trihydrate ($HAuCl_4 \cdot 3 H_2O$) was purchased from Alfa Aesar. Sodium chloride (NaCl) (99%), sodium borohydride ($NaBH_4$) (99%), silver nitrate ($AgNO_3$) and ascorbic acid (99%) were purchased from Aldrich. The surfactant used for the synthesis was hexadecyltrimethylammonium bromide (CTAB) 96% from Acros.

For the synthesis of ceramic pastes, aluminium oxide (Al_2O_3) (99.9%, metal basis) was purchased from Fisher and propionic acid, poly(vinyl alcohol) (PVA, 31-50 and 85-124 kDa) were purchased from Aldrich. 3D printing cartridges of 3 cc and 22G precision tips (0.4 mm inner diameter) were purchased from Nordson EFD. Coating of the ceramic supports was carried out using Geltrex and/or collagen IV, combined with fibronectin+AF633 (fluorophore), all from Corning. Polymer matrices were prepared using gelatin from porcine skin, N-isopropylacrylamide (97%) crosslinked with irgacure (2-hydroxy 4'(2 hydroxyethoxy) (98%), sodium alginate and calcium chloride, and chitosan (low molecular weight), all purchased from Aldrich. Control SERS assays were performed using methylene blue (for microscopy) and commercial pyocyanin (≥98% (HPLC)) purchased from Aldrich.

Studies of cell culture and bacterial infection were carried out using Mg63 and hFOB cells, kindly provided by Dr. Ander Abarrategi (CIC biomaGUNE), and *Pseudomonas Aureginosa* (both wild type and mutant) kindly provided by Dr. Gustavo Bodelón (University of Vigo). Fluorescence assays were performed using live/dead assays (propidium iodide (PI) and calcein) purchased from Invitrogen and cell trackers deep red and green 5-chloromethylfluorescein diacetate (CMDFA) from Thermo fisher. Cell media cDMEM, DMEM, DMEM:F12 and bacteria media Lysogenic Broth (LB) broth were purchased from Thermo Fisher. Cell viability tests MTT and LDH were purchased from Sigma and Thermo Fisher, respectively.

Instrumentation

Electron microscopy images were obtained with a transmission electron microscope (TEM) JEOL-JEM 1400 PLUS operating at 120 kV, equipped with a GATAN US1000 CCD camera. Microstructure of the scaffolds was analysed using a scanning electron microscope (SEM) JEOL JSM6490 operating at 10-15 keV. Optical images were obtained using a Leica microscope with a 10x objective. UV-vis-NIR spectra were acquired with an absorbance spectrophotometer Agilent 8453. Fluorescence assays for LDH and MTT studies were acquired using a microplate reader with 485 nm as the excitation wavelength and emission at 630 nm. Fluorescence imaging of the labelled cells and the scaffold was performed with a confocal fluorescence microscope Zeiss LSM 880, with an argon excitation laser at 488 nm and diode-pumped solid-state laser (DPSS) at 561 nm. SERS measurements were performed with a confocal Raman microscope Renishaw inVia Reflex using an excitation laser at 785 nm and equipped with an integrated Leica microscope with 10x and 40x objectives. Rheological measurements of the diverse ink formulations were conducted using a modular compact Anton Paar rheometer MCR 302 and a serrated plate with a diameter of 25 mm at a 1 mm gap. Amplitude sweeps were carried out at a constant frequency of 1Hz, with a gradual increase in strain from 0.01 to 150%. Frequency sweeps were performed within the viscoelastic range (1% amplitude), with a decreasing frequency from 100 to 0.1 rad/s. Flow curves were carried out within a range of applied shear stress from 1 to 2000 Pa.

Synthesis of gold nanorods

Synthesis of AuNR was performed as explained in previous works.[45,46] For the gold seeds, a solution of $HAuCl_4$ (50 μL, 25 mM) was added to 4.7 mL of CTAB (0.1 M) and kept in a warm bath at 27 °C to avoid crystallization of the surfactant. Under vigorous stirring, 300 μL of $NaBH_4$ were rapidly added to induce reduction from Au^{+3} to Au^0 (the colour changes from yellow to brown). Seeds were characterized by UV-vis spectroscopy, where no peak is expected due to the small particle size. For the subsequent growth into nanorods (10 mL batch), 10 mL of CTAB (0.1 M) were acidified with 190 μL of hydrochloric acid (HCl) 1M and mixed with 100 μL of $HAuCl_4$ solution (50 mM). Under strong stirring, $AgNO_3$ (120 μL, 10 mM), ascorbic acid (100 μL, 0.1 M), and 25 μL of the prepared seed solution were added. Stirring was kept for 5 more minutes before allowing the suspension to rest in a water bath for another 2 h to complete the reaction. The colour of the suspension changed from orange to transparent (after ascorbic acid addition) and then to red-brown as reaction time passed. The samples were finally washed by centrifugation at 6500 rpm for 20 minutes several times and the final suspension was kept in a 1 mM CTAB solution to avoid aggregation. The final AuNRs had dimensions of 78 ± 5 in length and 22 ± 1 in width.

Synthesis of 3D ceramic supports

Ink preparation: HIPE ceramic pastes were prepared following a published method.[21] In brief, ceramic inks were prepared by addition of Al_2O_3 powder into deionized water. The ratio was kept at a 50 wt% for all ink formulations. After complete wetting of the solid powder, the dense pastes were mixed with different ratios of the surface modifier propionic acid (0.04, 0.06 and 0.08

mmol/g with respect to alumina powder) and mixed thoroughly. The colloidal suspensions were then mixed with 200 µL of PVA (1 wt%) with 2 different molecular weights (either 31-50 or 85-124 kDa), previously heated to avoid addition of crystalline polymer. Addition of the oil phase was performed using *n*-octane, keeping the ratios of 30/70 of water/oil phases. Emulsification of the HIPE ceramic inks was achieved using an IKA ultraturrax disperser T25 digital with a dispersing element S25N-8G. Emulsification was performed for 3 minutes at 6600 rpm, solvent excess was later removed, the inks were stored in vials and stored for 3 days before printing.

3D printing of HIPE inks: 3D printing of the ceramic pastes was carried out using an extrusion-based printhead of a 3D Discovery RegenHU bioprinter. Cubic scaffolds (4.5 x 4.5 mm) were printed with a 3-layer zig-zag pattern of 1.2 mm in spacing and a total height of 1.2 mm. Printing was carried out at different pressures for each ink (0.10 (ink 1), 0.17 (ink 2), 0.2 (ink 3) and 0.5 (ink 4, 5 and 6) MPa using a printing speed of 20 mm/s and a needle with an inner diameter of 400 µm.

Sintering: Printed ceramic supports were submitted to a sintering process to remove any organic leftover and hard the scaffold. The process was carried out in an electrical furnace following a temperature ramp up to 1200 °C at 10 °C/min and then kept at that maximum temperature for 2 hours. Sintered scaffolds were retrieved and later washed with water/ethanol mixtures (1:0, 0.75:0.25, 0.5:0.5, 0.25:0.75, 0:1 and backwards) after cooling down overnight.

Polymer coating and characterization

Methacrylated gelatin (GelMA) synthesis: GelMA was synthesized as stated in previous work. [64] Briefly, 10 g of gelatin was dissolved in a PBS solution in a 200 mL beaker at high stirring rate at 60 °C. Subsequently, 0.8 mL methacrylic acid (MA) per gelatin gram was added and left under continuous stirring for several hours. After reaction completion, the suspension was dialyzed in 15 kDa dialysis bags against distilled water for 24 h at 40 °C. Water was replaced several times to avoid saturation and to promote the diffusion of un-reacted compounds. The cleaned suspension was finally lyophilized to acquire white foams and kept in closed vials to avoid external contamination.

Polymer loading with nanoparticles and embedding of ceramic support: polymers were loaded with a final concentration of 1 mM AuNRs by different approaches. GeLMA 7% was dissolved in a 10 mL vial in a water bath at 37 °C. Under mild stirring, a 100 µL of a 10 mM suspension of a cleaned AuNR was added dropwise into the polymer solution. Irgacure (1 wt%) was added to the mixture until fully dissolved. For scaffold preparation, 300 µL of the GelMA@AuNR solution was poured onto the ceramic support located inside a circular holder. The samples underwent crosslinking under UV light (365 nm) irradiation at 50 mW/s for 40 s. After preparation, the composite scaffolds were stored in closed vials and kept in a refrigerator at 4 °C to avoid drying and external contamination. Chitosan gels (from 1 to 10 wt%) were dissolved in MilliQ water (1 mL) before addition of AuNR (1 mM). Sodium alginate (5 and 10% wt) was dissolved in a small vial (10 mL) before mixing with AuNR to reach a final concentration of 1mM. For 1 mL of the nanoparticle-loaded polymer solution, 1mL of $CaCl_2$ (stock 80) was added for crosslinking.

Coating of the 3D ceramic with protein layer (collagen and fibronectin)

Sintered ceramic supports were coated with a protein layer to promote cell adhesion after cell seeding. The ceramic support was immersed in a PBS solution containing 30 µg of fibronectin and 12.5 µg of Collagen IV (final concentrations of 60 µg/mL and 25 µg/mL, respectively). The samples were rotated using a rotisseries rotor at 10 rpm for 3 h at room temperature. Samples were cleaned with fresh PBS after coating to remove non-associated proteins. Fluorescence imaging was performed after labelling with anti-fibronectin antibodies (F3648) (ratio 1/200 on rotation at room temperature). Samples were later washed and labelled with an antirabbit AF633 secondary antibody (1/500). Fluorescence images of the scaffold protein coating were acquired using a confocal microscope with a laser at 633 nm (fibronectin) and 405 with reflection.

Cell seeding and scaffold preparation

Seeding of either hFOB or MG63 cells was carried by addition of 500 µL containing $2 \cdot 10^5$ cells onto previously coated ceramic scaffolds. The cells were left on the roller for 30 minutes prior to transfer into an 8-well Ibidi microscope slide and filling them with cell media. Embedding of the seeded scaffolds with the AuNR-loaded polymer matrix was achieved by addition of 170 µL of GelMA@AuNR, previously dissolved in a water bath at physiological temperature (37 °C). Crosslinking of GelMA was acquired by UV light exposition for 40 seconds under a UV lamp as previously described. Seeded scaffolds were imaged at different times by transferring the scaffolds into new clean wells to remove non-attached-cells.

Cell survival/cytotoxicity studies and imaging

MTT test (cytotoxicity test): Cells were seeded at between $5 \cdot 10^3$-$2 \cdot 10^4$ cells/well (100 µL) in a 96-well plate and allowed to adhere. Cell media was replaced with test solutions (diluted drugs, media for biocompatibility tests, etc.) and stored for several time periods (each of 24 h). A working solution of MTT reagent (Lonza) was added (100 µL /well) and allowed to incubate at 37 °C for 1 h. DMSO (100 µL / well) was later added to solubilise the intracellular MTT reagent and promote its detection by absorbance at 550 nm in a plate reader. The shown results are expressed as a percentage of the average viable cells.

LDH test (cell survival test): 50 µL of cell supernatant was removed and mixed with 50 µL of LDH working reagent (Invitrogen) in a clean 96-well plate. The sample was left at room temperature and protected from light, for 30 min, followed by addition of 50 µL of STOP compound. The absorbance was read at 490 nm, with a reference background measurement at 630 nm. The results are expressed as a percentage of the positive dead cell control.

Labelling cells with trackers: Cells were fluorescently labelled with CellTracker (Invitrogen). To label the adhered cells, cell media was exchanged with a working solution of Celltracker diluted in FBS-free cell media. For suspension labelling, cells were trypsinized, counted, centrifuged, and then diluted in a working solution of Celltracker in FBS-free cell media. The concentration of CellTrackers was 10-25 µM (depending on the used fluorophore) for the CellTracker Green CMFDA or 10 µM for CellTracker Deep Red. Cells were left for 15-30 min at 37 °C, followed by washing to remove non-uptaken fluorophore.

Live/Dead labelling: Cells were labelled after several time periods to ensure cell adhesion to the coated ceramic scaffold. Cell media was replaced with a working solution of Live/Dead fluorophores (i.e. Calcein and PI, both from Invitrogen) at concentrations depending on the observed visibility. For all conditions, samples were incubated with the labels for 30 min at 37 °C.

Bacteria setup preparation with *Pseudomonas Aeruginosa*

Bacteria growth and material preparation: Lysogeny broth (LB) was dissolved in deionized water at a concentration of 15.5 g/L and autoclaved. Mixture of LB-agar was also prepared by mixing 25 g of LB and 15 g of Agar dissolved in 1 L milli-Q water and later autoclaved. Several Petri dishes were loaded with LB-agar inside an airflow biosafety cabinet and let cool down until the agar solidified. The plates were stored in a closed bag in a fridge at 4 °C until their use.

Bacteria growth: two different strains of *P. Aeruginosa* were used; wild type (PA14WT) and mutant (Δphz). Stock samples were scratched with a sterile stick and streaked onto the previously prepared LB-agar plates following a 3 zig-zag pattern. The cultured plates were placed upside-down in an incubator at 37 °C overnight. Single colonies should have been seen close to the end of the last streaked pattern. With the tip of a sterilized pipette tip, a single colony was scratched and deposited into a tube containing 10 mL of LB broth. A control sample was prepared in parallel to prove the lack of contamination from external bacteria. The loaded tubes were stored at 37 °C under shaking for 20 h. Changes in the turbidity proved the correct growth of Pseudomonas in the different tubes.

Bacteria incubation on composite scaffolds: 1 mL of each type of bacteria was loaded in small Eppendorf tube and washed by centrifugation at 7000 rpm for 3 minutes. This step was repeated 3 times to remove the PCN present in the media and acquire samples of pure bacteria. Concentrations of bacteria colonies (cfu/mL) were determined by recording their absorbance at 600 nm (OD_{600}) by UV-vis spectrometry ($OD_{600}=3 \Leftrightarrow 1 \cdot 10^9$ cfu/mL).

Antibiotic control assays: ciprofloxacin was dissolved into water/ethanol mixture 50% at a 10 mM concentration. Different concentrations of antibiotic (from 10 nM to 100 µL) were tested in suspension with *Pseudomonas (*$OD_{600}=0.85 \Leftrightarrow 2.83 \cdot 10^8$ cfu/mL). Samples were incubated for a couple of hours before checking the differences in bacteria population measuring their OD_{600} by UV-vis spectroscopy.

SERS measurements of bacteria-secreted PCN

Sample preparation: 3D-printed holders were prepared using an Ultimaker 3D printer to deposit the composite scaffolds inside located wells. Samples were deposited inside the well and covered with a cover slip to create a closed environment.

MB control assays: GelMA@AuNR and/or GelMA@AuNR-ceramic scaffold were incubated in 10 mL solutions at different concentrations of MB (from 10 nM to 1 mM) for 1 h. Gels were swiftly washed in fresh Milli-Q water for a couple of minutes to remove any excess of the analyte. Incubated scaffolds were measured using SERS. The corresponding SERS spectra and maps were obtained by scanning areas of 200x200 μm^2 and 1x1 mm^2 in area at different depth in Z-axis going from 100 µm to 1 mm.

PCN control assays: commercial PCN was dissolved in MilliQ water at different concentrations ranging from 10 nM to 1 mM. Scaffolds were incubated in the suspension for 2 h before swiftly washing in fresh MilliQ water. For bacteria-secreted PCN, the metabolite was removed from cultured bacteria by centrifugation at 7000 rpm for 3 minutes. The supernatant was removed and incubated with the scaffold for a couple of hours before measuring by SERS.

in situ SERS sensing of PCN secreted by Pseudomonas: The loaded wells of the printed holder were filled with 600 µL of LB broth prior to adding 10 µL of a bacteria solution with $OD_{600}=0.95$ (final concentration $3.33 \cdot 10^6$ cfu/mL). The loaded samples were stored at 37 °C for 18 h before sensing. The bacteria-incubated scaffolds were covered with a thin coverslip for biosafety measures.

SERS maps were obtained using the same parameters as in single point measurements and scanning areas of 1x1 and 2x1 mm^2 in xy and 300 µm in depth.

2.5 References

1. Guo, B., Lei, B., Li, P. & Ma, P. X. Functionalized scaffolds to enhance tissue regeneration. *Regenerative Biomater.* **2**, 47–57 (2015).
2. Ou, K.-L. & Hosseinkhani, H. Development of 3D in Vitro Technology for Medical Applications. *Int. J. Mol. Sci.* **15**, 17938–17962 (2014).
3. Nikolova, M. P. & Chavali, M. S. Recent advances in biomaterials for 3D scaffolds: A review. *Bioactive Mater.* **4**, 271–292 (2019).
4. Fontoura, J. C. *et al.* Comparison of 2D and 3D cell culture models for cell growth, gene expression and drug resistance. *Mater. Sci. Eng.: C* **107**, 110264 (2020).
5. Yuste, I., Luciano, F. C., González-Burgos, E., Lalatsa, A. & Serrano, D. R. Mimicking bone microenvironment: 2D and 3D in vitro models of human osteoblasts. *Pharmacol. Res.* **169**, 105626 (2021).
6. Kapałczyńska, M. *et al.* 2D and 3D cell cultures – a comparison of different types of cancer cell cultures. *Arch. Med. Sci.* **14**, 910-919 (2018).
7. Dutta, R. C. & Dutta, A. K. Cell-interactive 3D-scaffold; advances and applications. *Biotechnol. Advances* **27**, 334–339 (2009).
8. Williams, D. F. On the mechanisms of biocompatibility. *Biomaterials* **29**, 2941–2953 (2008).
9. Carletti, E., Motta, A. & Migliaresi, C. Scaffolds for Tissue Engineering and 3D Cell Culture. 3D Cell Culture. *Humana Press*. 17–39 (2011)
10. Kapałczyńska, M. *et al.* 2D and 3D cell cultures – a comparison of different types of cancer cell cultures. *Arch. Med. Sci.* **14**, 910-919 (2018).
11. Antoni, D., Burckel, H., Josset, E. & Noel, G. Three-Dimensional Cell Culture: A Breakthrough in Vivo. *Int. J. Mol. Sci.* **16**, 5517–5527 (2015).
12. Duoss, E. B., Twardowski, M. & Lewis, J. A. Sol-Gel Inks for Direct-Write Assembly of Functional Oxides. *Adv. Mater.* **19**, 3485–3489 (2007).
13. Lewis, J. A., Smay, J. E., Stuecker, J. & Cesarano, J. Direct Ink Writing of Three-Dimensional Ceramic Structures. *J. Am. Ceram. Soc.* **89**, 3599–3609 (2006).
14. Wang, X., Jiang, M., Zhou, Z., Gou, J. & Hui, D. 3D printing of polymer matrix composites: A review and prospective. *Compos. B. Eng.* **110**, 442–458 (2017).
15. Yan, Q. *et al.* A Review of 3D Printing Technology for Medical Applications. *Engineering* **4**, 729–742 (2018).
16. Lee, J. et al. A review on 3D printed smart devices for 4D printing. International Journal of Precision *Engineering and Manufacturing-Green Technology*. 4, 373-383 (2017)
17. Buj-Corral, I., Bagheri, A. & Petit-Rojo, O. 3D Printing of Porous Scaffolds with Controlled Porosity and Pore Size Values. *Materials* **11**, 1532 (2018).
18. Bokhari, M., Carnachan, R. J., Przyborski, S. A. & Cameron, N. R. Emulsion-templated porous polymers as scaffolds for three dimensional cell culture:

effect of synthesis parameters on scaffold formation and homogeneity. *J. Mater. Chem.* **17**, 4088 (2007).

19. Cameron, N. R. High internal phase emulsion templating as a route to well-defined porous polymers. *Polymer* **46**, 1439–1449 (2005).
20. Yang, T., Hu, Y., Wang, C. & Binks, B. P. Fabrication of Hierarchical Macroporous Biocompatible Scaffolds by Combining Pickering High Internal Phase Emulsion Templates with Three-Dimensional Printing. *ACS Appl. Mater. Interfaces* **9**, 22950–22958 (2017).
21. Alison, L. *et al.* 3D printing of sacrificial templates into hierarchical porous materials. *Sci. Rep.* **9**, 409 (2019).
22. Pulko, I. & Krajnc, P. High Internal Phase Emulsion Templating - A Path To Hierarchically Porous Functional Polymers. *Macromol. Rapid Commun.* **33**, 1731–1746 (2012).
23. Kantaros, A. & Piromalis, D. Fabricating Lattice Structures via 3D Printing: The Case of Porous Bio-Engineered Scaffolds. *Appl. Mechanics* **2**, 289–302 (2021).
24. Zhang, L., Yang, G., Johnson, B. N. & Jia, X. Three-dimensional (3D) printed scaffold and material selection for bone repair. *Acta Biomater.* **84**, 16–33 (2019).
25. Whitely, M. *et al.* Improved in situ seeding of 3D printed scaffolds using cell-releasing hydrogels. *Biomaterials* **185**, 194–204 (2018).
26. Wu, C. *et al.* Strong, elastic, and tough high internal phase emulsions stabilized solely by cod myofibers for multidisciplinary applications. *Chem. Eng. J.* **412**, 128724 (2021).
27. Cerioli, M. *et al.* Pseudomonas aeruginosa Implant-Associated Bone and Joint Infections: Experience in a Regional Reference Center in France. *Front. Med.* **7**, 513242 (2020).
28. Bodey, G. P., Bolivar, R., Fainstein, V. & Jadeja, L. Infections Caused by Pseudomonas aeruginosa. *Rev. Infect. Dis.* **5**, 279–313 (1983).
29. Poole, K. Pseudomonas Aeruginosa: Resistance to the Max. *Front. Microbiol.* **2**, (2011).
30. Kariminik, A., Baseri-Salehi, M. & Kheirkhah, B. Pseudomonas aeruginosa quorum sensing modulates immune responses: An updated review article. *Immunol. Lett.* **190**, 1–6 (2017).
31. Lau, G. W., Hassett, D. J., Ran, H. & Kong, F. The role of pyocyanin in Pseudomonas aeruginosa infection. *Trends Mol. Med.* **10**, 599–606 (2004).
32. Smith, R. P. aeruginosa quorum-sensing systems and virulence. *Curr. Op. Microbiol.* **6**, 56–60 (2003).
33. Price-Whelan, A., Dietrich, L. E. P. & Newman, D. K. Pyocyanin Alters Redox Homeostasis and Carbon Flux through Central Metabolic Pathways in *Pseudomonas aeruginosa* PA14. *J. Bacteriol.* **189**, 6372–6381 (2007).

34. Hill, E. H. & Liz-Marzán, L. M. Toward plasmonic monitoring of surface effects on bacterial quorum-sensing. *Curr. Op. Colloid Interface Sci.* **32**, 1–10 (2017).
35. Bodelón, G. *et al.* Detection and imaging of quorum sensing in Pseudomonas aeruginosa biofilm communities by surface-enhanced resonance Raman scattering. *Nat. Mater.* **15**, 1203–1211 (2016).
36. Tang, Y. *et al.* Detection methods for Pseudomonas aeruginosa: history and future perspective. *RSC Adv.* **7**, 51789–51800 (2017).
37. Sears, N. A., Dhavalikar, P. S. & Cosgriff-Hernandez, E. M. Emulsion Inks for 3D Printing of High Porosity Materials. *Macromol. Rapid Commun.* **37**, 1369–1374 (2016).
38. Minas, C., Carnelli, D., Tervoort, E. & Studart, A. R. 3D Printing of Emulsions and Foams into Hierarchical Porous Ceramics. *Adv. Mater.* **28**, 9993–9999 (2016).
39. Liu, Z., Zhang, M., Bhandari, B. & Wang, Y. 3D printing: Printing precision and application in food sector. *Trends Food Sci. Technol.* **69**, 83–94 (2017).
40. Wan, X., Luo, L., Liu, Y. & Leng, J. Direct Ink Writing Based 4D Printing of Materials and Their Applications. *Adv. Sci.* **7**, 2001000 (2020).
41. Barnes, H. A. A review of the rheology of filled viscoelastic systems. *Rheol. Rev.* 1–36 (2003).
42. Dobraszczyk, B. J. & Morgenstern, M. P. Rheology and the breadmaking process. *J. Cereal Sci.* **38**, 229–245 (2003).
43. Barnes, H. A. Rheology of emulsions: a review. *Colloids Surf. A: Physicochemical and Engineering Aspects* **91**, 89–95 (1994).
44. Janmey, P. A., Georges, P. C. & Hvidt, S. Basic Rheology for Biologists. Methods in Cell Biology. *Elsevier*. **83**, 1–27 (2007).
45. Scarabelli, L., Sánchez-Iglesias, A., Pérez-Juste, J. & Liz-Marzán, L. M. A “Tips and Tricks” Practical Guide to the Synthesis of Gold Nanorods. *J. Phys. Chem. Lett.* **6**, 4270–4279 (2015).
46. Pérez-Juste, J., Pastoriza-Santos, I., Liz-Marzán, L. M. & Mulvaney, Paul, P. Gold nanorods: Synthesis, characterization and applications. *Coord. Chem. Rev.* **249**, 1870–1901 (2005).
47. Langer, J. *et al.* Present and Future of Surface-Enhanced Raman Scattering. *ACS Nano* **14**, 28–117 (2020).
48. Alkilany, A. M. *et al.* Cellular Uptake and Cytotoxicity of Gold Nanorods: Molecular Origin of Cytotoxicity and Surface Effects. *Small* **5**, 701–708 (2009).
49. Jia, Y. P. *et al.* Effects of Cetyltrimethylammonium Bromide on the Toxicity of Gold Nanorods Both In Vitro and In Vivo: Molecular Origin of Cytotoxicity and Inflammation. *Small Methods* **4**, 1900799 (2020).

50. Rindzevicius, T., Alaverdyan, Y., Käll, M., Murray, W. A. & Barnes, W. L. Long-Range Refractive Index Sensing Using Plasmonic Nanostructures. *J. Phys. Chem. C* **111**, 11806–11810 (2007).
51. Echeverría, C. & Mijangos, C. A Way to Predict Gold Nanoparticles/Polymer Hybrid Microgel Agglomeration Based on Rheological Studies. *Nanomaterials* **9**, 1499 (2019).
52. Boularaoui, S. *et al.* Nanocomposite Conductive Bioinks Based on Low-Concentration GelMA and MXene Nanosheets/Gold Nanoparticles Providing Enhanced Printability of Functional Skeletal Muscle Tissues. *ACS Biomater. Sci. Eng.* **7**, 5810–5822 (2021).
53. Liu, Y., Alexandra Krez, & Emily M. Stein. Osteoporosis in organ transplant patients. *Academic Press* **2**, 1281–1307 (2020).
54. Merlen, A. *et al.* Surface enhanced Raman spectroscopy of organic molecules deposited on gold sputtered substrates. *Nanotechnology* **20**, 215705 (2009).
55. Li, P. Determination of nanomolar dissolved sulfides in water by coupling the classical methylene blue method with surface-enhanced Raman scattering detection. *Spectrochim Acta Part A: Mol. Biomol. Spectrosc.* **248**, 119162 (2021).
56. Dutta Roy, S., Ghosh, M. & Chowdhury, J. Adsorptive parameters and influence of hot geometries on the SER(R) S spectra of methylene blue molecules adsorbed on gold nanocolloidal particles: SER(R) S spectra of methylene blue molecules. *J. Raman Spectrosc.* **46**, 451–461 (2015).
57. Wu, X., Chen, J., Li, X., Zhao, Y. & Zughaier, S. M. Culture-free diagnostics of Pseudomonas aeruginosa infection by silver nanorod array based SERS from clinical sputum samples. *Nanomedicine* **10**, 1863–1870 (2014).
58. Ferrera, D. *et al.* Three-dimensional cultures of normal human osteoblasts: proliferation and differentiation potential in vitro and upon ectopic implantation in nude mice. *Bone* **30**, 718–725 (2002).
59. Sittichockechaiwut, A., Scutt, A. M., Ryan, A. J., Bonewald, L. F. & Reilly, G. C. Use of rapidly mineralising osteoblasts and short periods of mechanical loading to accelerate matrix maturation in 3D scaffolds. *Bone* **44**, 822–829 (2009).
60. Breen, E. C. *et al.* TGFβ alters growth and differentiation related gene expression in proliferating osteoblasts in vitro, preventing development of the mature bone phenotype. *J. Cell. Physiol.* **160**, 323–335 (1994).
61. Ong, J. *et al.* Functionalisation of a heat-derived and bio-inert albumin hydrogel with extracellular matrix by air plasma treatment. *Sci. Rep.* **10**, 12429 (2020).
62. Chim, S. M. *et al.* EGFL7 Is Expressed in Bone Microenvironment and Promotes Angiogenesis via ERK, STAT3, and Integrin Signaling Cascades: EGFL7 regulates endothelial cell activities. *J. Cell. Physiol.* **230**, 82–94 (2015).

63. Andrique, C. *et al.* Calpain-6 controls the fate of sarcoma stem cells by promoting autophagy and preventing senescence. *JCI Insight* **3**, e121225 (2018).
64. Yue, K. *et al.* Synthesis, properties, and biomedical applications of gelatin methacryloyl (GelMA) hydrogels. *Biomaterials* **73**, 254–271 (2015).

Chapter 3: Inverted Colloidal crystals as three-dimensional environments for cell culture and SERS biosensing

Abstract

Three-dimensional (3D) composite scaffolds have recently become a hot topic of interest for their application as *in vitro* supports for 3D cell culture. These systems do not just comprise a simple bulk matrix but also have to meet several criteria to support cell growth. The structure is expected to mimic the biochemical characteristics of natural tissue, to recreate an adequate microenvironment and promote cell diffusion and adhesion. Control over the internal structure and surface chemistry are therefore required to obtain 3D cellular supports with enhanced characteristics compared to conventional 2D cell cultures. In this regard, inverted colloidal crystals (ICC) have been used as porous supports for 3D cellular matrices due to the high control over their chemical composition, size, and organization of their multichannel porosity. This building strategy not only provides control over the structure of the final matrix but also allows the use of a wide range of building materials to provide further biomimicking characteristics that closely recreate the properties of the natural tissue. In this chapter, we describe the incorporation of plasmonic nanoparticles to ICC, to achieve a biocompatible cell support that can be used for surface-enhanced Raman scattering (SERS) sensing and imaging. These 3D-templated SERS-active scaffolds would give new insights into 3D cell growth, allowing for a deeper understanding on cellular interactions and the role of secreted biomolecules in specific cellular processes.

3.1 Introduction

In recent years, interest on the detection of cell-secreted biomarkers has increased, as a means to gain insights into the progression and early-stage detection of complex illnesses, such as cancer.[1,2] Biomarkers are specific cellular-secreted biomolecules that can be used to evaluate several aspects of the cell behaviour.[3,4] These aspects include the normal functionality of a biological process, the response to external additives such as pharmacological studies, or alterations in cell survival in the presence of infectious species.[5–7] The detection of such biochemicals would provide a better understating of the biological interactions and processes present in complex multicellular networks. In the case of cancer, tumour development requires of interactions with extracellular matrix (ECM) components to induce the attraction and recruitment of other cells of the affected organism, such as immune cells and fibroblasts.[8,9] Recruitment of the diverse cell population provides the tumour with the capacity to promote vascularization and attract blood vessel components to enhance the diffusion of nutrient and oxygen to the growing cellular complex. Due to the importance of cell-secreted biomolecules during cell communication, identification of key biomarkers would further unravel the cellular processes involved in such complex structures and therefore identify possible treatments against the evolution of the growing tumour.[10–12]

Study of such complex diseases *in vivo* remains a challenge due to the need of highly specialized equipment, in addition to the limitations of animal models. For this purpose, *in vitro* strategies have become an essential tool in current medicine as an alternative to the use of animal models. However, standard 2D approaches have been proven to fail in fully creating a suitable microenvironment due the simplicity of using flat surfaces, which fail to provide adequate stimuli to cells and limiting cell-cell interactions.[13] To overcome such a low reliability, recent research focuses on the use of novel scaffolds consisting of three-dimensional (3D) matrixes that support cell culture and help recreating a more realistic microenvironment for cells.[13–17] Moreover, the properties of the scaffold can be finely tuned to promote interactions with cells, favouring basic cellular mechanisms such as proliferation, cell division and adhesion.[18,19] Several strategies have been reported for the synthesis of 3D supports, such as biofabrication approaches or colloidal fabrication techniques.[20] This chapter will focus on the use of Inverted Colloidal Crystals (ICC) for the fabrication of 3D scaffolds to support cell growth.[21]

ICCs are porous structures obtained through the negative replica of an ordered assembly of colloidal particles, which are used as a sacrificial template. This methodology has been previously used for the synthesis of porous supports for 3D cell cultures, due to the high control over the size, order and chemical composition of their multichannel porosity.[22–24] In this regard, polymer-based ICCs result interesting for the fabrication of biocompatible supports due to their low cost and ease of manufacture. Control over the porosity influences cell interactions with the matrix and their behaviour in the presence of other cells or biochemical components.[17,25,26] An additional advantage of this strategy is the compatibility of the building process with a wide range of base building materials.[27] Most approaches for cell culture studies make use of hydrogels, due to their well-known biocompatibility for cell adhesion and survival.[23] Nonetheless, the capacity of creating a defined porosity using a predetermined template also opens the way to using other types of materials such as ceramics, metals and/or composite combinations.[28]

Despite the described advantageous characteristics of ICCs, some limitations in the acquisition of biological information in such complex structures still remain. The addition of a third dimension implies that cells are to be located inside a closed-packed environment, thereby limiting the access for imaging and biosensing techniques.[29] Common imaging strategies such as fluorescence confocal microscopy are limited within these structures due to the low penetration of light caused by the thickness and opacity of most supports.[29–31] The same principle is applied to biosensing approaches, because the detection of biomolecules depends on the diffusive properties of the support and the overall accessibility to the inner cavities. Moreover, the use of non-invasive methods is also desired to avoid damages to both the support and the cell culture.[32] Consequently, novel techniques are necessary to acquire significant biological information from complex 3D cell microenvironments. In this thesis, we propose the use of surface-enhanced Raman scattering (SERS) as a suitable approach for biosensing and imaging of 3D cell culture systems.[33,34] The principle of SERS resides in an enhancement of the vibrational signals of molecules located in close proximity to the surface of plasmonic nanoparticles (NPs).[34–36] The electromagnetic interaction of the metallic surface with an adequate incident laser is able to exponentially increase the commonly weak Raman signal of molecules, acquiring unique fingerprints indicative of the presence of a specific biomolecule in the cellular microenvironment.[37–39]

Therefore, the objective of this chapter is to design a biocompatible 3D porous support with intrinsic capabilities for SERS biosensing and bioimaging. The system consists of a composite structure composed of a hydrogel-based ICC, also known as inverse opal (IO), loaded with plasmonic nanoparticles. Considering the swelling characteristics of hydrogels, biomolecules present in the media would diffuse within the gel structure where the plasmonic particles would be located. This 3D material could then be applied for the identification of specific biomolecules in complex microenvironments, providing further information about their role in *in situ* biological phenomena. Moreover, the incorporated plasmonic nanoparticles can also be labelled with specific Raman reporters (molecules with high Raman cross-section) for imaging purposes and allow for the monitoring of cell behaviour within the 3D support.

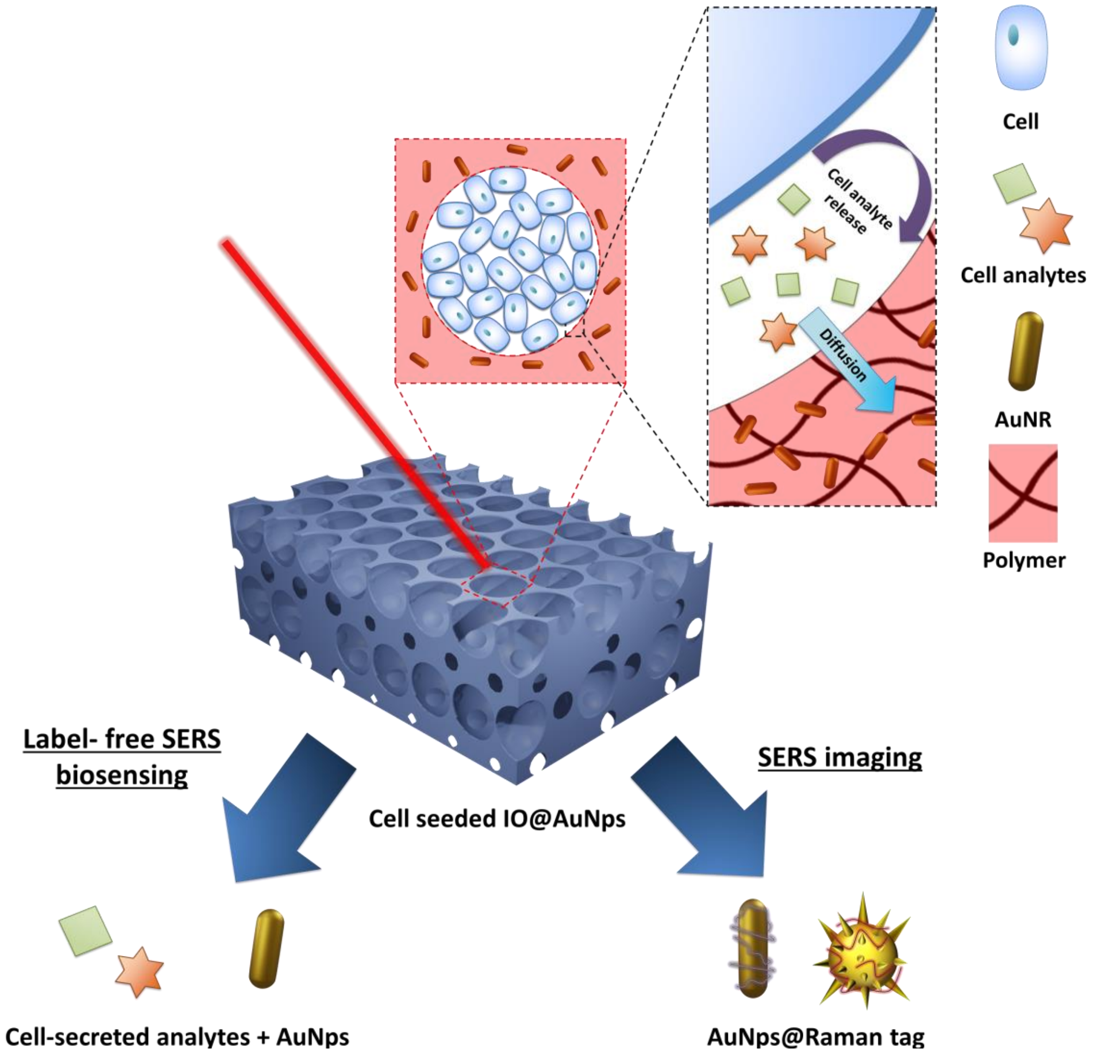

Figure 1. Schematic view of 3D SERS bioimaging and sensing within inverse opals, as cellular supports for *in vitro* studies. This system can be used following two approaches: label-free SERS sensing of cell-secreted analytes with bare AuNPs and/or combination of diverse types of Raman-reporter coated NPs for SERS imaging.

3.2 Results and discussion

Scaffolds were prepared by combining the building strategy of a negative replica from an ordered assembly of microparticles, with the loading of pre-made plasmonic particles. Due to the high biocompatibility of most hydrogels, the synthesis of the porous matrix was tested using different polymers to determine their suitability both for cell culture and SERS sensing.

3.2.1 Hydrogels loaded with gold nanoparticles

Synthesis of 3D supports with SERS sensing or imaging capacity required the combination of a building material with the appropriate plasmonic particles. The building material of choice for the synthesis of the 3D porous matrix should meet several criteria. First of all, the material should be fluid enough to diffuse within the assembled microparticle template and to allow their infiltration to later form the porous matrix. Moreover, after hardening/crosslinking of the polymer, the system had to show stability to avoid collapsing after removal of the solid template. Second, as the material will support a cell culture, the system must be biocompatible.[40] Finally, for SERS sensing and imaging, the systems should be as transparent as possible to reduce light scattering and ensure maximum light penetration depth into the matrix.[41]

Therefore, two different polymers were tested as the starting material for building the IO, methacrylated gelatin (GelMA) and Poly(N-isopropyl acrylamide) (PNIPAM) **(Figure 2**). As described in the previous chapter, gelatin proved to be an adequate candidate due to its biocompatibility and performance both as a cellular support and as a SERS biosensing platform. Cross-linking of GelMA discs was carried out by UV irradiation after adding the photo activator (2-hydroxy-4’-(2-hydroxyethoxy)-2-methylpropiophenone) into the mixture. After testing several irradiation times, short exposition times of 40 s with a constant light UV irradiation at 50 mW/cm^2 proved to be sufficient to crosslink the material.

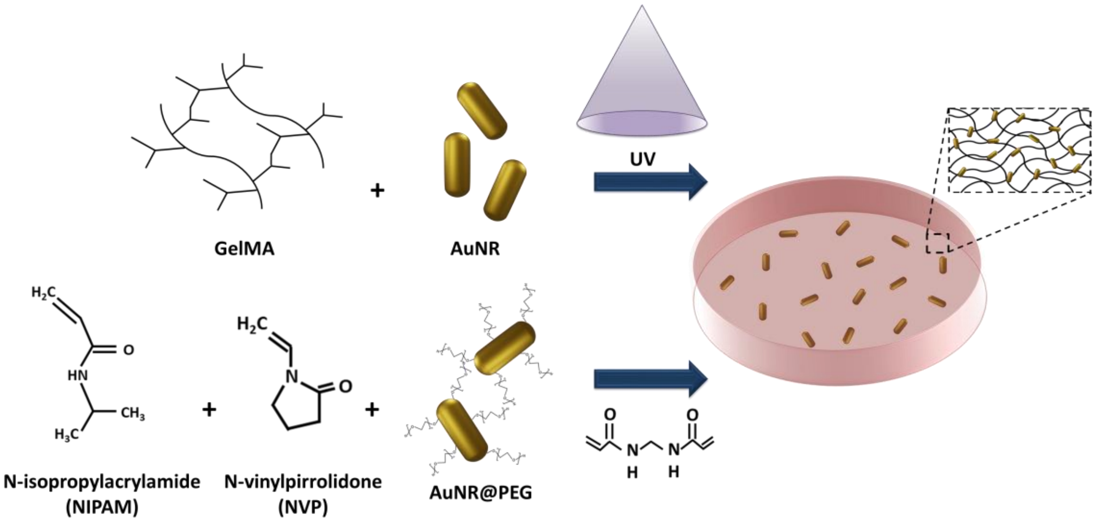

Figure 2. Summary of the synthesis of control gel discs with gold nanoparticles and different polymers. GelMA was UV crosslinked (50 mW/s for 40 s) and P(NIPAM-co-NVP) chemically cross-linked in the presence of bisacrylamide.

PNIPAM was also chosen as a candidate for hydrogel preparation due to its known hydrophilic nature and its swelling characteristics in aqueous media. Hydrogels were obtained by polymerization of NIPAM monomer in the presence of N,N'-methylenebis(acrylamide) (BIS) as a crosslinker and ammonium persulfate (APS) and N,N,N',N'-tetramethylethylenediamine (TEMED) as initiators. The resulting exothermic reaction formed a gel with a white tone. This phenomenon is explained by the lower critical solution temperature (LCST) of PNIPAM. LCST is defined as a critical temperature value in which higher applied temperature causes the components to become immiscible.[42] In the case of PNIPAM, the LCST temperature has been determined to be at 32 °C, below the required temperature for cellular studies (normally closer to physiological temperature at 37°C).[43] This change in the hydrophilicity of the system limited its applicability as building material to achieve transparent IO. To modify the LCST of the gel, a copolymer, in this case 1-vinyl-2-pyrrolidone (NVP), was added to the mixture (**Figure 3A**). Poly((N-isopropyl acrylamide-co-vinyl pyrrolidone (P(NIPAM-co-NVP)) polymer mixtures resulted in transparent hydrogels, even when heated at 37 °C.[44] **Figure 3B and C** show a clear difference in opacity when comparing both hydrogels soaked in a water bath at 38 °C. The polymer mixture was able to retain its transparency at physiological temperature.

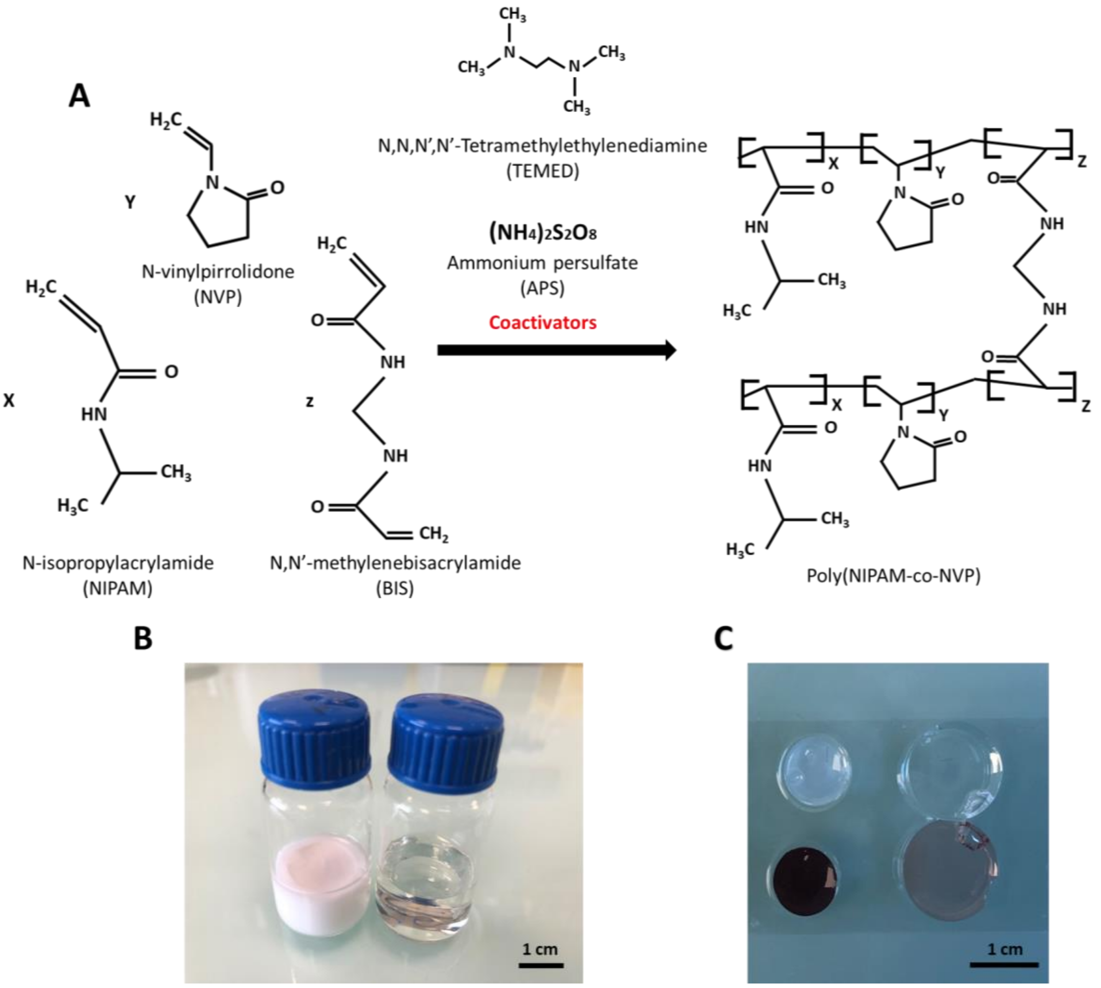

Figure 3. A) Scheme of the polymerization reaction of NIPAM with NVP. **B)** Comparison of gel transparency after incubation at physiological temperature of PNIPAM (left) and P(NIPAM-co-NVP) (right)). **C)** Image of different gels with (red) or without (colourless) gold nanorods. From left to right: GelMA and P(NIPAM-co-NVP)

To obtain hydrogels with SERS sensing ability, both polymers were loaded with gold nanorods (AuNR). Synthesis of AuNR was controlled to have their LSPR close to 785 nm, in resonance with the laser that will be used for the SERS studies. This wavelength has the added advantage of being located within the range of the so-called biological window (650 to 1350 nm), known to have a high penetration within living tissues while having minimal effect on cells. Loading of the gold nanoparticles within the gels was carried out by dropwise addition of AuNR aqueous dispersions under gentle stirring of the polymer solution to homogenise the nanoparticle dispersion before polymer cross-linking. Although AuNR remained dispersed in the presence of hexadecyltrimethylammonium bromide (CTAB), their incorporation into the polymer solution resulted in the formation of NP aggregates after a short time. Such a non-desired alteration in the particle stability needed to be controlled to retain the LSPR close to the initial value. Furthermore, CTAB removal prior to incorporation into the polymer solution was necessary because the presence of surfactant could be cytotoxic. Therefore, particles were to be washed until reaching a minimal concentration of surfactant to retain the dispersion of AuNRs until gelation. Colloidal stability was monitored by UV-vis spectroscopy at all steps, from the stock solution to the loading into the polymer matrix and gelling reaction.

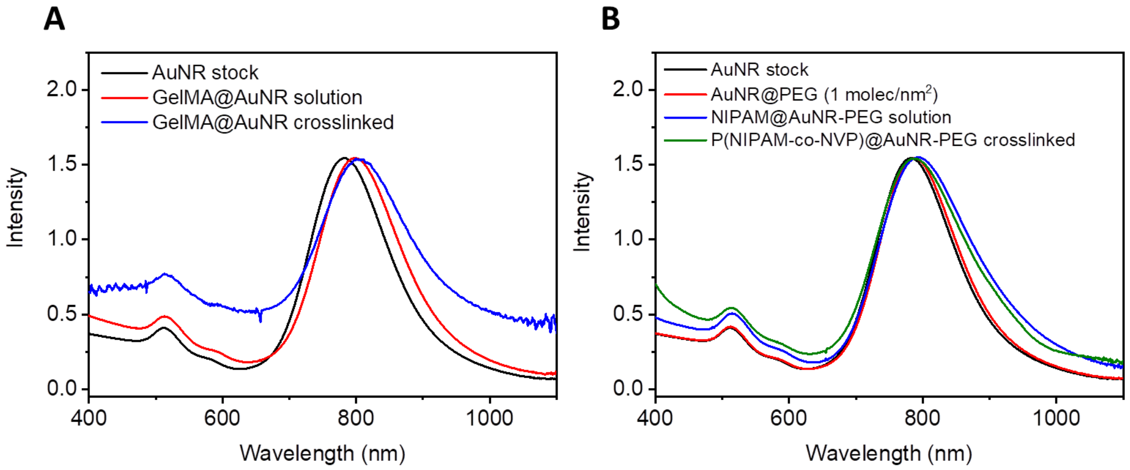

Figure 4. UV-Vis-NIR spectra of AuNRs during dispersion in polymer gels. **A)** GelMA, **B)** P(NIPAM-co-NVP).

UV-vis spectra demonstrated minimal differences in the maximum absorbance of the loaded particles when comparing between different polymer matrixes (**Figure 4**). In the initial studies using the NIPAM system, addition of the plasmonic particles to the polymer mixture induced fast aggregation that could be optically seen as a transition from a red solution to transparent with the presence of eye-visible particle clusters. Affinity between the gold surface and the aromatic moieties of some of the co-activators were likely able to induce interactions between nearby particles, promoting their aggregation.

For the purpose of the project, gold particles were required to have the maximum available free surface, so as to increase the chances of interacting with biomolecules present in the cell media. However, aggregation during gel preparation hindered the reproducibility of the system due to the lack of control over particle interaction and therefore the uncontrollable changes in the LSPR in each individual sample. Therefore, in the case of NIPAM-based hydrogels, the stability of the particles was improved by minimal functionalization with thiolated polyethylene glycol (PEG-SH). As thiolated groups have high binding affinity with gold, attachment onto the surface of the particles was ensured, even in presence of other affine moieties in the polymer solution. The addition of PEG groups on the surface of the newly coated particles was required to retain solubility in aqueous media, making use of its amphiphilic nature. Data shown in

Figure 4B demonstrates that functionalization of AuNR with PEG-SH (AuNR@PEG) could avoid particle aggregation, as the maximum in absorbance was minimally shifted when incorporated into the gels, therefore retaining its original LSPR as in the stock solution. Although the particles retained their LSPR after polymer crosslinking, it was important to consider that partial occupation of the particle surface with PEG-SH would limit the achievable SERS signal, diminishing the chances to interact with external biomolecules. This behaviour was not observed when using GelMA because AuNR were able to stay in dispersion with a low CTAB concentration.

3.2.2 Characterization of composite hydrogels: rheological and swelling studies

The stability of the different gels loaded with plasmonic nanoparticles was also studied. The material used for the subsequent synthesis of IO was required to retain its properties despite the addition of metal particles. To study the viscoelastic properties of the diverse gels, rheological assays were performed (**Figure 5**). Amplitude sweep assays were performed in each gel to study the linear viscoelastic region (LVE), where both the storage and loss modulus were found to be independent of the applied frequency. This region was maintained up to approximately 10% strain both for AuNR loaded gels and control gels without AuNR.

Regarding the frequency sweeps, gels were tested working under constant amplitude (within the LVE previously determined) and varying the angular frequencies to check the stability of the gel. Data shown in **Figure 5B** for P(NIPAM-co-NVP) show that the presence of AuNPs induced a higher degree of crosslinking of the matrix. This well-known reinforcement phenomena of polymer nanocomposites is likely due to electrostatic interactions of the nanoparticles with the polymer, as the modulus was higher after the incorporation of AuNR. On the other hand, as seen in **Figure 8** of the previous chapter for GelMA, the polymer gel without nanoparticles had slightly higher moduli (both G’ and G’’), indicating that the metal NPs disrupted its conformation, resulting in softer materials. Nonetheless, G’ was constant within the frequency range and parallel to G’’, indicating in all cases a typical hydrogel-like behaviour.

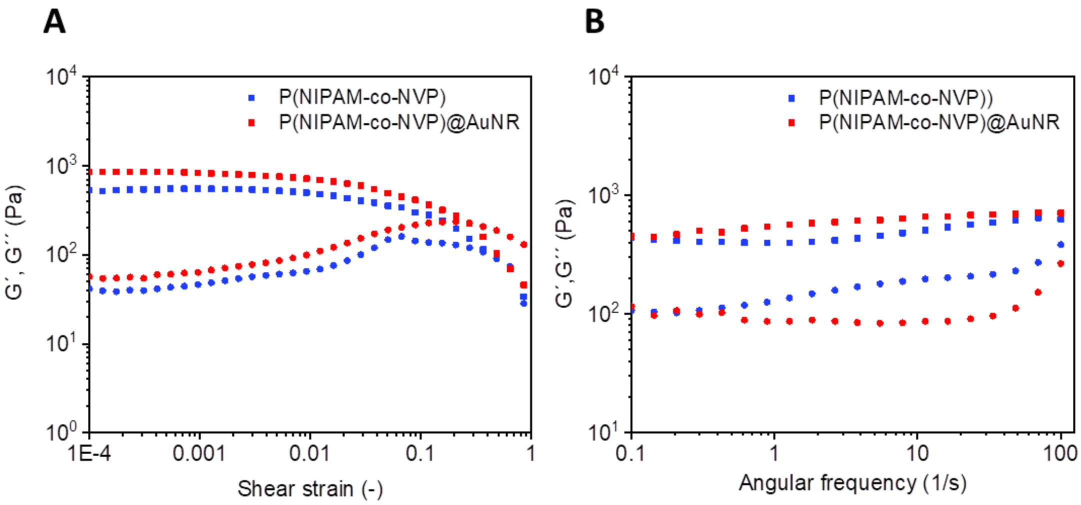

Figure 5. Rheological studies of P(NIPAM-co-NVP) gels with/without gold nanoparticles. **A)** amplitude sweep and **B)** frequency sweep. Moduli are represented as storage (G', ■) and loss (G'', ●) moduli, respectively.

The stability of the hydrogels was also tested in cell culture-like conditions, by incubating the materials in cellular media over a prolonged period of time. The study was aimed to check their capacity to retain transparency under physiological conditions, alongside their swelling capacity. Scaffolds for cell culture were expected to retain their shape while avoiding degradation, when immersed in the cellular aqueous solution.

Gels with or without AuNR were soaked in complete cell media (cDMEM) for a period of 20 days. During this time, swelling was also measured to ensure the capacity to absorb water and to retain their shape at several time points (1, 2, 4, 8, 18, 24 h, and 2, 4, 8, 14 and 21 days, see **Figure 6**). Swelling studies for both hydrogel systems showed that gels were capable of increasing their size to a complete swollen gel without significant observable damages on the gel integrity. P(NIPAM-co-NVP) gels reached their maximum swelling ratio within the firsts 2 h, increasing in weight up to 6 times the original value. Such a hydrated state was retained over the rest of the incubation time.

After the addition of AuNR, differences in the swelling behaviour could be appreciated. For P(NIPAM-co-NVP) hydrogels it was observed that the loading with gold nanoparticles limited the increase in weight only up to 4 times the original dry state (**Figure 6**). This difference with the control P(NIPAM-co-NVP) gel was maintained during the incubation period, showing no significant differences in gel swelling over time. This behaviour follows the previous explanation on the affinity of P(NIPAM-co-NVP) towards the metal particles, working as nucleation points and promoting close proximity between polymer chains in solution, thereby increasing the degree of crosslinking and, thus, reducing the swelling.[45] Regarding hydrogel transparency, P(NIPAM-co-NVP) proved to work as expected, with no change in the gel transparency appreciated at any given time. In the case of GelMA, no significant differences were observed in the swelling behaviour after the addition of AuNR.

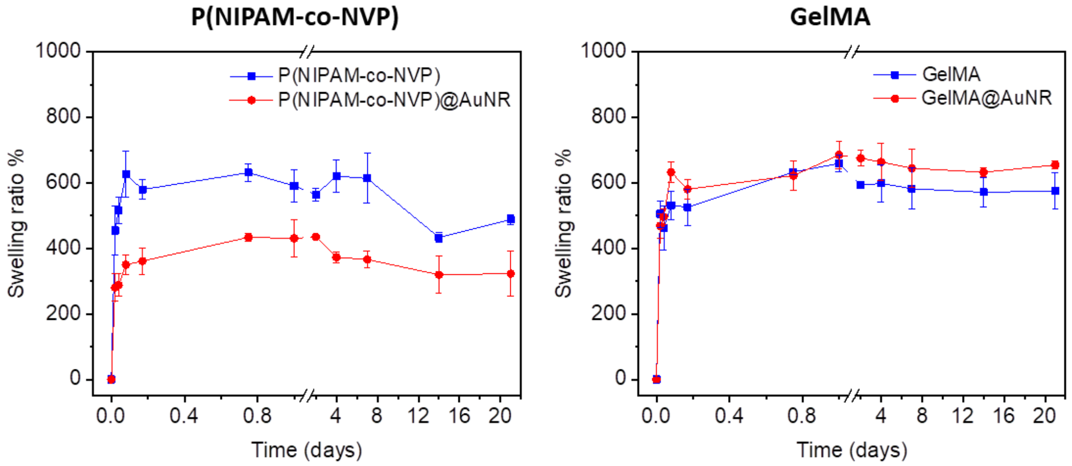

Figure 6. Swelling studies of polymer gels of P(NIPAM-co-NVP) and GelMA (with and without AuNR) in cell media.

3.2.3 Biocompatibility of AuNR-loaded hydrogels

Biocompatibility of the hydrogel composites was studied using MTT and LDH assays. **Figure 7** demonstrates that cell viability was achieved using both hydrogels. GelMA gels were slightly less biocompatible as compared with the P(NIPAM-co-NVP) system, as cell viability remained around 80% over three days, whereas for P(NIPAM-co-NVP) gels the value was closer to 100%. Regarding the cytotoxicity of both loaded hydrogels, no significant effect could be observed, both reaching 6% only. Therefore, both hydrogel systems proved to be biocompatible and could be used for the targeted application.

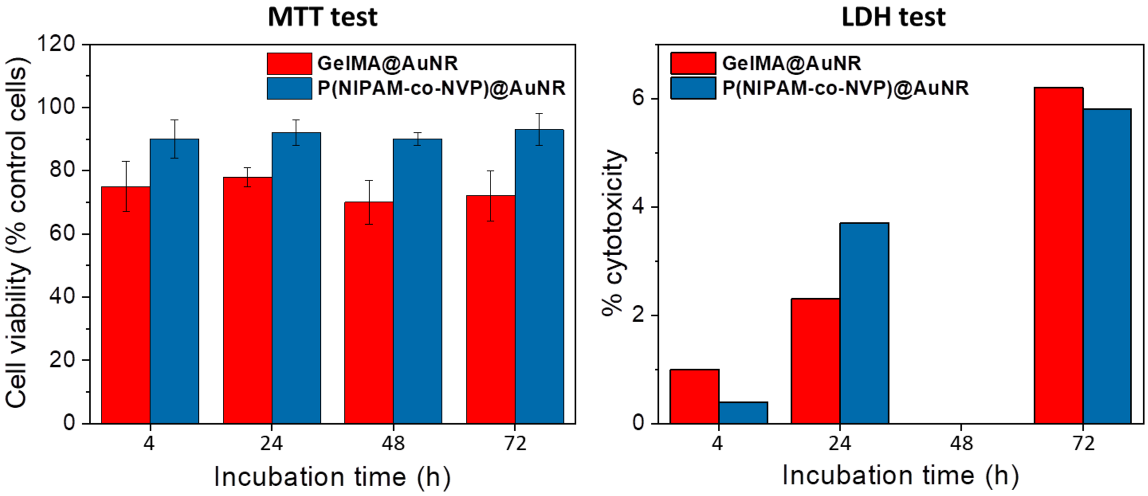

Figure 7. Biocompatibility assays of GelMA and P(NIPAM-co-NVP) hydrogels loaded with AuNR.

3.2.4 SERS sensing within AuNR-loaded polymer hydrogels

To determine which hydrogel system was suitable as a building material for the synthesis of the porous 3D supports, their SERS performance was studied. Methylene blue (MB) was chosen as a model Raman molecule. Sensing studies were performed in a series of solutions with decreasing concentration, from 50 µM to 5 µM, by soaking the hydrogel in the analyte solution for a couple of hours until attaining the equilibrium swelling according to swelling studies. **Figure 8A and B** show the acquired SERS signal in each system, indicating that it was possible detect the signal of MB in both composites down to a concentration of 1 µM, at which point neither GelMA nor P(NIPAM-co-NVP) nanoparticle-loaded gels could give a meaningful signal. Comparison of both hydrogels indicated that GelMA@AuNR showed higher intensities in most controls.

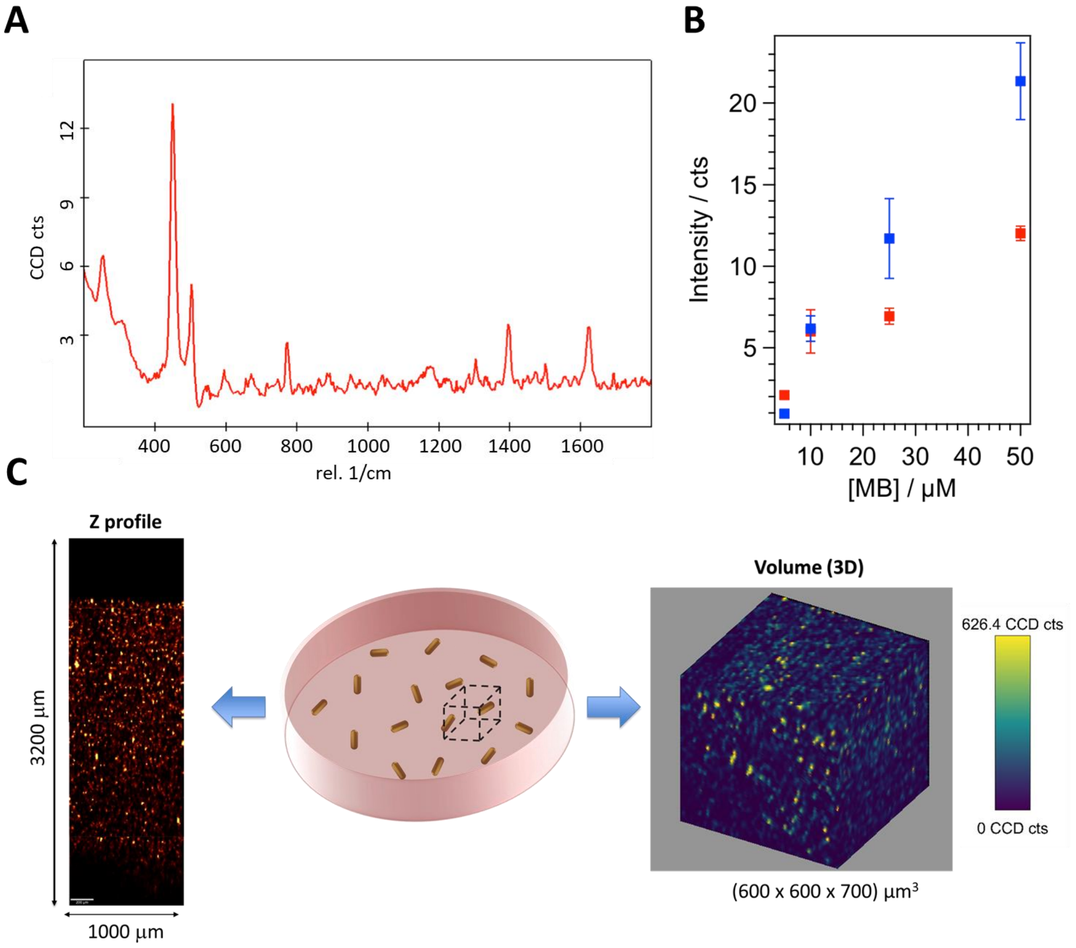

Figure 8. Control SERS performance of gels loaded with AuNR using MB. **A)** MB spectra acquired on the surface of P(NIPAM-co-NVP)@AuNR. **B)** Comparison of the SERS intensity for each gel system, at selected concentrations of analyte (from 50 down to 5 µM). **C)** SERS maps inside AuNR-loaded gels using MB (50 µM). The Z profile (1x3.2 mm) was acquired in GelMA@AuNR and the cube (600x600x720 µm^3) in P(NIPAM-co-NVP)@AuNR.

The maximum penetration depth of the sensing measurements was also investigated (**Figure 8C**). Using the MB control (50 µM), volumetric SERS maps showed the presence of meaningful MB signals at different depths, down to a limit of 700 µm (using the intensity of the peak at 475 cm^{-1}).

3.2.5 Synthesis of inverse opals

Inverse opals are porous structures characterized by having a controlled and highly ordered inner porosity. This type of porous matrix makes use of opal-like structures as a template to be replicated in a negative replica. Synthesis of these structures can be summarized in a 3-step process: i) building of a colloidal micro/nanoparticle assembly, ii) infiltration of the template with a suspension containing the building material, and iii) a final step consisting of hardening the infiltrated components alongside removal of the colloidal template (**Figure 9**).[24] The use of a particle template provides control over the pore dimensionality and the interconnectivity between the inner cavities.

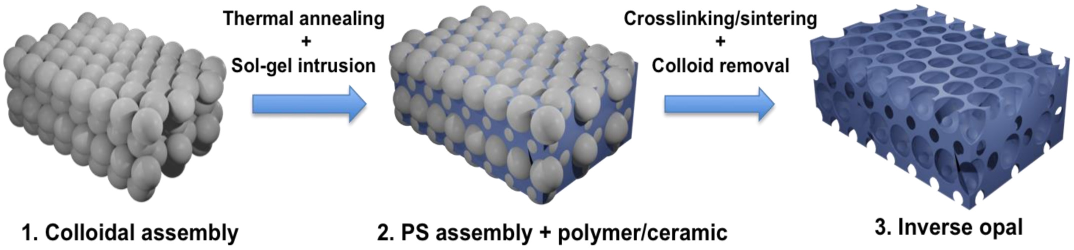

Figure 9. Summary of the strategy for the synthesis of inverse opals.

During the first step, spherical particles were assembled in a multi-layered template following a hexagonal close-packed (HCP) spatial arrangement. Synthesis of the ordered colloidal template was carried out using polystyrene beads (140 µm in diameter) by dropwise particle deposition into a purposely prepared holder, coupled with sonication in a water bath (**Figure 10, 1st stage**). The holder was prepared by gluing the base of a cut Eppendorf tube (200 µL) onto a glass slide and depositing it onto a petri dish working as a floating platform to be placed inside the water bath for sonication. Sonication was used to minimally shake the added microparticles into the template, thereby promoting the formation of ordered monolayers without empty spaces between close adjacent particles. Polymer particles were then added dropwise into the holder under constant sonication every 10 minutes, to allow time for the particles to organize under shaking in between additions. The particles were previously washed and later immersed in a solution of 2-propanol. The use of an alcohol solution instead of water allowed for the solvent to rapidly evaporate, therefore not filling the holder and leaving more space for the addition of subsequent droplets. During the assembly process, it was important to keep the bath at a temperature no higher than the evaporation temperature of 2-propanol, to avoid complete drying that would cause the sudden deposition of later droplets and damage the already formed assembly. Once the microparticle suspension was fully added, the loaded holder was dried in an oven at 37 °C overnight to remove the solvent leftovers. This step had to be carried out at a temperature lower than the melting temperature of polystyrene because a high temperature could induce uncontrolled damage on the bead morphology.

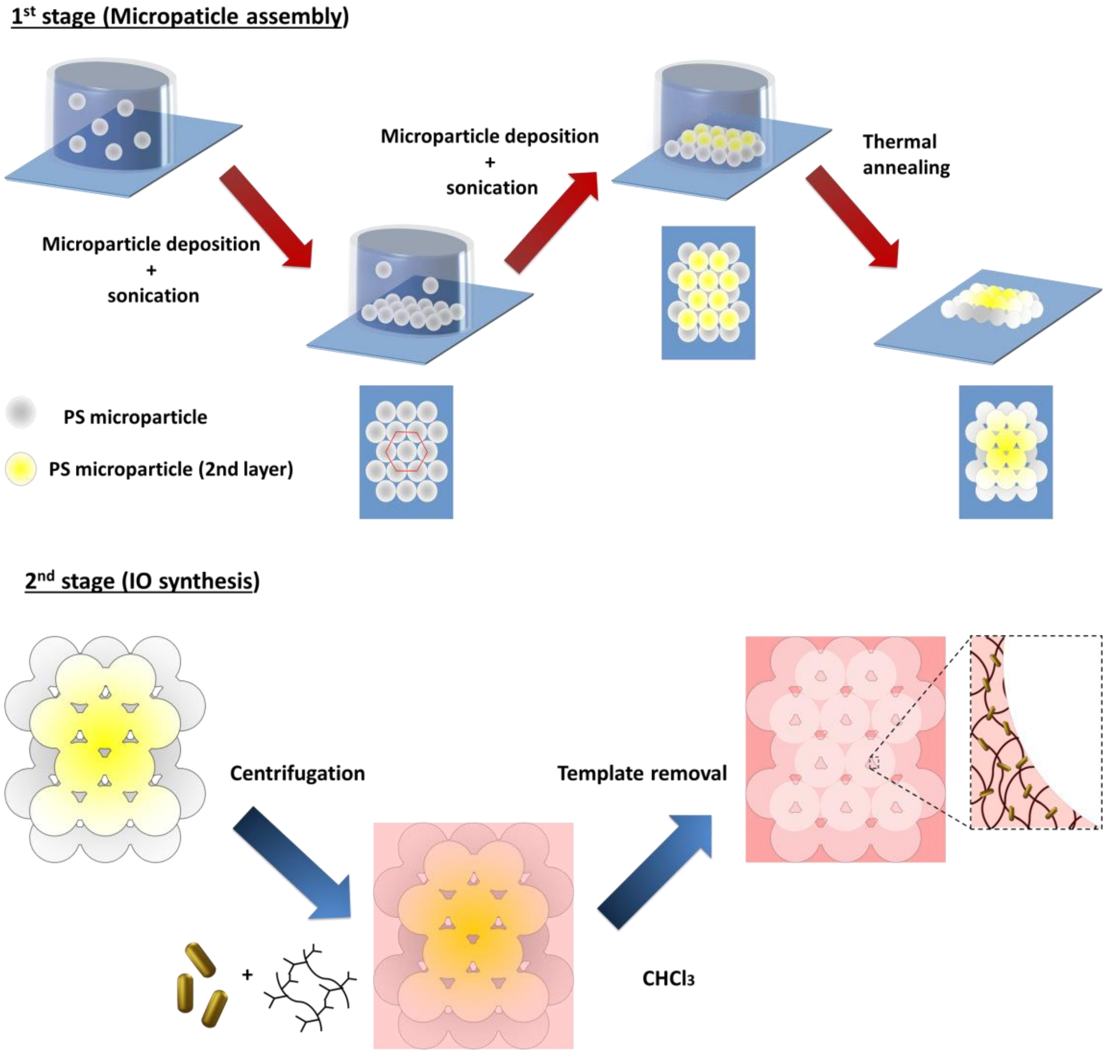

Figure 10. Summary of the synthesis process of a microparticle assembly, as a sacrificial template in IO synthesis. In the first stage, the microparticles are assembled by sedimentation coupled with sonication to ensure the correct organisation. The formed template is thermally annealed to bind adjacent spheres and consolidate the sacrificial template. In the second stage, the template is filled with the building material (polymer+AuNps) by centrifugation and subsequently crosslinked to form the IO. The template is finally removed to acquire the empty porous support.

Completion of the colloidal template was achieved by creating “necks” between adjacent particles by thermal annealing. By using temperatures close to the melting temperature of polystyrene, it was possible to partially melt the PS and create bridges between particles without compromising their spherical shape. These “necks” will create interconnections between adjacent cavities and be used as sacrificial templates in the final support. The inclusion of such interconnections would complete the formation of the final interconnected porosity. Moreover, the creation of the bridges enhances the mechanical strength of the microparticle template, facilitating its manipulation and avoiding disassembly (**Figure 11A**). Microparticle assemblies were maintained in an oven at 120 °C for 4 hours until the bridges were formed. SEM images in **Figure 11B, C and D** show how particles were able to retain their spherical morphology while small bridges of around 40 µm appeared to be interconnecting adjacent particles.

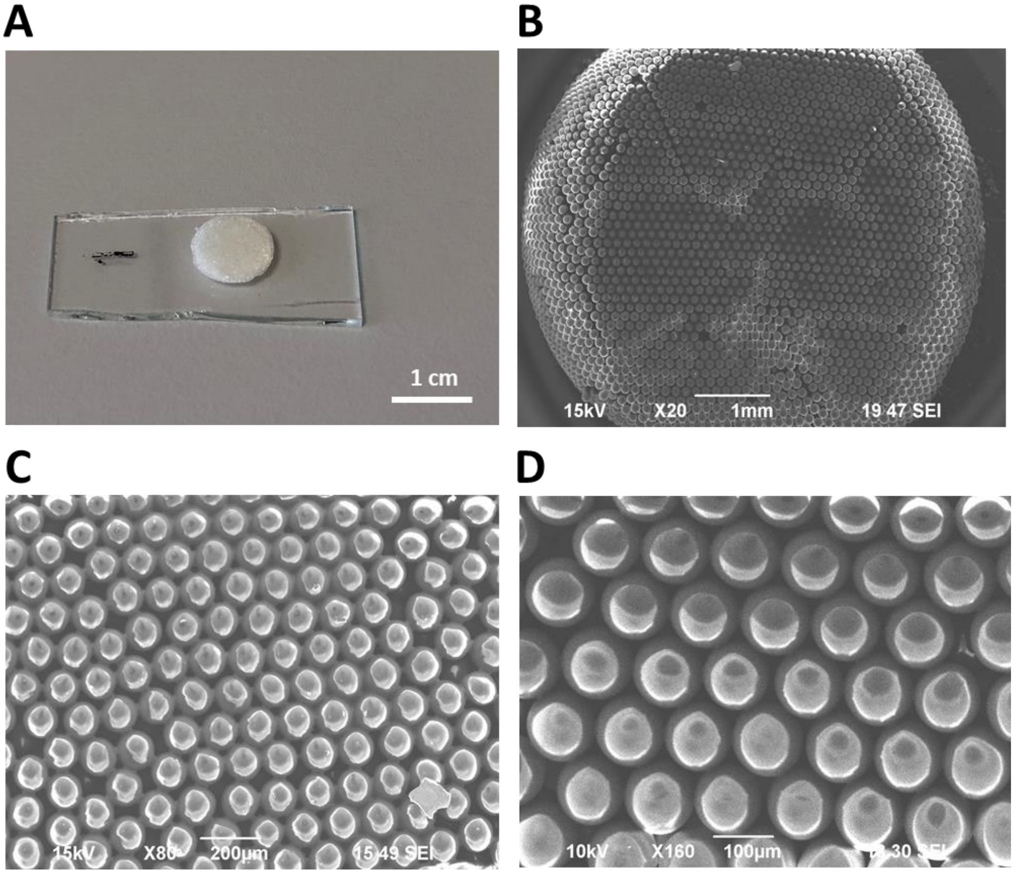

Figure 11. Imaging of PS assemblies (microparticle template). **A)** Photograph of the template. **B, C and D)** SEM images of the ordered microparticle assembly. The SEM image in D shows the necks interconnecting adjacent particles formed after thermal annealing.

The second main step on the synthesis of the IO consisted of the infiltration of the polymer/nanoparticle solution into the empty spaces between the microparticle templates by centrifugation (**Figure 10, 2nd stage).** For this step, a 3D printed holder was previously built to hold the templates in a flat surface, to avoid possible collision during centrifugation **(Figure 12B).** Polymer IOs made of either GelMA or P(NIPAM-co-NVP) were prepared by soaking the template in the polymer solution incorporating also AuNRs. Centrifugation in both systems was carried out at 3500 rpm to force infiltration of the composite mixture (gold particles and polymer) towards the polymeric template. To retain the stability of the polymer mixture during centrifugation, each process was performed at different conditions, depending on the chemical nature of the polymer. NIPAM with NVP solution was centrifuged keeping the temperature at 4 °C. whereas GelMA was required to be at a constant temperature of 38 °C. In this latter scenario, GelMA needed to be under constant heating because centrifugation at room temperature would lead to gelatin not being in the liquid state, thus hindering the infiltration into the template. On the other hand, higher temperatures were not desired because temperatures higher than 40 °C could induce reshaping of the gold particles, losing their controlled dimensionality and consequently their LSPR.

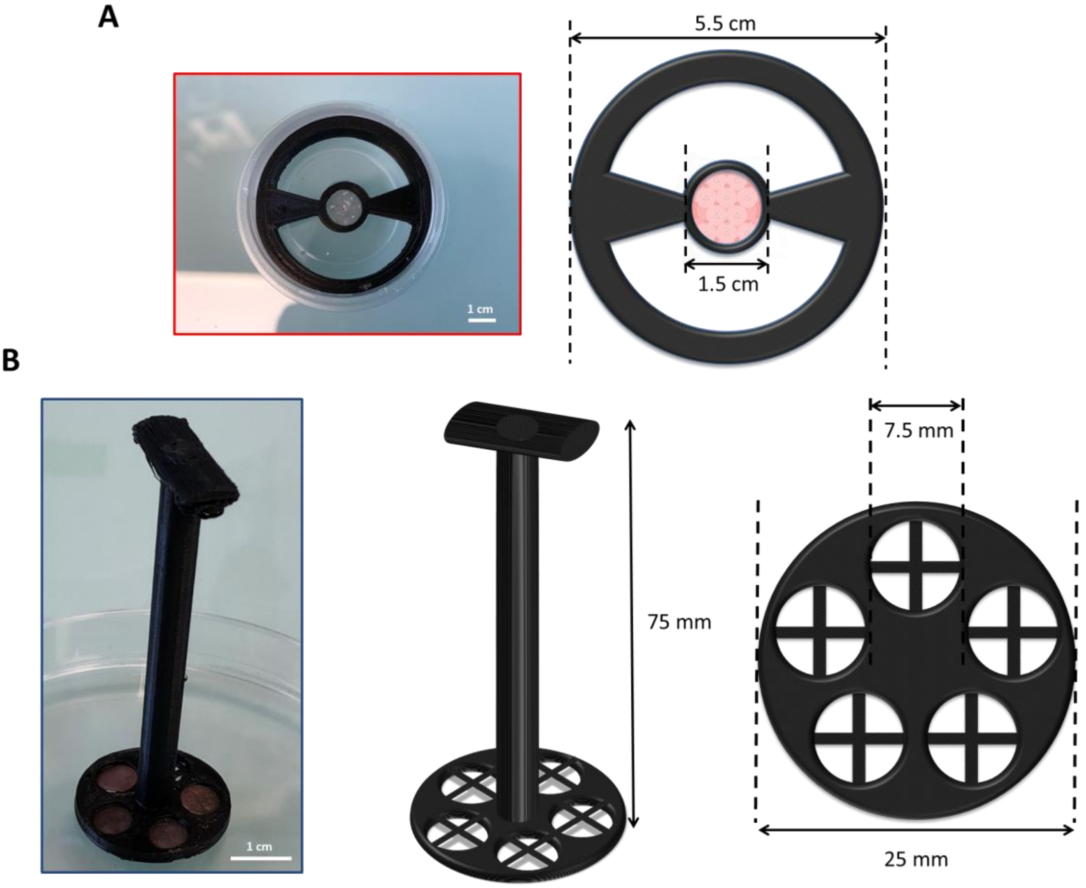

Figure 12. 3D printed holders for the synthesis and cell seeding of IO. **A)** Holder for cell seeding onto IO. **B)** Centrifuge support for IO preparation.

After each centrifugation step, sonication was applied to recover the excess of non-infiltrated nanoparticles and polymer solution. Centrifugation-sonication steps were repeated up to 4 times to ensure complete filling of the template before gelation. Inverse opals made of GelMA (GelMA IO) templates were removed from the holder and later cross-linked by UV irradiation for 1 minute. For the case of P(NIPAM-co-NVP), the final resuspended solution was mixed with APS, BIS and TEMED to activate the crosslinking reaction. Due to the short reaction time, samples had to undergo a final centrifugation step rapidly after addition of the initiator. For this last cycle, a slower centrifugation speed (1500 rpm) was used to avoid damage to the template after the gel is crosslinked. Once P(NIPAM-co-NVP) has been crosslinked, excess of the outer polymer gel was removed from the embedded microparticle templates by gently scratching with a blade. This last step was required prior to the removal of the sacrificial template to open the cavities of the support and avoid the formation of a closed box (**Figure 13A**). In contrast to this strategy, soaked templates with GelMA@AuNR could be removed from the excess of solution after infiltration, allowing for later UV crosslinking without the excess of polymer solution. Therefore, little scratching was required to only remove a thin polymer layer to open the internal cavities.

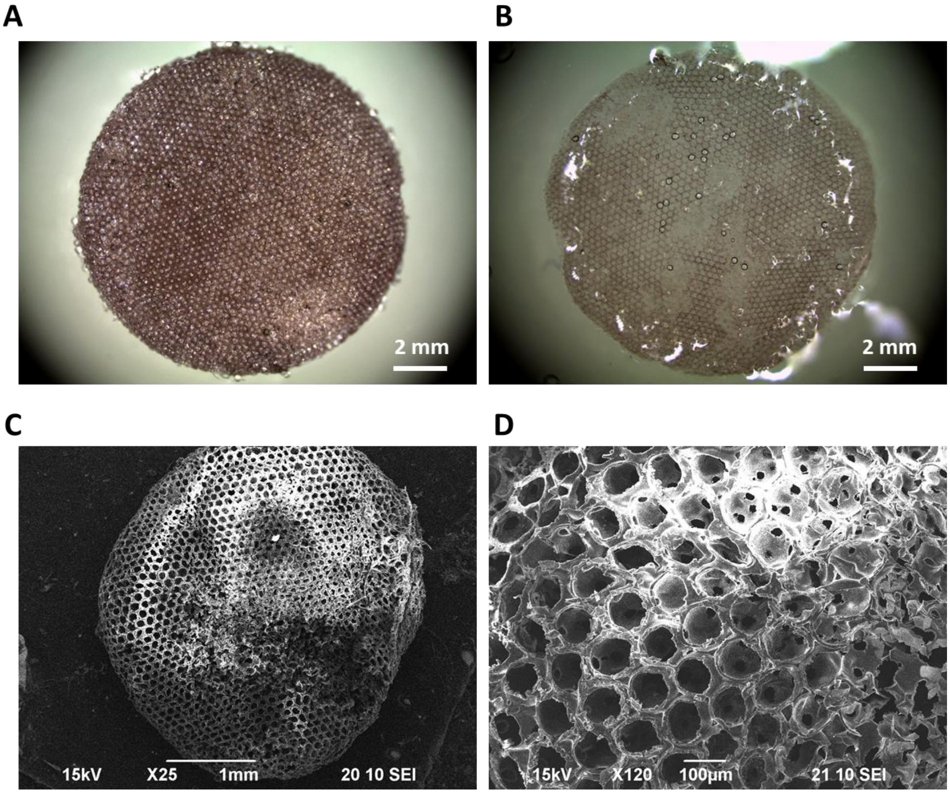

Figure 13. Imaging of the different steps during IO preparation (2nd stage). **A)** PS template soaked with P(NIPAM-co-NVP)@AuNR. **B)** P(NIPAM-co-NVP)@AuNR IO after removal of the sacrificial template. **C and D)** SEM images of the porous scaffold (GelMA@AuNR IO) at different magnifications. In the image, channels interconnecting adjacent pores can be appreciated.

The final step of the IO synthesis consisted of the removal of the sacrificial template to achieve the required multichannel porosity. Polystyrene was dissolved using chloroform by immersion overnight. This process was repeated on the following day in a second chloroform bath to ensure complete removal of remaining PS. Polymer scaffolds were finally soaked in a fresh milli-Q water bath to remove the absorbed chloroform and hydrate the polymer support. The final samples were easily deformable gels with a reddish colour indicative of the presence of AuNR inside the polymer matrix (**Figure 13B**). SEM images of the scaffolds (**Figure 13C and D**) also showed a homogeneous ordered open porosity where small channels could be differentiated in between pores.

3.2.6 Characterization of inverse opals

The use of a microparticle template demonstrated to be an optimal approach for the acquisition of supports with ordered porosity. Perfectly spherical cavities with a high degree of order were achieved in both polymer supports. The cavities seemed to be interconnected with adjacent pores through short bridges acquired during thermal annealing of the particle template. However, the dimensions of both final pores and channels differed from the original diameter of the microparticles. Confocal imaging of GelMA@AuNR IO showed that mean pore diameter was around 130.3±13.2 μm, being close to the original diameter of 140 μm. On the other system made of P(NIPAM-co-NVP)@AuNR IO, the final pore diameter increased up to 167.9±10.1 μm with interconnecting windows of around 40 μm (**Figure 14A**). The observed differences in size could be explained by the crosslinking and swelling capacities of each polymer. Swelling studies in cell media with GelMA showed no significant increase in size when compared with the original gel after UV crosslinking, retaining its shape as in the fully swollen state. On the other hand, P(NIPAM-co-NVP) gels were able to absorb additional water after crosslinking, increasing their volume when soaked in media. Although the final pore diameters differed from the ones of the original template, the acquired pores were still within the desirable range to promote interactions between cells with the overall porosity. Having channels of at least 20 μm would allow cells to diffuse between pores while working with pore diameters of around 150 μm would promote cell-cell interactions while avoiding far distancing as in 2D flat systems.

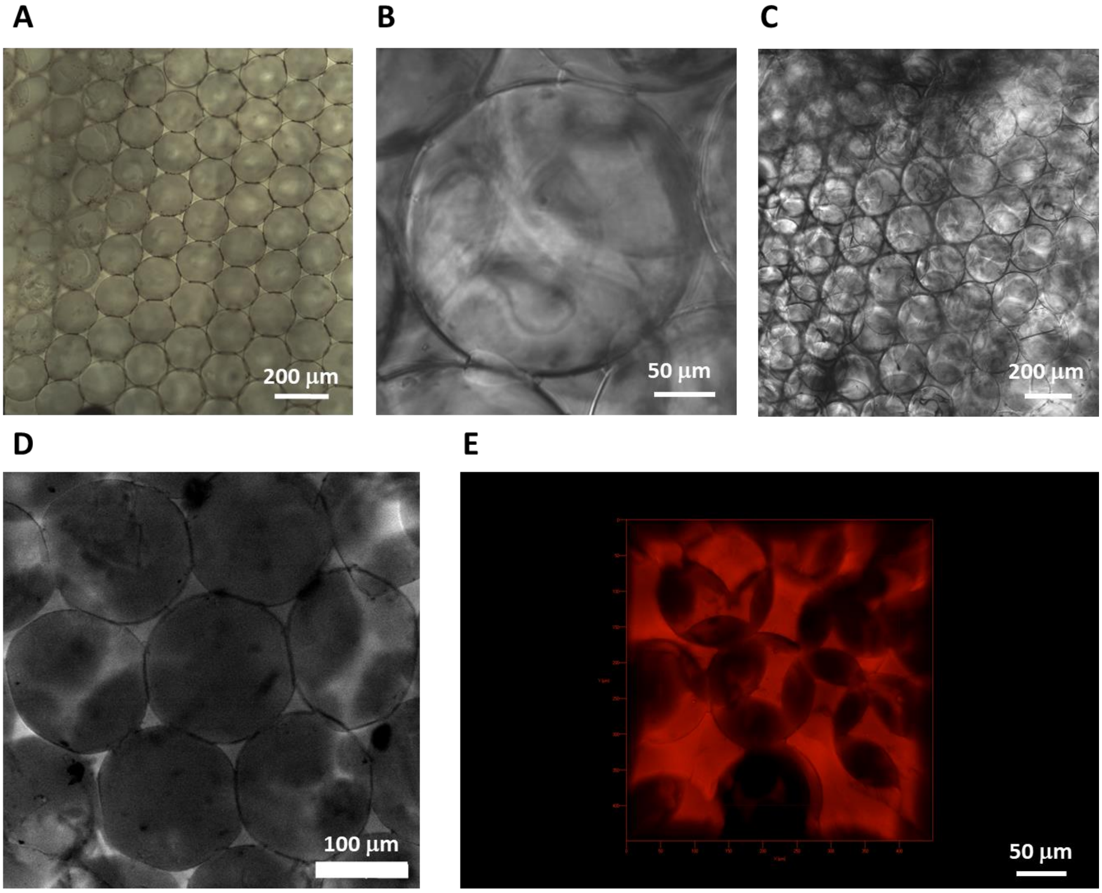

Figure 14. Confocal microscopy images of P(NIPAM-co-NVP)@AuNR IO. **A)** Optical image of an IO. **B and C)** Transmission images of a single cavity and of a monolayer, respectively. **D)** Fluorescence image of an IO using rhodamine 6G as a fluorescent dye. **E)** Upper view of a 3D stack of fluorescence images using rhodamine 6G.

Imaging of the inner multi-layered cavities was performed using light transmittance and fluorescence assays (**Figure 14**). Optical and transmission images (**Figure 14A to C**) clearly showed an ordered monolayer composed of perfectly interconnected spherical cavities. For fluorescence imaging, the polymer IOs were soaked in a rhodamine (10 µM) solution for an hour before observation in the microscope (**Figure 14D and E**). Fluorescence images demonstrated how the order of the pores was retained, even in layers located below, proving the correct ordering and interconnectivity of the synthesized IO. When comparing the light transmittance imaging in both polymer systems, it was found that it was harder to focus on the inner cavities in the GelMA system rather than with P(NIPAM-co-NVP). Although both systems proved to have a proper transparency suitable for SERS sensing, it was important to be able to differentiate the shape of the inner cavities where cells were expected to diffuse and interact forming the cellular clusters. Therefore, P(NIPAM-co-NVP) will be used as scaffolding material for the later cellular and SERS studies.

In addition to determining the final dimensionality of the porous support, it was still necessary to determine the distribution of the loaded gold nanoparticles within the system. P(NIPAM-co-NVP)@AuNR IO was embedded in a resin to harden the scaffold for subsequent slicing with a microtome (**Figure 15A**). Thin layers of 200 nm in thickness were cut and imaged by TEM and confocal microscopy (**Figure 15B and C**).

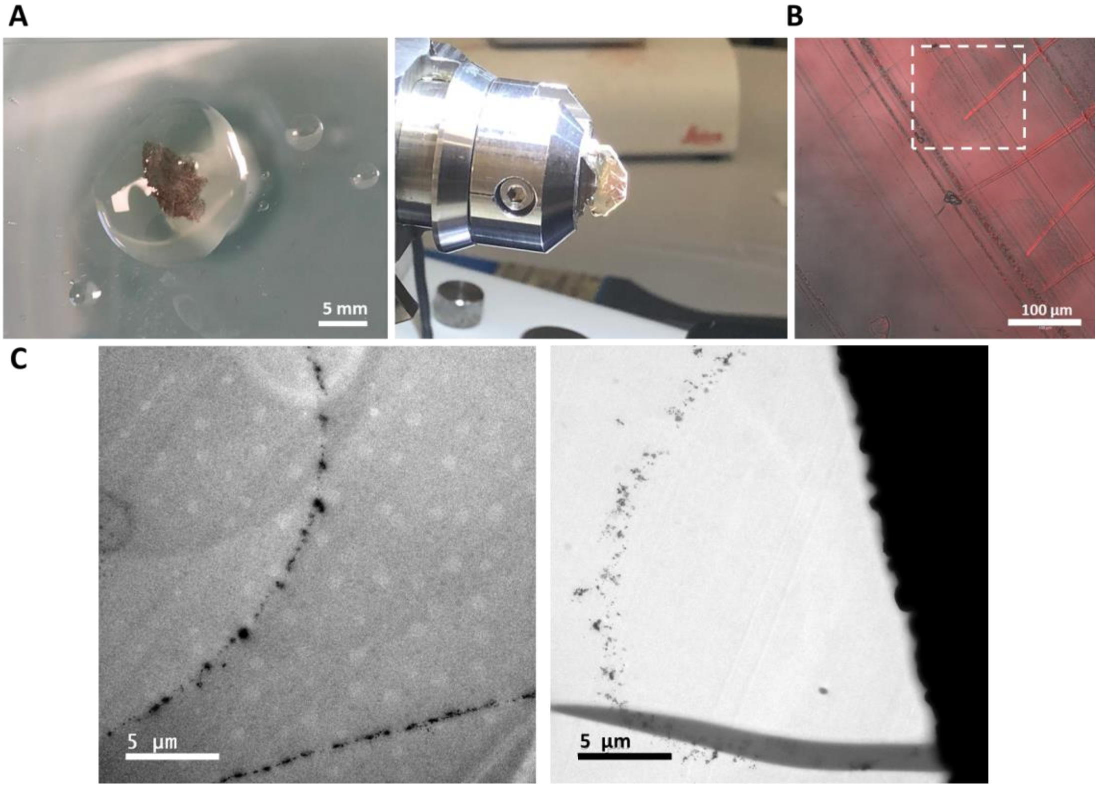

Figure 15. Microtome sample preparation and TEM images of IO loaded with gold nanoparticles. **A)** Photographs of the IO embedded in the resin and held for sample preparation. **B)** Optical images (transmission + fluorescence) of the thin layers of IO@AuNR to demonstrate the complete circular pattern of the spherical cavities. The squares in C show the presence of complete circles containing AuNR. **C)** TEM images of AuNR in a 200 nm thick cut-layer following the circular pattern of the spherical cavities from the IO structure.

Optical images of the cut IO showed the presence of circular shapes demonstrating the presence of a contrast material on the perimeter and the presence of spherical cavities (**Figure 15B**). TEM images demonstrated the presence of dispersed AuNR following a circular pattern (**Figure 15C**), proving that particles were distributed alongside the periphery of the spherical cavities. Therefore, as expected, by entrapping of the particles inside the material would leave them in proximity to the later seeded cells, while avoiding direct contact with the cellular objects.

3.2.7 3D cell culture of cancer cells using P(NIPAM-co-NVP)@AuNR IO as porous supports

The prepared IOs were fabricated to serve as support for cell culture, to create a niche capable of promoting cell diffusion and to allow cell-cell interactions. Considering the objectives of the project, cancer cells were used to create the 3D cell culture. For these assays, Green Fluorescent Protein (GFP)-expressing MCF7 cells were used and their evolution inside the 3D scaffold was monitored, replacing the need of external fluorescence labelling. MCF7-GFP were seeded onto P(NIPAM-co-NVP)@AuNR IO in cDMEM and examined after different incubation times to study the cell evolution by fluorescence confocal microscopy.

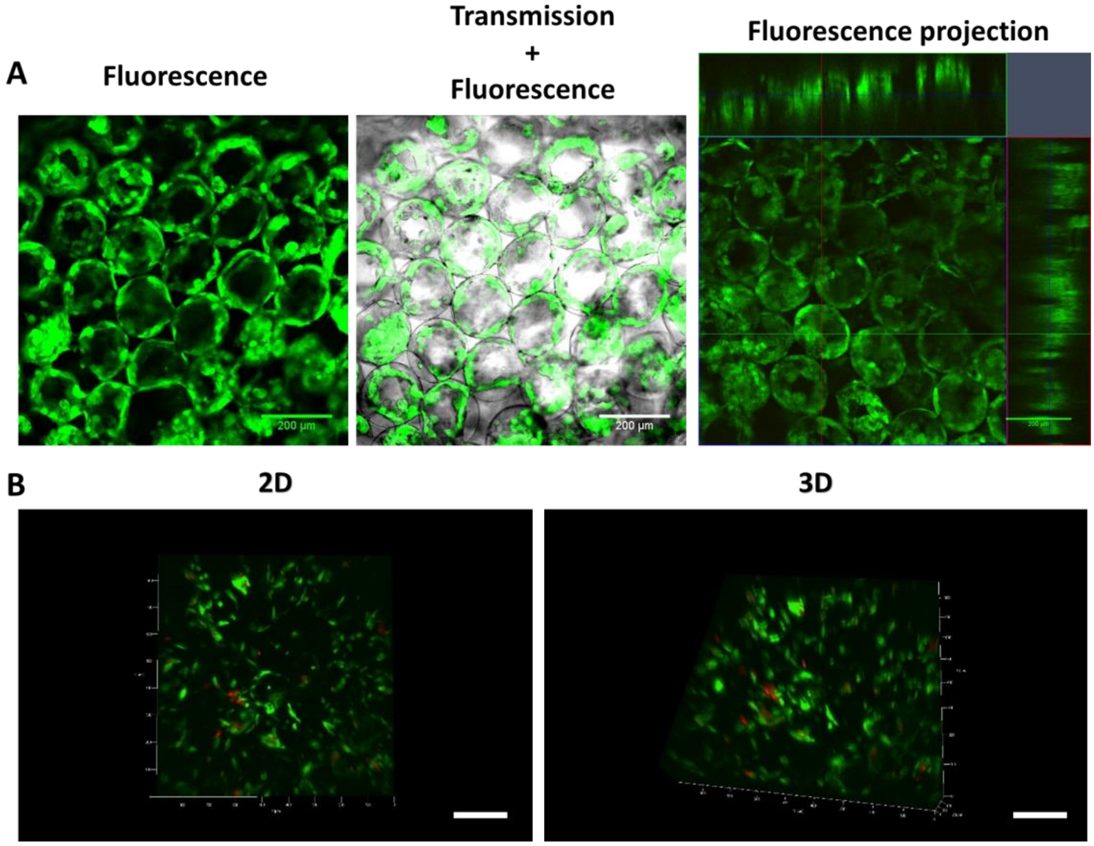

Figure 16. Cell culture of MCF7 cells in P(NIPAM-co-NVP)@AuNR IO support after 24h of incubation. **A)** Confocal fluorescence images of cells inside the porous support. **B)** Z-stack of 200 µm seeded scaffold. Top view (left, 2D) and side view (right, 3D). All scale bars represent 200 µm,

Confocal images acquired few hours after cell seeding showed no sign of cell death (**Figure 16A**). Cells could be seen forming circular patterns following the shape of the porous cavities. Observations at different depths inside the support discovered the presence of cells located in inner layers within the IO. The presence of cells al lower layers would be indicative that cells were able to diffuse through the pores, using the interconnecting windowing channels. The capacity of cells to diffuse within the matrix and their long-time (21 days) survival proved that the matrix support works as a biocompatible support for cell studies. Z stacks showed that cells were starting to agglomerate over time, up to the point of completely filling some of the pores (**Figure 16B**). The newly formed "spheroids" had dimensions similar to the total diameter of the cavity, with diameters ranging 150-160 µm. The capacity of cells to form spherical cellular aggregates both on the outer layer and inside the matrix proved the dimension of the pore to provide a closed niche able to promote interactions between adjacent cells. However, although the transparency provided by the hydrogel allowed the visualization into the porous matrix, it was only possible to focus on few of the most external layers. It could be possible that more cells had been capable of diffusing into deeper layers but due to limitations on light penetration and sample thickness, such cellular complexes could not be identified.

Overall, the system proved to be highly biocompatible as cells were mostly alive over prolonged periods (over 7 days) of time, with no appreciable increase in cell death. Interactions of MCF7 cells with the matrix allowed diffusion within the interconnected porosity up to the point of promoting close interactions between cells and creating dense cell aggregates.

3.2.8 SERS sensing of P(NIPAM-co-NVP)@AuNR IO

Once the capabilities of the polymer matrix as a support for 3D cell culture studies were demonstrated, the last approach consisted of determining its SERS sensing capacity. The 3D matrix loaded with the plasmonic nanoparticles was expected to detect cell-secreted biomolecules present in cellular media by combining the swelling properties of the polymer material and the loaded sensing particles.

SERS assays were performed using methylene blue (MB) and 4-aminothiophenol (4-ATP) as model Raman-active molecules, to test the SERS sensing capacity in the system due to their high affinity towards the gold particle surface.[46,47] Sample preparation was carried out by immersing the polymer scaffolds P(NIPAM-co-NVP)@AuNR IO into 50 µM solution of each molecule for 2 h to allow the analyte to diffuse inside the gel matrix. During SERS assays, it was observed that the polymer scaffold suffered from continuous shrinking or degradation that caused trouble with maintaining the focus during the measurements. To avoid these problems, the system was immersed in liquid media to retain its hydrated shape and a lower power laser was used. SERS studies were thus achieved under liquid immersion with an incident a laser (785 nm) at minimal power (5 mW/s).

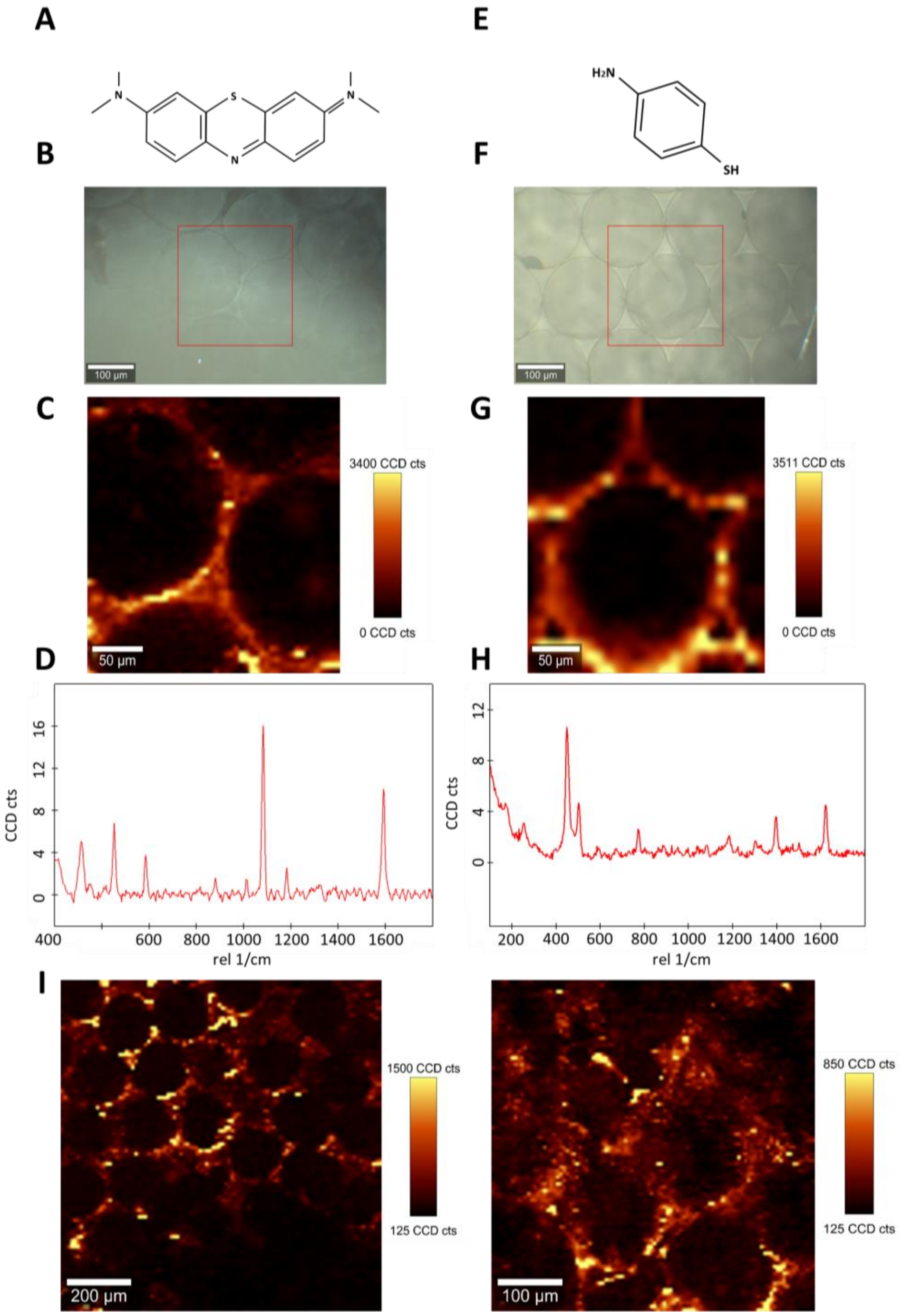

Figure 17. SERS sensing in P(NIPAM-co-NVP)@AuNR IO supports using MB and 4-ATP as analytes. **A)** MB structure. **B)** Optical image of the IO layer after incubation with MB. **C)** SERS map of the scanned area (red square in B, intensity at 475 cm^{-1}). **D)** SERS spectrum of MB within the IO. **E)** 4-ATP structure. **F)** Optical image of the IO after immersion in 4-ATP. **G)** SERS map of the scanned area (red square in F, intensity from the most intense peak in the spectrum). **H)** SERS spectrum of 4-ATP within the IO. **I)** SERS maps of a wider area using MB (same condition as in C).

SERS spectra shown in **Figure 17** demonstrated the detection of the characteristic Raman spectra of both analytes within the sample. 2D SERS maps were obtained by representing the spatial localization of the identified Raman signals. As expected, the recreated images clearly illustrate the morphology of the circular pore in contrast with the empty interior. This type of signalling could be explained by the location of the AuNRs on the perimeter of the pores, as observed in the TEM microtome images. These results demonstrated that IO supports had SERS sensing capacity to work as a biosensing platform capable of identifying biomolecules in the liquid microenvironment without invasive approaches to the seeded cells.

Despite the newly synthesised 3D matrices did demonstrate favourable sensing capabilities with the identification of diverse type of molecules by SERS, the acquired intensities proved to be weaker than expected. This low SERS signal could be explained by diverse factors. As mentioned before, the functionalization of the particles with PEG chains for their stabilization in the hydrogel could diminish the total amount of free surface on plasmonic particles available to interact with molecules. Another possible explanation for the weak observed SERS signal could be associated with the nanoparticle concentration of the porous IO. Despite having control on the initial nanoparticle solution concentration, after the infiltration process made by centrifugation, the number of nanoparticles retained in the final IO was likely lower. Centrifugation was repeated several times with the aim to ensure a high AuNR concentration in the polymer matrix. These limitations in NP infiltration, combined with the pore's thin layers limiting the number of particles on the pore's wall, seemed to be the main causes for the weak signal.

However, even if the signal was low, it was possible to scan inner layers of the support providing a 3D recreation of the porous system. SERS maps in **Figure 18A, B and C** demonstrated that identification of the SERS signals of the model molecules made possible a 3D reconstruction of pores from the scanned area. The imaged pores had a total diameter close to 160 μm, matching the real pore diameter of the P(NIPAM-co-NVP)@AuNR IO in its swollen state. Therefore, this strategy was expected to open the way towards novel non-invasive label-free biosensing approaches for the detection of biomolecules in complex media.

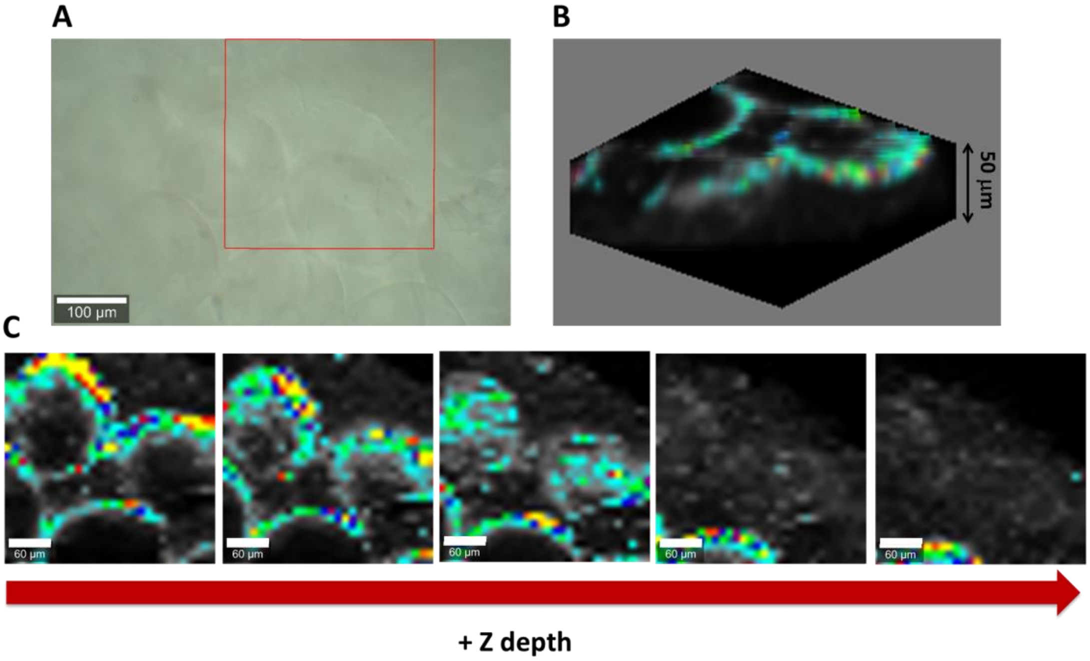

Figure 18. 3D images of IO recreated using SERS sensing of MB. **A)** Optical images of the IO. **B)** 3D SERS map of the scanned area (red square in A; depth is 50 µm). **C)** 2D SERS maps at different Z of the IO. Scale bars in C represent 60 µm.

As demonstrated in the control assays, by associating the obtained SERS data with their spatial localization, it was possible to even recreate 3D images of the analyte distribution inside the porous matrix. Such information could become relevant for the identification of cell-secreted biomolecules and studying their role during biological processes. However, there still exist significant challenges to face for its use in *in vitro* applications. One of the main challenges was that SERS signals were too weak to be clearly identifiable in more complex environments where other competitive species may also interact with the plasmonic particles. Moreover, the addition of cells into the support also became an important obstacle due to the formation of dense opaque biological layers onto the plasmonic support. This reduction of transparency reduced the laser penetration depth into the matrix, hindering signal acquisition. Therefore, the system should be improved for measuring complex 3D cell models in vitro.

3.2.9 3D SERS bioimaging using IO labelled with SERS tags

Loading of a polymer matrix with plasmonic nanoparticles proved to work as an approach towards the synthesis of 3D cellular supports with sensing capabilities. Therefore, the incorporation of SERS-labelled plasmonic nanoparticles was also explored for SERS bioimaging within these 3D structures.

To study the possibility to perform 3D SERS imaging within the prepared IO, diverse types of gold nanoparticles were labelled with Raman tags and incorporated to the formulation of the IO. The use of these SERS-labelled IO in combination with SERS-labelled cells, using a combination of tags with differentiable SERS spectra, was proposed to image complex areas in which common imaging techniques fail to distinguish between the cellular complexes and the 3D synthetic support.

3.2.10 Synthesis of nanoparticles labelled with Raman reporters for 3D SERS imaging (SERS tags)

To prepare the SERS-labelled materials, different molecular Raman reporters (RaRs) were chosen to decorate the nanoparticle surface based on their Raman spectra. The enhancement provided by the plasmonic NP leads to an intense SERS signal that can be selectively imaged without interferences, demonstrating the multiplexing capacity of SERS. The encoded NPs are usually known as SERS tags.

For SERS imaging, two types of gold nanoparticles, gold nanorods (AuNRs) and gold nanostars (AuNSt), were chosen in combination with two different Raman reporters to label either the polymeric IO or the cells (**Figure 19**). For this experiment, biphenyl-4-thiol (BPT) and 2-naphthalenethiol (2-Nat) were chosen due to their well-separated main Raman bands, being at 1280 and 1600 cm^{-1} for BPT (C-C bond stretching and ring stretching respectively) and at 1400 and 1620 cm^{-1} for 2-NAT (both ring stretching). [48–51] On the other hand, AuNR and AuNSt were chosen as plasmonic particles because of their tuneable LSPR towards ranges close to the 785 nm, in resonance with the wavelength of the laser.

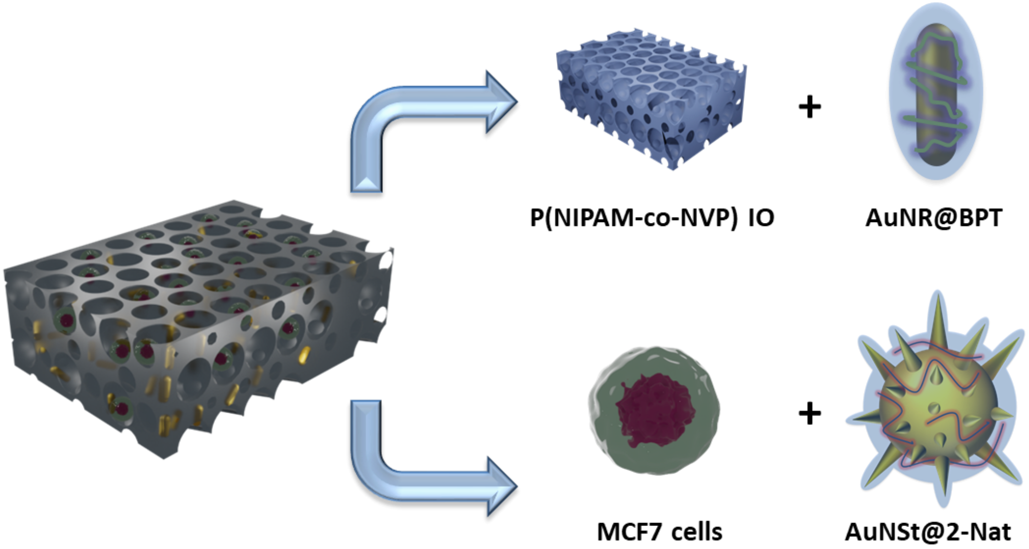

Figure 19. Summary of the strategy for the SERS labelling of the polymeric IO and the MCF7 cells. The composite system comprised 2 main components: the IO was loaded with AuNR@BPT and the cells to be seeded (MCF7) were labelled with AuNSt@2-Nat.

Preparation of the AuNPs@tag was carried out making use of a phase transfer process explained in previous works.[52,53] The process consisted of an initial particle functionalization with the Raman tag and a later encapsulation within a polymeric shell to stabilize and protect the tags without compromising their attachment to the nanoparticle (**Figure 20**). To coat the particle with the Raman tag, a transfer to chloroform was required. To allow their displacement from water towards the new media, gold nanoparticles were initially coated with PEG-SH moieties. The amphiphilic nature of PEG had been studied to provide solubility in chloroform so particles could be transferred into the new phase to be functionalized with the Raman tag. The presence of thiol groups also favoured strong binding to the gold surface, facilitating the transfer and avoiding NP aggregation. Coating with PEG was tested using different numbers of molecules per area unit (molec/nm^2) to retain dispersion of the particles (having a controlled LSPR) while retaining the maximum available free surface for the later functionalization with the tag. UV-vis spectra in **Figure 22C** demonstrated that AuNR required a minimal concentration of 1 molec/nm^2 to avoid aggregation after CTAB removal while AuNSt needed 10 molec/nm^2.

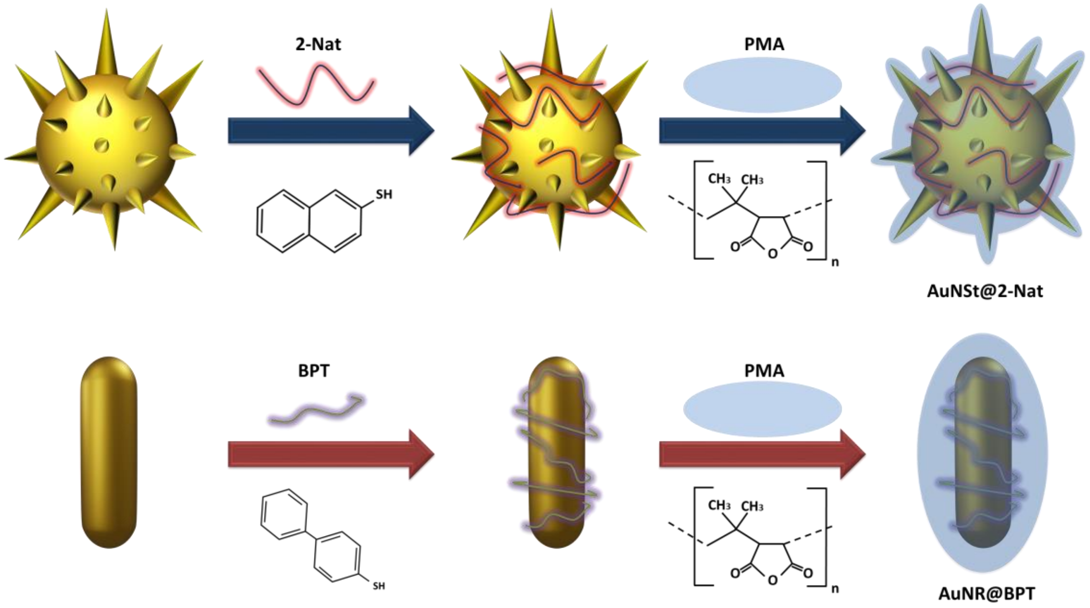

Figure 20. Schematic of the coating process for AuNPs with Raman reporters.

Phase transfer was carried out by forcing the transfer of both types of PEGylated particles from water to the organic phase (10 µM solution of the Raman tag in chloroform) under vigorous stirring for a couple of hours. Once particles were transferred, tag-functionalized AuNR and AuNSt were coated with a polymer shell of polyisobutylene-*alt*-maleic anhydride (PMA). The coating was performed by addition of a 10 mM solution using an approximate ratio of 100 molec/nm^2 (in excess) combined with gentle shaking to ensure full mixture with the polymer. After complete drying of chloroform by slow evaporation using a rotavapor, redispersion of the functionalized particles in water was achieved by using a sodium borate solution (pH=9) accompanied with short-time sonication. The addition of a basic solution was used to avoid aggregation of the newly transferred particles by weakening the interactions between the polymer shells alongside free polymer present in the solution. UV-vis spectra showed differences in the particles LSPR after their complete functionalization (**Figure 22C**). Comparison between both types of nanoparticles showed that AuNSt had a higher shift than AuNR (40 vs. 5 nm, respectively). Taking into consideration the observed changes in their LSPR after functionalization, AuNSt particles were newly prepared to have their initial LSPR at lower wavelength and compensate for the later shift. AuNSt were synthesized to have an LSPR maximum at 745 nm, with average particle dimensions of 45 nm (core) and 70 nm (tip to tip) **(Figure 21B).** In the case of AuNR, LSPR shift proved to be minimal and particles were prepared with their LSPR at 785nm as in previous works. After the final modifications on the AuNSt LSPR, both Raman-labelled particles had their LSPR close to the desired 785 nm, thus being in resonance with the laser wavelength. SERS controls in solution of the different AuNPs@tag (**Figure 21D**) ensured the acquisition of the Raman signal of both tags after complete functionalization.

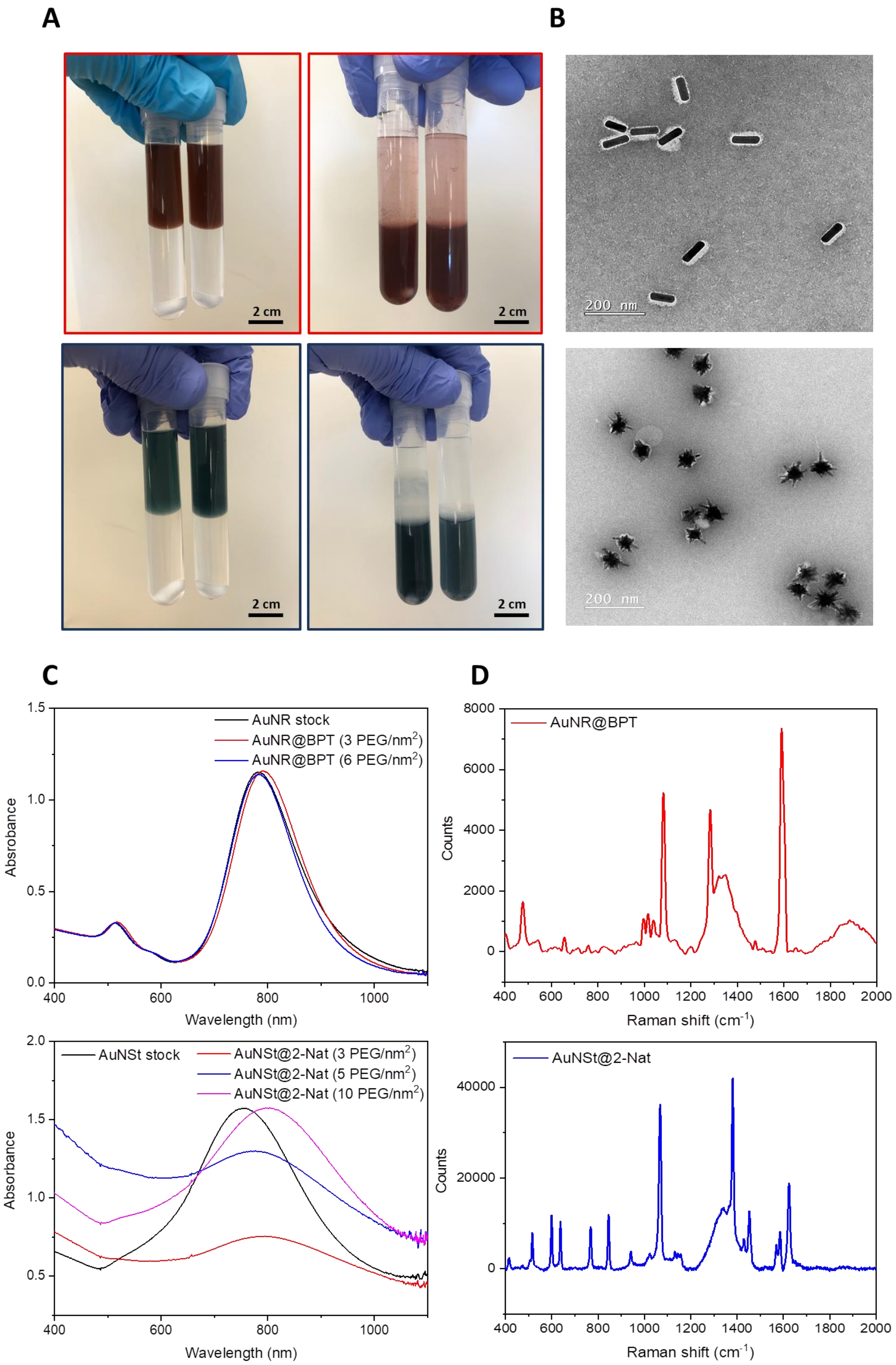

Figure 21. Images of the procedure for the synthesis of AuNPs@tag. In each figure the top images are AuNR@BPT (red) and the bottom images are AuNSt@2-Nat (blue). **A)** Phase transfer of AuNPs into chloroform (before and after the process). **B)** TEM images of the tag-functionalized particles. **C)** UV-vis spectra of particles with different ratios of PEG during phase transfer. **D)** SERS spectra of the SERS tags.

3.2.11 SERS imaging of P(NIPAM.co-NVP)@SERS tag IO

As decided previously, IO supports were synthesized with P(NIPAM-co-NVP) as the building material. In this case, gold particles functionalized with the desired Raman reporter were loaded into the polymer suspension prior to crosslinking. Determination of their dispersion inside the polymer matrix was checked by studying their LSPR. UV-vis spectra shown in **Figure 22** indicate that AuNR@BPT remained stable with no sign of significant aggregation. The polymeric PMA shell proved to work as a protective membrane capable of isolating the gold particles from interacting with the polymer network and avoiding aggregation. Small red-shifts are indicative of a change in the refraction index, caused by the presence of the polymer matrix when compared with the liquid control stock solution. Nonetheless, their LSPR remained close to the desired resonance wavelength proving their adequacy for SERS testing.

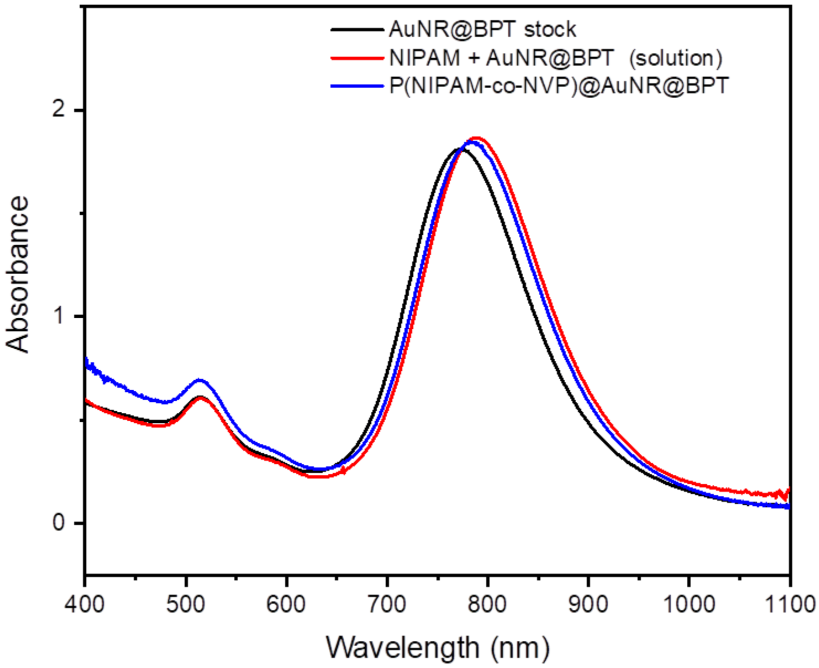

Figure 22. UV-vis stability of AuNR@BPT inside P(NIPAM-co-NVP) gel.

Polymer gels loaded with either AuNR@BPT or AuNR@2-Nat (1 mM) were characterized by SERS, to determine which particle/tag combination provided the higher SERS performance. The selected particle would be used as the loading material in the P(NIPAM-co-NVP) IO, whereas the second candidate would be used for imaging of the seeded cells. SERS spectra of either system were acquired keeping the system in the same conditions described before to avoid drying of the gel. Comparison between systems seemed to show no relevant differences regarding their SERS performance because the different acquired signals had similar intensities (**Figure 23A and B**). Further testing on their performance for SERS imaging was carried out by imaging diverse areas of the nanoparticle-loaded gels to determine the penetration depth (Z depth) in the system (**Figure 23C and D**). Signal recording for both tags was possible within 500 µm (in depth) of the bulk matrix, indicating the possibility to sense in areas deeper than the dimensions of the pores inside the IO (160 µm).

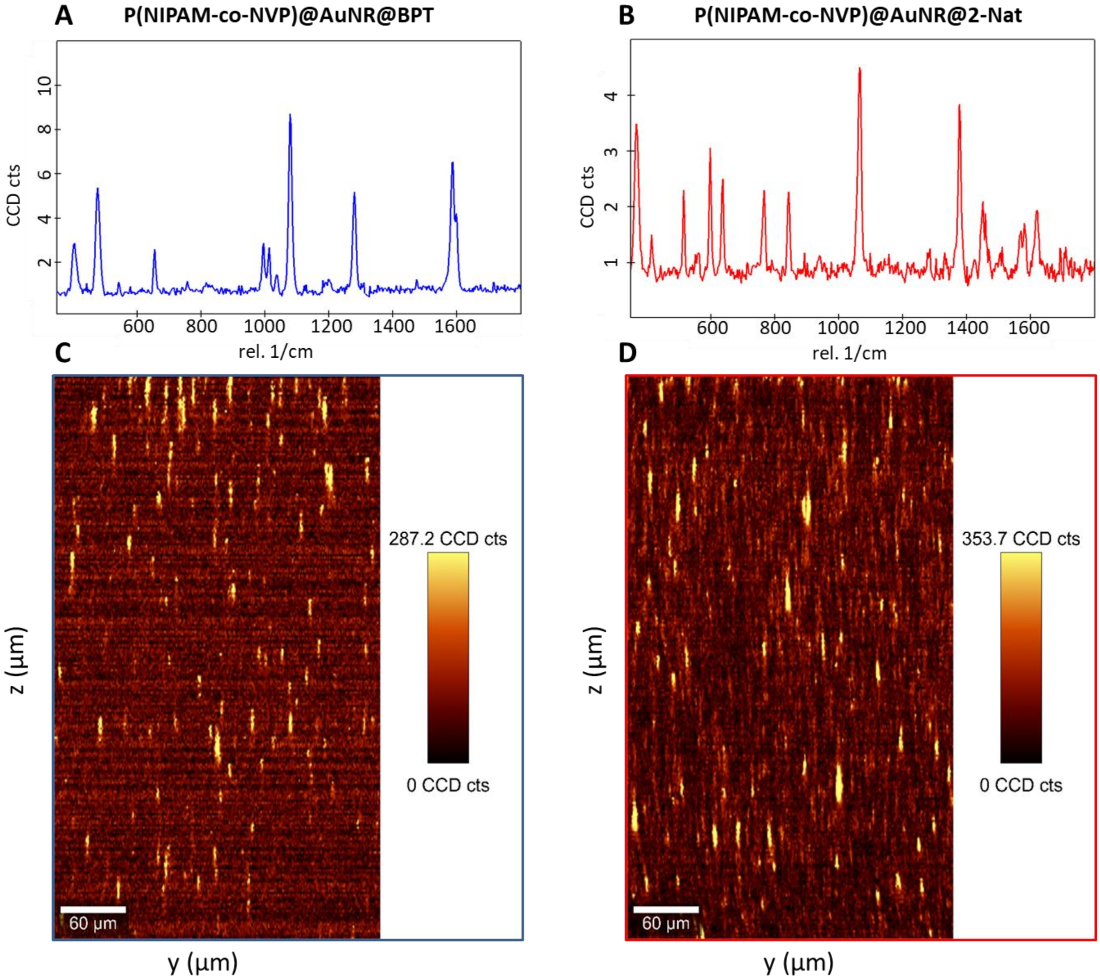

Figure 23. SERS measurements of AuNR@BPT and AuNR@2-Nat loaded inside P(NIPAM-co-NVP) gels. **A and C)** AuNR@BPT. **B and D)** AuNR@2-Nat. A and B are SERS spectra from the encoded particles inside the gel; C and D are SERS maps in Z (500 µm deep).

The acquired information from these SERS assays indicated that both types of nanoparticle/RaR combination could be used for the imaging of the polymer IO. Following these similarities, it was decided to use AuNR@BPT to label the polymer IO scaffold while AuNSt@2-Nat were used for imaging of the cultured cells.

3.2.12 3D SERS mapping of polymer IO using SERS tags (AuNR@BPT)

Synthesis of the P(NIPAM-co-NVP) IO loaded with the Raman-tagged plasmonic particles (AuNR@BPT) was carried out following the same strategy as explained previously. 3D SERS imaging was performed with the samples immersed in cell media (cDMEM) to replicate the conditions as with seeded cells. The laser power was varied until reaching intermediate conditions that allowed detection of the Raman tag without damaging the structure (final of 5 mW/s).

SERS maps shown in **Figure 24C, D and E** demonstrated that the intensity of the SERS tags signal was located around the perimeter of the spherical cavities. Therefore, 3D images could be recreated by correlating the acquired SERS data with the spatial distribution of the IO, as achieved with the label-free approach. SERS signals could be detected at 200 μm in depth, allowing to fully recreate the porous structure on the first layer. However complete recreation of a 3D porous scaffold remained a challenge due to the limited signal acquisition in the bottom layers of the support.

The observed SERS signal intensities proved to be weaker than expected from using Raman tags based on the control assays in solution. Some of the possible explanations for such a decrease in signal intensity would follow the same reasoning as with the previous label-free approach. Most of the reasons would reside in the uncontrolled infiltration of the tagged particles into the porous scaffold thorough centrifugation coupled with the small available space within the thin pore's wall. The overall presence of a low concentration of particles would therefore reduce the amount of available hot spots. In addition to the effects originated by the concentration of nanoparticles, other possible factors such as the fact of having a 3D matrix (instead of a flat 2D surface) would increase light scattering and reduce the number of photons capable of interacting with the metallic nanoparticles. In order to overcome some of the mentioned limitations, the support could be further enhanced by using alternative polymers with higher transparency, increase the nanoparticle-loading using higher stock concentrations or by improving the particle infiltration into the template.

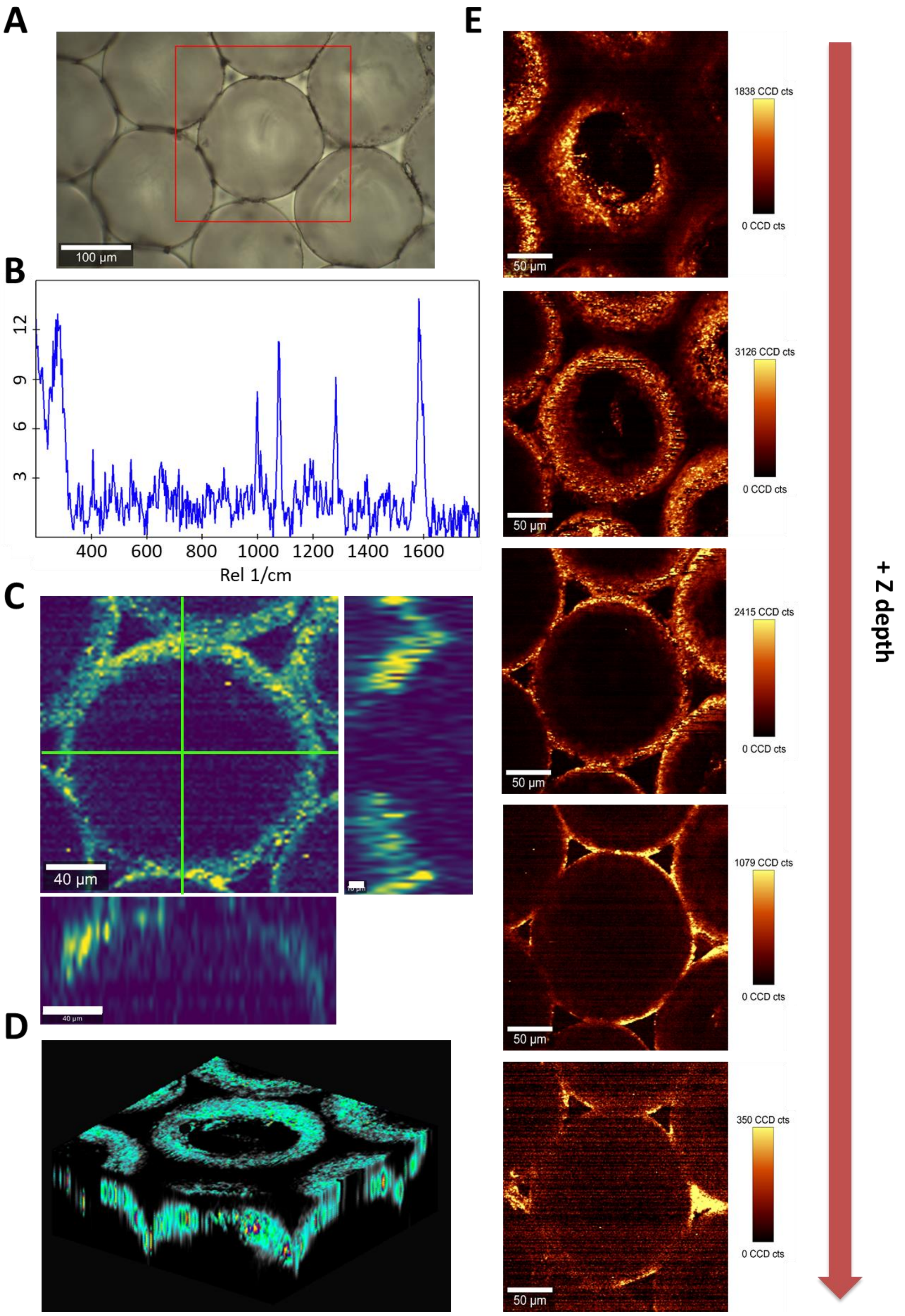

Figure 24. 3D SERS imaging of P(NIPAM-co-NVP)@AuNR@BPT IO. **A)** Optical image of the P(NIPAM-co-NVP) IO. **B)** SERS spectra of BPT detected inside the nanoparticle-loaded scaffold. **C)** Projection maps of the spherical cavities using the SERS signal of BPT. **D)** 3D SERS map of the scanned area (200x200x80 µm). **E)** Z stacks of the 3D spherical IO cavities recreated using the SERS signal from BPT. The maps were acquired using the Raman band close to 1600 cm^{-1}. Scale bars in C are of 40 µm, except for the one at the right, being of 10 µm.

3.2.13 SERS bioimaging of MCF7 cells labelled with SERS tags

To perform 3D imaging of cells inside the porous matrix, the encoded nanoparticles were to be previously internalized by the cells. Previous works in our group demonstrated that plasmonic nanoparticles coated with a PMA shell showed no preferential uptake by cells. To force the internalization of particles, further functionalization was required to expose moieties capable of trespassing the cellular membrane. For this reason, AuNSt@2-Nat particles were later coated with polyarginine (polyR). PolyR is classified within a group of peptides known as cell-penetrating peptides (CPPs). These short peptides are known for having a positive charge that facilitates their penetration across cellular membranes. Using this strategy, coatings with CPPs would enhance delivery of the plasmonic particles inside cells through endocytosis.

In this work, AuNSt@2-Nat nanoparticles were coated with different ratios of polyR (1, 5 and 10 molec/nm^2). To demonstrate the presence of polyR on the particle surface, the charge of the particles was characterised through the zeta-potential, using a Z sizer (**Figure 25A).** Differences in the surface charge proved to correlate with the increasing concentration of polyR, shifting from a negative surface charge going in the control (PMA only, -25 mV) to positive values (10 molec/nm^2 polyR, +40 mV) when adding polyR. The acquired results demonstrated the correct functionalization of polyR onto the PMA coated particles. SERS performance of particles labelled with different amounts of polyR (**Figure 25B**) showed to be similar, demonstrating that the diverse AuNSt@2-Nat were all correctly labelled and the differences in polyR coating did not have an effect on the SERS signal enhancement. After demonstrating that NPs were correctly coated and working as Raman probes, a final test was carried out to check their cellular uptake. The study was performed visualizing the presence of the internalized particles inside the cells by confocal imaging. For this test, polyR-functionalized nanoparticles were incubated into wells containing MCF7 cells for 24 h at physiological conditions, to provide time for cells to internalize the particles.

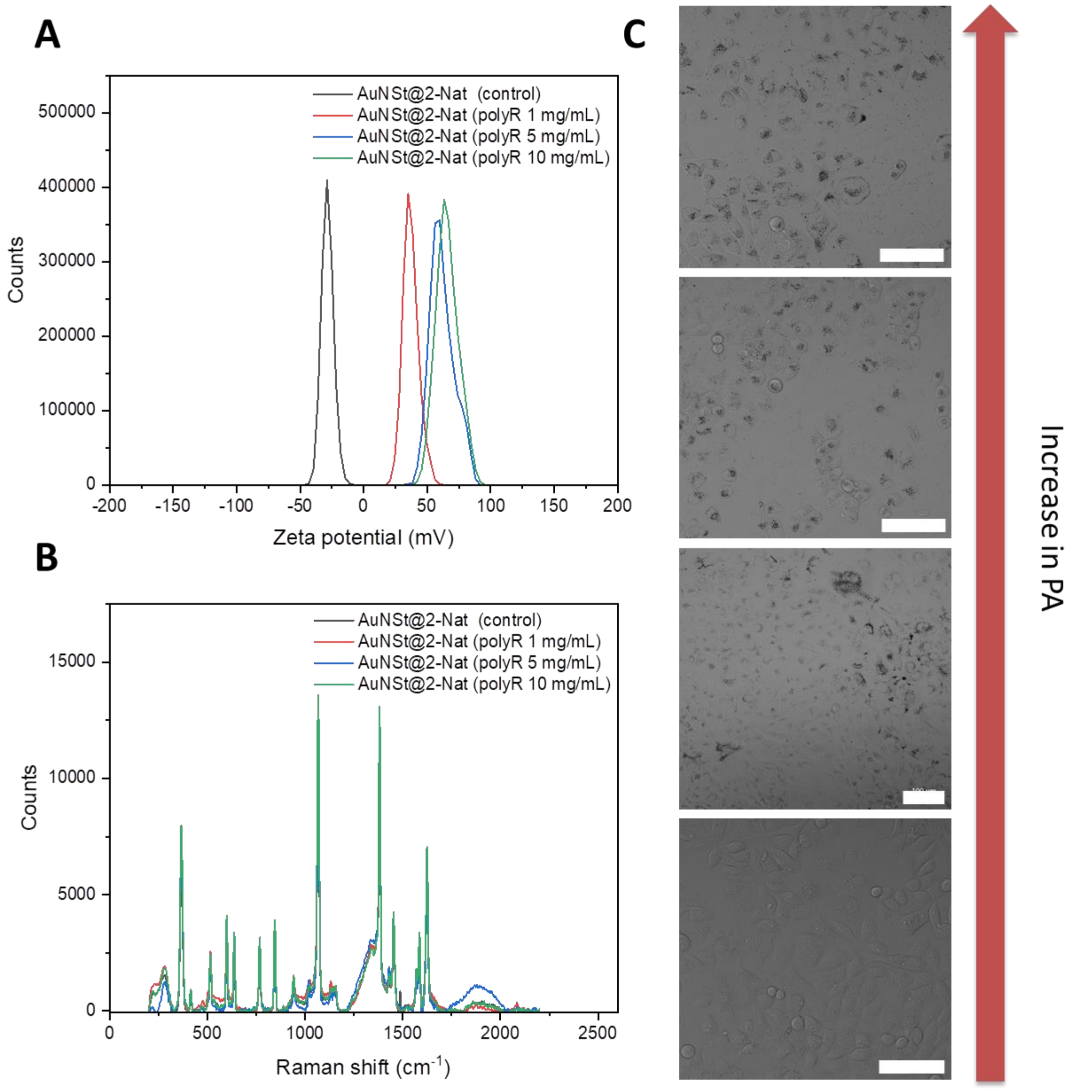

Figure 25. Functionalization of AuNSt@2-Nat particles with polyR and cell uptake studies. **A)** Zeta-potential of Raman-coated particles with different ratios of polyR. **B)** SERS spectra of particles with different concentrations of polyR. **C)** Cell uptake of AuNSt@2-Nat particles coated with polyR. Confocal images of cells showed differences in the amount of uptaken particles (black spots) alongside the increase in the amount of polR molecules. The first image at the bottom is a control using AuNR@2-Nat with no polyR. All scale bars in D represent 100 µm.

Confocal images of MCF7 cells (**Figure 25C**) showed significant differences in the observed number of internalized nanoparticles for each polyR concentration. Control samples without polyR and with the lowest amount of polyR (1 molec/nm^2) showed no signs of cell uptake as no particles could be seen inside the cells. On the other hand, samples with higher polyR loadings (5 and 10 molec/nm^2) were clearly visible as dark spots located within the cell. Despite the differences in the amount of polyR in these later samples, both seemed to induce no cytotoxic effects on the cells over time. Having demonstrated that cells were able to retain the nanoparticles with no appreciable effects on their survival, a 5 molec/nm^2 ratio was used for SERS bioimaging studies.

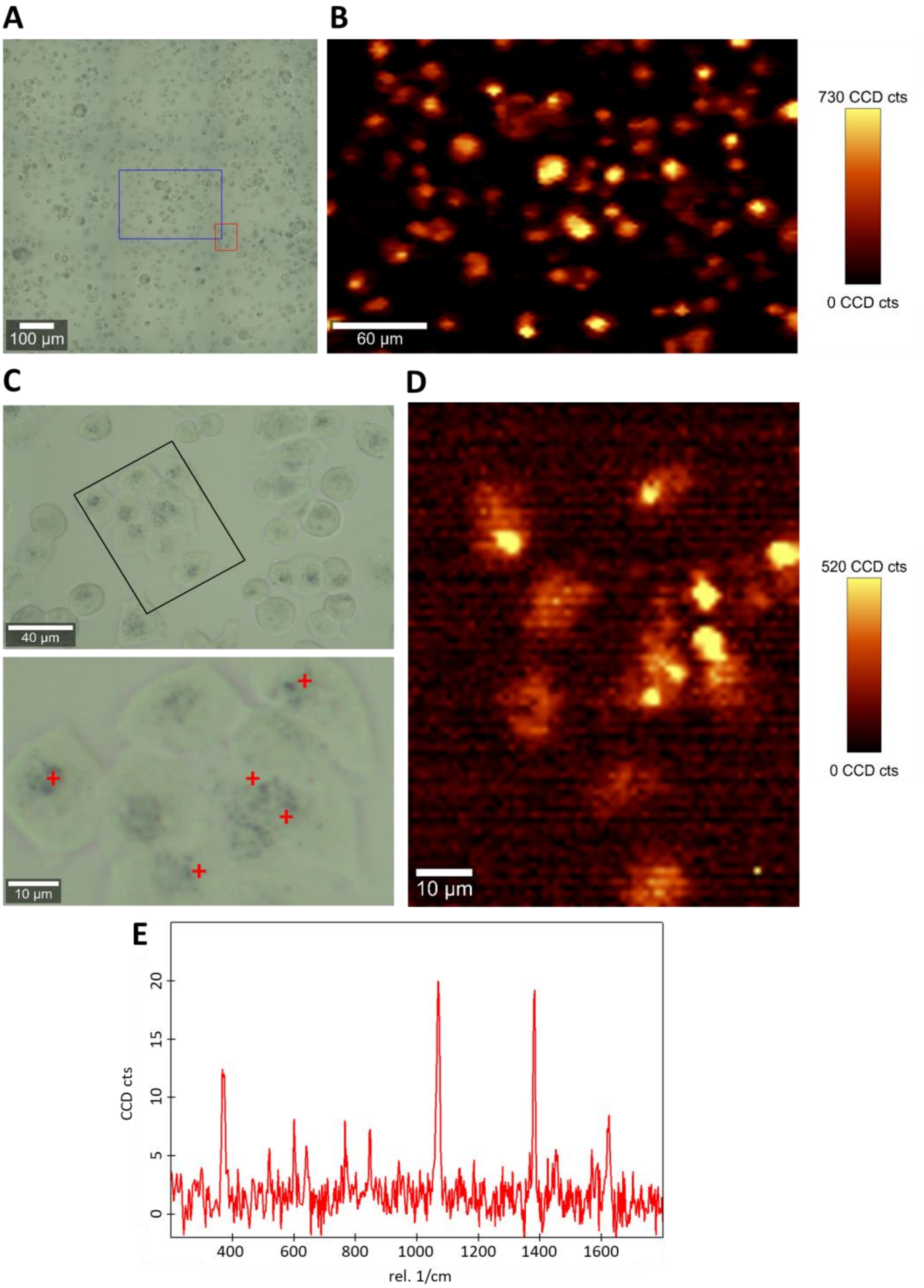

Figure 26. SERS imaging of MCF7 cells with AuNSt@2-Nat coated with polyR. **A and C)** Optical images of labelled cells (different areas). Bottom image in C is a zoomed area within the black square. **B and D)** SERS maps of Raman-labelled gold particles inside cells (square areas). E) SERS spectra of 2-Nat from internalized particles inside cells.

Then, SERS imaging of the labelled cells was carried out. The SERS signal from a scanned area of 1x1 mm where cells were growing was clearly identifiable as the SERS spectra of 2-Nat (**Figure 26C**). SERS maps were then acquired using the intensity of the band at 1380 cm^{-1} (ring stretch) matching with optical images of cells within the scanned areas (**Figure 26A with B, C with D (square areas**).

Once the SERS signal from MCF7 cells was confirmed, SERS imaging experiments were performed into IO seeded with MCF7 to acquire images of the cells growing inside a closed 3D environment. Cells were previously loaded with AuNst@2-Nat nanoparticles while the support was prepared with AuNR@BPT. After cells were seeded onto the support and incubated for 2 h, SERS assays were carried out on the outer surface of the seeded support because cells were mostly located within the first layers of the matrix, as observed in the confocal microscope (**Figure 27A**).

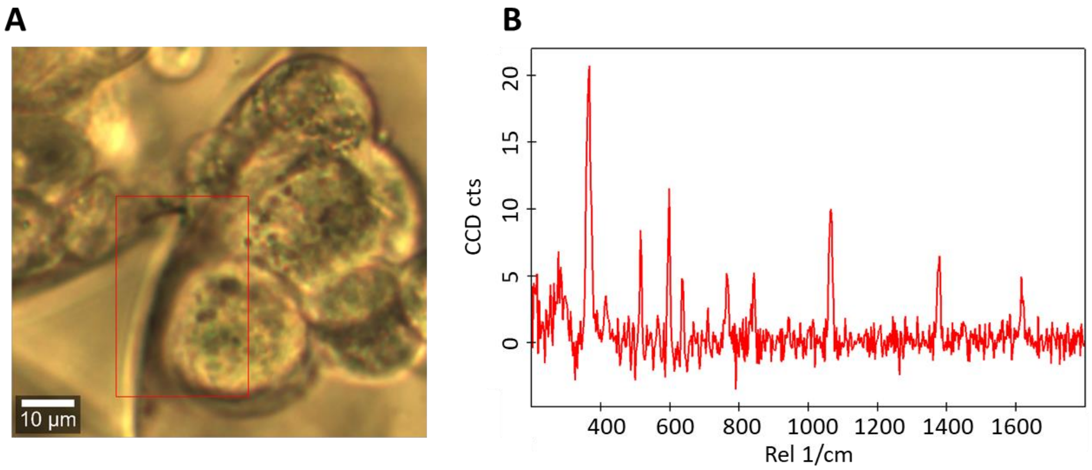

Figure 27. SERS detection of AuNSt@2-Nat labelled MCF7 cells into IO@AuNR@BPT. **A)** Optical image of the cell-seeded support. **B)** SERS spectrum of 2-Nat acquired from cells within the marked red square area in A.

As shown in **Figure 27B**, SERS studies demonstrated the presence of the Raman tag within the seeded cells. After demonstrating the possibility to acquire SERS signalling from the tags within the cell-seeded support (outer layers), further testing would still be required to recreate SERS maps of both IO and cells. To detect the tags into such complex environment, optimization of the working conditions, such as laser power and exposure time, is still necessary to detect the tag signal while avoiding cell damage.

3.3 Conclusions

This project proved to be challenging towards the creation of novel 3D cellular supports coupled with biosensing and imaging features. Synthesis of porous supports based on the negative replica of a microparticle template resulted in the formation of an ordered multi-layered template with pores with controllable dimensionality and interconnectivity. By using microparticles with sizes of hundreds of microns, the final pore dimension was within the desired range to allow 3D cell diffusion within the support, while providing a closed niche capable to promote cell-cell and cell-matrix interactions. Regarding the working material, the synthesis of such a complex matrix required several conditions to be met, ranging from biocompatibility as a cellular support to efficient SERS performance. Both employed polymers, GelMA and P(NIPAM-co-NVP), proved to be suitable for such a goal, as their performance in all tests was similar. However, P(NIPAM-co-NVP) gels proved to be better candidates because its higher transparency facilitated the visualization of inner pores inside the porous scaffold.

During the building process, the addition of plasmonic nanoparticles into the IO system proved to be a critical step due to the necessity to obtain a reproducible scaffold with well-defined SERS capabilities. Particle stability was a key factor to have the LSPR of the system in resonance with incident laser wavelength, to acquire the maximum SERS enhancement as possible. However, the dispersion of NPs proved to be affected by the presence of the polymer solution, consequently inducing aggregation, and shifting the LSPR. To retain the desired LSPR, protection of AuNR in the NIPAM-co-NVP solution was achieved by partial coating of the particle surface using PEG-SH. The addition of this amphiphile in small ratios proved to be enough to avoid aggregation at the cost of reducing the amount of total free surface for sensing purposes. Other factors such as NP loading into the template by centrifugation proved to be helpful for the fabrication of the composite scaffold but with low control over the exact internalised concentration.

Sensing capacities of the composite cellular scaffold proved to be sufficient to acquire both 2D and 3D maps reconstructed using the SERS signals from model analytes (MB and 4-ATP). The acquired 3D SERS maps proved to perfectly recreate the spherical interconnected network of the IO, visualized as circular bright contours, verifying that sensing was taking place close to the internal cavities were AuNR were located. However, due to the weak SERS signal, recreation of the cavities could only be achieved on the first outer layers. Imaging of lower inner cavities remained impossible because the focus inside the scaffold was limited by the thickness of the bulk material and the weakly detectable SERS signal.

Regarding the functionality of the composite scaffold as a cell culture support, cell studies within the 3D matrix demonstrated high biocompatibility. Differences in cell distribution over time (even in deeper layers) proved that the scaffold was able to provide enhanced cell adhesion and diffusion towards adjacent cavities, forming similar cell aggregates like in spheroids. The acquired "spheroids" had a diameter delimited by the dimensionality of the pores while the scaffold did not suffer changes in morphology. This positive functionality combined with the long-term stability of the synthesised matrix in cell media demonstrated the utility of using the composite IO as a support for *in vitro* cell culture studies.

In a second approach, the use of encoded nanoparticles with Raman tags was expected to allow for SERS imaging of the porous support and SERS-labelled MCF7 cancer cells. The use of 2 different types of encoded NPs facilitated the differentiation between objects within a complex 3D environment. Loading of the newly functionalized particle into the polymer support proved to be easier than with the label-free approach as the outer polymer shell was able to protect the metallic nuclei from the polymer solution. On the other hand, a second type of encoded particles was required to label the cells with Raman tags. Coating with polyR at low ratios proved to be enough to enhance their internalization into cancer cells with minimal cytotoxic effects, while retaining SERS performance, thereby permitting the acquisition of SERS maps of the loaded cells. Combination of both encoded systems showed initial information proving the possibility to acquire SERS signalling of the tags within the cell-seeded scaffold. However, it was still necessary to further optimize the working conditions to avoid damaging the cells and the loaded tags during the SERS measurements. Control over the laser irradiation and the setup conditions was necessary to ensure the survival of cells over light irradiation and acquiring SERS signals from inside the cell-seeded IO, to recreate SERS maps of the 3D matrix.

Overall, all acquired data demonstrated the possibility to combine SERS sensing and imaging within 3D systems suitable for cellular studies. The combination of a highly biocompatible support with SERS capabilities could become an interesting system as a bioanalytical tool to study *in situ* cellular microenvironments. However, some of the most important limitations of the SERS technique, such as the chemical affinity between the gold nanoparticles and analyte or the need for low light scattering, remained a challenge to uncover the complete potential of such complex systems.

3.4 Experimental section

Chemicals

For the synthesis of the different types of gold nanoparticles hydrogen tetrachloroaurate (III) trihydrate ($HAuCl_4 \cdot 3\ H_2O$) was purchased from Alfa Aesar. Sodium chloride (NaCl), sodium borohydride ($NaBH_4$), silver nitrate ($AgNO_3$) and ascorbic acid were purchased from Aldrich. The surfactants used for the synthesis of either gold spheres or nanorods were cetyltrimethylammonium chloride (CTAC) from Aldrich and hexadecyltrimethylammonium bromide (CTAB) 96% from Acros. Raman tags (2-napthalenethiol (2-Nat) and bisphenyl thiol (BPT)) in addition to to O-[2-(3-mercaptopropionylamina)ethyl]-O'-methylpolyethylene glycol (PEG-SH, mw:5000 Da) were purchased from Aldrich. For coating of the Raman-tag labelled NPs, polyisobutylene-alt-maleic anhydride (PMA) and polyarginine (polyR) were purchased from Aldrich.

For hydrogel synthesis, gelatin from porcine skin A, methacrylic anhydride (94%) and 2-hydroxy-4'-(2-hydroxyethoxy)-2-methylpropiophenone, N-isopropylacrylamide, ammonium persulfate (APS), N-vinyl pyrrolidone (NVP), N,N'-methylenebis(acrylamide) (BIS) and N,N,N',N'-tetramethylenediamine (TEMED) were purchased from Aldrich. Microparticle assemblies were prepared using PS 4000 series monosized particles (140 µm) purchased from Fisher. 2-isopropanol and chloroform were acquired from Scharlab. Resins for microtome sample preparation were composed of Nonecyl Succinic Anhydride Modified (NSA), D.E.R. 736 epoxy resin, N,N-dimethylaminoethanol (DMAE) and ERL 422 purchased from Polysciences Inc. 3D holders were printed using Ultimaker though PLA black 2.85 mm.

Cell culture studies were carried out using MCF7 cells provided by the American Type Culture Collection (ATCC). Fluorescence assays were performed using MitoLite Deep red FX660 and green 5-chloromethylfluorescein diacetate (CMDFA) from Vitro S.A.-Cayman Chemical. Complete cell media (cDMEM) was purchased from Aldrich. Cytotoxicity assays (LDH) and cell proliferation (MTT) kits were also purchased from Thermo Fisher and Sigma, respectively.

Instrumentation

Electron microscopy images were taken with a transmission electron microscope (TEM) JEOL-JEM 1400 PLUS operating at 120 kV equipped with a GATAN US1000 CCD camera and Scanning Electron Microscopy (SEM) images were taken using SEM microscope JEOL JSM6490 operating at 10-15 keV. SEM images were acquired from previously freeze-dried samples. Optical images were obtained using a Leica microscope with an x10 objective. UV-vis data were acquired with absorbance spectrophotometer Agilent 8453. Surface charge of the plasmonic particles was measured with a Zetasizer Ultra Red Label using ZS Xplorer software.

Fluorescence assays for LDH and MMT studies were acquired using a microplate reader with 485 nm as the excitation wavelength and emission at 530 nm. Fluorescence imaging of the labelled cells and scaffold was performed with a confocal fluorescence microscope Zeiss LSM 880 with an argon excitation laser at 488 nm and DPSS at 561 nm. 3D Z stacks of the internal IO interconnected network were acquired by soaking the gel in a 10 µM solution of rhodamine. Images were taken from 1 x 1mm x 300 µm volumes. SERS control assays and cell seeded supports SERS studies were performed using an alpha 300R confocal Raman microscope (WITec GmbH, Ulm, Germany) equipped with a 785 nm diode laser (120 mW nominal output) and a Peltier-cooled CCD camera with chip size 1064 px x 275 px and a 20x immersion objective. Data was processed using the software Project 5/5+ and Wire 4.4.

Thin layers of the scaffold were acquired by a ultramicrotome Leica EM UC7 at fast speed with thicknesses of 200 nm. Samples for the microtome were previously embedded in a resin by multi-step soaking of the gel in a mixture of ethanol and resin (Nonenyl Succinic Anhydride Modified (NSA) (3 mL), ERL 422 (1.1 mL), D.E.R. 736 epoxy resin (0.815 mL) and N,N-dimethylaminoethanol (DMAE) (0.055 mL). The resin:ethanol ratios were changed every 30 minutes, starting with 1:1, then 2:1 and later 2 more times with 100% resin. The embedded IO were left to dry before slicing. Microtome samples were obtained by slicing 200 nm thick slices and imaged at TEM. Preparation of microparticle templates was achieved using an electric oven Carbolite Gero CWF1300. PLA holders for centrifuge tubes were 3D printed using an Ultimaker 2 with the Ultimate Cura software for the printing parameters.

Synthesis of gold nanoparticles

Gold stars (AuNSt)

AuNSt were synthetized following the procedure explained in previous works.[54] For the preparation of gold seeds, s gold chloride solution (500 mL, 0.25 mM) was heated at 100 °C before rapidly adding a previously heated sodium citrate solution (25 mL, 1% wt) under vigorous stirring. After 15 minutes, the solution changed to a dark-red colour and was checked by UV-vis (LSPR at 518 nm would mean a small seed of 13 nm) and let cool down before storage at 4°C to avoid possible aggregation.

To perform the growth of the spikes, an aqueous solution of $HAuCl_4$ (25 µM) was acidified by addition of 10 µL of HCl 1M. Growth of the particles was acquired by fast addition of ascorbic acid (50 µL, 100 mM), silver nitrate ($AgNO_3$ 30 µL, 1 mM) and the gold seeds (50 µL). The mixture showed a change in the colour of the suspension from red to a dark blue within few seconds after addition. Newly synthetized particles had to be cleaned several times in fresh Milli-Q water after centrifugation at 3000 rpm for 15 minutes.

Gold nanorods (AuNR)

AuNR were prepared using the method explained in other reference works.[55,56] For seeds preparation, a gold solution (50 µL, 25 mM) was added to 4.7 mL of CTAB (0.1 M) and kept in a warm bath at 27 °C to avoid the crystallization of the surfactant. Then, 300 µL of a $NaBH_4$ solution (10 mM) was rapidly added under vigorous stirring to induce the fast reduction from Au^{+3} to Au^0 (from yellow to brown change in colour). Seeds were later checked at UV-vis to the correct location of the LSPR at 514 nm.

For a 10 mL batch of gold nanorods (AuNRs), 10 mL of CTAB (0.1 M) was acidified with 190 µL of HCl 1M and mixed with 100 µL of the auric solution (50 mM). Later, $AgNO_3$ (120 µL, 10 mM) and ascorbic acid (100 µL, 0.1 M) were added into the solution and checked at UV-vis to ensure gold pre-reduction before adding the prepared seeds (25 µL) under vigorous stirring. The stirring was kept for 5 more minutes before allowing the suspension to rest in a water bath for another 2 h before completing the reaction. Correct reactivity was observed by changes in the suspension colour, from orange to transparent (after ascorbic acid addition) and to red-brown as reaction time passed. The samples were finally washed by centrifugation at 6500 rpm for 20 minutes several times and the final suspension was kept in a CTAB solution 1mM to avoid aggregation.

Functionalization with Raman tags (phase transfer) and PA coating

Phase transfer: functionalization of gold nanoparticles with the different tags was performed as explained in other works.[52,53] Gold particles were initially functionalized with PEG-SH at different ratios (1 molec/nm^2 for AuNR and 10 molec/nm^2 for AuNSt). In a 10 mL tube, 5 mL of chloroform with a 10 mM concentration of Raman tag (either BPT or 2-Nat) was mixed with 5 mL of NP-PEG particles. To the separated phase, 40µL of HCl 1 M was added and later kept under vigorous stirring conditions overnight (at room temperature and protected from light). After transfer, removal of the aqueous phase was achieved by adding 1 mL of ethanol (EtOH) prior to centrifugation at 7500 rpm. Particles redispersed in fresh chloroform were coated with PMA (stock 10 mM, ratio 100 molec/nm^2) under gentle shaking. Encoded particles were removed from chloroform by evaporation using a rotavapor and redispersed in fresh milli-Q using a sodium borate solution (pH=9) with sonication. Finally, the particles were cleaned by centrifugation (15 min, 7500 rpm) and resuspended in milli-Q water 3 times. Particles were later checked by UV-vis.

PpolyR coating of AuNps@tag for cell uptake was performed using diverse ratios (1, 5 and 10 polyR molec/nm^2) from a 10 mM stock solution of polyR. Particles were kept under constant shaking overnight and later washed 3 times with fresh milli-Q water. Surface charge of the newly coated particles was checked with a Z-sizer 3 times each sample.

Polymer gels preparation and nanoparticle loading

Methacrylated gelatin (GelMA) synthesis. GelMA was synthesized as stated in previous work.[57,58] Briefly, 10 g of gelatine from porcine skin was dissolved in a PBS solution in a 200 mL beaker under vigorous stirring at 60 °C. Later addition of 0.8 mL of methacrylic acid (MA) per gram of gelatin was performed and let in continuous stirring for 3 h. After reaction completion, the suspension was dialyzed with 15 kDa dialysis bags in distilled water for one week at 40°C. The water was replaced several times to avoid saturation and promote the diffusion of the non-reactive reagents. The cleaned suspension was finally lyophilized to acquire white foams and kept in closed vials to avoid external contamination.

Polymer loading with nanoparticles: polymers loading with AuNRs was performed by different approaches to have a final concentration of 1 mM. GeLMA 7% wt was dissolved in a 10 mL vial in a water bath at 37 °C. Under gentle stirring, 100 µL of a 10 mM suspension of cleaned AuNR (washed by centrifugation at 6000 rpm 2 times an resuspended in fresh milliQ water) was added dropwise into the polymer solution. 2-hydroxy-4'-(2-hydroxyethoxy)-2-methylpropiophenone (1% wt) was added to the mixture until fully dissolved.

Poly(isopropylacrilamide) (PNIPAM)-based hydrogels were obtained by mixing 290 µg/µL of NIPAM in Milli-Q water with a 1:05 ratio of 1-vinyl-2-pyrrolidone (NVP) with respect to NIPAM. The solution was later mixed with 200 µL of a N-N-methylenebis(acrylamide) (BIS) (stock 25 mg/mL) and 28 µL of ammonium persulfate (APS) (stock 0.1 g/mL). The mixture was loaded with AuNR until reaching a final concentration of 1 mM. Gel formation of NIPAM-co-NVP was finally carried out by adding 10 µL of tetramethylethylenediamine (TEMED).

Synthesis of polymer IO loaded with plasmonic nanoparticles

Microparticle assembly: 600 mL of PS particles (5% wt.) were first washed and resuspended in 1 mL of isopropanol. Assembly was prepared in a holder composed of an Eppendorf tube (200 µL) glued onto a glass slide. The system was deposited onto a Petri dish as a floating platform and moved into a sonicator. Under continuous sonication, a couple of droplets of the microparticle solution were dropwise added into the holder after every 10 minutes. This time was used to allow the added particles to assemble into ordered layers. The water bath was kept under 30 °C to avoid evaporation of 2-propanol during the assembly. After the final microparticle addition, holders with the new assemblies were deposited in an oven at 37 °C overnight to remove the solvent remnants. Thermal annealing was later performed at 120 °C for 4 h to form the interconnecting bridges. SEM images were taken to check the correct assembly and dimensionality of the microparticle template.

Polymer infiltration: polymer solutions were infiltrated within the microparticle template by centrifugation. Assemblies were deposited into a 3D printed holder to fit inside a falcon tube (50mL). 10 mL of the nanoparticle-loaded polymer solution was added into the falcon and centrifuged for 40 minutes at 6500 rpm. For NIPAM samples, centrifugation was carried out keeping a low temperature of 4 °C, whereas GelMA IO were centrifuged at 38 °C to retain their liquid state. After centrifugation, the holder was removed and the particle suspension was resuspended with sonication and shaking. The process was repeated up to 4 times. For NIPAM-co-NVP IO, crosslinking was later achieved by adding TEMED (0.1% wt) into the polymer solution. Due to the fast reactivity, upon addition the samples were rapidly soaked into the falcon and centrifuged one last time at 2000 rpm for 15 minutes. In the case of GelMA, the template was irradiated under UV light for 40 seconds at 50 mW/s.

Template removal and characterization: excess polymer on the infiltrated templates was removed by slight scratching with a blade. This step was required to free the cavities of the IO for their later cell seeding. Samples were soaked in chloroform overnight to dissolve the PS microparticles. The acquired gels were then transferred into a second fresh chloroform bath to remove any dissolved PS remnant for a couple of hours. Polymer scaffolds were finally transferred into milli-Q water for one day to remove chloroform and fully swell.

Cell seeding within the IO

Seeding of MCF7-eGFP transfected cells was carried out by addition of 500 µL containing $2 \cdot 10^5$ cells onto polymer IO. Seeded scaffolds were incubated in an incubator at physiological conditions (37 °C, 5% CO_2) for different time points. Confocal imaging was performed up to 300 µm deep using an argon excitation laser at 488 nm and DPSS at 561 nm to detect both GFP and propidium iodide (PI) and study cell survival. Z stack of the cellular complexes were acquired at different times over a 2-week period to check difference in cell diffusion and cell stability.

SERS labelling of MCF7 cells

Cell uptake of AuNSt@2-Nat nanoparticles coated with polyR (5 molec/nm^2) was achieved by incubation of 10 µL of a 1 mM solution into a well containing MCF7 cells for a 24 h. Cells were imaged by confocal microscopy to check nanoparticle uptake and later imaged by SERS using an incident 785 nm laser wavelength.

Cell survival/cytotoxicity studies and imaging

MTT test (cytotoxicity test): Cells were seeded at between $5 \cdot 10^3$-$2 \cdot 10^4$ cells/well (100 µL) in a 96-well plate and allowed to adhere. A working solution of MTT reagent (Lonza) was added (100 µL /well) and allowed to incubate at 37 °C for 1 h. DMSO (100 µL/well) was later added to solubilise the intracellular MTT reagent and promoting its detection by absorbance at 550nm read in a plate reader. The showed results are expressed as a percentage of the average viable cells.

LDH test (cell survival test): 50 µL of cell supernatant was removed and mixed with 50 µL of LDH working reagent (Invitrogen) in a clean 96-well plate. The sample was left at room temperature and protected from light, for 30min, followed by addition of 50 µL of STOP compound. The absorbance was read at 490 nm with a reference background measurement at 630 nm. The results are expressed as a percentage of the positive dead cell control.

Fluorescence labelling: provided MCF7 were previously transfected with Lentivirus to express GFP (MCF-eGFP). For cell death imaging, cells were labelled with propidium iodide (PI) (Invitrogen) by adding 1:200 from a 10 µM stock solution 2 h before checking by confocal microscopy.

SERS sensing and imaging

SERS sensing: P(NIPAM-co-NVP)@AuNR and GelMA@AuNR control gels were soaked in MB (from 50 to 5 µM) and 4-ATP (50 µM) for 1 h. Gels were later irradiated with a laser (785 nm wavelength) and the SERS signal of the model molecules recorded. Samples were glued on a petri dish and filled with Milli-Q water to avoid drying. SERS assays were performed using an immersion objective at different areas on the surface and deep inside the scaffold. 2D and 3D SERS maps were acquired at regions of 600x600x300 µm integrating the area of the most intense Raman bands on their SERS spectra.

SERS imaging: P(NIPAM-co-NVP)@AuNR@BPT and P(NIPAM-co-NVP)@AuNR@2-Nat were studied by SERS (785 nm laser). Both gels were scanned on the 2D surface and in Z-Y axis for their later SERS mapping.

P(NIPAM-co-NVP)@AuNR@BPT IO were glued to a petri dish and filled with milli-Q water to avoid drying. SERS maps were acquired from the surface and inside the scaffold up to 200 µm deep, using a laser power of 5 mW for 10 ms. For MCF7@AuNSt@2-Nat cells, imaging was performed with cells incubated in a Petri dish with cDMEM, with a laser power of 10 mW for 50 ms. Finally, assays combining both AuNR@BPT IO seeded with MCF7@AuNSt@2-Nat cells were performed immersed in cDMEM and retained with a 3D printed holder. SERS signal acquisition of both components was achieved using a 785 nm laser varying the laser power between 10-25 mW for 25-50 ms.

3.5 References

1. La Thangue, N. B. & Kerr, D. J. Predictive biomarkers: a paradigm shift towards personalized cancer medicine. *Nat. Rev. Clin. Oncol.* **8**, 587–596 (2011).
2. Srinivas, P. R., Kramer, B. S. & Srivastava, S. Trends in biomarker research for cancer detection. *Lancet Oncol.* **2**, 7 (2001).
3. Henry, N. L. & Hayes, D. F. Cancer biomarkers. *Mol. Oncol.* **6**, 140–146 (2012).
4. Mayeux, R. Biomarkers: Potential uses and limitations. *NeuroRX* **1**, 7 (2004).
5. Hwang, H., Hwang, B.-Y. & Bueno, J. Biomarkers in Infectious Diseases. *Disease Markers* **2018**, 1–2 (2018).
6. Sim, S. C. & Ingelman-Sundberg, M. Pharmacogenomic biomarkers: new tools in current and future drug therapy. *Trends Pharmacol. Sci.* **32**, 72–81 (2011).
7. Anderson, D. C. & Kodukula, K. Biomarkers in pharmacology and drug discovery. *Biochem. Pharmacol.* **87**, 172–188 (2014).
8. Roussos, E. T., Condeelis, J. S. & Patsialou, A. Chemotaxis in cancer. *Nat. Rev. Cancer* **11**, 573–587 (2011).
9. Foster, D. S., Jones, R. E., Ransom, R. C., Longaker, M. T. & Norton, J. A. The evolving relationship of wound healing and tumor stroma. *JCI Insight* **3**, e99911 (2018).
10. Bianco, R., Melisi, D., Ciardiello, F. & Tortora, G. Key cancer cell signal transduction pathways as therapeutic targets. *Eur. J. Cancer* **42**, 290–294 (2006).
11. Dhillon, A. S., Hagan, S., Rath, O. & Kolch, W. MAP kinase signalling pathways in cancer. *Oncogene* **26**, 3279–3290 (2007).
12. Bhatt, A. N., Mathur, R., Farooque, A., Verma, A. & Dwarakanath, B. S. Cancer biomarkers - Current perspectives. *Indian J. Med. Res.* **132.2**, 129–149 (2010).
13. Sensi, F., D'Angelo, E., D'Aronco, S., Molinaro, R. & Agostini, M. Preclinical three - dimensional colorectal cancer model: The next generation of in vitro drug efficacy evaluation. *J. Cell Physiol.* **234**, 181–191 (2019).
14. Fontoura, J. C. *et al.* Comparison of 2D and 3D cell culture models for cell growth, gene expression and drug resistance. *Mater. Sci. Eng.: C* **107**, 110264 (2020).
15. Emmert, M. Y., Hitchcock, R. W. & Hoerstrup, S. P. Cell therapy, 3D culture systems and tissue engineering for cardiac regeneration. *Adv. Drug Delivery Rev.* **69–70**, 254–269 (2014).
16. Antoni, D., Burckel, H., Josset, E. & Noel, G. Three-Dimensional Cell Culture: A Breakthrough in Vivo. *Int. J. Mol. Sci.* **16**, 5517–5527 (2015).

17. Panzavolta, S. *et al.* 3D interconnected porous biomimetic scaffolds: *In vitro* cell response: 3D interconnected porous biomimetic scaffolds. *J. Biomed. Mater. Res.* **101**, 3560–3570 (2013).
18. Dutta, R. C. & Dutta, A. K. Cell-interactive 3D-scaffold; advances and applications. *Biotechnol. Adv.* **27**, 334–339 (2009).
19. Owen, S. C. & Shoichet, M. S. Design of three-dimensional biomimetic scaffolds. *J. Biomed. Mater. Res.* **94**, 1321-1331 (2010).
20. Vila-Parrondo, C., García-Astrain, C. & Liz-Marzán, L. M. Colloidal systems toward 3D cell culture scaffolds. *Adv. Colloid Interface Sci.* **283**, 102237 (2020).
21. Ou, K.-L. & Hosseinkhani, H. Development of 3D in Vitro Technology for Medical Applications. *Int. J. Mol. Sci.* **15**, 17938–17962 (2014).
22. Zhang, Y., Wang, S., Eghtedari, M., Motamedi, M. & Kotov, N. A. Inverted-Colloidal-Crystal Hydrogel Matrices as Three-Dimensional Cell Scaffolds. *Adv. Funct. Mater.* **15**, 725–731 (2005).
23. Zhang, Y. S., Zhu, C. & Xia, Y. Inverse Opal Scaffolds and Their Biomedical Applications. *Adv. Mater.* **29**, 1701115 (2017).
24. Zhang, Y. S., Choi, S.-W. & Xia, Y. Inverse opal scaffolds for applications in regenerative medicine. *Soft Matter* **9**, 9747 (2013).
25. Williams, D. F. On the mechanisms of biocompatibility. *Biomaterials* **29**, 2941–2953 (2008).
26. Sgarminato, V., Tonda - Turo, C. & Ciardelli, G. Reviewing recently developed technologies to direct cell activity through the control of pore size: From the macro - to the nanoscale. *J. Biomed. Mater. Res.* **108**, 1176–1185 (2020).
27. Turnbull, G. *et al.* 3D bioactive composite scaffolds for bone tissue engineering. *Bioactive Mater.* **3**, 278–314 (2018).
28. João, C. F. C., Vasconcelos, J. M., Silva, J. C. & Borges, J. P. An Overview of Inverted Colloidal Crystal Systems for Tissue Engineering. *Tissue Eng. Part B: Reviews* **20**, 437–454 (2014).
29. Van Zundert, I., Fortuni, B. & Rocha, S. From 2D to 3D Cancer Cell Models: The Enigmas of Drug Delivery Research. *Nanomaterials* **10**, 2236 (2020).
30. Booij, T. H., Price, L. S. & Danen, E. H. J. 3D Cell-Based Assays for Drug Screens: Challenges in Imaging, Image Analysis, and High-Content Analysis. *SLAS Discovery* **24**, 615–627 (2019).
31. Martinez, N. J., Titus, S. A., Wagner, A. K. & Simeonov, A. High-throughput fluorescence imaging approaches for drug discovery using *in vitro* and *in vivo* three-dimensional models. *Exp. Op. Drug Discovery* **10**, 1347–1361 (2015).
32. Cortesi, M. & Giordano, E. Non-destructive monitoring of 3D cell cultures: new technologies and applications. *PeerJ.* **4**, e13338 (2022)

33. Mosier-Boss, P. Review of SERS Substrates for Chemical Sensing. *Nanomaterials* **7**, 142 (2017).
34. Zong, C. *et al.* Surface-Enhanced Raman Spectroscopy for Bioanalysis: Reliability and Challenges. *Chem. Rev.* **118**, 4946–4980 (2018).
35. Stiles, P. L., Dieringer, J. A., Shah, N. C. & Van Duyne, R. P. Surface-Enhanced Raman Spectroscopy. *Annu. Rev. Anal. Chem.* **1**, 601–626 (2008).
36. Langer, J. *et al.* Present and Future of Surface-Enhanced Raman Scattering. *ACS Nano* **14**, 28–117 (2020).
37. Li, P. *et al.* Fundamentals and applications of surface-enhanced Raman spectroscopy–based biosensors. *Curr. Op. Biomed. Eng.* **13**, 51–59 (2020).
38. Wang, X. & Guo, L. SERS Activity of Semiconductors: Crystalline and Amorphous Nanomaterials. *Angew. Chem. Int. Ed.* **59**, 4231–4239 (2020).
39. Li, J.-F., Zhang, Y.-J., Ding, S.-Y., Panneerselvam, R. & Tian, Z.-Q. Core–Shell Nanoparticle-Enhanced Raman Spectroscopy. *Chem. Rev.* **117**, 5002–5069 (2017).
40. Chen, H., Yuan, L., Song, W., Wu, Z. & Li, D. Biocompatible polymer materials: Role of protein–surface interactions. *Progr. Polym. Sci.* **33**, 1059–1087 (2008).
41. Li, Z., Huang, X., & Gang Lu. Recent Developments of Flexible and Transparent SERS Substrates. *J. Mater. Chem. C* **8**, 3956–3969 (2020).
42. Hu, J. L. & Lu, J. Memory polymer coatings for smart textiles. Active Coatings for Smart Textiles. *Woodhead Publishing*. 11–34 (2016).
43. Pasparakis, G. & Tsitsilianis, C. LCST polymers: Thermoresponsive nanostructured assemblies towards bioapplications. *Polymer* **211**, 123146 (2020).
44. Xiaoguang Fan, Shiya Gu, Liyan Wu, & Lei Yang. Preparation and characterization of thermoresponsive poly(N-isopropylacrylamide) copolymers with enhanced hydrophilicity. *E-Polymer* **20**, 561–570 (2020)
45. Budhlall, B. M., Marquez, M. & Velev, O. D. Microwave, Photo- and Thermally Responsive PNIPAm–Gold Nanoparticle Microgels. *Langmuir* **24**, 11959–11966 (2008).
46. Ye, J. *et al.* Excitation wavelength dependent surface enhanced Raman scattering of 4-aminothiophenol on gold nanorings. *Nanoscale* **4**, 1606 (2012).
47. Merlen, A. *et al.* Surface enhanced Raman spectroscopy of organic molecules deposited on gold sputtered substrates. *Nanotechnology* **20**, 215705 (2009).
48. Zhou, Q., Yang, Y., Ni, J., Li, Z. & Zhang, Z. Rapid recognition of isomers of monochlorobiphenyls at trace levels by surface-enhanced Raman scattering using Ag nanorods as a substrate. *Nano Res.* **3**, 423–428 (2010).
49. Ganbold, E.-O. & Joo, S.-W. Raman Spectroscopy of Biphenyl-4,4'-dithiol and p-Terphenyl-4,4-dithiol on Gold Surfaces. *Bull. Korean Chem. Soc.* **36**, 4 (2015).

50. Agarwal, N. R. *et al.* SERS detection and DFT calculation of 2-naphthalene thiol adsorbed on Ag and Au probes. *Sens. Actuators B: Chemical* **237**, 545–555 (2016).
51. Alvarez-Puebla, R. A., Dos Santos Jr, D. S. & Aroca, R. F. Surface-enhanced Raman scattering for ultrasensitive chemical analysis of 1 and 2-naphthalenethiols. *Analyst* **129**, 1251 (2004).
52. Serrano-Montes, A. B. *et al.* A General Method for Solvent Exchange of Plasmonic Nanoparticles and Self-Assembly into SERS-Active Monolayers. *Langmuir* **31**, 9205–9213 (2015).
53. Jimenez de Aberasturi, D. *et al.* Surface Enhanced Raman Scattering Encoded Gold Nanostars for Multiplexed Cell Discrimination. *Chem. Mater.* **28**, 6779–6790 (2016).
54. Yuan, H. *et al.* Gold nanostars: surfactant-free synthesis, 3D modelling, and two-photon photoluminescence imaging. *Nanotechnology* **23**, 075102 (2012).
55. Pérez-Juste, J., Pastoriza-Santos, I., Liz-Marzán, L. M. & Mulvaney, Paul, P. Gold nanorods: Synthesis, characterization and applications. *Coord. Chem. Rev.* **249**, 1870–1901 (2005).
56. Scarabelli, L., Sánchez-Iglesias, A., Pérez-Juste, J. & Liz-Marzán, L. M. A “Tips and Tricks” Practical Guide to the Synthesis of Gold Nanorods. *J. Phys. Chem. Lett.* **6**, 4270–4279 (2015).
57. Celikkin, N., Mastrogiacomo, S., Jaroszewicz, J., Walboomers, X. F. & Swieszkowski, W. Gelatin methacrylate scaffold for bone tissue engineering: The influence of polymer concentration: Gelatin methacrylate scaffold for bone tissue engineering. *J. Biomed. Mater. Res.* **106**, 201–209 (2018).
58. Yue, K. *et al.* Synthesis, properties, and biomedical applications of gelatin methacryloyl (GelMA) hydrogels. *Biomaterials* **73**, 254–271 (2015).

General conclusions

The research work performed in this thesis has provided a general overview on the possibility of combining SERS as a biosensing and bioimaging tool with the synthesis of complex 3D porous scaffolds for biomedical studies. SERS-active materials were achieved by combining the porous scaffolds with plasmonic gold nanoparticles. The internalization of SERS-active biosensors inside the matrix was then aimed to provide the system with intrinsic SERS sensing capabilities, avoiding the need for post-seeding cell manipulation. With this goal, several types of constructs were tested to demonstrate the wide versatility of SERS as a biosensing and imaging approach, toward gaining further insight on *in situ* bioanalysis in 3D.

In the first chapter, the scaffolding strategy comprised a combination of 3D printing of ceramic emulsions with polymer-based materials, to create a multi-porous composite support. The main goal of the research was to propose a 3D model to monitor bone infection by SERS. To mimic the properties of bone, the printed support was composed of ceramics (alumina) prepared through a HIPE procedure to achieve a high porosity. The use of emulsions for the synthesis of dense inks provided further complexity to the material by creating an interconnected porosity, offering the possibility to mimic the mechanical properties and morphology of natural bone. The printed supports demonstrated to have the desired microporosity, with high stiffness after sintering, thereby creating an interesting solid matrix to support bone growth. Despite the complexity of the matrix and its demonstrated biocompatibility, the bioinert nature of alumina proved to play a major role on cell growth, failing at promoting cell spreading on the scaffold. To circumvent this drawback, incorporation of a protein layer (made of collagen and fibronectin) favoured cell adhesion to the ceramic support, demonstrating the importance of the chemical nature of the support for cellular studies.

To impart SERS sensing capacity to the scaffold, a hydrogel-based matrix containing gold nanorods was used. The addition of the polymer matrix was not only aimed at retaining the biosensing nanoparticle but also expected to mimic the bone cartilage, further enhancing the biocompatibility of the complete scaffold. Methacrylated gelatin (GelMA) was the polymer of choice for hydrogel formation, due to its well-known biocompatibility and outstanding gel-forming properties. For its use as bone infection model, *Pseudomonas Aeruginosa, a* bacteria commonly found in bone implants, was chosen and the detection of bacterial-secreted molecules, such as pyocyanin (PCN), was studied. Control assays carried out using commercial PCN demonstrated the suitability of the biosensing platform because detection of the biomolecule was achieved both in

Milli-Q water and in cell culture media, down to concentrations of 1 and 10 µM, respectively. Further assays demonstrated that the detection of PCN was possible both on the surface and inside the scaffold, down to a depth of 1 mm, thus permitting spatial localization of the desired biomolecule even in areas close to the embedded ceramic.

After demonstrating the biosensing capabilities of the composite support for PCN, the scaffold was tested for *in situ* sensing of bacteria-secreted PCN by *Pseudomonas Aeruginosa*. For these tests, the use of two types of bacteria (wild type and mutant (do not produce PCN)) became useful to prove the correct detection of the desired biomolecule, discarding possible competition with other biomolecules secreted by the same bacteria. Both studies, performed using the bacteria supernatant (without bacteria) and in the presence of bacteria, clearly demonstrated the precise detection of PCN. Although it was clear that PCN was only present in the WT variant, the acquired SERS intensities indicated that the presence of dense bacteria populations diminished the obtainable signal. Alongside the diverse SERS assays with commercial and bacteria-secreted PCN, the obtained SERS data could be used to recreate SERS maps of the scaffold structure. This approach demonstrated reliable biosensing properties of the scaffold, permitting the spatial-localization and visualization of detected biomolecules present inside the 3D volumetric support. To sum up, the demonstrated biosensing capabilities in addition to the high biocompatibility of the 3D composite support proved the suitability of the prepared materials as supports for *in vitro* cellular studies. Nonetheless, long-term studies with species such as bacteria proved to require for more resilient materials, as bacteria would swiftly deteriorate GelMA, hindering their suitability for long-time studies.

In a second approach, a 3D porous scaffold was prepared using inverted colloidal crystals as templates, regarded as inverse opals (IO). The building of the scaffold comprised several stages. Initially, a microparticle template was obtained by assembling polystyrene (PS) microparticles into ordered arrays, combined with thermal annealing to create “necks” between adjacent particles. Subsequently, the template was infiltrated with the building material to fill the inter-particle empty spaces, prior to consolidating and removing the template, thus obtaining its negative replica. Such a building method generated a support with controllable pore dimensionality, which retained the properties of the template employed. Regarding the used material, the decision was based not only on its biocompatible properties but also on its high transparency and reliable SERS biosensing performance (when loaded with gold nanoparticles), to facilitate the study inside the pores of the scaffold. Following these criteria, GelMA and P(NIPAM-co-NVP) were chosen as the main candidates.

Loading of the diverse polymers with gold nanoparticles was carried out by means of different approaches. In the case of GelMA, nanoparticles could be mixed with a minimal concentration of CTAB to retain their colloidal dispersion in presence of the polymer. However, NIPAM seemed to interact with the gold surface of the loaded nanoparticles, causing them to aggregate and thus lose their LSPR. To overcome this undesired effect, nanoparticles were functionalized with PEG-SH to retain a suitable colloidal dispersion, at the expense of reducing the available free surface for subsequent SERS studies. Overall, both polymers demonstrated to have a similar performance on both biocompatibility and SERS detection, using MB as control. Nonetheless, confocal imaging performed on IO of each polymer demonstrated that visualization of the inner pores was more reliable when using P(NIPAM-co-NVP), thus proving to be a more suitable polymer for the desired strategy.

Control SERS assays of the composite IO using MB not only demonstrated the capacity of the support to detect the biomolecules present in the nearby microenvironment, but it also made possible to recreate volumetric 3D SERS maps of the scaffold interior. SERS sensing proved to take place on the wall of the pores, thus providing a system in which the interior of the pores stays empty, whereas the nanoparticles remain entrapped inside the wall of the pore, thus avoiding direct interactions with the later seeded cells. This feature was further confirmed by TEM imaging, where gold nanoparticles could be identified, following a circular pattern in agreement with the spherical shape of the pores. Having demonstrated the biosensing capabilities of the scaffold, later tests with cancer cells (MCF7-eGFP) indicated the possibility to visualize cells located within the 3D matrix using standard fluorescence imaging. MCF7-eGFP cells remained alive for a 21-day period, in which cells were capable to adhere to the interior of the pores, thus demonstrating high biocompatibility for long-term cell studies. However, *in situ* detection of cell-secreted biomolecules still proved to remain a challenge because the increased opacity of the system, caused by the presence of dense cellular populations, alongside the already weak cross-section Raman signalling of most biomolecules, hindered the detection of any specific signals.

On a last approach, the scaffold was loaded with Raman reporter-coated plasmonic NPs (SERS tags), which proved to work as an interesting strategy for multiplex bioimaging of seeded cells within 3D scaffolds. The high performance of the used SERS tags, coupled with the low light scattering of the transparent polymer materials, would allow for SERS imaging inside the support, even in the presence of cells. In contrast to the previously observed behaviour of gold nanoparticles with NIPAM, the use of SERS tags coated with the amphiphilic polymer PMA demonstrated a good dispersibility in the polymer, with no need for further functionalization. For cell studies, it was necessary to functionalize

SERS tags with polyarginine to promote cell uptake into the cells. Control SERS maps of both IO and MCF7 cells demonstrated the possibility to recreate images of the different objects by using the SERS signals of the loaded SERS tags. Finally, SERS studies combining cell seeding into the porous scaffold demonstrated that, although cells remained adhered to the pore walls (retaining a high biocompatibility), signalling from both SERS tags was hindered by the presence of the dense cellular population. Therefore, 3D SERS imaging of cells inside the 3D-porous scaffold still required further optimization to improve the detection of SERS signals from inside such a complex environment.

In summary, the diverse scaffolding strategies explored in this thesis demonstrated the possibility of combining complex 3D environments with intrinsic SERS biosensing and bioimaging capabilities. By taking into consideration the chemical nature and the mechanical properties of the building material (such as transparency and porosity), it has been possible to stabilize and entrap the biosensing particles within the support. By taking both components altogether, the diverse scaffolding systems proved to be highly biocompatible for each respective cell under study, while permitting SERS detection of biomolecules present within the 3D cellular microenvironments. Moreover, acquisition of SERS signals from confined 3D environments can be further used to recreate SERS images of the composite, thus providing a useful tool towards the visualization of evolving *in situ* cellular processes. Although most SERS assays were mainly tested with biomolecules of high Raman cross sections, there is room to further improve the biosignalling properties of the support for the detection of other biomolecules of interest with weaker Raman response. Therefore, this thesis can be considered as a step towards the creation of novel types of *in vitro* supports, able to recreate complex biological phenomena with intrinsic bioanalytical capabilities. Such systems would be of interest to obtain relevant biological information by non-invasive bioanalytical approaches and modified according to the desired type of cellular study.

Appendix

Publication title: **Vila-Parrondo, C.**, García-Astrain, C. & Liz-Marzán, L. M. Colloidal systems toward 3D cell culture scaffolds. *Adv. Colloid Interface Sci.* **283**, 102237 (2020).

Advances in Colloid and Interface Science 283 (2020) 102237

Contents lists available at ScienceDirect

Advances in Colloid and Interface Science

journal homepage: www.elsevier.com/locate/cis

Historical Perspective

Colloidal systems toward 3D cell culture scaffolds

Christian Vila-Parrondo [a], Clara García-Astrain [a,*], Luis M. Liz-Marzán [a,b,c,*]

[a] CIC biomaGUNE, Basque Research and Technology Alliance (BRTA), Paseo de Miramon 182, 20014 Donostia San Sebastián, Spain
[b] Centro de Investigación Biomédica en Red, Bioingeniería, Biomateriales, y Nanomedicina (CIBER-BBN), Paseo de Miramón 182, 20014 Donostia-San Sebastián, Spain
[c] Ikerbasque, Basque Foundation for Science, 48013 Bilbao, Spain

ARTICLE INFO

Available online 8 August 2020

Keywords:
Porous scaffolds
Hierarchical materials
Inverse opals
Tissue engineering
Microstructure

ABSTRACT

Three-dimensional porous scaffolds are essential for the development of tissue engineering and regeneration, as biomimetic supports to recreate the microenvironment present in natural tissues. To successfully achieve the growth and development of a specific kind of tissue, porous matrices should be able to influence cell behavior by promoting close cell-cell and cell-matrix interactions. To achieve this goal, the scaffold must fulfil a set of conditions, including ordered interconnected porosity to promote cell diffusion and vascularization, mechanical strength to support the tissue during continuous ingrowth, and biocompatibility to avoid toxicity. Among various building approaches to the construction of porous matrices, selected strategies afford hierarchical scaffolds with such defined properties. The control over porosity, microstructure or morphology, is crucial to the fabrication of high-end, reproducible scaffolds for the target application. In this review, we provide an insight into recent advances toward the colloidal fabrication of hierarchical scaffolds. After identifying the main requirements for scaffolds in biomedical applications, conceptual building processes are introduced. Examples of tissue regeneration applications are provided for different scaffold types, highlighting their versatility and biocompatibility. We finally provide a prospect about the current state of the art and limitations of porous scaffolds, along with challenges that are to be addressed, so these materials consolidate in the fields of tissue engineering and drug delivery.

Contents

Abbreviations: CNFs, Carbon nanofibers; CS, Chitosan; CLSM, Confocal Laser Scanning Microscopy; T_c, Critical temperature; P_c, Critical pressure; ENCPs, Embryonic neural progenitor cells; EA, Ethyl acetate; EL, Ethyl lactate; T_F, Foaming temperature; GOx, Graphene oxide; GF, Growth Factor; HIPE, High Internal Phase Emulsions; hBMSC, Human bone marrow stromal cell; hiPC-NPCs, Human induced pluripotent stem cells derived from neural precursor cells; hMSCs, Human mesenchymal stem cells; hPSC, Human pluripotent stem cells; hUVECS, Human umbilical vein endothelial cells; HAp, Hydroxyapatite; ISISA, Ice segregation-induced self-assembly; iPs, Induced pluripotent stem cells; IO, Inverse opal; MSCs, Mesenchymal stem cells; MWCNTs, Multi-walled carbon nanotubes; NPC, Neural precursor cells; PhC, Photonic crystal; PCL, Polycaprolactone; PLGA, Poly(D,L-lactic-co-glycolic acid); PEG, Polyethylene glycol; PEGDA, Polyethylene glycol diacrylate; γ-PGA, Poly (γ-glutamic acid); PLA, Polylactic acid; PMMA, Polymethyl methacrylate; PS, Polystyrene; PVA, Polyvinyl alcohol; rBMSCs, Rat bone marrow-derived mesenchymal stem cells; rhBMP-2, Recombinant human bone morphogenic protein-2; $scCO_2$, Supercritical CO_2; SCFs, Supercritical fluids; TZ, Thermoplastic zein; TMPTA, Trimethylolpropane triacrylate; VEGF, Vascular endothelial growth factor.

* Corresponding author at: CIC biomaGUNE, Basque Research and Technology Alliance (BRTA), Paseo de Miramon 182, 20014 Donostia San Sebastián, Spain.
E-mail addresses: cgarcia@cicbiomagune.es (C. García-Astrain), llizmarzan@cicbiomagune.es (L.M. Liz-Marzán).

https://doi.org/10.1016/j.cis.2020.102237
0001-8686/

1. Introduction

To truly understand how cell tissues behave, grow and repair themselves, it is essential to create cell models that can reproduce the complex 3D structure found in living beings. However, most studies are based on either *in vitro* two-dimensional (2D) cell cultures or *in vivo* animal models, which fail to reproduce the human cellular microenvironment [1]. Despite the advances obtained through 2D cell cultures, cells grown on a flat surface cannot reproduce the cell-cell and cell-matrix interactions present in 3D living tissues and discrepancies are thus commonly observed when translating the obtained results into clinical trials in humans. Similar discrepancies apply when dealing with animal models that may differ, for example, in terms of stem cell differentiation or therapeutic drug response [2]. Therefore, there is a clear need for the development of 3D cell cultures supported by scaffolds that can promote cell attachment and migration, thereby providing the appropriate biochemical and biophysical cues, and enabling the diffusion of nutrients and oxygen to better mimic living tissues. In order to achieve this goal, the scaffolds need to fulfil a set of requirements that include biocompatibility, reproducibility, high porosity (with specific pore size and interconnectivity), tailored biodegradability, adequate mechanical properties to support tissue growth, and appropriate biochemical functionalities [3].

In this context, appropriate material selection and scaffold fabrication strategies are critical to produce compelling scaffolds for tissue engineering applications. These applications include porous biomedical implants, 3D cell models and *in vivo* tissue-induced regeneration, but may offer additional functionalities such as drug delivery, diagnostics or sensing. Therefore, morphological and microstructural features, as well as degradation time, are to be tailored to the intended application [4]. Ceramic, metallic and polymer-based materials have been widely applied to the preparation of scaffolds for biomedical applications. Resistance against corrosion and high biocompatibility have boosted the use of metallic materials such as titanium, cobalt or magnesium alloys, for dental applications and orthopaedics [5]. Ceramic materials in turn feature high thermal and chemical stability, as well as good mechanical properties for their use as implants, usually being the material of choice for bone tissue engineering. Examples of these materials include alumina, zirconia, bioactive glass, tricalcium phosphate and, their greatest exponent for bone engineering, hydroxyapatite (HAp) [6]. Finally, biocompatible polymers of both natural (*i.e.* collagen, gelatin, hyaluronic acid, chitosan, alginate, cellulose) and synthetic origins (*e.g.* polycaprolactone (PCL), polylactic acid (PLA), poly(lactic-*co*-glycolic acid) (PLGA), are extensively used for the fabrication of scaffolds due to their ease of processing, chemical versatility, tunable degradability and, in the case of some natural polymers, their resemblance to extracellular matrix (ECM) components [7,8].

Regarding scaffold fabrication, several techniques have been proposed including electrospinning, impregnation and sintering, melt molding, solvent casting, particulate leaching, gas foaming and freeze-drying, or usually combinations thereof. However, most of these techniques show limitations, particularly related to the generation of a controlled porosity with the desired pore size and enough pore interconnectivity to promote cell proliferation, differentiation and growth. It is thus important to understand the various fabrication approaches that have been implemented to control the above mentioned parameters, toward achieving scaffolds with well-organized microstructures. Examples of fabrication strategies with porosity control are inverse opals, which are obtained from colloidal templates to obtain ordered porous structures, ice-templating using frozen ice as the interconnecting porogen, emulsion templating or foaming using supercritical fluids technology. Recently, 3D printing has also emerged as an appealing alternative to the fabrication of 3D scaffolds with sophisticated architectures. For the sake of brevity, we left 3D printing out from this review, details about this fabrication technique can be found in dedicated works [9–12]. We thus focused on highlighting recent advances in the fabrication of hierarchical porous 3D scaffolds and their applications in tissue engineering. We discuss the state of the art of different fabrication approaches to achieve scaffolds with controlled microstructure, along with their associated challenges. We finally propose future directions and perspectives for further research on 3D porous scaffolds for cell culture, toward a better understanding of tissue growth and dynamics, as well as for the development of *in vitro* disease models and drug screening of new therapeutics.

2. Requisites for scaffold development

Synthetic scaffolds not only work as templates for the cultured cells, but are also required to provide the necessary stimuli to ensure cell survival, close cell-cell interaction, and further cell differentiation to obtain the desired organ [13]. The ideal conditions for tissue engineering depend on the type of cells and the conditions needed to recreate the microenvironment and induce cell differentiation [14]. Notwithstanding, the basic properties for any scaffold to be suitable for biomedical applications can be summarized into porosity, mechanical properties, biocompatibility and bioresorbability [15], which we briefly introduce below (see Table 1 for common characterization techniques used to study each property).

2.1. Porosity

The structure of the scaffold must ensure that cells can circulate through it, which makes it necessary to create a highly interconnected inner network (over 70% of the total volume) of adjacent pores, with large enough diameters to allow cell diffusion and flow of extracellular matrix (ECM) components [15]. Porous scaffolds can contain pores of different diameters, ranging from several nanometers up to tens of microns, each pore size range being able to promote specific interactions to modulate cell behavior [16]. Depending on the pore diameter, empty cavities can be classified as macro-, micro- and nanopores. Macropores are cavities with diameters larger than 100 μm, used as the niches in which cells are able to group altogether, promoting cell-cell and cell-matrix interactions. These cavities ought to have a high pore volume, not only to provide space for the growing tissue but also to allow for the diffusion of oxygen and nutrients during tissue growth [17]. Micropores (ranging from 0.3 to 100 μm) are normally used as windows between macropores to enhance permeability and support cell diffusion by capillary forces [16]. Finally, nanopores (< 300 nm) can interact directly with cells, thereby promoting cell adhesion by increasing the available surface area [16].

Table 1
Properties and characterization techniques required to study the suitability of synthetic scaffolds for biomedical applications.

Scaffold requisite	Characterization technique	Measured property/magnitude	Refs.
Porosity	SEM, Cryo-etch-SEM, FE-SEM	Porosity Pore size	[30,33–36,38–42,44,46,47,51–55,57,64,70,86,92,99,107–111,121,122,124–129,138–140]
	Mercury porosimeter	Bulk density Skeletal density Porosity Pore size Pore volume Surface area Open porosity	[53,55,57,64,72,81,82,96]
	Nitrogen adsorption-desorption measurements	Total pore volume Micropore volume Surface area Open porosity Pore size distribution	[68,76,78,82,89,90,91,107]
	Helium pycnometer	Porosity	[82,111]
	Gravimetric methods (Sartorius Balance)	Porosity Density values	[83,84,89,91,125,127]
Biocompatibility	Cell seeding (SEM, confocal microscopy, DNA content, light microscopy analysis)	Cell adhesion and proliferation	[33,34,37,41,42,46,53,80,82,86,96,99,103,107,108,110,111,112,118,122,124–127,129,130–132,136–140]
	Cytotoxicity tests (MTT test)	Cell viability	[81,86,98,41,110–113,124,125,127,131]
	Live/dead staining	Cell viability and proliferation	[42,99,110,128,132,133]
Mechanical Properties	Compression tests	Compressive strength Elastic compression modulus Compression yield strength and strain	[42,59,64,79,80,90,91,96,99,108,109,110,121,122,129]
	Bending tests	Bending strength Young modulus	[41,76]
	Tensile tests	Tensile strength	[41,96,103,111,129]
Bioresorbability (degradation rate)	Gravimetric measurements	*In vitro* degradation	[80,86,110,121,129]
	SEM	Morphology	[80,121]

2.2. Biocompatibility

The biocompatibility of a scaffold can be defined as its ability to support cell activity by means of molecular signaling, while avoiding any toxic effect on the growing tissue [18]. The main factors involved in these mechanisms include the chemical composition of the synthetic structure, along with the presence of other types of functional biomolecules [19]. Regarding chemical composition, porous scaffolds can be classified into inorganic, such as metals, ceramics or glass ceramics, and organic materials like polymers and composites [20]. Additionally, the biocompatibility of the porous matrix can be enhanced by the addition of biomolecules such as growth factors, either to the bulk matrix or by attaching them onto the pore walls to promote direct interactions with the cells [19]. Apart from the chemical composition, other factors such as the morphology, roughness and rigidity of the pores can also influence cell adhesion and biocompatibility of the porous matrix [20,21].

2.3. Mechanical properties

3D scaffolds should be able to withstand the pressure exerted by the tissue during its development. It is important to maintain the shape and mechanical properties of the interconnected network, as small variations in the pore matrix can influence the biological activity of the cells [17]. Nonetheless, one of the disadvantages of using porous scaffolds is the partial reduction of mechanical strength due to the loss of bulk volume, being replaced by empty cavities and thus increasing the complexity of the system. In addition to providing mechanical support, the scaffold characteristics should also match the mechanical properties of the tissue to mimic the conditions responsible for differentiation stages during tissue formation [22]. As an example, bone tissue engineering is expected to recreate different types of bone structures by varying the compressive strength and Young modulus of the synthetic network [23].

2.4. Bioresorbability

During development, the tissue grows to occupy the whole volume of the interconnected porosity. At this point, vascularization is hindered and can lead to a deficit of nutrients and oxygen into the tissue, ending in cell death and tissue malfunction [24]. For this reason, the degradation rate of the scaffold should be proportional to tissue ingrowth, until the whole support is resorbed once it has accomplished its function as a template [18,25].

3. Scaffold fabrication

Despite much progress, designing porous scaffolds with well-organized and tailored microstructures for biomedical applications remains a challenge. Special attention is to be paid to the building process to achieve the features required for the targeted application. A number of strategies have been followed to prepare biomaterials with appropriate porosity and interconnectivity. However, most such strategies fail at reproducing a truly ordered and defined microporosity. We review in this section the most important fabrication strategies toward ordered scaffolds with controlled microstructures.

3.1. Inverse opals

Most of the strategies used to create biocompatible structured materials aim at mimicking the unique properties of natural biological systems [26]. As an example, natural opals contain 3D crystalline micropatterns composed of silica spheres with diameters ranging

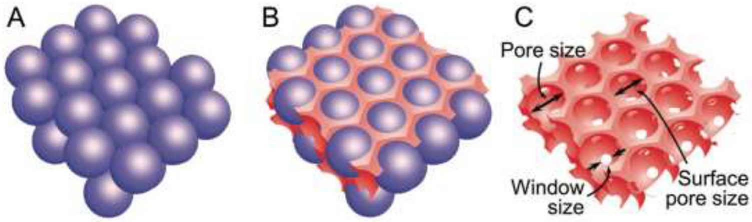

Fig. 1. Schematic representation of the main steps through the fabrication of an inverse opal: A) Colloidal assembly and thermal annealing. B) Infiltration of a sol-gel or polymer precursor into the cavities of the ordered assembly. C) Hardening of the inverse crystal (by crosslinking, sintering or freeze drying) and removal of the colloidal template. Copyright (2017) Wiley. Used with permission from ref. 33 (Zhang et al. Inverse Opal Scaffolds and Their Biomedical Applications. Adv Mater 2017;29:1701115).

from 150 to 300 nm [27]. Such organized structures form within natural systems, such as opal gemstones or butterfly wings, and can manipulate the transmission of incident light, opening up potential applications such as optical switching or photocatalysis [28,29]. These systems are also known as photonic crystals (PhC) for their ability to manipulate the propagation of light by diffraction effects [30]. Synthetic opals have been fabricated by different methods, including the self-assembly of monodisperse colloidal particles. The optical properties of such artificial opals can be tuned by tailoring different parameters, such as the size of the colloidal particles, their chemical composition (and refractive index), and the lattice constant defined by the spatial distribution of the spheres [30,31]. Inspired by photonic crystals, the idea of ordered assemblies has been translated to the fabrication of 3D biomaterials based on the negative replica of a solid template made of colloidal particles [32]. The acquired porous negative lattices thus become porous matrices with well-defined porosity and interconnectivity. They are known as inverse opals (IOs) and can be used in a wide range of applications according to the degree of order and the dimensions of their inner cavities [33,34]. In comparison with other pore-inducing strategies such as salt-leaching or gas foaming [4], the main advantage of these materials is their high homogeneity determined by the monodispersity of the particle building blocks, which promotes similar cell-matrix and cell-cell interactions within the whole volume of the scaffold. In this context, inverse opals can be constructed from different materials, ranging from malleable common polymers to solid inorganic oxides [35]. Regardless of the material used for the colloidal template, IOs aimed for tissue engineering purposes are required to contain pores with diameters in the micrometer scale, as cells have average sizes around 20 μm, depending on cell type [33].

The synthesis of inverse opals can be summarized into 3 main steps: building an ordered colloidal assembly, infiltration of a precursor sol-gel solution through the template and subsequent solidification and removal of the sacrificial template (Fig. 1). For the first step, monodisperse colloidal particles are required so they can be arranged into ordered multilayer arrays. The chemical nature of the beads can range from polymers, such as of polystyrene (PS) or polymethylmethacrylate (PMMA), to inorganic particles like silica [25]. For the colloidal assembly, several methods can accelerate the process while yielding high quality ordered structures [36]. It is worth noting that, despite simple strategies such as sedimentation can lead to organization of the particles by self-assembly, the process may be assisted or improved by applying external forces. Shaking or sonication can often help displace non-ordered particles into available empty cavities in each layer of the assembly [36].

Once the colloidal particles have been organized, the colloidal crystal is thermally annealed to create connections between adjacent particles, thereby stabilizing the assembly and building necks that act as templates for channels between pores in the resulting inverse crystal. Parameters such as the diameter of the colloidal particles, annealing time and temperature will determine the dimensions of the obtained channels. In a detailed study it was concluded that, although longer annealing times resulted in an increase of channel size, temperature proved to have a major effect, so that even small variations result in channels with significantly different width [34]. The next step includes the infiltration of a precursor through the empty gaps within the annealed template. This process essentially comprises soaking the consolidated template with the precursor solution until the voids get fully covered. In order to accelerate infiltration, external forces such as centrifugation or pressure are typically used [37]. Nonetheless, some conditions such as viscosity of the precursor solution and the size of the available empty spaces in the assembly must be taken into consideration to ensure complete infiltration of the precursor solution. For example, solvents with high viscosity will be hard to force their path into the template, which can be fixed by simple dilution [38]. However, in exchange to reducing the precursor concentration into a bigger volume, it will also be necessary to repeat the infiltration step several times to ensure that all empty cavities are filled up with the organic/inorganic material [38].

The final step comprises the solidification of the infiltrated solution and removal of the colloidal template. IOs composed of either organic or inorganic materials are required to retain their shape and structure upon removal of the sacrificial template. Precursor solutions composed of polymer can be either cross-linked or freeze dried, whereas inorganic IOs are usually obtained through sintering [33]. The methods employed to remove the ordered sacrificial template are dictated by the chemical composition of the colloidal particles. Polymer-based assemblies can be removed either by chemical etching or calcination, while inorganic templates such as silicates require a chemical treatment [39]. It is important to mention that both strategies may affect the stability and porosity of the obtained inverse colloidal crystal. It has been proposed that removal of a polymer template by calcination has a huge impact on the final sizes of the pores, as the template is likely to shrink [39]. This reduction in size also lowers the stability of the hardened-to-be colloidal crystal as it loses its physical support. Thereby, pores can reshape and non-desired cracks may form.

3.2. Emulsion templating

High internal phase emulsions (HIPEs) are those emulsions in which droplets (internal phase) occupy at least 74% of the total emulsion volume, being the minimum volumetric space required to ensure contact between adjacent droplets [40]. Emulsions are obtained by the mixture of two immiscible phases, known as the continuous phase and the internal or dispersed phase. The dispersed phase usually contains water and constitutes the interconnected network of droplets [41]. On the other hand, the continuous phase is to become the “skeleton” of the 3D matrix and its composition commonly consists of hydrophobic solvents (oils) mixed with monomers, surfactants and a photo-initiator. These systems result in droplets with sizes ranging from few to several hundred micrometers, depending on the synthesis procedure and the composition of each phase [40]. After curing and drying, 3D complex porous morphologies are obtained, containing spherical cavities that originated from droplets, which we refer to as pores, while interconnected channels are termed windows. The tailored dimensionality and interconnectivity

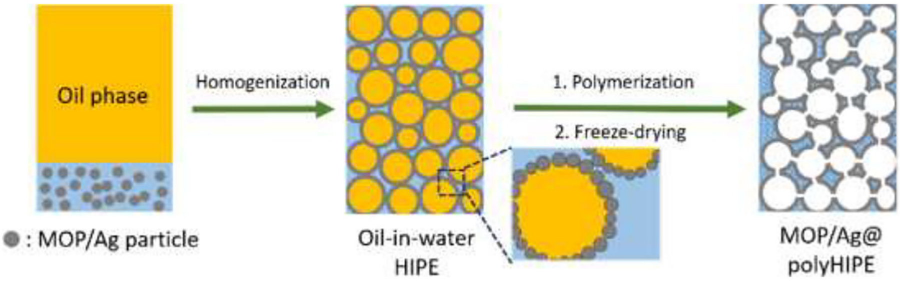

Fig. 2. Schematic representation of the preparation of HIPE with silver-incorporated melamine-based microporous organic polymer (m-MOP/Ag). Adapted with permission from ref. 52. Copyright © 2019 Elsevier.

of the formed emulsion render these materials suitable templates for porous scaffolds in 3D cell culture and tissue engineering. In addition to the porosity obtained through emulsification, further levels of porosity can also be defined by varying the degree of cross-linking of the resulting polymer. In tissue engineering, variations in cross-linking also induce changes in the viscosity of the polymeric network, thus promoting retardation in cell diffusion [42].

In the context of tissue engineering, the porous matrix should have pore diameters above 100 μm and windows of at least the diameter of the cells under study, so as to provide an open path for easy cell diffusion [43]. Some of the parameters that are known to play an important role on droplet size and formation of open/closed pores are the volume ratio of the internal phase, the chemical nature of the surfactant and its concentration [44,45]. In order to stabilize droplets with large diameters, polymers such as partially hydrolyzed polyvinyl alcohol (PVA) are commonly used as co-surfactants, due to their amphiphilic nature and biocompatibility. By increasing the molecular weight of the polymers, it is possible to achieve higher droplet stability, within a certain concentration range. However, the same weight increment can also induce a higher viscosity, which would in turn hinder the emulsification step [46].

When referring to the presence of open/closed pores and to the size of the windows, surfactant concentration plays a major role. In a selected piece of work [47], the excessive use of amphiphile was found to cause wall thinning at the contact site between adjacent emulsions. Upon further shrinkage during crosslinking, open windows formed where the emulsion walls were thinnest. This could become a method to obtain open cavities by introducing large surfactant concentrations to replace polymer in the droplet membrane. We should however give a word of caution, as an increase in surfactant concentration can also lead to formation of smaller droplets because of the concomitant decrease in surface energy per unit area [48]. On the other hand, the presence of surfactants may also affect the behavior of cultured cells by damaging the cytomembrane, even inducing cell death [49]. Alternative techniques have been reported to reduce the required amount of surfactant for pore synthesis, coupled with HIPE. In one such strategy, emulsions can be further stabilized by addition of solid colloidal particles [50]. The system composed by the combination of solid beads with two immiscible phases is known as Pickering emulsion and its improved stability is explained by the irreversible adsorption of the particles at the oil/water interface, which provides enough mechanical hindrance to avoid coalescence and retain the original pore size [51,52]. A schematic representation of HIPE preparation is shown in Fig. 2. A different strategy to obtain large pores comprises the addition of small amounts of water-miscible organic solvents into the aqueous phase [44]. For example, tetrahydrofuran 1% (v/v) facilitates the transport of water molecules from smaller droplets to larger ones through the continuous phase, thus promoting Ostwald ripening and increasing the diameter of the resulting pores.

In addition to the use of surfactants, a drawback of emulsion templating is the use of significant amounts of organic solvents. Not only they are often environmentally harmful, but also require consideration of viable strategies for subsequent removal, due to potential toxic effects that would hinder the biocompatibility of the porous matrix [53]. In this respect, supercritical carbon dioxide-in-water emulsions can be considered toward solving this problem, as they can generate homogenous droplets while using only CO_2 and water as the dispersion media [53]. Supercritical CO_2 ($scCO_2$) has indeed become of interest for biomedical applications due to its low toxicity and high abundance, as will be described below regarding the preparation of foams from supercritical fluids [54]. Notwithstanding, despite its multiple advantages with respect to other solvents, it also poses drawbacks when related to emulsions, due to the low solubility of most polar biomolecules and polymers [55]. Some types of fluorinated polymers and silicon proved to be highly soluble in CO_2, but we still need to find alternative low-cost and easily degradable materials for droplet templating [56].

3.3. Ice templating

As described above, the most common processes to fabricate porous scaffolds involve the use of solvents or templates that are subsequently removed, while ensuring biocompatibility. In this context, cryogenic processes become an interesting alternative for the preparation of porous scaffolds due to the high biocompatibility of the template (ice crystals) and its easy removal (no chemical reactions, by-products or purification steps) [57,58]. Cryogenic processes are based on freezing

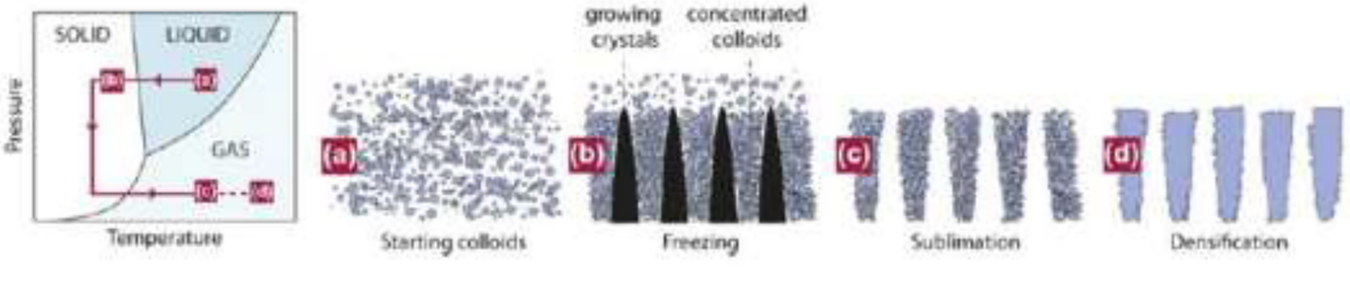

Fig. 3. Schematic representation of the ice-templating fabrication process. Reprinted with permission from ref. 66 © Copyright: © Materials Research Society 2013.

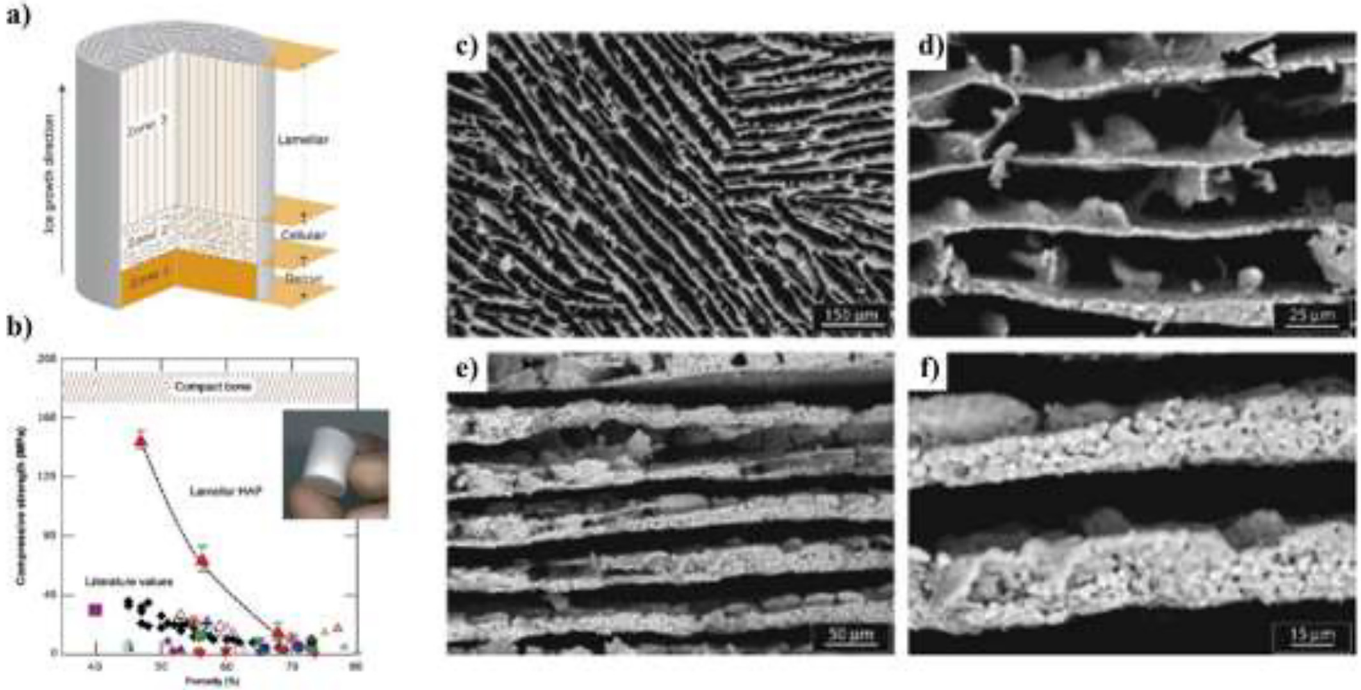

Fig. 4. (a) Structure of an ice-templated sample featuring three distinct zones with pore dimensions depending on the processing conditions. (b) Maximum compressive strength achieved by freeze-casting at a cooling rate of 5 °C/min *vs.* porosity, including the comparison of porous hydroxyapatite scaffolds with compact bone and literature values. (c–f) SEM images of porous hydroxyapatite scaffolds with 64% porosity (cross-section parallel to the ice front (c, d) and section perpendicular to the ice front (e, f)). Adapted with permission from ref. 59. Copyright © 2006 Elsevier.

aqueous colloidal suspensions (either ceramic, metallic or polymer-based), followed by defrosting [59,60]. When ceramic composites are employed, a purely inorganic material can be obtained upon high temperature calcination of the composite scaffold to remove the organic phase [61]. During the freezing process, ice crystallization segregates the solutes dispersed in the aqueous phase from the ice phase, resulting in structures characterized by "walls" or "fences" of matter enclosing ice crystals (Fig. 3) [57,62]. Subsequent drying, involving simple thawing or freeze-drying, results in cryogels that contain macropores corresponding to the empty areas left by the ice crystals. Thus, the microstructure of the scaffold is a negative replica of ice before drying [63]. It is worth noting that the use of freeze-drying instead of simple thawing avoids drying stresses and shrinkage, which usually lead to crack formation and warping [59].

The morphology of the macroporous structure can be further tuned by controlling the freezing conditions, such as temperature or the direction of sample immersion into the cryogenic fluid. Lamellar thickness, inter-lamellar spacing, bridge density or surface roughness can thus be tailored to achieve the desired microstructure [64]. By controlling the growth direction of ice crystals, materials with a preferential porosity orientation and highly sophisticated structures can be prepared [59,65,66]. Therefore, unidirectional freezing can be employed for the production of different types of morphologies. Tamon et al. were arguably the first to use unidirectional freezing with silica gels, for the preparation of honeycomb-like scaffolds after the pseudosteady state growth of ice crystals [67,68]. A different method was used for the directional freezing of ceramic slurries using polytetrafluoroethylene molds placed between two copper cold fingers [63], typically resulting in scaffolds with open interconnected macropores, ranging from 20 to 100 μm in their smallest dimension and 50 to 500 μm in the largest one. Interestingly, the speed of the solidification front can be tuned through the temperature of the cold fingers, thereby defining the size of the obtained ice crystals. Using this procedure, materials with three distinct porous zones were obtained (Fig. 4), depending on the distance to the cold finger, with varying porosity. The formation of heterogeneous pores along the scaffold can be prevented by continuous immersion into liquid nitrogen at a constant rate [62]. The ice front is thereby maintained at a constant distance from the nitrogen level during immersion, leading to homogeneous porous structures [69].

Del Monte et al. introduced the term "ice segregation induced self-assembly" (ISISA), to describe this unidirectional freezing bottom-up approach and employed this technique to aqueous gels made of colloidal silica, PVA solutions, PEG-based hydrogels or chitosan/multi-walled carbon nanotubes (MWCNT) and chitosan/carbon nanofibers (CNF) composites (Fig. 5) [57,58,70–75]. The authors additionally demonstrated that ISISA is a versatile and biocompatible technique allowing the incorporation of enzymes or liposomes into the hierarchical materials [70,76]. Another major advantage of unidirectional freezing is that it offers the possibility to encapsulate living cells within the 3D scaffolds [77]. Scaffolds with pore sizes ranging from 25 to 90 μm and 85% porosity were achieved by varying the freezing rate.

The chemical composition of ice-templated scaffolds can also be tailored to achieve different microstructures. Aging of the gelling solution is critical, as soft hydrogels result in microhoneycombs, whereas firmer hydrogels form fibers with polygonal cross-sections (Fig. 6) [78]. Additionally, slurry concentration and particle size also affect the porosity thickness/layer thickness and the pore morphology [64]. Metallic nanoparticles, such as gold nanoparticles, are also compatible with ISISA and their incorporation has been shown to affect the microporous morphology of the scaffolds [69]. The viscosity of the solution or the gel strength of polymer-based hydrogels also affect the microporous structure, varying from lamellar-type to cellular-type morphologies, as the strength of the network increases. It has been observed that, when using polymers, their molecular weight influences the size of the crystals and smaller ice crystals are observed as the molecular weight increases. Ice-templating can also enhance the mechanical properties of scaffolds made of colloidal particles in the presence of polymers and crosslinkers [79]. In this approach, cross-linking takes place in the frozen state, where the exclusion from growing ice consolidates particles and polymer into the walls

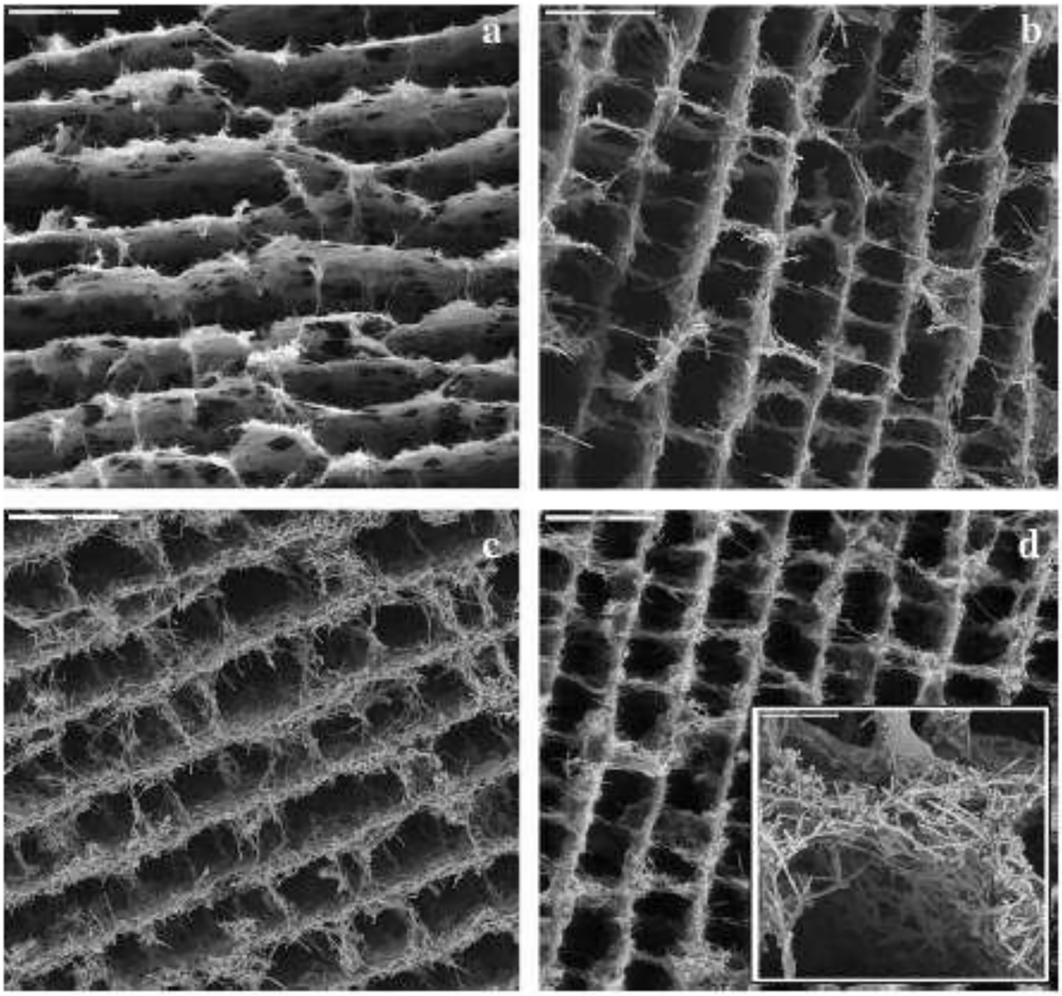

Fig. 5. SEM micrographs of cross-sectioned MWCNT/chitosan scaffolds with different MWCNT concentrations: 66 wt% (a), 80 wt% (b) and 89 wt% (d). Scale bars = 20 μm. The inset shows interconnected MWCNTs forming the walls of the scaffold (scale bar is 5 μm). Reprinted with permission from ref. 71 (J. Phys. Chem. C 2007, 111, 15, 5557–5560) Copyright (2007) American Chemical Society.

of the scaffold, yielding elastic composite scaffolds due to the formation of connections by the cross-linked polymeric mesh.

3.4. Supercritical fluids (SCFs)

Gas foaming of polymers or composites using supercritical fluids (SCFs), such as supercritical CO_2 ($scCO_2$) or nitrogen, can be used to fabricate 3D porous scaffolds with controlled pore structure, with no need for harmful organic solvents, incompatible with cells and biological tissues [80]. For the same reason, the working conditions during foaming with SCFs are compatible with the incorporation of biomolecules such as growth factors or antibacterial agents [81–83]. Therefore, the use of supercritical fluids represents a green, low cost alternative for scaffold fabrication.

When working with $scCO_2$ for polymer processing, pressure and temperature are maintained above the critical point of CO_2

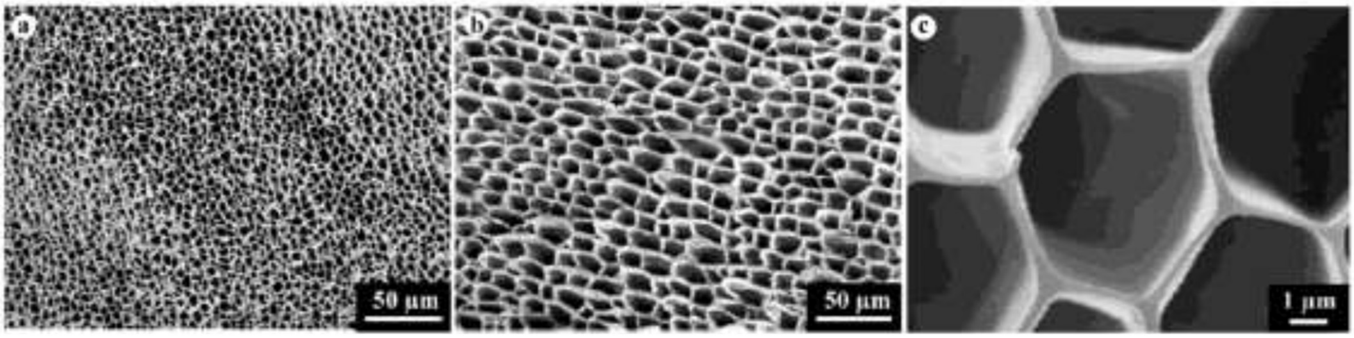

Fig. 6. SEM images of the cross-sections of silica gel microhoneycombs with different macropore sizes, prepared at 77 K using different immersion rates of 20 cm/h (a) and 6 cm/h (b). (c) High magnification image of the microhoneycombs. Adapted with permission from ref. 78, (Chem. Mater. 2005, 17, 3, 683–689) Copyright (2005) American Chemical Society.

Table 2
Processing conditions and resulting pore size and porosity of scaffolds prepared via SCFs technology.

Scaffold composition	Blowing agent	Foaming T (°C)	Saturation pressure (MPa)	Soaking time (h)	Depressurization (MPa/min)	Pore size (μm)	Porosity (%)	Ref.
PCL	CO_2	37	10	0.5	1.5	50–200	62	[82]
	CO_2	40	20	1	4	87–525	60–75	[97]
	CO_2	30–40	10–20	–	0.1–2	110–1500	–	[85]
	CO_2/ethanol	35–45	12.3–20.5	–	–	50–80	–	[86]
	CO_2	30–40	10–18	–	0.1–2	150–340	40–70	[83]
	CO_2/organic solvent	50	20	1	Two step venting/foaming	50–1500	–	[91]
				17		400–700		
PCL/TZ	CO_2	44	150	–	4200	40	47.5	[80]
PCL/TZ/HA		80					35.3	
		100				200	39.5	
PCL	CO_2	45	20	17	Two step non-isothermal	500–700	82–84	[81]
PCL-Eugenol					Vessel venting	500–700	82–84	
					Single non-isothermal	80	74	
PCL	CO_2	40	20	1–17	Two step depressurization	50	65–70	[84]
PCL-HA		45				100	80	
	CO_2/EL	40				100–200	80–85	
		45				100–50		
						200–400		
	CO_2/EA	40				<100	70	
						200		
		45				100	80	
						200–300		
PCL/silica	CO_2	160	16	2	–	40–930	50–60	[92]
PLGA	CO_2	–	5.51	48	–	190–440	85–97	[95]
		30–35	25	1	–	250	81	[121]
PLGA/HA/Collagen	CO_2	35–60	8–30	1.5	–	97–730	48–92	[115]
PLA	CO_2/EL	35	20	1.5	Fast (30 s) or	50–500	–	[96]
		40			Slow (360 s)	25–150		
	CO_2/acetone	60–80	14–61	–	–	5–400	–	[87]
PDLLA	CO_2	35	20	0.5	0.5	200–400	56–67	[118]
			17.32	–	–	250	70	[120]
			23.2	–	2.32	10–1200	–	[116]
					0.77	10–1000		
					0.52	10–800		
					0.39	10–600		
CS	CO_2	37	6–16	–	1	30–40	–	[98]
Elastin	CO_2	37	3–15	0.5	–	14–5	–	[99,102]
		37	0.1–6			20–80		
Chitin	CO_2	80	6.5–12.5	3	–	60–160	–	[100]
Gelatin	CO_2	26	5–8-11	2	–	300–25-22	–	[101]
Gelatin/CS		40	100			50		

($T_c = 31.1$ °C, $P_c = 73.8$ bar) to saturate the polymer with $scCO_2$, thereby reducing the apparent glass transition temperature or melting point of the polymer to its processing temperature [84]. During quenching by depressurizing or increasing temperature, thermodynamic instability results in supersaturation of dissolved CO_2 in the polymeric matrix and pore nucleation takes place, with pores growing until the polymer vitrifies or the matrix viscosity is increased. Several parameters such as pressure, temperature, supercritical fluid composition and depressurization profile play a key role in defining the porosity and pore size distribution of the scaffolds (Table 2, Fig. 7) [81,84–86]. When dealing with semi-crystalline polymers, CO_2 sorption facilitates chain mobility and the rearrangement of polymer chains becomes easier, usually reducing the crystallization temperature [87]. The melting temperature is also likely affected because polymer swelling induces a tendency of the chains to rearrange into more extended configurations, disturbing the crystalline structure. To increase the solubility of crystalline polymers, organic solvents can be incorporated to the mixture [88], which can also be combined with other strategies, such as thermally induced phase separation, for the preparation of porous scaffolds [89–91]. The main weakness of this technique is the reduced pore interconnectivity, which can again be increased by addition of compatible organic solvents, micro or nanoparticles, or plasticizers [81,92,93]. Another disadvantage of foaming using SCFs, which is particularly relevant for the use of these materials as cell culture scaffolds, is the formation of a dense nonporous skin attributed to the rapid diffusion of the fluid out of the edges of the sample [87]. This issue can be solved by mechanical removal of such a skin, after scaffold formation. Bhamidipati et al. and Reverchon et al. nicely reviewed the use of carbon dioxide for the preparation of 3D porous scaffolds, following different processing options such as CO_2 into gas foaming, SCF-assisted phase separation or SCFs emulsion templating [94,95]. Even if interesting materials result from the application of these approaches, we focus on scaffolds produced by foaming with SCFs to achieve a more homogeneous and well organized porosity. In an early study of the use of SCF foaming toward porous scaffolds for tissue engineering [96], poly(D,L-lactic-*co*-glycolic acid) (PLGA) was the polymer of choice and porous scaffolds were obtained with pore sizes around 100 μm and porosities up to 93%, using CO_2 at 5.5 MPa and room temperature. In a subsequent work by the same authors, NaCl particles were incorporated into the formulation to increase the porosity and interconnectivity of the scaffolds [96]. The successful adhesion and proliferation of smooth muscle cells within the scaffolds revealed their potential for tissue engineering.

Salerno et al. extensively applied the SCF technology to porous scaffolds using typical polymers for biomedical applications, such as polylactic acid (PLA) or polycaprolactone (PCL) [80,81,84,97,98].

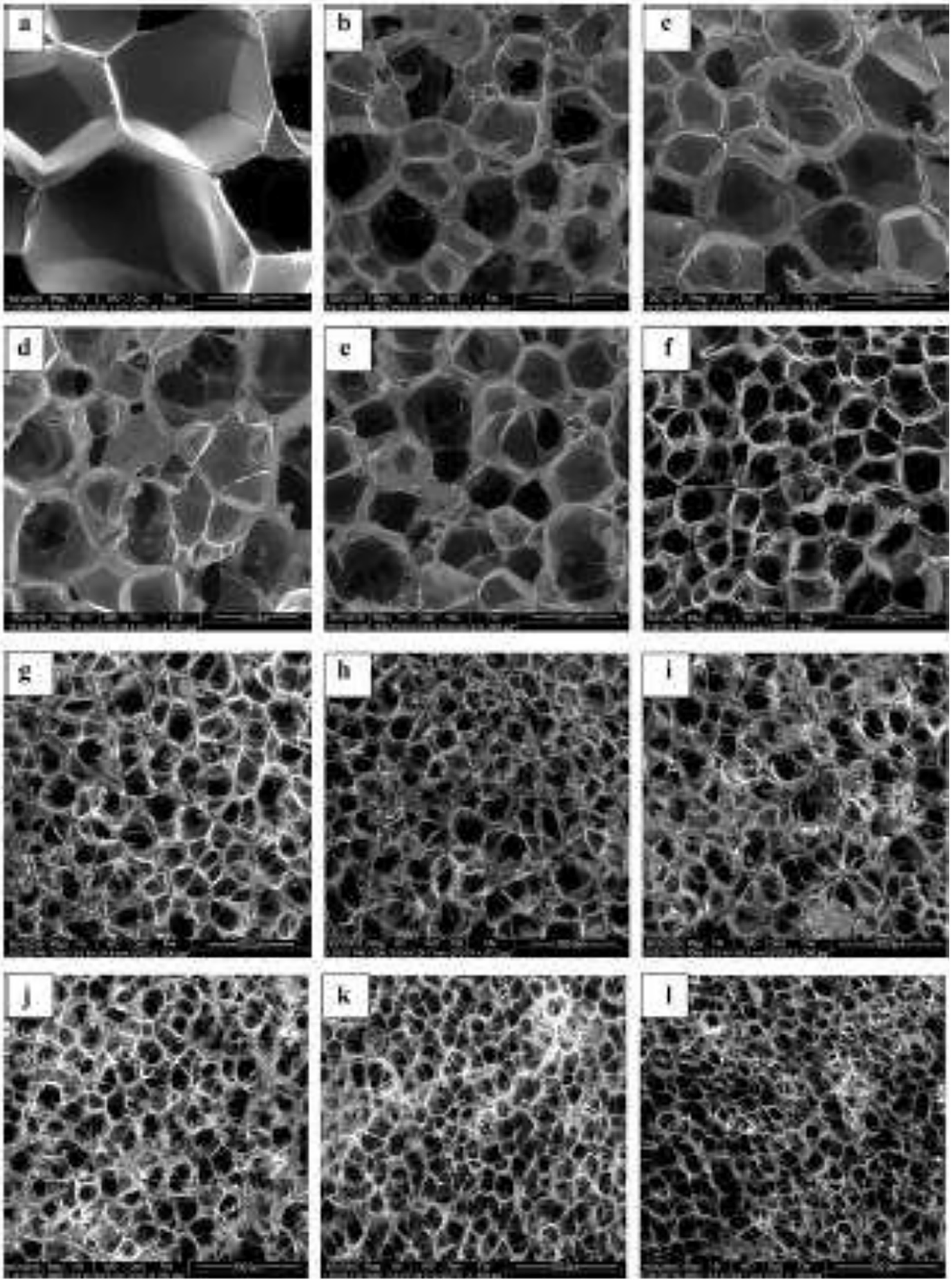

Fig. 7. Environmental SEM micrographs of PLGA/HAp/collagen scaffolds prepared at different saturation pressures. Scaffolds were prepared at 40 °C for 45 min at: a) 8 MPa, b) 10 MPa, c) 12 MPa, d) 14 MPa, e) 16 MPa, f) 18 MPa, g) 20 MPa, h) 22 MPa, i) 24 MPa, j) 26 MPa, k) 28 MPa, and l) 30 MPa. Reprinted with permission from ref. 86. Copyright © 2011 Elsevier.

Table 3
Characteristics, main advantages and drawbacks of 3D scaffolds produced by different fabrication techniques.

Fabrication technique	Pore size (µm)	Interconnectivity	Reproducibility	Advantages	Drawbacks	Applications in TE
Inverse Opals	0.01–200	Tunable by thermal annealing (High)	High	• High level of organization • Homogeneous porosity • Tunable interconnectivity • Diversity in chemical composition • Possible post-functionalization to enhance biocompatibility	• Need for materials with enough mechanical strength • Full infiltration of precursor solution to avoid scaffold collapse • Removal of the colloidal assembly may damage scaffold structure	Bone TE [33,106–108] Cardiac TE [137–140] Neural cell growth [25,124–128]
Emulsion Templating	0.1–100	Tunable by chemical composition (Poor to high)	Poor/Medium	• Heterogeneous porosity (similar to natural tissue morphology) • Possibility to couple with colloidal particles for controlled porosity • Diversity in chemical composition • Fast process	• Hard to obtain pore/channel size homogeneity • Low reproducibility • Need for organic solvents • Need for co-surfactants to open porosity	Bone TE [109,110] Neural cell growth [42,129,130]
Ice Templating	10–500	High	High	• Wide variety of materials • Biocompatible • Easy template removal • Incorporation of enzymes, liposomes, living cells • Tailored microstructure (honeycomb, lamellar, cellular) • Good mechanical properties • Gradient porosity	• Cell proliferation limited to few layers • Limited sample size • Long processing time for big samples	Bone TE [63,111–114] Neural cell growth [131–133]
SFCs	50–500	Reduced/Poor	Medium	• Avoids harmful organic solvents • Compatible with biomolecule incorporation (growth factors, antibacterial agents) • Low cost • Good mechanical properties	• Formation of dense nonporous skin • Limited pore interconnectivity • CO_2 solubility in the foaming phase limits application	Bone TE [80,81,115–122]

Biodegradable PCL-based scaffolds were prepared *via* supercritical CO_2 foaming, in combination with thermoplastic zein (TZ) and HAp particles [80]. By modulating composition and foaming temperature (T_F), the porosity of the scaffolds could be controlled. If foaming takes place at a T_F above the melting temperature, pores nucleating in the PCL phase coalesce before crystallization of the polymer matrix and bigger pores are formed. At even higher temperature, larger pores (200 µm) grow due to a lower stiffness of the matrix. To preserve heat-labile molecules, supercritical CO_2 foaming can be also performed at low temperature, known as "solid-state foaming" [97]. However, this approach becomes more difficult in the case of semi-crystalline polymers, where the highly ordered structure reduces the diffusion of $scCO_2$ and polymer plasticization. Therefore, the resulting scaffolds show inhomogeneous pore structures and low porosity. This is the case of PLA, an interesting choice toward biodegradable scaffolds, also affected by CO_2-induced crystallization during the sorption stage. To circumvent these problems,

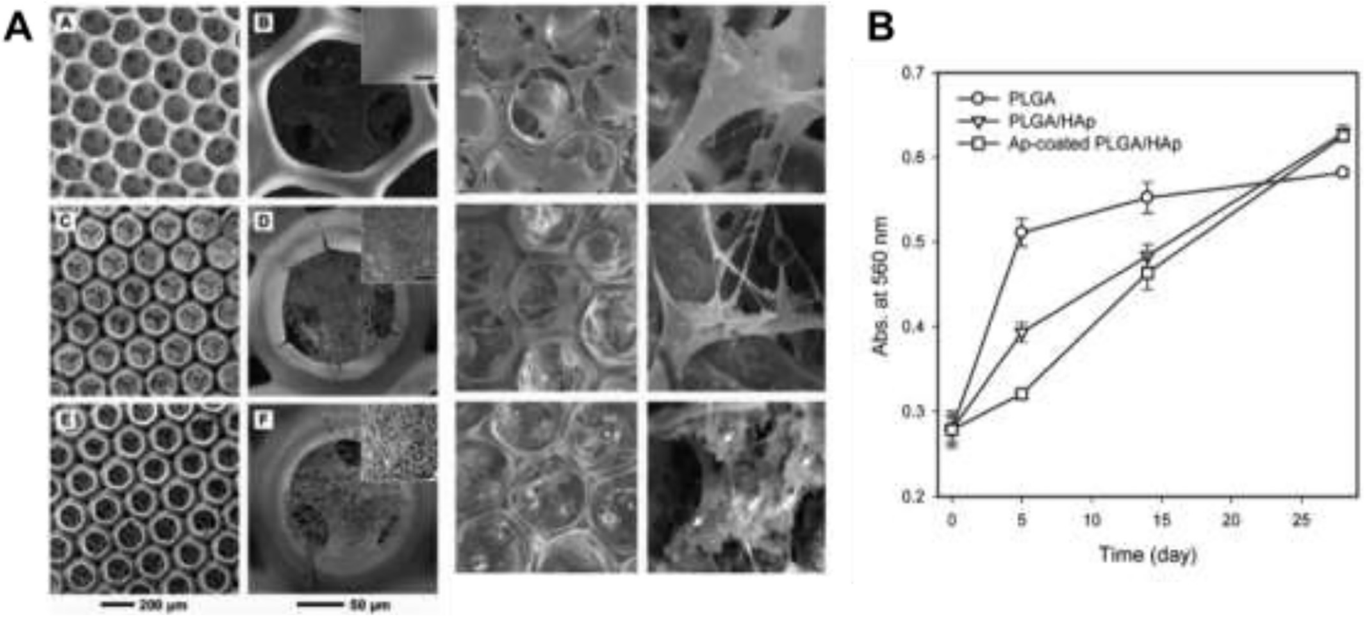

Fig. 8. A) SEM images of scaffolds made of: PLGA (A, B), PLGA/HAp (C, D), and HAp-coated (E, F). SEM images on the right-hand side panels show the respective scaffold cultured with preosteoblast cells. B) Proliferation of preosteoblasts cultured on various scaffolds (n = 3). Adapted with permission from ref. 109, Langmuir 2010, 26, 14, 12,126–12,131. Copyright (2010) American Chemical Society.

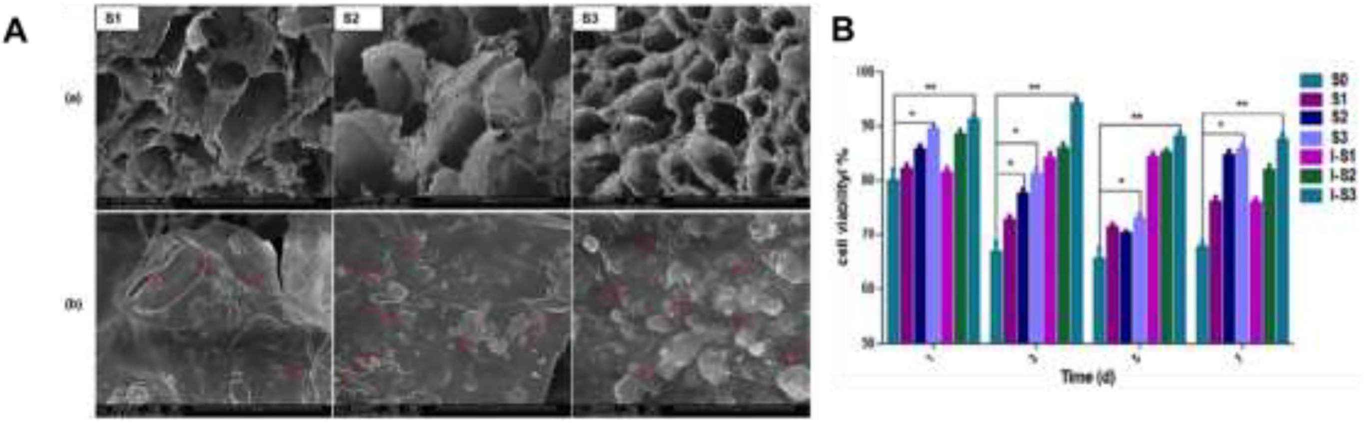

Fig. 9. A) SEM images of *in vitro* mineralized HaP/carboxymethyl cellulose/PLGA scaffolds with different wt% of nHAP: S1 (0.75 wt%), S2 (1.5 wt%), S3 (3.0 wt%). The red arrows point toward inorganic apatite crystals. B) Osteoblast proliferation in various scaffolds, by CCK-8 assay. Adapted with permission from ref. 110. © 2020 Elsevier.

solid-state foaming of PLA can be performed in the presence of ethyl lactate, resulting in scaffolds with homogeneous morphology and pore sizes ranging from 50 to 500 μm (Fig. 7) [97].

When using hydrophilic polymers, such as hydrogels, pore formation takes place by dissolving CO_2 in the aqueous phase [99]. Hydrogel foaming can be applied to either water-insoluble polymers such as chitin or elastin, which form swollen dispersions in aqueous solution, or to water-soluble polymers such as chitosan or gelatin, being also compatible with the incorporation of cross-linkers such as glutaraldehyde or genipin [99–103]. It is worth noting that the drying step after foaming is critical to maintain the porous structure. Air-drying can produce extensive shrinking and collapse of the porous structure, thus mild freeze-drying is generally the technique of choice to produce stable porous materials [102]. The increase in processing pressure leads to a reduction in pore size, which also depends on hydrogel composition, cross-linking degree and processing temperature [100,103]. This processing technique reduces also the pore wall thickness, as compared to conventional hydrogels, and creates channels through the 3D structure [100]. Another advantage is that this type of foaming avoids the formation of a skin layer, commonly observed in hydrogel processed by traditional methods [99].

4. Porous scaffolds for tissue engineering

3D scaffolds with hierarchical porous structures have received considerable attention in the biomedical field, with a special focus on tissue engineering applications. As mentioned in the previous section, certain requirements are to be fulfilled by the scaffolds, to support tissue growth and regeneration. The fabrication techniques discussed in this review open the way toward the design of porous scaffolds with tailored features to support the target tissue. Table 3 summarizes the main characteristics of scaffolds produced by different processing routes, as well as the main advantages and disadvantages to be faced in each case. This section highlights the most recurrent tissues engineered on the basis of well-organized porous scaffolds.

4.1. Bone tissue engineering

In tissue regeneration, the cells involved in organ repair must reach the damaged region, so as to create an extracellular matrix that induces the formation of replacement tissue [104]. The healing process can be supported by porous scaffolds that facilitate cell adhesion and growth, while allowing the diffusion of oxygen and nutrients to the adhered cells [105]. In order to mimic the same environment as that in real bone, the scaffold ought to feature optimal porosity for osteoblasts to properly diffuse, and contain osteogenic factors to promote bone repair [106]. The supporting scaffold is usually loaded with derivatives from the apatite family, which are known to induce cell differentiation in biological tissue [107]. We review in this section the use of various scaffolds introduced above.

Colloidal inverse opals are appealing for tissue regeneration because their physicochemical properties can be readily controlled [108]. One of the main advantages is the possibility to tailor the surface of the inner cavities by either preparation of sol-gel composites and/or post-functionalization [33]. Although both strategies can promote cell differentiation when growth factors are included, it is important to take into consideration that sol-gel processes will determine both the chemical and mechanical properties of the porous construct, whereas post-functionalization would mainly change the functional groups on the pore surfaces [107,109]. As an example of the importance of cell-differentiation factors, Choi et al. studied the enhanced differentiation of osteocytes at PLGA scaffolds loaded with HAp (Fig. 8) [109]. Over a 4-week period, preosteoblasts showed a lower proliferation rate in non-coated PLGA scaffolds, as compared to the constant rate observed within a PLGA/HAp porous network. The failure to significantly increase the number of proliferated cells in the coated scaffold was explained by changes in preosteoblasts differentiation, due to interactions of the precursor cells with bone growth factors present in the functionalized porous matrix.

On the other hand, HIPE template scaffolds have the advantage of allowing the introduction of precursors within solvents of different polarity. The application of emulsions as templates not only provides control over pore morphology but also allows the addition of water-soluble materials to an inorganic matrix solubilized in the continuous phase [110]. In an interesting example, PLGA hybrid scaffolds were functionalized with nanohydroxyapatite (nHAp), previously mixed within the aqueous phase. After hardening the structure by UV-crosslinking, the growth factors were entrapped into the walls of the voids, ultimately resulting in more extensive cell differentiation than for non-functionalized matrices (Fig. 9). Pickering emulsions have also been used to synthesize heterogeneous porous scaffolds by mixing PMMA beads with a polymeric emulsion containing droplets smaller than the colloidal beads [111]. Upon self-assembly and annealing of the colloidal particles, the template was impregnated with a HIPE of divinyladipate and cross-linked to acquire a polyester network. Biocompatibility and cell adhesion of human osteoblasts were found to be superior for scaffolds templated by Pickering emulsions than for other HIPE scaffolds. The presence of bigger pores resulting from the removal of colloidal particles was proposed to be responsible for the enhancement of the overall cell viability.

A limiting factor of scaffolds for bone regeneration is still their poor mechanical response associated with their porous nature. Therefore, their applications are often limited to the regeneration of bones

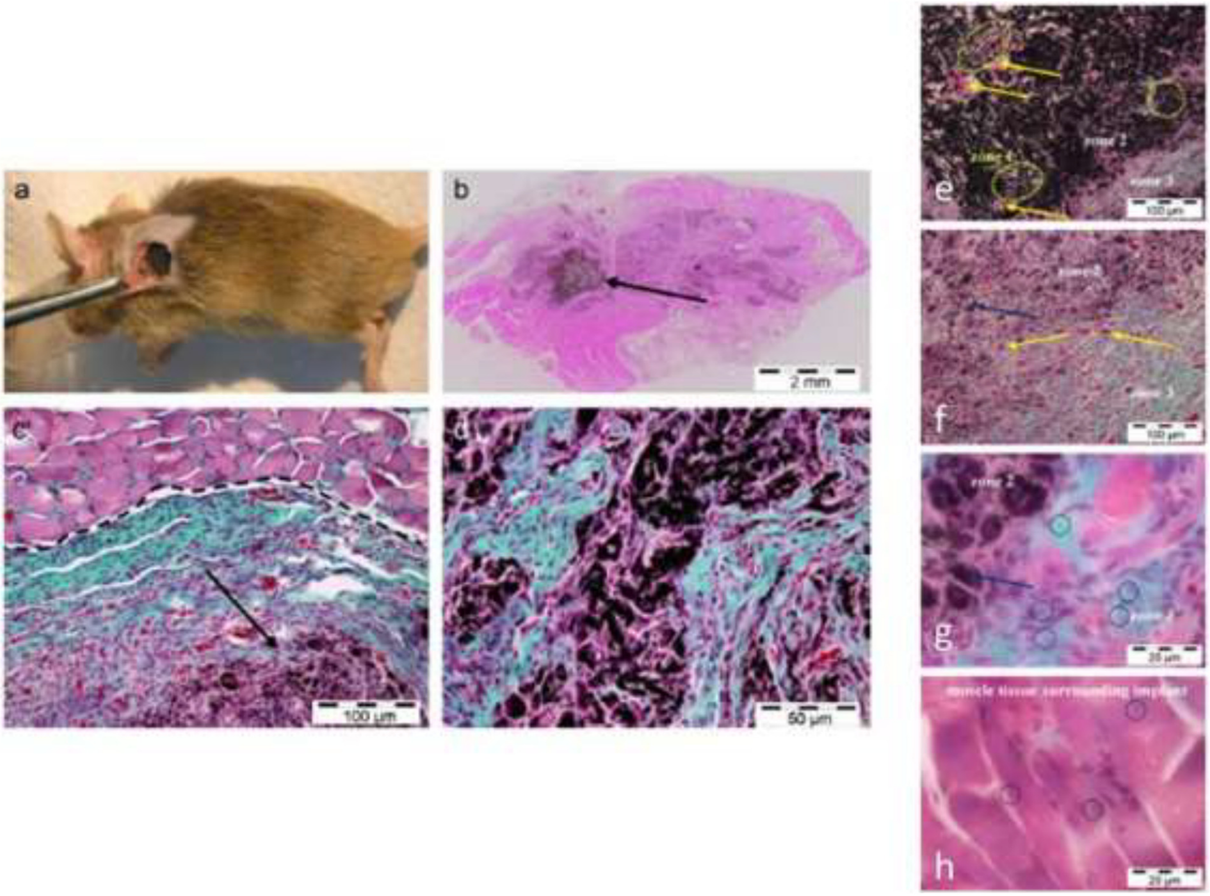

Fig. 10. (a) Surgery implantation of rhBMP-2 adsorbed MWCNT/chitosan scaffolds into mouse subcutaneous muscular pocket. (b) Optical micrograph showing regenerated bone tissue and a fraction of MWCNT/chitosan scaffold. (c) Optical micrograph showing a detail of regenerated bone tissue (collagen expressing cells in blue-green, muscle tissue in pink). (d) Optical micrograph showing a detail of remaining scaffold plenty of fibroblasts (purple), prior to its disassembly and colonization by collagen expressing cells (blue-green). (e–g) Optical micrographs showing 3 zones observed after 3 weeks of scaffold implantation with intact scaffold (green circles), non-differentiated fibroblasts (purple cells) and fully disassembled scaffold, respectively. (h) Optical micrograph of few single MWCNT/chitosan dispersed within muscle tissue surrounding the implant. Adapted with permission from ref. 112. Copyright © 2007 Elsevier.

submitted to low stress. To circumvent this drawback, stronger porous scaffolds are needed. The ice templating approach can be employed for the preparation of HAp-based porous scaffolds with good mechanical properties for bone tissue engineering [63]. Inspired by nacre, layered materials have been developed by controlled unidirectional freezing of ceramic suspensions. These porous scaffolds are then filled with a selected second phase (epoxy or metallic) to obtain dense composites. Scaffolds with well-defined pore connectivity and open porosity to allow bone ingrowth were achieved. The resulting scaffolds showed mechanical properties similar to those of bone, despite of their high porosity. Following the ISISA approach, del Monte and coworkers prepared MWCNT/chitosan scaffolds with high MWCNT loadings (up to 89 wt%), featuring a well-defined 3D microchannel porous structure for supported cell growth [112]. Efficient cell growth and proliferation was observed after 4 day cell culture within the scaffolds, both lateral and in depth. However, as also observed for inverse colloidal crystals, cell proliferation within the scaffold is limited to just a few layers of cells since nutrient diffusion deeper inside the material is hindered. The authors studied the evolution of mouse-derived muscle myoblasts (C2C12) to an osteoblastic lineage both *in vitro* and *in vivo* (following implantation of the scaffolds in muscle tissue), in the presence of the recombinant human bone morphogenic protein-2 (rhBMP-2), an osseoinductor protein (Fig. 10). Bone tissue regeneration was observed after 3 weeks along with scaffold degradation, which was replaced by cells. Following this work, similar scaffolds were prepared by incorporating HAp [113]. The scaffolds were formed by interconnected MWCNT/chitosan sheets arranged in parallel layers crossed by pillars and with homogeneously distributed HAp clusters at the internal surface of the macrostructure. *In vitro* experiments proved the potential of these scaffolds for bone tissue growth upon differentiation of C2C12 cells toward collagen-expressing cells. Similar scaffolds with pore size ranging between 20 and 150 μm have also been prepared using doped MWCNTs, to study their effect on cell viability of periosteum mesenchymal stem cells [114]. The effect of doped MWCNT was more pronounced for longer times of cell culture and nitrogen-doped MWCNTs were less effective than oxygen-doped ones, indicating that the functionality of MWCNTs was important for their affinity to specific cells.

Ice-templating has also been employed for the preparation of HAp scaffolds with gradient channel structures displaying a capillary behavior that favors transport of water and nutrients within the scaffold (Fig. 11). [115]. To generate the gradient, lamellar ice crystals were grown preferentially from a central copper rod, outward to the plastic mold used during the freezing process. Therefore, an increasing channel width was formed from the center toward the edge of the scaffold. In this case, scaffolds with self-seeding ability when in contact with mesenchymal stem cells (MSCs) were prepared, and spontaneous capillary flow was observed and attributed to the presence of gradient channel structures, showing promising properties for bone tissue-engineering applications.

Scaffolds processed using SCF technology can also meet the requirements for use in bone tissue engineering applications. For example, PCL-

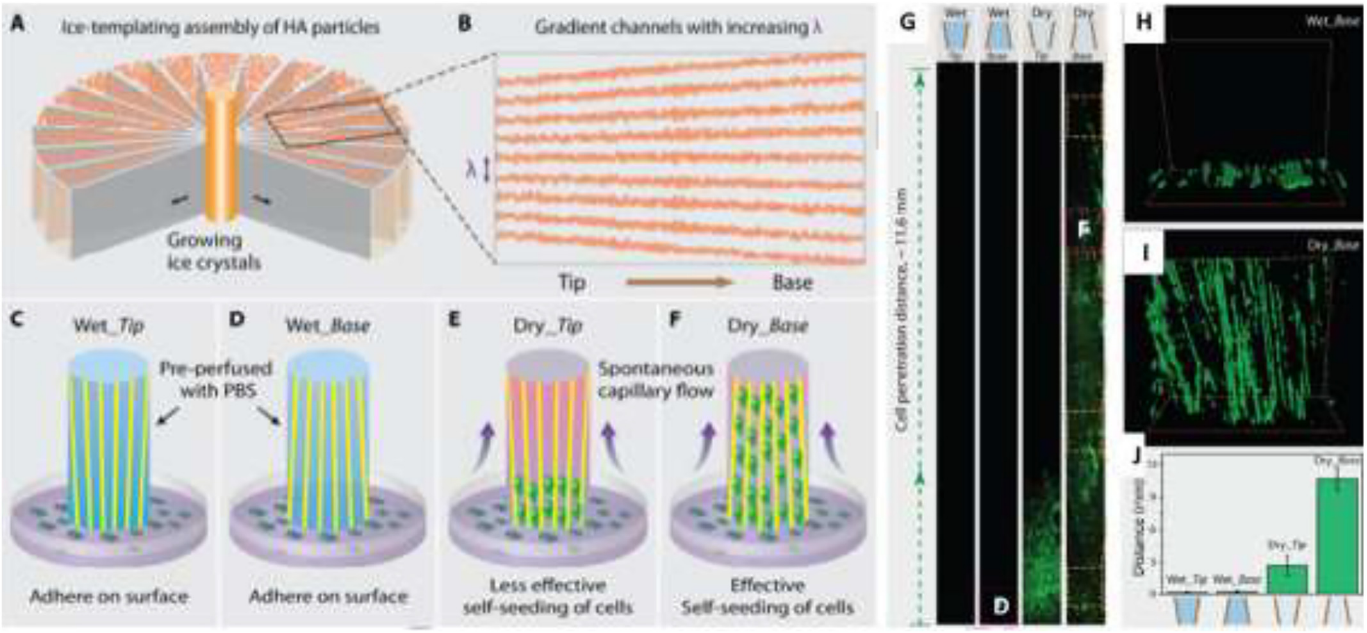

Fig. 11. (A, B) Scheme of the fabrication of the gradient ceramic scaffold and cell-seeding experiment. Fabrication of the scaffold where a ceramic slurry is frozen from the cold finger at the center, creating a lamellar structure oriented parallel to the freezing direction. (C–F) Study of the capillary effect of the gradient channels on seeding cells. (G–J) Cell-seeding experiments on wet and dry gradient scaffolds: fluorescent images after seeding cells (G), 3D confocal fluorescent image showing cells for wet base and dry base (H, I), statistical data about the penetration distance of cells (J). Adapted with permission from ref. 115. Copyright © 2015 Elsevier.

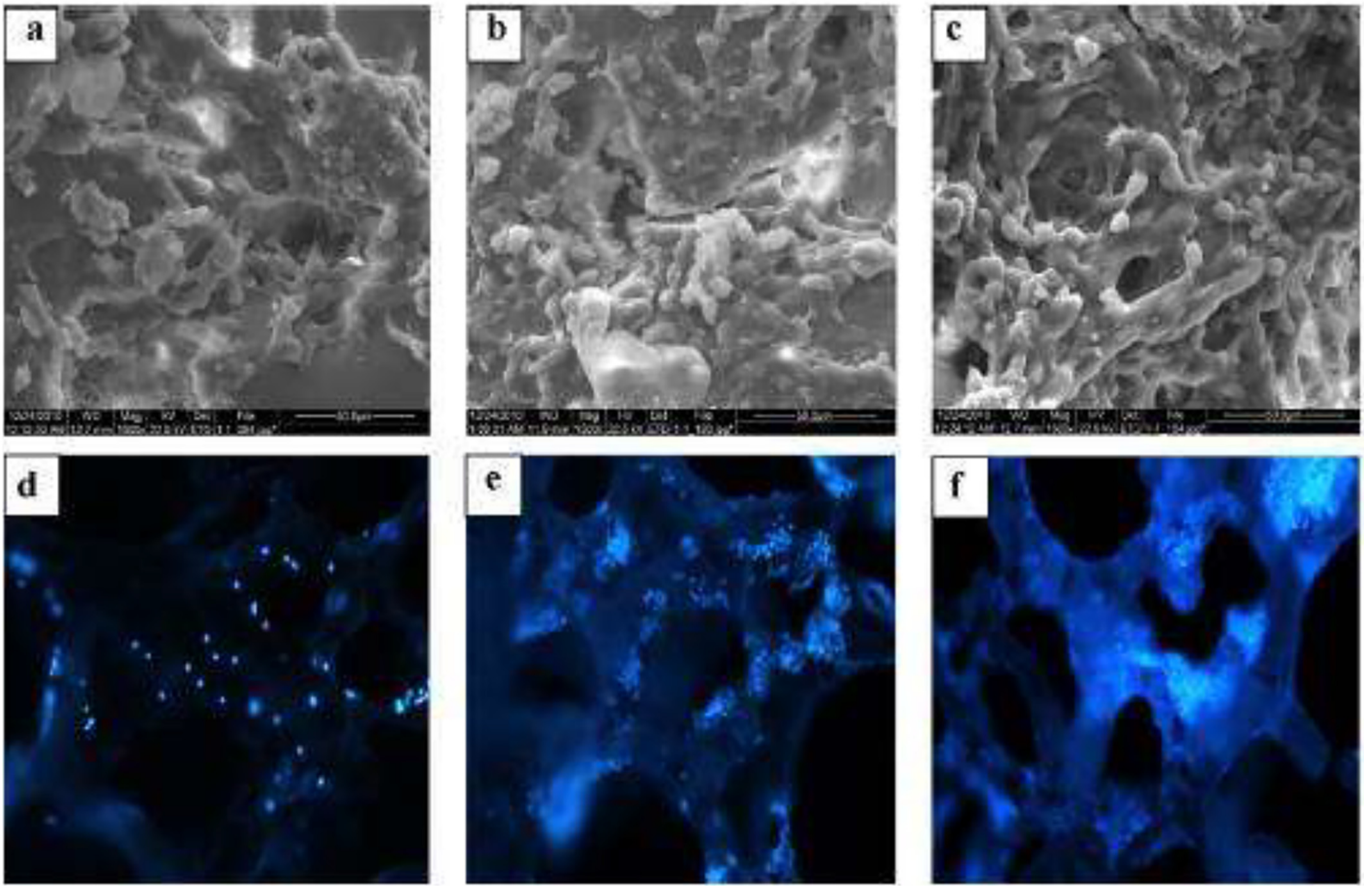

Fig. 12. Environmental SEM micrographs and confocal scanning laser microscopy photographs of cell-seeded PLGA-collagen-HAp scaffold after culture for 3 days (a, d), 7 days (b, e), and 14 days (c, f). Reprinted with permission from ref. 86. Copyright © 2011 Elsevier.

TZ blends have been combined with HAp for the preparation of 3D porous scaffolds for bone repair [80]. Composites processed at a T_F of 100 °C achieved suitable porosity (39.5%), pore size distribution (200 μm), mechanical properties (with elastic compression modulus higher than 10 MPa) and biodegradability for bone tissue engineering. Extraction of TZ resulted in scaffolds with 60% overall porosity and open macropore structure. Biocompatibility studies with osteoblast-like MG63 and human mesenchymal stem cells (hMSCs) showed good cell adhesion and colonization. The incorporation of eugenol to $scCO_2$ increased PCL plasticization, thereby reducing its viscosity and formation of scaffolds with larger pores [81]. By adjusting the depressurization profiles, scaffolds with up to 84% porosity and mean pore size of 530 μm were obtained. Incorporation of eugenol also improved pore interconnectivity and water permeability in the scaffolds. Interestingly, *in ovo* CAM assays confirmed the ability of the scaffolds to promote cell and tissue growth. Moreover, the antimicrobial activity of eugenol could prevent bacteria adhesion after implantation.

An alternative formulation of scaffolds with PLGA/collagen/Hap was also prepared under supercritical conditions [86]. The authors studied the effect of saturation temperature, pressure and saturation time on the properties of the scaffold to achieve large pore sizes, ranging from 100 to 500 μm. These results revealed that this polymer composition is more sensitive to the processing conditions than other polymers, such as PCL. Cell growth studies confirmed osteoblast cell attachment and proliferation, as well as cell infiltration and migration deep into the 3D network (Fig. 12). The depressurization rate and the molecular weight of the polymer can also affect the properties of PLA-based scaffolds [116]. Rapid depressurization resulted in scaffolds with homogeneous pore distributions, whereas a lower depressurization rate leads to a wider pore size distribution and more interconnected pores. Regarding the mechanical properties, an increased depressurization rate produces scaffolds with larger Young's modulus due to the increased relative density of the scaffolds. PLA-based scaffolds foamed by supercritical fluids showed mechanical properties similar to bone when high molecular weight (57 kDa) PLA was used [116].

3D porous scaffolds can be employed to simultaneously support cell and tissue growth, while delivering specific growth factors or drugs to target a particular disease, or to serve as models to test the efficacy of drugs in 3D cell models. The scaffolds can also protect the drug against environmental factors such as moisture, temperature or pH, which can jeopardize its therapeutic efficacy [117]. As mentioned above, a simple way to process polymers while preserving the bioactivity of entrapped drugs, growth factors or other relevant biomolecules is the use of supercritical CO_2, so as to avoid the use of toxic solvents and high temperatures required for polymer melting. In an interesting example, chitosan-chondroitin sulfate nanoparticles were loaded with platelet lysate, an autologous source of growth factors (GFs) that provides several bioactive agents that promote bone regeneration, and then incorporated into PLA scaffolds produced by SCF foaming [118]. In a similar direction, Kanczler et al. prepared PLA-based scaffolds for the encapsulation of vascular endothelial growth factor-165 (VEGF) to prove that the release of GFs can stimulate the development of therapeutic neovascularisation [119]. A continuation of this work tackled bone regeneration by PLA scaffolds containing VEGF with human bone marrow stromal cells (hBMSC), implanted in a mouse femur segmental defect [120]. One of the main challenges in tissue engineering is related to vascularization within artificial scaffolds, and, in the case of bone, adequate blood supply is key toward a successful implant. Therefore, the incorporation of VEGF to modulate angiogenesis might address vascularization during bone repair. The presence of VEGF within scaffolds seeded with hBMSC resulted in significant bone regeneration, as compared to bare PLA scaffolds.

Bioactive glasses that can stimulate osteoblast proliferation and act as angiongenic factors, have also been incorporated within PLGA scaffolds for bone tissue engineering [121]. Such bioactive glasses can act as nucleation agents during foaming under supercritical conditions, thereby affecting pore formation, and have been explored as an alternative to the incorporation of GFs. The sustained release of bioactive lipids, together with calcium and silicon ions was shown to enhance biological activities such as adhesion, proliferation and osteogenic differentiation of rat bonemarrow-derived mesenchymal stem cells (rBMSCs), as well as the proliferative and *in vitro* angiogenic ability of human umbilical vein endothelial cells (hUVECs). *In vivo* analysis of the critical-sized rat calvarial bone defect model demonstrated that the scaffolds improved vascularized bone regeneration.

4.2. Neural cell growth

In order to fully understand how information is exchanged in the human brain, the study of synaptic interactions in the neuronal network is required, where neurons are to be localized in a 3D environment [122]. Current *in vivo* studies make use of animal models, which are poorly related to the human brain, while most *in vitro* techniques are still limited to unrealistic 2D planar cell culture systems [42]. Modern neuroscience is thus in need of novel scaffolds that can support neuronal differentiation while allowing the formation of the synaptic construct, to mimic a natural neuronal network. Research in this respect has focused on the implementation of biocompatible constructs to guide embryonic cells toward differentiation and growth of neuronal circuits [123]. However, the recreated networks lack a suitable 3D architecture, thus limiting the number of formed synapsis and hindering the communication of the overall neuronal system. To overcome these limitations, engineered 3D porous scaffolds have been recently used to achieve a spatially controlled synaptic neuronal system to obtain further insight into the signaling present in natural central nervous systems [122].

Inverse opals have been considered as support scaffolds for neuronal studies, again due to their ordered interconnected porosity [25]. The ordered structure of IOs facilitated studies on the effect of matrix chemical composition on nerve regeneration and tissue differentiation. As an example, Kuo et al. studied the viability of a polymer colloidal crystal composed of three different polymers [124]. By varying the polymer composition of the porous matrix, differences in cell adhesion, viability and stability of the solid support were observed, so that the impact of each individual component on the whole system could be understood. This study demonstrated that the overall biocompatibility of a scaffold not only depends on the chemical affinity but also on the mechanical properties of the porous matrix. Other works from the same group showed improved biocompatibility by functionalizing the pore surface with biomolecules (Fig. 13) [125–128]. By loading additional functional groups cell growth and differentiation were induced further, in comparison with the nude scaffold, which highlights the importance of the interactions between cells and the functional surface of the empty cavities. This technique opens up the path for a wide range of materials to be used as scaffolding materials, as biocompatibility can always be further improved by post-synthesis functionalization.

HIPE-templated porous matrices have also been tested for neuronal tissue engineering. In a work by Murphy et al., a comparison of different thiol-ene photo-polymerized materials was carried out to study their impact on the development of a neuronal network over a 3-day culture [129]. Through diverse staining techniques, neural precursor cells (NPC) were observed in all scaffolds. The effect of the supporting scaffold on the maturation of the cultured cells was monitored through the expression of vimentin, an intermediate filament protein present during the development of the central nervous system [130]. Subsequent staining results demonstrated the ability of all matrices to induce neural differentiation. To demonstrate the importance of the mechanical properties of the support structure toward long-term cell differentiation, a second work from the same group investigated the influence of a poly(ethylene glycol) diacrylate (PEGDA) poly-HIPE scaffold on the growth of two different neuronal cell lines (Fig. 14) [42]. To verify the obtained results, the scaffold was compared with other poly-HIPE scaffolds of similar morphology but with diverse elastic and storage moduli. Over a period

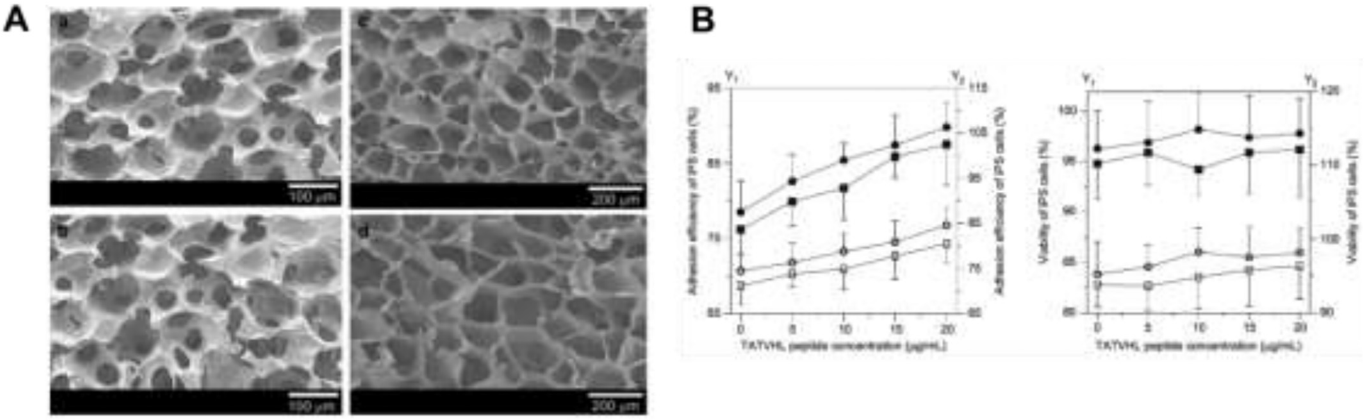

Fig. 13. A) SEM images of alginate/poly(γ-glutamic acid) (γ-PGA) ICC (a, b) and freeform scaffolds (c, d) with 1% (w/w) *Ca*. Ratios of alginate/γ-PGA: 2:3 (a, c); 3:2, (b, d). B) Adhesion efficiency and viability (respectively) of induced pluripotent stem cells (iPs) cultured in TATVHL peptide-grafted alginate/γ-PGA scaffolds. (●) ICC, alginate/γ-PGA = 2:3 (a); (■) ICC, alginate/γ-PGA = 3:2 (c); (○) freeform alginate/γ-PGA = 2:3 (b); (□) freeform alginate/γ-PGA = 3:2 (d). Adapted with permission from ref. 125. Copyright © 2012 Elsevier.

of 14 days, although PEGDA scaffolds showed limitations regarding cell imaging ability, they proved to be able to promote cell adhesion and differentiation faster than other comparable hydrogels, as their mechanical properties were prepared to be as similar as possible to that of mammalian brain tissue.

The ISISA approach has also been applied to the preparation of scaffolds for neural cell growth. Using this technique, free-standing, porous and flexible 3D graphene oxide (GOx)-based scaffolds were prepared with 80% porosity, uniform layer thickness of 100–120 μm, and pore dimensions from 150 to 180 μm in length and 40 μm in width [131]. Aqueous GOx suspensions were processed by ISISA and subsequently crosslinked using hexamethylene diisocyanate to reinforce the network. A thermal treatment (200 °C for 30 min) was then applied and the scaffolds were coated with poly-lysine. Their use for neural repair was evaluated by exploring the behavior of embryonic neural progenitor cells (ENPCs) on the 3D substrates (Fig. 15). Limited colonization was observed within the scaffolds, around 50 μm in depth, and neural cell growth and maturation were supported for 14 days *in vitro*. Interconnected neural networks conformed by both neurons and glial cells were obtained in the scaffolds, along with dendrites, axons and synaptic

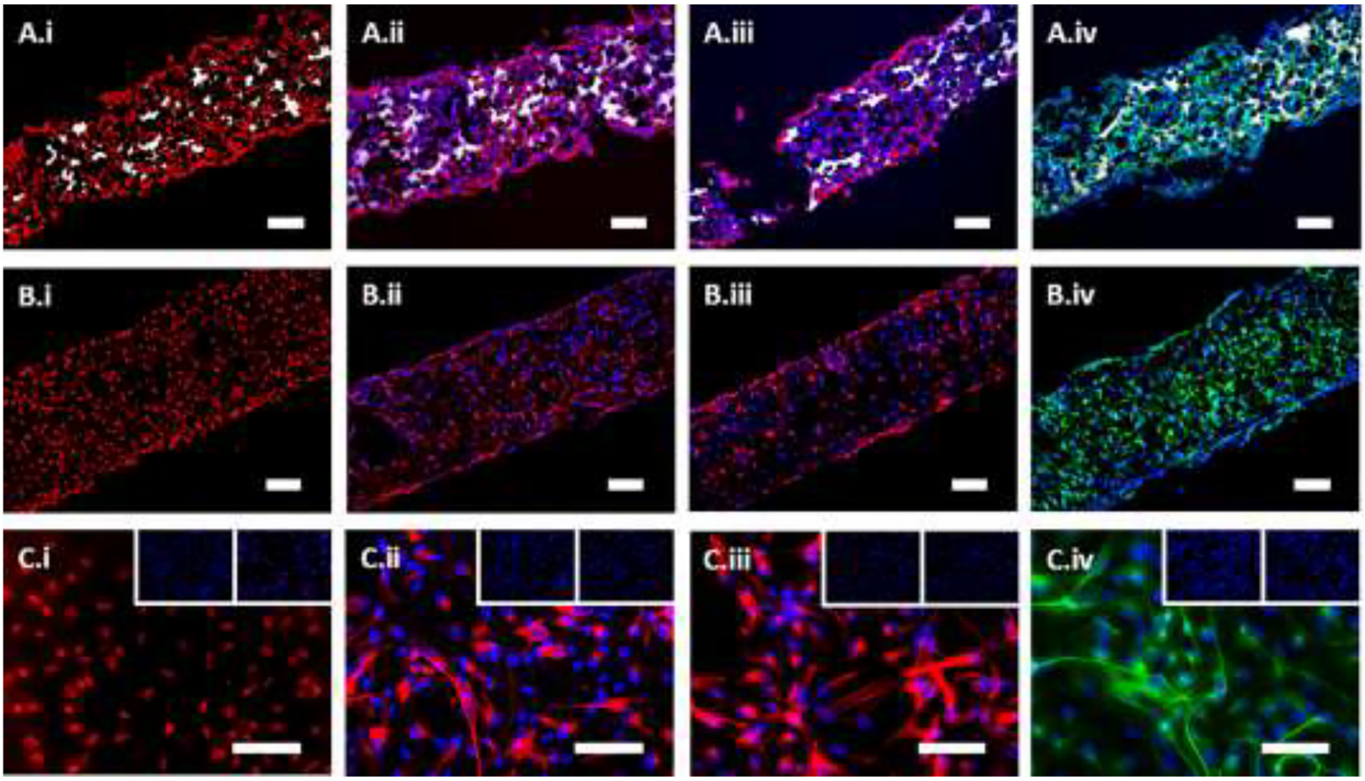

Fig. 14. Immunocytochemical detections of early neural protein markers in human induced pluripotent stem cells derived from neural precursor cells hiPSC-NPCs cultured in PEG-diacrylate (PEGDA) and trimethylolpropane triacrylate (TMPTA) polyHIPE scaffolds for 14 days: A) PEGDA polyHIPE scaffolds, B) TMPTA polyHIPE scaffolds and C) 2D control-glass slides. The stainings are: i) SOX1 detected with AF568 (red), ii) VIMENTIN with AF568 (red), iii) NESTIN with AF568 (red), iv) βIII-Tubulin with AF488 (green). Reproduced with permission from ref. 42 © 2019 Acta Materialia Inc. Published by Elsevier.

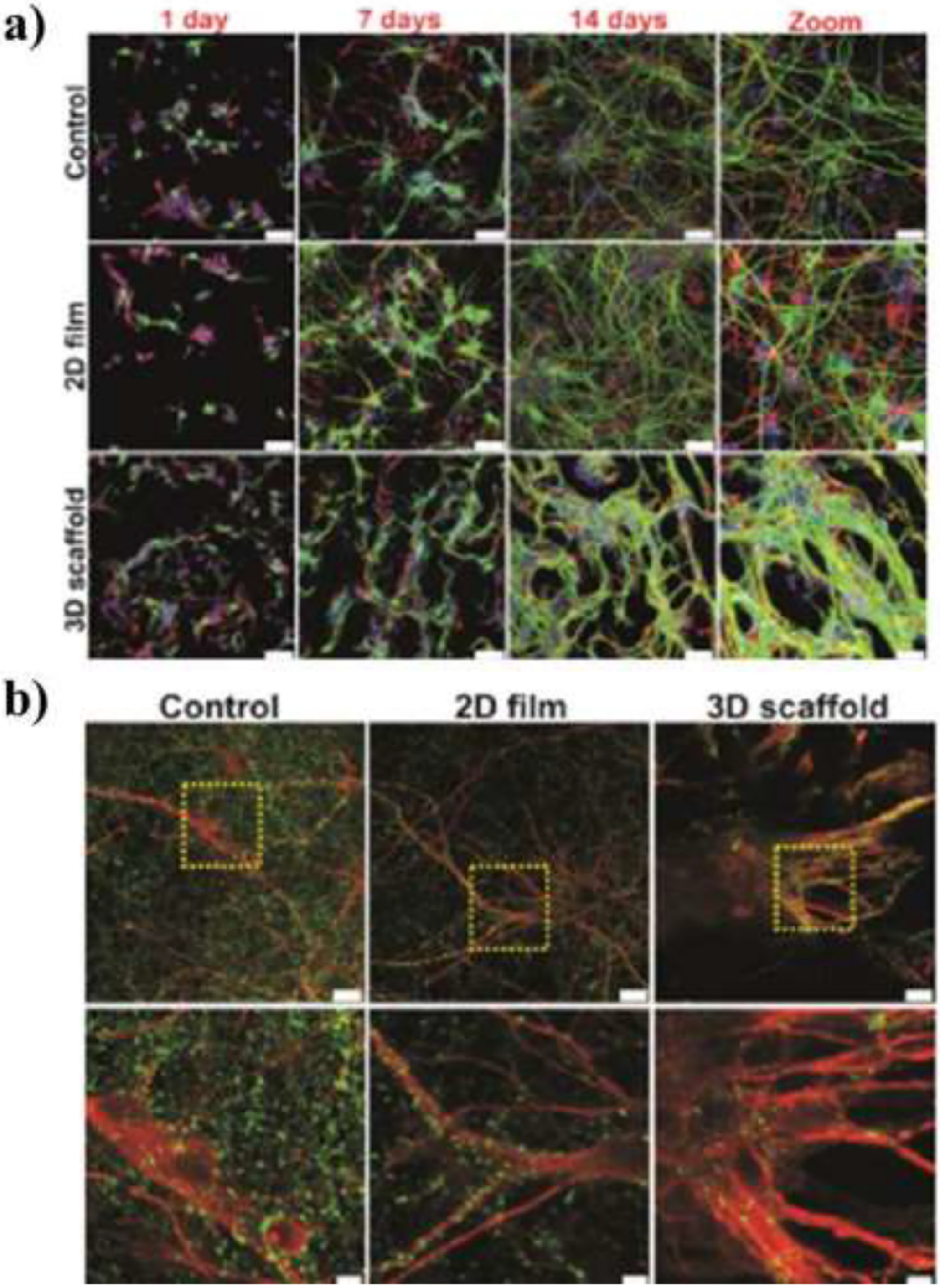

Fig. 15. (a) ENPC differentiation studies on graphene oxide-based substrates over time. CLSM images showing staining for map-2 (green), vimentin (red) and cell nuclei (blue) at different time points (scale bars are 50 μm, scale bars in zoom images are 25 μm). (b) Synapsis formation on the substrates. CLSM images showing staining for synaptophysin (green) and map-2 (red) at 14 days (scale bars are 25 μm for top images, 10 μm for bottom images in control, and 7.5 μm in 2D film and 3D scaffold). Adapted from ref. 131 with permission from the Royal Society of Chemistry.

connections. The authors attributed the equal differentiation of ENPCs toward both neurons and glial cells, to the higher adsorption of proteins within the scaffold because of a higher content of oxygenated functional groups compared to previously reported graphene-based substrates.

In view of the potential of carbon-based 3D scaffolds for cell growth and neural tissue repair, del Monte and co-workers explored their cytocompatibility for three types of mammalian cells (murine fibroblasts, human bone sarcoma cells and porcine endothelial progenitor cells). Time-lapse confocal laser scanning microscopy was employed for the first time to study cell migration processes in real time, within these 3D scaffolds [132]. The chemical nature of the polymers (chitosan, chondroitin sulfate, gelatin), the temperature of the ISISA treatment and the type of MWCNTs affected the porosity and surface roughness of the scaffolds. The scaffold architecture and morphology were found to be responsible for cell behavior. The highest viability was observed for scaffolds with a pore size similar to that of cells, and with lower surface

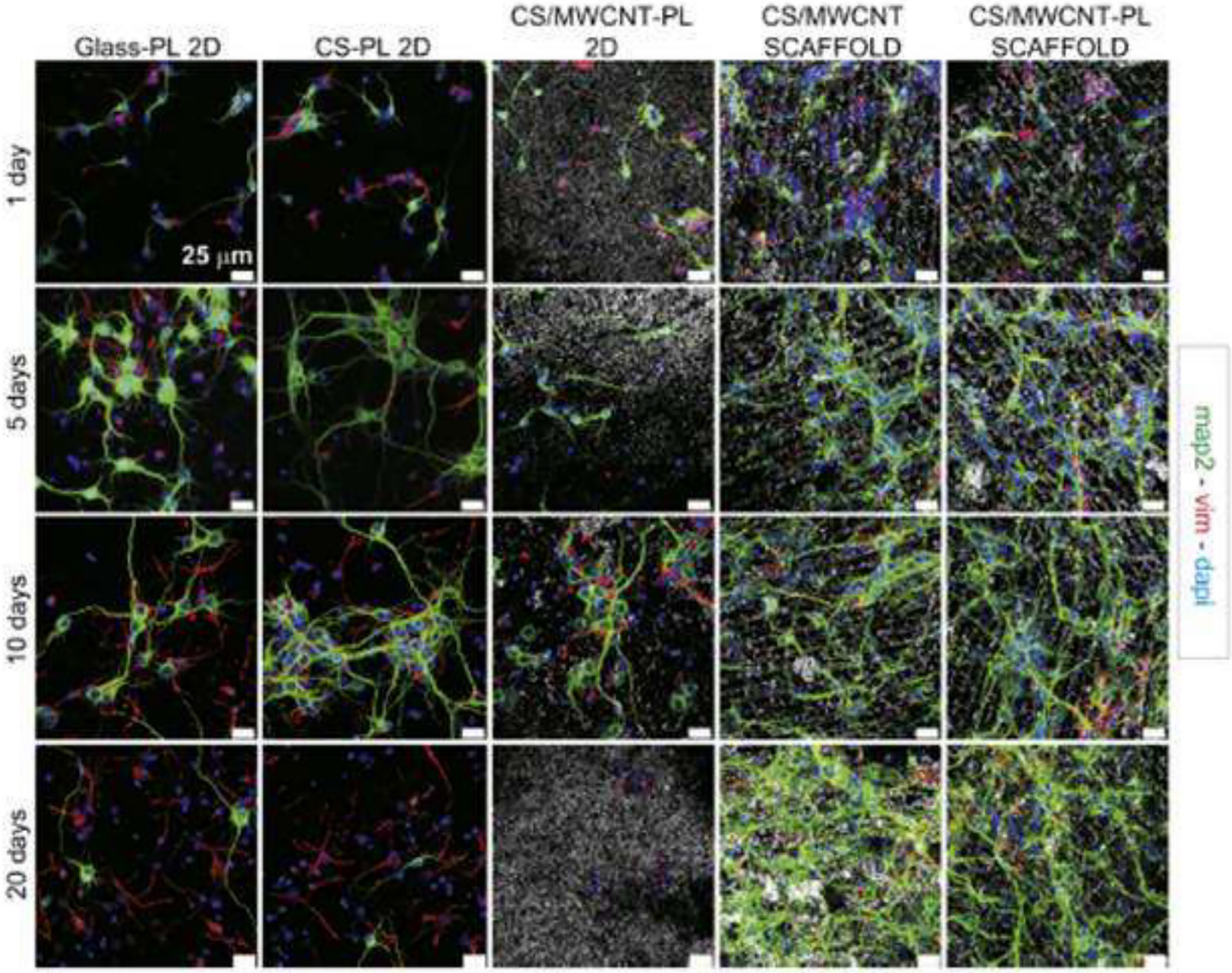

Fig. 16. ECNP differentiation studies on MWCNTs/chondroitin sulfate substrates. Representative CLSM images showing staining for map-2 (green), vimentin (red) and cell nuclei (blue) in different cell cultures. The reflection of the substrates containing MWCNTs can be observed to reveal substrate architecture. Scale bars represent 25 μm in all images. Reprinted with permission from ref. 133. Copyright © 2013 Elsevier.

roughness. The presence of MWCNTs was reported to not affect cell adhesion and morphology, so that the cells were mostly suspended in air, within pore spaces between walls. Therefore, if the size of the pore was comparable to that of the cells, contact points between cells and scaffold would be minimized. The results revealed that suitable cell-material interactions depend on material- and cell-dependent parameters, so optimization is required in every case. As a general rule, by minimizing the contact points between cells and scaffold, as well as surface roughness of the material, cell viability is improved.

Taking into account these results, Gutierrez et al. explored the use of chondroitin sulfate-based 3D scaffolds containing MWCNTs for nervous tissue repair (Fig. 16) [133]. These scaffolds featured an estimated pore area of 51% and an averaged pore width of 8.9 μm. A significant result was the formation of viable cultures enriched in neuron cells for up to 20 days, with the ability to display calcium transients and active mitochondria potential, even in the absence of poly-lysine coating, which was not the case for 2D substrates. The 3D structure of the scaffold appeared to protect the embryonic neural progenitor cells as compared to 2D cultures, while cell viability was supported up to 20 days within 3D scaffolds. It is worth mentioning the importance of developing new imaging and analytical tools for the study of complex 3D cell models as, in this case, the number and length of neurites including axons per surface unit could not be monitored over time, due to the complex 3D architecture of the substrate.

4.3. Cardiac tissue and neovascularization

The heart is known to be one of the most important organs in the human body, for its capacity to recycle and pump blood to all other organs. Cardiac engineering has progressed toward the fabrication of functional cardiac tissues through the use of artificial scaffolds that mimic the biological complexity of the required environment [134]. However, the biological mechanisms for heart tissue building need to fulfil some requirements that remain challenging for current tissue-engineering approaches. For example, it is important to introduce factors affecting the organization of the precursor cardiac cells (known as cardiomyocytes) or to achieve synchronized beating [135,136]. To study such diverse parameters, solid porous structures are required to support tissue growth while allowing the diffusion of oxygen and other factors required for cell growth and differentiation [25]. Efforts have been made to enlighten the relationship between pore size, shape and interconnected channels in porous scaffolds and the growth

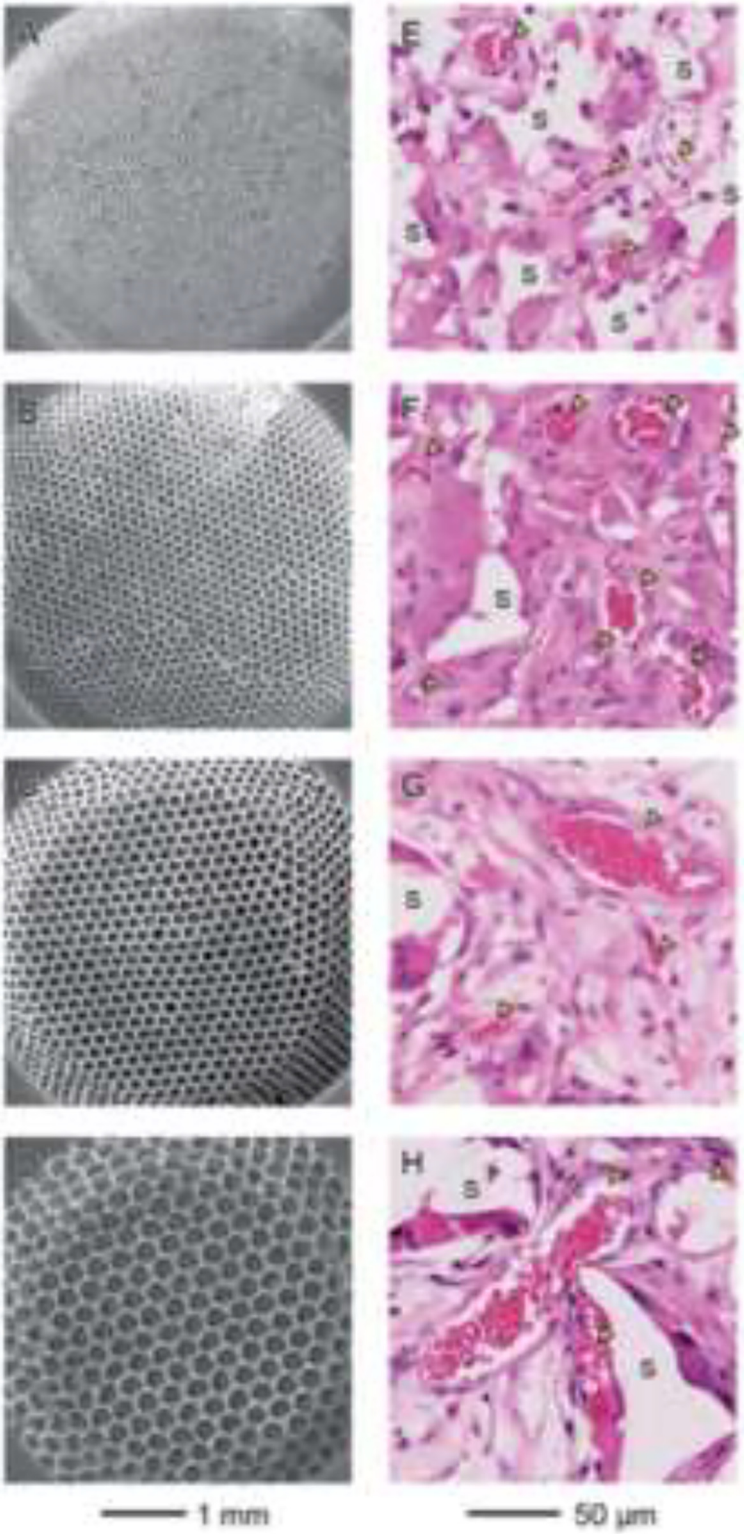

Fig. 17. (A–D) SEM images of PLGA inverse opals with pore sizes of 79, 147, 224 and 312 μm, respectively. (E–H) Bright field images representative of hematoxylin- and eosin-stained sections of the surface of each respective scaffold 4 weeks post-implantation. The areas marked with "S" correspond to the scaffold, while the yellow arrowheads indicate blood vessels. Reproduced from ref. 140 with permission from the Royal Society of Chemistry.

of cardiac tissue [137]. Most of the studies related to the use of IO for cardiac tissue engineering attempted to correlate the impact of pore size to the growth of new blood vessels. Several *in vitro* studies proved the existence of size thresholds that define the density and thickness of the new blood vessels [137,138]. Pores smaller than 200 μm favor the formation of smaller vessels in higher density, whereas bigger cavities induced a reduction in the amount of formed vessels, promoting increased diffusion (Fig. 17) [139,140]. Notwithstanding, excessively large pores would be unable to retain control over the interactions between cardiac cells due to far distancing, thus impeding the formation of new vessels. In a closer *in vivo* approach, Madden et al. studied the neovascularization and fibrous encapsulation by implanting diverse collagen-modified poly(2-hydroxyethyl methacrylate-*co*-methacrylic acid) scaffolds (with pores ranging from 20 to 80 μm) into the myocardium of immunocompetent rats [141]. After a 4 week time period, differences in the density of perfused vessels led to the conclusion that smaller pores achieved maximum vascularization while minimizing fibrous encapsulation. To explain the observed differences in neovascularization, variances in the phenotype of the interiorized cells were evaluated, concluding that an increase in neovascularization was promoted by the size of the pores inducing a shift toward prohealing, thereby enhancing the required vascularization.

5. Conclusions and outlook

Although porous scaffolds for tissue engineering have been around for quite a long time, the field is still blossoming, as new materials and techniques are developed. We have reviewed selected (colloid-oriented) fabrication methods toward 3D porous scaffolds with well-organized microstructures, as well as relevant applications thereof. In our view, the ideal scaffold should possess suitable pore size and porosity to promote cell-matrix and cell-cell interactions, as well as interconnected porosity to facilitate cell diffusion, and transport of nutrients and oxygen. Excellent advances in scaffold fabrication techniques already provide control over the above mentioned parameters, while offering the possibility to achieve scaffolds with gradient porosity and specific morphologies. Special attention should be paid to reducing the use of toxic chemicals, such as surfactants or harmful solvents that can damage cells and reduce the overall biocompatibility of the scaffold. Along with the fabrication technology, modulating the material composition enables tuning scaffold degradability, mechanical properties, bioactivity and biocompatibility for the target application. It is also quite obvious that targeted delivery of regulatory biomolecules or therapeutics will further benefit tissue development.

Concerning applicability, porous 3D scaffolds are generally aimed at tissue engineering or drug delivery applications. Besides optimized porosity, the mechanical properties and morphology of the scaffolds determine their suitability for each particular case of tissue regeneration. Specific materials or growth factors can also be incorporated, either before or after fabrication, to promote cell-differentiation into the targeted tissue. An important challenge in tissue engineering is to achieve vascularization within the artificial support and to provide the required blood supply for a successful implant. Drug encapsulation and sustained release from porous scaffolds over long periods of time are also possible, opening the way to disease treatment or drug screening within *in vitro* 3D models. The scaffold must ensure cell attachment and proliferation, but in most cases, cell migration deep into the 3D network can hardly be achieved and challenges remain to ensure nutrient diffusion deeper inside the material and cell proliferation beyond a few layers.

Despite of the continuous development of fabrication techniques to create scaffolds with ever-increasing sophisticated structures, we propose that future research should head toward the development of imaging tools which maintain high spatial and temporal resolution to monitor cellular events within the whole volume of the scaffold. As mentioned above, one of the main challenges faced when dealing with 3D scaffolds is to study cellular processes far from the surface of the material. Up to date, confocal fluorescence microscopy has generally been the technique of choice for cell imaging. However, this technique is still hindered by a limited penetration depth, and thus minimally invasive high resolution techniques with increased penetration depth are required for live-cell imaging within 3D scaffolds. Besides deeper penetration, other aspects such as long-term monitoring of cellular behavior in the absence of photobleaching, phototoxicity or quenching issues, will be of great importance toward a better understanding of tissue growth or disease progression. Other bioimaging options include Computed Tomography (TC), Magnetic Resonance Imaging (MRI) or Positron Emission Tomography (PET). However, their spatial resolution is still limited to 1 - 2 mm and single cell studies are not possible. Emerging techniques such as surface-enhanced Raman scattering (SERS) spectroscopy are interesting alternatives for bioimaging due to their non-invasive nature avoiding cell-fixation, deeper light penetration for biological tissues within the NIR window and high sensitivity. Since this technique takes advantage of the plasmonic properties of noble-metal nanoparticles, the use of colloid-based approaches to the construction of porous scaffolds offers plenty of possibilities toward the use of hybrid nanocomposite materials. The analytical capability of SERS for highly specific detection of relevant analytes may facilitate the *in situ* detection of cell-secreted molecules and relevant biomarkers that could give important clues to understand disease progression. SERS and related techniques are expected to facilitate *in vitro* drug screening and treatment validation, thereby speeding up the translation of materials into *in vivo* models or clinical trials. Therefore, significant advances in bioimaging and bioanalytical tools related to *in situ* monitoring of cellular processes within 3D scaffolds are expected to complement the development of more realistic 3D tissue models.

Dedication

Dedicated to our colleague and friend Ramón González Rubio.

Declaration of Competing Interest

The authors declare no conflict of interest.

Acknowledgements

The authors acknowledge financial support by the European Research Council (ERC-AdG-2017# 787510). C. G. A. thanks the Spanish State Research Agency for a Juan de la Cierva Formación Fellowship (FJCI-2016-28887). This work was performed under the Maria de Maeztu Units of Excellence Programme – Grant No. MDM-2017-0720 Ministry of Science, Innovation and Universities.

References

[1] Huh D, Hamilton GA, Ingber DE. Trends Cell Biol 2011;21:745–54.
[2] Yamada KM, Cukierman E. Cell 2007;130:601–10.
[3] Salerno A, Pascual CD. Process Biochem 2015;50:826–38.
[4] Loh QL, Choong C. Tissue Eng Part B Rev 2013;19:485–502.
[5] Qu H, Fu H, Han Z, Sun Y. RSC Adv 2019;9:26252–62.
[6] Zhu L, Luo D, Liu Y. Int J Oral Sci 2020;12:1–15.
[7] Shoichet MS. Macromolecules 2010;43:581–91.
[8] Hsu SH, Hung KC, Chen CW. J Mater Chem B 2016;4:7493–505.
[9] Li YC, Zhang YS, Akpek A, Shin SR, Khademhosseini A. Biofabrication 2017;9:1–16.
[10] Murphy SV, Atala A. Nat Biotechnol 2014;32:773–85.
[11] Gungor-Ozkerim PS, Inci I, Zhang YS, Khademhosseini A, Dokmeci MR. Biomater Sci 2018;6:915–46.
[12] Truby RL, Lewis JA. Nature 2016;540:371–8.
[13] Dutta RC, Dutta AK. Biotechnol Adv 2009;27:334–9.
[14] Williams DF. Biomaterials 2008;29:2941–53.
[15] Deb P, Deoghare AB, Borah A, Barua E, Das Lala S. Mater Today Proc. , 5Elsevier Ltd; 2018; 12909–19.
[16] Sgarminato V, Tonda-Turo C, Ciardelli G. J Biomed Mater Res B Appl Biomater 2020; 108:1176–85.
[17] Carletti E, Motta A, Migliaresi C. Methods Mol Biol 2011;695:17–39.
[18] Bose S, Roy M, Bandyopadhyay A. Trends Biotechnol 2012;30:546–54.
[19] B G, B L, P L, PX M. Regen Biomater 2015;2.
[20] Nikolova MP, Chavali MS. Bioact Mater 2019;4:271–92.
[21] Alvarez K, Nakajima H. Materials (Basel) 2009;2:790–832.
[22] Hollister SJ. Adv Mater 2009;21:3330–42.
[23] Olszta MJ, Cheng X, Jee SS, Kumar R, Kim YY, Kaufman MJ, et al. Mater Sci Eng R Reports 2007;58:77–116.
[24] Bramfeld H, Sabra G, Centis V, Vermette P. Curr Med Chem 2010;17:3944–67.
[25] João CFC, Vasconcelos JM, Silva JC, Borges JP. Tissue Eng Part B Rev 2014;20:437–54.
[26] Mishchenko L, Hatton B, Kolle M, Aizenberg J. Small 2012;8:1904–11.
[27] van Blaaderen A. Science 1998;282:887–8.
[28] Lange B, Metz N, Tahir MN, Fleischhaker F, Theato P, Schröder H-C, et al. Macromol Rapid Commun 2007;28:1987–94.

[29] Li X, Yu J, Jaroniec M. Surface science of photocatalysis. Interface Science and Technology. , 31Elsevier; 2020 (Chapter 3).
[30] Armstrong E, O'Dwyer C. J Mater Chem C 2015;3:6109–43.
[31] Aguirre CI, Reguera E, Stein A. Adv Funct Mater 2010;20:2565–78.
[32] Lima MJ, Correlo VM, Reis RL. Mater Sci Eng C 2014;42:615–21.
[33] Zhang YS, Zhu C, Xia Y. Adv Mater 2017;29:1701115.
[34] Zhang YS, Regan KP, Xia Y. Macromol Rapid Commun 2013;34:485–91.
[35] Meseguer F, Blanco A, Míguez H, García-Santamaría F, Ibisate M, López C. Colloids Surf A Physicochem Eng Asp 2002;202:281–90.
[36] Velev OD, Lenhoff AM. Curr Opin Colloid Interface Sci 2000;5:56–63.
[37] Carpenter R, Macres D, Kwak J-G, Daniel K, Lee J. Tissue Eng Part C Methods 2020;26:143–55.
[38] Kuai S-L, Truong V-V, Haché A, Hu X-F. J Appl Phys 2004;96:5982–6.
[39] Stein A, Li F, Denny NR. Chem Mater 2008;20:649–66.
[40] Pulko I, Krajnc P. Macromol Rapid Commun 2012;33:1731–46.
[41] Owen R, Sherborne C, Paterson T, Green NH, Reilly GC, Claeyssens F. J Mech Behav Biomed Mater 2016;54:159–72.
[42] Murphy AR, Haynes JM, Laslett AL, Cameron NR, O'Brien CM. Acta Biomater 2020;101:102–16.
[43] Sgarminato V, Tonda-Turo C, Ciardelli G. J Biomed Mater Res B Appl Biomater 2020;108:1176–85.
[44] Cameron NR. Polymer 2005;46:1439–49.
[45] Williams JM, Wrobleski DA. Langmuir 1988;4:656–62.
[46] Luo W, Zhang S, Li P, Xu R, Zhang Y, Liang L, et al. Polymer 2015;61:183–91.
[47] Cameron NR, Sherrington DC, Albiston L, Gregory DP. Colloid Polym Sci 1996;274:592–5.
[48] Barbetta A, Cameron NR, Cooper SJ. Chem Commun 2000:221–2.
[49] Kirkpatrick FH, Gordesky SE, Marinetti GV. Biochim Biophys Acta Biomembr 1974;345:154–61.
[50] Yang Y, Fang Z, Chen X, Zhang W, Xie Y, Chen Y, et al. Front Pharmacol 2017;8:287.
[51] Zhu Y, Huan S, Bai L, Ketola A, Shi X, Zhang X, et al. ACS Appl Mater Interfaces 2020;12:11240–51.
[52] Lee J, Chang JY. Chem Eng J 2020;381:122767.
[53] Luo W, Xu R, Liu Y, Hussain I, Lu Q, Tan B. RSC Adv 2015;5:92017–24.
[54] Palocci C, Barbetta A, La Grotta A, Dentini M. Langmuir 2007;23:8243–51.
[55] Chen K, Grant N, Liang L, Zhang H, Tan B. Macromolecules 2010;43:9355–64.
[56] Beckman EJ. J Supercrit Fluids 2004;28:121–91.
[57] Gutiérrez MC, García-Carvajal ZY, Jobbágy M, Rubio F, Yuste L, Rojo F, et al. Adv Funct Mater 2007;17:3505–13.
[58] Gutiérrez MC, García-Carvajal ZY, Hortigüela MJ, Yuste L, Rojo F, Ferrer ML, et al. J Mater Chem 2007;17:2992–5.
[59] Deville S, Saiz E, Tomsia AP. Biomaterials 2006;27:5480–9.
[60] Poursamar SA, Azami M, Mozafari M. Colloids Surf B Biointerfaces 2011;84:310–6.
[61] Zhang H, Hussain I, Brust M, Butler MF, Rannard SP, Cooper AI. Nat Mater 2005;4:787–93.
[62] Gutiérrez MC, Ferrer ML, Del Monte F. Chem Mater 2008;20:634–48.
[63] Deville S, Saiz E, Nalla RK, Tomsia AP. Science 2006;311:515–8.
[64] Ghosh D, Dhavale N, Banda M, Kang H. Ceram Int 2016;42:16138–47.
[65] Naglieri V, Bale HA, Gludovatz B, Tomsia AP, Ritchie RO. Acta Mater 2013;61:6948–57.
[66] Deville S. J Mater Res 2013;28:2202–19.
[67] Mukai SR, Nishihara H, Tamon H. Chem Commun 2004;4:874–5.
[68] Nishihara H, Mukai SR, Fujii Y, Tago T, Masuda T, Tamon H. J Mater Chem 2006;16:3231–6.
[69] Hortigüela MJ, Aranaz I, Gutiérrez MC, Ferrer ML, Del Monte F. Biomacromolecules 2011;12:179–86.
[70] Ferrer ML, Esquembre R, Ortega I, Reyes Mateo C, Del Monte F. Chem Mater 2006;18:554–9.
[71] Gutiérrez MC, Hortigüela MJ, Manuel Amarilla J, Jiménez R, Ferrer ML, Del Monte F. J Phys Chem C 2007;111:5557–60.
[72] Gutiérrez MC, García-Carvajal ZY, Jobbágy M, Yuste L, Rojo F, Abrusci C, et al. Chem Mater 2007;19:1968–73.
[73] Nieto M, Nardecchia S, Peinado C, Catalina F, Abrusci C, Gutiérrez MC, et al. Soft Matter 2010;6:3533–40.
[74] Guan LZ, Gutiérrez MC, Roldán-Ruiz MJ, Jiménez R, Ferrer ML, del Monte F. Adv Mater 2019;31:1903418.
[75] Gutiérrez MC, Jobbágy M, Ferrer ML, Del Monte F. Chem Mater 2008;20:11–3.
[76] Gutiérrez MC, Jobbágy M, Rapún N, Ferrer ML, del Monte F. Adv Mater 2006;18:1137–40.
[77] Christoph S, Kwiatoszynski J, Coradin T, Fernandes FM. Macromol Biosci 2016;16:182–7.
[78] Nishihara H, Mukai SR, Yamashita D, Tamon H. Chem Mater 2005;17:683–9.
[79] Rajamanickam R, Kumari S, Kumar D, Ghosh S, Kim JC, Tae G, et al. Chem Mater 2014;26:5161–8.
[80] Salerno A, Zeppetelli S, Di Maio E, Iannace S, Netti PA. Compos Sci Technol 2010;70:1838–46.
[81] Salerno A, Diéguez S, Diaz-Gomez L, Gómez-Amoza JL, Magariños B, Concheiro A, et al. Biofabrication 2017;9:35002.
[82] Diaz-Gomez L, Concheiro A, Alvarez-Lorenzo C, García-González CA. Carbohydr Polym 2016;142:282–92.
[83] Fanovich MA, Ivanovic J, Misic D, Alvarez MV, Jaeger P, Zizovic I, et al. J Supercrit Fluids 2013;78:42–53.
[84] Salerno A, Fanovich MA, Pascual CD. J Supercrit Fluids 2014;95:394–406.
[85] Fanovich MA, Jaeger P. Mater Sci Eng C 2012;32:961–8.
[86] Mou ZL, Zhao LJ, Zhang QA, Zhang J, Zhang ZQ. J Supercrit Fluids 2011;58:398–406.
[87] Tsivintzelis I, Pavlidou E, Panayiotou C. J Supercrit Fluids 2007;42:265–72.
[88] Kiran E. J Supercrit Fluids 2010;54:296–307.
[89] Salerno A, Domingo C. Microporous Mesoporous Mater 2014;184:162–8.
[90] Salerno A, Fernández-Gutiérrez M, San Román Del Barrio J, Domingo C. J Supercrit Fluids 2015;97:238–46.
[91] Salerno A, Fernández-Gutiérrez M, San Román Del Barrio J, Pascual CD. RSC Adv 2014;4:61491–502.
[92] Salerno A, Domingo C. J Supercrit Fluids 2019;143:146–56.
[93] Collins NJ, Bridson RH, Leeke GA, Grover LM. Acta Biomater 2010;6:1055–60.
[94] Bhamidipati M, Scurto AM, Detamore MS. Tissue Eng Part B Rev 2013;19:221–32.
[95] Reverchon E, Cardea S. J Supercrit Fluids 2012;69:97–107.
[96] Harris LD, Kim B, Mooney DJ. J Biomed Mater Res 1998;42:396–402.
[97] Salerno A, Domingo C. Polym Int 2014;63:1303–10.
[98] Salerno A, Saurina J, Domingo C. Int J Pharm 2015;496:654–63.
[99] Ji C, Annabi N, Khademhosseini A, Dehghani F. Acta Biomater 2011;7:1653–64.
[100] Annabi N, Mithieux SM, Weiss AS, Dehghani F. Biomaterials 2009;30:1–7.
[101] Tsioptsias C, Panayiotou C. J Supercrit Fluids 2008;47:302–8.
[102] Tsioptsias C, Paraskevopoulos MK, Christofilos D, Andrieux P, Panayiotou C. Polymer 2011;52:2819–26.
[103] Annabi N, Mithieux SM, Weiss AS, Dehghani F. Biomaterials 2010;31:1655–65.
[104] Gong T, Xie J, Liao J, Zhang T, Lin S, Lin Y. Bone Res 2015;3:15029.
[105] Hollister SJ. Nat Mater 2005;4:518–24.
[106] Kanczler JM, Wells JA, Gibbs DMR, Marshall KM, DKO Tang, ROC Oreffo. Principles of Tissue Engineering. Elsevier; 2020 (Chapter 50).
[107] João C, Almeida R, Silva J, Borges J. Mater Lett 2016;185:407–10.
[108] Cuddihy MJ, Kotov NA. Tissue Eng Part A 2008;14:1639–49.
[109] Choi S-W, Zhang Y, Thomopoulos S, Xia Y. Langmuir 2010;26:12126–31.
[110] Hu Y, Cao S, Chen J, Zhao Y, He F, Li Q, et al. Chem Eng J 2020;394:124895.
[111] Paljevac M, Gradišnik L, Lipovšek S, Maver U, Kotek J, Krajnc P. Macromol Biosci 2018;18:1700306.
[112] Abarrategi A, Gutiérrez MC, Moreno-Vicente C, Hortigüela MJ, Ramos V, López-Lacomba JL, et al. Biomaterials 2008;29:94–102.
[113] Hortigüela MJ, Gutiérrez MC, Aranaz I, Jobbágy M, Abarrategi A, Moreno-Vicente C, et al. J Mater Chem 2008;18:5933–40.
[114] Fonseca-García A, Mota-Morales JD, Quintero-Ortega IA, García-Carvajal ZY, Martínez-López V, Ruvalcaba E, et al. J Biomed Mater Res Part A 2014;102:3341–51.
[115] Bai H, Wang D, Delattre B, Gao W, De Coninck J, Li S, et al. Acta Biomater 2015;20:113–9.
[116] White LJ, Hutter V, Tai H, Howdle SM, Shakesheff KM. Acta Biomater 2012;8:61–71.
[117] Fenton OS, Olafson KN, Pillai PS, Mitchell MJ, Langer R. Adv Mater 2018;30:1705328.
[118] Santo VE, Duarte ARC, Popa EG, Gomes ME, Mano JF, Reis RL. J Control Release 2012;162:19–27.
[119] Kanczler JM, Barry J, Ginty P, Howdle SM, Shakesheff KM, Oreffo ROC. Biochem Biophys Res Commun 2007;352:135–41.
[120] Kanczler JM, Ginty PJ, Barry JJA, Clarke NMP, Howdle SM, Shakesheff KM, et al. Biomaterials 2008;29:1892–900.
[121] Li S, Song C, Yang S, Yu W, Zhang W, Zhang G, et al. Acta Biomater 2019;94:253–67.
[122] Bosi S, Rauti R, Laishram J, Turco A, Lonardoni D, Nieus T, et al. Sci Rep 2015;5:9562.
[123] Murphy AR, Laslett A, O'Brien CM, Cameron NR. Acta Biomater 2017;54:1–20.
[124] Kuo YC, Lin CC. Colloids Surf B Biointerfaces 2013;103:595–600.
[125] Kuo YC, Chung CY. Biomaterials 2012;33:8955–66.
[126] Kuo YC, Wang CC. Colloids Surf B Biointerfaces 2013;104:194–9.
[127] Kuo YC, Chiu KH. Biomaterials 2011;32:819–31.
[128] Yang JT, Kuo YC, Chiu K-H. Colloids Surf B Biointerfaces 2011;84:198–205.
[129] Murphy AR, Ghobrial I, Jamshidi P, Laslett A, O'Brien CM, Cameron NR. Polym Chem 2017;8:6617–27.
[130] Pérez-Álvarez MJ, Isiegas C, Santano C, Salazar JJ, Ramírez AI, Triviño A, et al. J Neurosci Res 2008;86:1871–83.
[131] Serrano MC, Patiño J, García-Rama C, Ferrer ML, Fierro JLG, Tamayo A, et al. J Mater Chem B 2014;2:5698–706.
[132] Nardecchia S, Serrano MC, Gutiérrez MC, Ferrer ML, Del Monte F. J Mater Chem B 2013;1:3064–72.
[133] Serrano MC, Nardecchia S, García-Rama C, Ferrer ML, Collazos-Castro JE, Del Monte F, et al. Biomaterials 2014;35:1543–51.
[134] Zhang YS, Aleman J, Arneri A, Bersini S, Piraino F, Shin SR, et al. Biomed Mater 2015;10:034006.
[135] Ahmed M, Yildirimer L, Khademhosseini A, Seifalian AM. J Nanosci Nanotechnol 2012;12:4775–85.
[136] Camci-Unal G, Annabi N, Dokmeci MR, Liao R, Khademhosseini A. NPG Asia Mater 2014;6:e99.
[137] Feng B, Jinkang Z, Zhen W, Jianxi L, Jiang C, Jian L, et al. Biomed Mater 2011;6:015007.
[138] Ye X, Lu L, Kolewe ME, Hearon K, Fischer KM, Coppeta J, et al. Adv Mater 2014;26:7202–8.
[139] Choi S-W, Zhang Y, MacEwan MR, Xia Y. Adv Healthc Mater 2013;2:145–54.
[140] Zhang YS, Choi SW, Xia Y. Soft Matter 2013;9:9747–54.
[141] Madden LR, Mortisen DJ, Sussman EM, Dupras SK, Fugate JA, Cuy JL, et al. Proc Natl Acad Sci 2010;107:15211–6.